Controlling the collective dynamics in systems of active oscillators through geometry and hydrodynamic entrainment

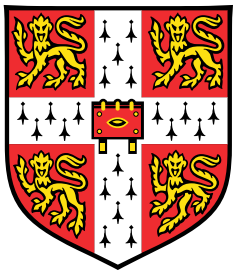

Evelyn Alexandra Waterhouse Hamilton

Department of Physics
University of Cambridge

This dissertation is submitted for the degree of
Doctor of Philosophy

King's College

April 2019

Declaration

This dissertation is the result of my own work and includes nothing which is the outcome of work done in collaboration except as declared in the Preface and specified in the text. It is not substantially the same as any that I have submitted, or, is being concurrently submitted for a degree or diploma or other qualification at the University of Cambridge or any other University or similar institution except as declared in the Preface and specified in the text. I further state that no substantial part of my dissertation has already been submitted, or, is being concurrently submitted for any such degree, diploma or other qualification at the University of Cambridge or any other University or similar institution except as declared in the Preface and specified in the text. It does not exceed the prescribed word limit for the relevant Degree Committee. It contains fewer than 60,000 words, including summary/abstract, tables, footnotes and appendices, but excluding table of contents, photographs, diagrams, figure captions, list of figures/diagrams, list of abbreviations/acronyms, bibliography and acknowledgements.

Evelyn Alexandra Waterhouse Hamilton
April 2019

Summary

Controlling the collective dynamics in systems of active oscillators through geometry and hydrodynamic entrainment
Evelyn Alexandra Waterhouse Hamilton

Synchronisation is broadly defined as the coordinated action of two or more individual elements that exhibit some time periodic behaviour. It is widely observed across different systems, where it is often a help or hindrance. Here the focus is on synchronisation facilitated by hydrodynamic coupling, with the viscous forces dominating. This style of coupling is spatially dependent, and so the steady state dynamics of the oscillators can be controlled using their positions. I study 'rower' oscillators, a highly simplified model for motile cilia that approximates each cilium by a rigid sphere that is driven by a geometrically updated force. The simplicity of the model lends itself to generic results that could be observed in many systems with hydrodynamic coupling.

This thesis is broken into two main parts. The first focuses on developing an analytical framework to further understand the synchronisation between two oscillators coupled through hydrodynamic forces. To achieve this a phase reduction is applied to the geometric oscillators. To apply a phase reduction first the transformation the natural phase is determined; the natural phase is characterised by constant phase velocity and involves a moving reference frame. Following the transformation, the interaction is subjected to an averaging process. The result is a continuous interaction function characterised by the phase difference of two oscillators. This dramatically simplifies the system and allows standard dynamical system techniques to be applied. The new interaction is verified through a comparison of relaxation time, before it is used to predict the steady state through the examination of fixed points. This framework is then used to demonstrate the ability to entrain a rower is not sensitive to changes in the characteristics of the rower motion, while the synchronisation between rowers is susceptible. Estimates of the relative synchronisation strength vis-a-vis the entrainment were calculated for two single cells flagellates and two types ciliated epithelium. Early results indicate different susceptibility between the species, and conclusions regarding interactions between oscillators should be drawn carefully from their behaviour under external flow. Applying

phase reduction to active, 'rower' oscillators reduces their dynamics to an interaction function depending exclusively on the phase difference. This ties them into the larger context of Kuramoto oscillators, one of the simplest and most widely studied types of phase oscillators. The phase reduction also allows fixed point analysis and other standard nonlinear techniques to be applied. Facilitating direct comparison between different oscillator motions and the prediction of the steady state dynamics.

The second part of this thesis departs from the earlier framework and instead phenomenologically explores how to control subset formation in rower arrays. This is achieved either through the array configuration or through characteristics of the oscillators. Often the arrays in this section are too large to be easily understood through the phase reduction approach, leading to investigations carried out predominantly by simulation. The hydrodynamic nature of the coupling allows the strength and coupling range to be altered using the geometry of the array. This can then influence the preferred geometry of any sub-populations that form in the array. Inspiration for specific controlling geometries is drawn from biological systems and abstract work focused on generic oscillators. Irregularities in the oscillators are also introduced in a regular way as an alternative control option that could be relevant for biological organisms. The geometric controls investigated showed the most consistent control of subset formation, but previously transient states were stabilised with each control mechanism. This section demonstrates the rich and complex collection of behaviours that can occur in systems with hydrodynamic coupling. This has applications in actualising states that are usually investigated more abstractly, and in biological systems where hydrodynamic forces are suspected to play a defining role.

Acknowledgements

I would like to thank everyone that has made my years in Cambridge such an enjoyable experience.
Firstly, many thanks to my supervisor Prof. Pietro Cicuta for his guidance and advice. Without his support I never would have had this opportunity.
My thanks also go to all of the people in BSS, past and present, who have offered their guidance and friendship. I particularly have to thank everyone in Room 903 for engendering such a great working environment. Many thanks to Nicola Pellicciotta and Luigi Feriani for being my cilia compatriots, and to Theresa Jakuszeit and Sam Bell who were there for many a Mathematica or CUDA malfunction. I have to thank Viola Introini for countless discussions, science related, email related, and otherwise. Thanks also to Nicolas Bruot for providing his code and starting off this work with rowers.
Many thanks to the Cambridge Trust and the Winton Programme for Sustainability for funding this PhD and providing opportunities for me to attend a range of international events.
I would also like to thank Marco Polin, Kirsty Wan, and Karl-Ferdinand Lechtreck who provided high quality videos of a range of different cilia for me to study.
Big shout out to all my friends inside and outside of the lab who put up with consistently slow responses to even the shortest of messages. Finally, many thanks to my family for their constant support. This would not have been possible without them.

Abstract

Emergent coordinated phenomena between groups of oscillators is grouped broadly as synchronisation behaviour. It is widely observed across different systems, where it is often crucial to function. Here the focus is on synchronisation facilitated by hydrodynamic coupling, in flow regimes where the viscous forces are dominant. The interest in synchronisation facilitated by this style of coupling is biologically motivated, but increasing miniaturisation of sensing devices is broadening its appeal. Coupling when strong viscous force are in effect is spatially dependent, and so the steady state dynamics of physical oscillators can be controlled using their positions. To investigate oscillators in this coupling the "rower model" is used. This is a highly simplified model that was inspired by living systems where viscous forces are critical to the dynamics, specifically by motile cilia. The model approximates each cilium by a rigid sphere that is driven by a geometrically updated force. The simplicity of the model lends itself to generic results that could be observed in many systems with hydrodynamic coupling. To study small arrays of rowers a phase reduction is applied in this thesis. This is a new framework when studying these geometric oscillators. The technique leads to a separation in the role of driving motion from the hydrodynamic coupling. The effects of each can then be investigated independently. This allows the steady state for different geometric configurations and pairs of non-identical oscillators to be predicted. The phase reduction model is useful when studying small systems or important subsets of oscillators, but at this stage it is cumbersome to visualise large systems. Instead larger systems with more complex behaviour are explored via simulation. The focus of the simulations is on the formation of subsets, with particular configuration encouraged through the layout of the system. Inspiration for systems demonstrating subset formation can be biological or more abstract work involving oscillators. In this work the swimming motion of starfish larva motivated an investigation into geometric and physical control mechanisms subset formation in long chains of oscillators. Inspiration was also drawn from more theoretical work, with the 'chimera state' observed in systems of rowers; the 'chimera state' is the incongruous situation where identical oscillators break into two populations: one coherent the other incoherent. This state had not previously been reported in systems coupled with hydrodynamic forces. The phase reduction model ties this oscillator model in the large context of generic phase oscillators,

while the hydrodynamic allows the coupling of the oscillators to be controlled and linked to a fundamentally well-understood phenomenon. The link is beneficial to understanding emergent properties of hydrodynamically coupled system, and for actualising states that are reported in oscillatory system with regular coupling but without a specific coupling method.

Table of contents

List of figures

List of tables

Publications

Some of the work in this thesis has been already published or submitted in peer reviewed journals.

- **The chimera state in colloidal phase oscillators with hydrodynamic interaction**

  E. Hamilton, N. Bruot, and P. Cicuta, *Chaos: An Interdisciplinary Journal of Nonlinear Science*, **27**(12):123108, 2017, is discussed in chapter 8

- **Interpreting the synchronisation of driven colloidal oscillators via the mean pair interaction**

  E. Hamilton, and P. Cicuta, *New Journal of Physics*, **20**(9):093028, 2018, is discussed in chapter 5

- **Synchronisation of mammalian motile cilia with hydrodynamic forces**

  N. Pellicciotta , E. Hamilton, J. Kotar , M. Faucourt , N. Spassky, P. Cicuta, *submitted*, is discussed in chapter 6

Chapter 1

Introduction

1.1 Setting the scene

Synchronisation is the coordinated action of two or more individual elements with some time periodic behaviour. It fits broadly under the umbrella of emergent behaviour where individual components demonstrate some collective outcome, and is widely observed across natural and technological systems, and studied in diverse scientific disciplines. Coordinated movement of elements submerged in a fluid with recurring motion have been the focus of research due to their biological relevance. Repetitive motions comes with some counter-intuitive requirements when high viscosities or small length scales are involved. Purcell coined the term "Scallop Theorem" to explain how when swimming in such a fluid the sequence of configurations becomes important, leaving a scallop stranded in viscous media. He explains

> inertial [force] plays no role whatsoever. If you are at very low Reynolds number, what you are doing at the moment is entirely determined by the forces that are exerted on you at that moment, and by nothing in the past. [1]

The Reynolds' number quantifies the relative importance of viscous compared to inertial forces when submerged in a fluid. Consequently oscillators that ignore the effect of inertia require some adaptation from traditional cyclic motion, with the organisms that live in this regime a rich source of inspiration.

Developing the connection between oscillators used specifically to investigate synchronisation in viscous fluids with work involving abstract and more generic concepts of oscillators is critical to informing the research into hydrodynamic coordination. In this work I connect one of the simplest oscillators used to study synchronisation in systems coupled with viscous forces to a simple fundamental class of oscillator, the phase oscillator. Further, I use the

opportunity provided by the hydrodynamic coupling to control the strength and range of the interaction.

The work in this thesis can be separated into two categories. The first is the development of the phase viewpoint for the specific model used. To test its validity established results are reproduced within this framework before it is related to questions involving the application of an external flow. External flows are used widely to probe living biological oscillators, and are a common event in hydrodynamic systems. The work reinforces the connection between the hydrodynamic niche and the field at large. Further it allows techniques developed for other systems to be applied to this style of hydrodynamic oscillator. The second part of the thesis involves numerical studies of oscillator arrays. The theme here is control of emergent subsets through spatial configuration. Inspiration is drawn from directly observing biological systems and more abstract, theoretical work involving oscillators. A deeper understanding of the changes resulting from spatial variation would shed light on systems that exhibit shape change or experience heterogeneous thinning in their carpet of cilia.

1.2 Layout of the thesis

I will first provide some background to research in the area of synchronisation in chapter 2. Some emphasis is placed on the style of coupling and on one specific type of oscillator, the phase oscillator. Further technical detail concerning coupling at low Reynolds' number is expanded upon in chapter 3. This is where the hydrodynamic tensors that are relevant to my work are discussed. The focus of chapter 4 is numerical implementation and data analysis. Here I discuss the oscillator model involved in my research, as well as a variety of measurements used to quantify and understand the systems investigated. Details of the code used to investigate these systems is also reviewed here, including both the code I developed and what was adapted from the earlier work of others. This chapter concludes the background and methods sections of the thesis.

A phase reduction is applied to the oscillator model in chapter 5, which is new to this particular type of oscillator; adapted from my work in [2]. The specifics of how this technique was applied are included in appendix B. An outcome of this is an expanded range of non-linear dynamic techniques can be applied. In chapter 6, developments using the phase reduction are used to address the difference between synchronisation and entrainment. Specifically the difference between detuning mutually interacting oscillators as opposed to a one directional interaction. The focus then shifts to the formation of subsets in populations of oscillators. In chapter 7 inspiration is taken from starfish larva to test a range of control mechanisms for creating smaller synchronised subgroups of oscillators. Following in a similar vein, the

existence of a chimera state, the incongruous situation where incoherent and coherent subsets coexist in a large set identical oscillators, is shown to form in a small array of oscillators coupled through hydrodynamics in chapter 8; adapted from my work in [3]. The work is then summarised in chapter 9, where the results are reviewed in a larger context and some future projects are discussed.

1.3 External contributions

The C++ code used throughout this thesis is based on code originally developed by Loic Damet. Nicolas Bruot included his own extensions to Loic's original code, and this was my starting version. In chapter 4 I state what changes I implemented in the code.

In chapter 6 a mix of published and unpublished video data is used to track the flagella of different species. Luigi Feriani developed the code that calculates a flagellum's centre of drag and the GUI to specify the flagellum for these calculations. Nicola Pellicciotta was responsible for tracking of the different flagella, and the in house cultivation of the mouse cilia. I would also like to thank Marco Polin, Kirsty Wan, and Karl-Ferdinand Lechtreck who provided high quality videos of their published data that Nicola could track.

1.4 Publication list

Completed papers

- N. Pellicciotta, E. Hamilton, J. Kotar, M. Faucourt, N. Spassky, P. Cicuta, Synchronisation of mammalian motile cilia with hydrodynamic forces, *submitted*
- E. Hamilton, and P. Cicuta, Interpreting the synchronisation of driven colloidal oscillators via the mean pair interaction. *New Journal of Physics*, **20**(9):093028, 2018.
- E. Hamilton, N. Bruot, and P. Cicuta, The chimera state in colloidal phase oscillators with hydrodynamic interaction. *Chaos: An Interdisciplinary Journal of Nonlinear Science*, **27**(12):123108, 2017.

Paper in preparation

- E. Hamilton, N. Pellicciotta, L. Feriani, P. Cicuta, Synchronisation and flow entrainment show different susceptibility to swimming stroke in viscous fluids.

- E. Hamilton, P. Cicuta, Hydrodynamic control mechanisms for subset formation in arrays of oscillators.

Chapter 2

Background information on synchronisation

2.1 The importance of synchronisation

Synchronisation is a phenomenon widely observed across a diverse range of different systems. An encompassing definition of synchronisation is required to capture the range of different behaviours. At a general level synchronisation can be understood "as an adjustment of rhythms of oscillating objects due to their weak interaction" [4]. This definition applies to systems of classical physical oscillators like the pendulum clock and quantum harmonic oscillators [4, 5]. Beyond mechanical and physical systems, oscillations and synchronisation extend to a variety of scientific disciplines, a range of which a shown in figure 2.1 [4, 6, 7]. One of the most famous examples in chemistry is the BZ oscillator or Belousov-Zhabotinsky oscillators [8, 9]. These oscillators interact through reactant diffusion and exhibit self-organisation, with the systems programmable with external light signals [10–12]. Biology is rife with examples of synchronisation [7, 13]. We are all acquainted with our circadian rhythms and the alignment with the day/night cycle; this becomes particularly apparent when crossing time zones [14, 15]. The response of plants to the day/night cycle is similarly well known, think of the blooming of flowers over a day [16–18]. These are all examples of biological systems reacting to an external signal, but they also exhibit self-organisation [7, 19]. The classic example is the flashing of fireflies [4, 19, 20]. While each firefly will have its own frequency, swarms will sometimes manage to flash in unison.

Synchronisation can be an aid or a hindrance in a system. In some cases synchronisation leads to an increase in efficiency or some other useful amplification feature [19, 24]. Blooming flowers align their scent production to the time when pollinators are most ac-

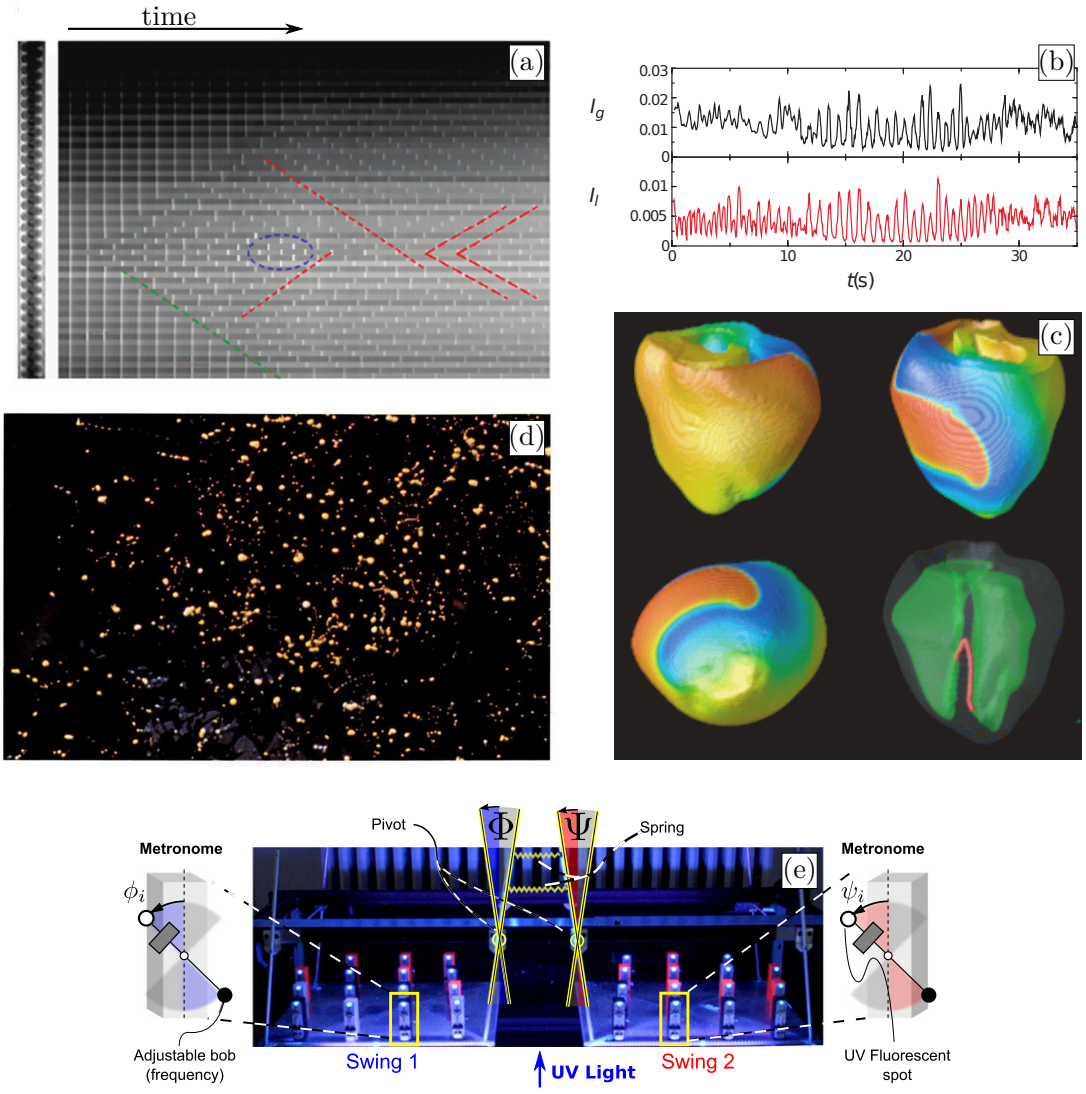

Fig. 2.1 Examples of different systems exhibiting synchronisation. (a) Starting from in-phase a chain of BZ oscillators, the chain shifts to a phase-locked state over time; adapted from [10]. (b) Intensity of applause when measured locally and globally. It shows clear sections of coordinated clapping; adapted from [21]. (c) A spiral wave in the rabbit ventricular geometry when simulating ventricular tachycardia, adapted from [22]. (d) A swarm of fireflies flashing in unison, adapted from [19]. (e) Coupled populations of pendulums, adapted from [23].

tive [25, 26]. Night blooming flowers are pollinated by moths and other insects at night, while day blooming are pollinated by bees and butterflies [26]. In the case of fireflies, the coordinated flashing is thought to increase visibility for mating pairs in dense jungle [19]. In other cases the amplification effect of synchronisation can have unfortunate consequences. There are several famous examples of bridges undergoing unanticipated deformation due to pedestrians inadvertently coordinating their steps [27, 28]. A more abstract case showing the disadvantage of synchronisation are financial markets [29, 30]. Upon receiving some external signal a synchronised sell-off can ensue. In the worst cases revealing mutual financial vulnerabilities across institutions. The synchronisation of financial decision making is of increasing importance in globalised markets attracting increasing scrutiny of market operators and regulators [29, 30].

2.2 Oscillator models

The vast array of different phenomena that fall into the category of synchronisation has resulted in a matching range of different models to understand their behaviour. At its most general an oscillator constitutes some periodic signal. In standard terminology the 'phase' of an oscillator indicates its relative position within its cycle, and the 'amplitude' is the observable signal. Oscillators can interact over different time-scales. Pulse oscillators only emit a signal at one point in their cycle, which is also their mode of interaction. The simplest example would be the integrate-and-fire oscillator, which is used to model neuron signalling or firefly flashing on an appropriate time scale [20, 31]. Alternatively oscillators can be constantly interacting, but with varying strength. Many of these oscillators fall inside the broad category of limit cycle with an important subset phase oscillation, but some are so sensitive to initial conditions that they are chaotic [4].

2.2.1 Limit-cycle oscillators

Oscillators that follow some closed attractive trajectory in phase space are called limit-cycle oscillators [4]. Moving along the attractive trajectory creates self-sustaining oscillations. Limit cycle oscillators are often used to model biological systems, including predator-prey cycles [32] and oscillations in different types of cells [33–36], as well as walking [37]. Limit cycle oscillators are used when the amplitude is important in the dynamics. This is often the case when oscillators are strongly coupled together or the important time scale is shorter than one cycle.

Limit cycle oscillators can interact in a pulsatile or smooth manner. If they are interacting at discrete times, the oscillators are usually referred to as pulse coupled oscillators. Pulse coupled oscillators or PCOs can be either inhibitory or excitatory. Excitatory oscillators encourage other oscillators to pulse once they do, inhibitory discourage. PCOs often display robust synchronisation due to minimal frustration in the system [38, 39]. The preference for firing all together or half a cycle apart (two special cases of phase-locking) depends on the nature of the oscillator, inhibitory or excitatory, and the rise time or speed of the pulse [40]. In extremely rapid interactions, excitatory oscillators fire together and inhibitory a half cycle apart. However when the rise time is slower, inhibitory oscillators fire together. In neuronal systems, it was found counter-intuitively that the rise time indicates inhibitory neurons play a greater role in synchronising neuronal firing than excitatory interaction [40]. Beyond being a popular model for neurons [41, 42], PCOs have also been used to model other phenomena which include earthquakes and market crashes [20, 29, 43–45].

When considering limit oscillators that interact in a continuous or smooth manner, one of most extensively studied is the Stuart-Landau oscillator. It has a perfect separation of the amplitude and phase variables, making it one of the simpler cases to study [46]. Stuart-Landau oscillators have been used to study amplitude oscillations and their coordination [47–49]. They are also used to investigate "oscillation death", where two autonomous oscillators approach a stable rest state when coupled [50, 49]. Often applied to systems with flow, Stuart-Landau oscillators have been used in to study fluid flows such as ocean gyres, vortex shedding, and the wake transitions [51–53]. Other common continuous limit cycle oscillators include Fitzhugh-Nagumo oscillators [54–56], which are often used to model neuronal spiking, and van der Pol oscillators, which are used as a model in a wide range of applications including the human circadian pace maker [57], animal gaits [37], among others [58–61].

2.2.2 Phase oscillators

A special subset of limit cycle oscillators are phase oscillators. The dynamics of these oscillators can be described with only the phase, as the amplitude can be calculated from the phase directly. This is an important simplification that is useful in many different cases. Generally phase oscillators are only studied in the context of weak coupling [62]. This is a result of the assumptions made to simplify into the phase only description, i.e. that perturbations do not move the oscillators far from their limit cycles [36]. The process to convert to a phase oscillation description is called phase reduction theory [62]. Applying phase reduction to interacting oscillators leads to an equation where the phase θ_i depends on

its own frequency ω_i and an interaction function depending on the phase difference [62–65],

$$\frac{d\theta_i}{dt} = \omega_i + \sum_{j=1}^{N} \Gamma_{ij}(\theta_j - \theta_i), \quad i = 1, \cdots, N. \tag{2.1}$$

The interaction is represented by the function Γ, which is often an integral averaging terms from the original limit cycle. The frequency ω_i is drawn from some continuous distribution. The Kuramoto model corresponds to the simplest case of Γ, with a single trigonometric function, the frequencies drawn from a symmetric unimodal distribution, and all the oscillators coupled equally,

$$\Gamma_{ij}(\theta_j - \theta_i) = \frac{K}{N} \sin(\theta_j - \theta_i). \tag{2.2}$$

K is the total coupling, and $1/N$ prevents problematic behaviour in large systems [63, 66]. There are a variety of extensions to the basic Kuramoto model. The oscillator's natural frequency is drawn from a range of distributions, including Gaussian and Lorentzian, or can be identical [67–70]. The style of coupling is extended from all equally coupled to other types including nearest neighbour coupling and complex network structures [69, 71–74]. The form of the periodic function can include a phase offset, transforming the function into a linear combination of sin and cos [69, 75–77]. This is often referred to as the Sakaguchi-Kuramoto model and has exhibited interesting partial synchrony behaviour [46, 78]. Including a further harmonic introduces even richer dynamics, which is useful when drawing parallels with some integrate-and-fire models [77, 79]. While the original model included only a single population of oscillators, situations with several different populations have also been developed [75, 76, 80, 81]. Recently, Kuramoto oscillators have been linked to some self-propelled agents, where the phase creates some attractive or repulsive mechanisms between the agents [82].

The simplicity of the phase model, exemplified by the Kuramoto model, has led to a diverse range of practical applications [63, 66]. It has been applied to systems throughout mammalian bodies. Examples range from neurons and neural networks [34, 83–86], circadian rhythms [87], to pacemaker cells in the heart [88]. Beyond internal systems within a body, phase models have also been used to further understand certain types of collective behaviour [20, 89]. The phase model also has applications in more traditional physics and engineering fields [6]. It has been used to understand synchronisation in superconducting Josephson junctions [90, 91], arrays of lasers [92], as well as in power networks [93, 94].

2.2.3 Other oscillators beyond limit cycles

Despite the broad classification for limit cycle oscillators, there are types of oscillators that do not fit inside this category. One group of such oscillators are chaotic-oscillators. While these oscillators display repetitive behaviour, their chaotic nature means it is impossible to predict their future trajectory from a given set of initial conditions. Despite their nature it is possible to entrain and synchronise chaotic oscillators, though it often requires an abstraction of ideas concerning phase. Two common chaotic oscillators are Rossler and Lorenz oscillators [95]. Chaotic oscillators can be supremely sensitive to signals and immune to others, and have applied to measuring weak signals [96, 97].

2.3 Classes of behaviour included under the umbrella of synchronisation

A number of different characteristics are included within the category of synchronisation. Here are listed some common types of coordination that apply to phase oscillators, though not exclusively. There are some further abstractions of these ideas that apply to other oscillator types, but they are not discussed in this thesis.

Frequency-locking or phase-locking

One example of synchronisation is when two or more oscillators with non-identical frequencies converge and persist with the same frequency. This behaviour is called frequency locking, or phase-locking as the phase difference between the oscillators is constant when the frequencies are equal [4]. The example that most intuitively exhibits this behaviour is the firefly swarm [20]. Each firefly has its own natural frequency, but the swarms flash in unison. This is the special case where there is no phase difference in the phase-locked state. The range of the frequency mismatch that will exhibit locking is often used as a measure for the coupling strength between oscillators.

In-phase or splay states

The special case where a population of oscillators are frequency locked and the phase difference is either zero (in-phase) or they are dispersed evenly through the cycle (splay, $2\pi/n$) [91, 98]. This is a more restrictive definition than frequency locking, but is especially useful when looking at identical oscillators. The oscillators naturally have the same frequency,

and so further restriction is required to distinguish between coupled synchronised oscillators, and oscillators with the consistent phase difference due to a lack of drift.

Chimera state

The chimera state is a mixture of synchronous and asynchronous behaviour within groups of identical oscillators [99, 100]. It is a type of partial synchronisation state. It is a more recent addition to the field, with many experimental realisations of chimera states being published [23, 101, 102]. This state is incongruous due to the identical nature of the oscillators. It is a clear example of emergent behaviour, where the collective behaviour differs despite having the same underlying unit.

2.4 Coupling structures

Historically the focus has been on either globally coupled oscillators or locally coupled oscillators [39, 103–105]. Recently there has been a shift to coupled complex networks or other forms of non-local coupling; non-local coupling is generic term for the coupling structures that are neither global or nearest-neighbour [73, 104, 106–108]. Schematics of different coupling styles, including non-local coupling, are shown in figure 2.2. A motivating force behind the focus on non-local coupling has been biological oscillators. Most living systems involving oscillators are interconnected but not omniscient, and are not well described as either locally or globally coupled [44, 104, 109]. The structure of the coupling is important when determining the behaviour of large systems.

2.4.1 Global coupling

Systems with oscillators experiencing force with equal contributions from all the other oscillators are called globally coupled [4, 63, 64]. This particular structure lends itself to mean field theory, in which the oscillators are viewed as interacting with some average field rather than each individual oscillator [63, 64, 75, 100]. The mean field approach revealed a ‘phase transition’ at some critical coupling strength for infinitely large systems of Kuramoto oscillators [63]. Since then the mean field approach has been used to look at multiple populations of globally coupled phase oscillators with some weaker interaction between the groups, in both finite and infinite systems [75, 76, 100]. The synchronisation between more complex oscillators that include amplitude effects that are globally coupled has also been considered with averaged parameters [64, 112, 113]. Though a long studied coupling structure there are still unresolved questions. Finite size fluctuations appear for smaller

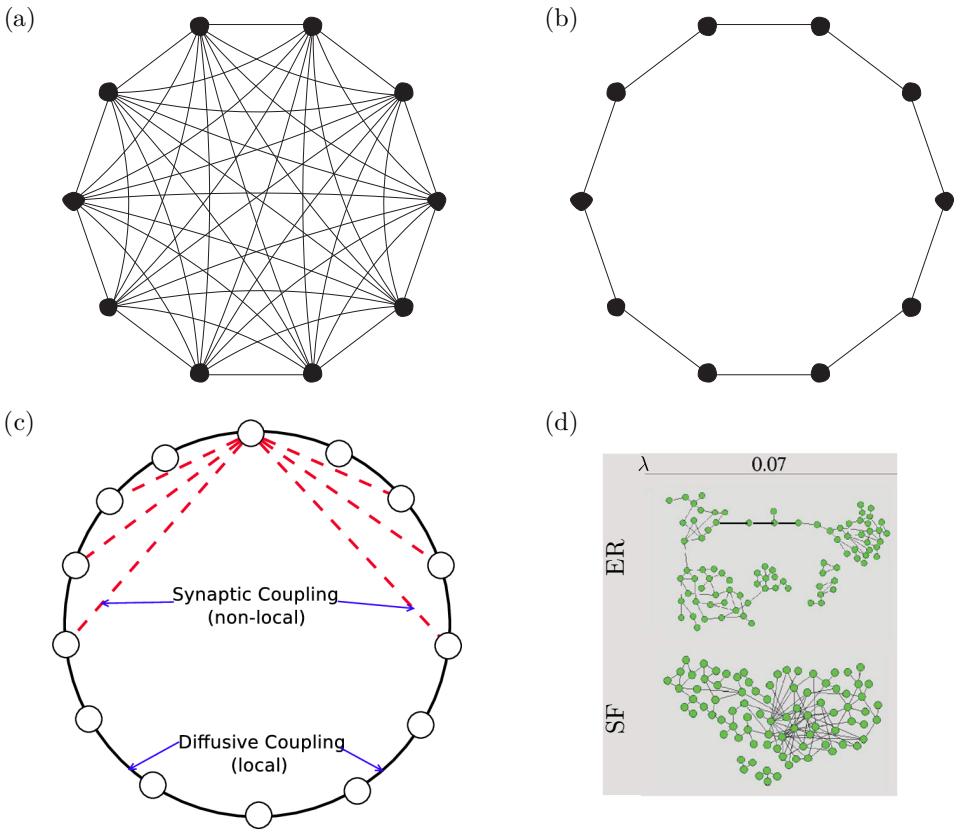

Fig. 2.2 Illustrating several coupling structures. (a) When oscillators are globally coupled they interact with all other oscillators; adapted from [110]. (b) The other extreme is local coupling, where oscillators only interact with their nearest neighbours; adapted from [110] (c) Nonlocal coupling refers to regimes somewhere between global and local and is of interest in biological systems, adapted from [111]. (d) Complex networks have some underlying structure that is neither regular or purely random, here are examples of Erdös-Renyi and scale free networks; adapted from [71].

systems globally coupled [63, 114], and how to understand the rich dynamics and chaos that is observed in systems with stronger coupling and more complex functions that include higher harmonics [65, 115].

Systems that can be reasonably understood to be globally coupled usually interact through some perceived mean field. This is intuitive when considering the synchrony that can occur during applause, in which case each person is responding to the crowd's noise not coordinating with their neighbours [4, 89]. Similarly for chirping crickets and flashing fireflies it is the sound or light from the group that the individuals respond to [116]. Not quite so intuitive is the synchronisation of a suspension of yeast cells [117]. The cells will synchronise their glycolitic processes, with the coupling occurring through the shared medium. Within the medium the transport occurs via diffusion, which for relevant scales has been approximated as global coupling [118, 119].

2.4.2 Local coupling

In global coupling every oscillator interacts, whereas when locally coupled only the nearest-neighbours oscillators interact. In one dimensional systems, nearest neighbours only includes two other oscillators. All the oscillators are connected in these systems through a sequence of neighbours, but they only directly interact with those nearest. Despite the indirect links between the oscillators, a one-dimensional infinite chain of Kuramoto oscillators cannot achieve global synchronisation when locally coupled [120, 121]. This is reminiscent of the Mermin-Wagner theorem, however synchronisation in finite chains can occur, with the required strength depending on the chain length [122, 123]. Higher dimensional lattices do display larger levels of cohesion, with the cohesion of oscillators in 2-dimensional systems depending on the number of nearest neighbours in the lattice [124, 125]. There are still open questions regarding the minimum number of dimensions that leads to macroscopic entrainment. When the oscillators are identical, nearest-neighbour coupling has demonstrated wave-like structures including solitons [126, 127]. The emergent behaviour of Kuramoto oscillators coupled locally depends on the type of oscillator, with pulse-coupled oscillators displaying synchrony even for one-dimensional infinite systems [128]. Consequently the time scale of the interaction and whether it can be approximated as discrete changes can dramatically shift the final behaviour of a population.

Systems that are coupled through diffusion are modelled using local coupling. This is particularly relevant for chemical oscillators which are often coupled through diffusion [9, 10, 129], but local coupling can also occur in other systems, for example in arrays of lasers or antennas [61, 130]. Diffusive coupling has particular relevance in terms of wave propagation and cell oscillations [62]. Agent based models with high density are often implemented with

local coupling, due to screening of visual or other sensory input [125, 131–133]. Pedestrians can self-organise due to visual cues, i.e. local, creating lanes of foot-traffic leading to faster travel [134, 135]. Humans display other collective behaviour through local coupling, for example the 'Mexican' wave in crowds [131]. Further, various gaits or styles of movement can be reproduced using locally coupling oscillators, with each limb represented by an oscillator and a stable state of the system being a gait [37, 136].

2.4.3 Non-local coupling

The regime between local and global coupling is classified as non-local coupling. Often this coupling is implemented through power law decay. This ties in with many physical interactions, and at the extremes replicates global and nearest-neighbour interactions [73, 105]. This can include nano-mechanical oscillators and vortices, to coupling in agent based models which approximate sensory limits using a power law [82, 137]. Varying the extent of the interaction can lead to phase transitions in oscillators systems [105, 106], and has motivated some interest in such transitions for hydro-dynamically coupled systems which has a power law interaction [138]. In recent years non-local coupling has been of particular interest in the chimera community, with chimera states observed in a variety of systems modelled with this coupling structure [100, 139–142].

2.4.4 Complex networks

Oscillators coupled with a complex network structure have connections between elements which are neither completely regular (lattice structure) nor purely random. Some examples are tree networks, with branching, Erdös-Renyi, and scale-free networks [72, 143]. Complex networks is another coupling structure designed to bridge the gap between global and nearest-neighbour coupling. Increasing the number of links between oscillators would intuitively convert the system to the global regime. In the limit this is true, but the transition is heavily dependent on the coupling structure. Random long range connections increase the robustness and rapidity of synchrony when compared to local dense coupling or nearest-neighbour coupling [103]. The stability of clustering and local pockets of synchronisation varies widely with underlying link structure.

Complex networks are particularly useful in biological and social systems which involve some element of randomness or agency in their interaction. Examples include the internet which involves complex networks for its hardware implementation and user networks, and human decision making models e.g. voting [143]. The study of oscillators in complex

networks has been particularly motivated by applications in neurology, genetic networks, and conservation efforts for endangered species [104].

2.5 Synchronisation facilitated by hydrodynamic coupling

Hydrodynamical coupling of oscillators is of interest due to the extensive range of systems where fluid is present [144]. Swimming is the obvious extension of walking when in fluid. The motion itself is often studied as an oscillator, similarly to walking, and the collective motion of groups of swimmers is an active area of research. Swimmers is a broad definition and include blue whales down to bacteria and algae, covering the extremes of organism size. The collective behaviour of larger swimmers like fish is thought to be the result of some judgement process of the animal, but in contrast micro-organisms are postulated to self-organise by coupling via the fluid [145–148]. When swimming at this length scale, it is the viscous forces which dominate rather than the inertial. This produces some initially counter-intuitive restraints on their motion [1, 145]. Beyond just swimming, building and engineering devices at this scale requires an understanding of oscillations in this regime, as to avoid unexpected resonances or to take advantage of self-organisation [149].

The minimal contribution from inertial forces for very small organisms results in an equation without a time derivative governing their motion,

$$\eta \nabla^2 \boldsymbol{u} - \overrightarrow{\nabla} P = -F, \tag{2.3}$$

where η is the viscosity. The velocity field of the fluid is $\boldsymbol{u}$ and P the pressure field. F is any external forces. This equation, its derivation, and some key results are discussed in detail in chapter 3. The critical aspect to note here is the absence of a time derivative, which leads to the system being purely position dependent unless F itself is time dependent in some way. Further, as will be shown in section 3.5, altering the boundary conditions leads to changes in the interaction range. The combination of position dependence and the boundary condition effect allows the coupling structure of oscillators coupled through a viscous fluid to be tuned. This is a useful control feature, and different coupling structures can lead to distinct emergent dynamics through slight changes in physical parameters of the system [106, 138].

2.5.1 Applications

Micro-swimmers

There are multitudes of micro-organisms that swim using flagella, and studies focus on a set of model organisms [150, 151]. *E. coli* is a favourite model organism among bacteria, but their flagella have a different motor and structure than eukaryotes [147]. The common models for eukaryotes include: *Chlamydomonas*, a single cell algae with usually two flagella swimming in a breaststroke style [152–157] and *Volvox*. *Volvox* are colonies of thousands cells, which have two types: somatic and germ cells. The somatic cells have two flagella, the strokes of which are coordinated across the colony allowing it to swim [146, 158]. *Paramecium* is another popular microswimmer but, though a single cell organism, it has a carpet of flagella with which it swims [159–161]. Experiments have revealed changes from in-phase and anti-phase behaviour [153, 162], and a dependence on spatial separation consistent with hydrodynamic coupling [162]. Other experiments have seen evidence of coupling beyond that which is expected from the fluid, and have postulated other coupling mechanisms [152, 163, 164]. Example include an internal elastic interaction or some form of cell-body rocking [163, 164]. Studies of these flagella have also informed choices for driving potentials for the different hydrodynamic oscillators [98, 160, 165, 166].

Fluid transport

The structure of flagella is conserved across eukaryotes, but in larger organisms they perform a variety of different functions. Motile cilia are the subset of flagella or cilia in a body that move. They beat periodically and are expressed by many species. In mammals they cover some of the epithelia, where they are critical for driving fluid movement along surfaces. In larger animals the cilia form carpets and are involved in several crucial processes: assisting in ova transport in the fallopian tubes, the delivery of cerebro-spinal fluid in the brain [167], and integral to mucous clearance, a critical aspect of defence against microbes and dust in the lungs. For all these processes, synchronised dynamics are essential. Cilia are of such importance, that their loss of function is studied medically as both a primary and secondary symptom [168, 169]. In primary cilia dyskinesia for example, anomalies in the cilia structure can inhibit their motion and ability to coordinate, leading to severe health complications [170]. Long term respiratory illness or trauma can also damage carpets of cilia or inhibit their ability to coordinate. Complications involving the motion of cilia (or their coordination) have been noted in cases of cystic fibrosis [171], asthma [172], and more broadly in chronic obstructive pulmonary disease [173]. Given the range and severity of

diseases involving cilia, many aspects of cilia, including their motion and synchronisation, are the subject of current research.

Artificial microswimmers

Mixing and transport of fluid at micron scales is growing in importance due to the miniaturisation of many processes and devices. Research into artificial micro-swimmers attempts to resolve this problem. Many applications for microswimmers are medical, hence the main constraint for microswimmers is bio-compatibility. Consequently, this has resulted in a push for externally driven artificial microswimmers. The two main approaches used to drive artificial swimmers are an external magnetic field, or an external electric field [174–177]. The swimmers themselves are often magnetic particles bound and functionalised using DNA [175, 178, 179], or thin filaments of a specialised material [174]. The magnetic particles can be small swimming dimers [179], or larger chains more similar to flagella. There remain challenges manufacturing artificial microswimmers at truly low Reynolds number [174], and controlling more than one swimmer is an issue [180].

2.5.2 Oscillator models specific to hydrodynamic coupling

There are several types of oscillator model that were developed to study synchronisation in systems with fluid coupling in a low Reynolds' number regime. Two very simple models which can be worked on experimentally using optical tweezers and colloidal particles are the rower and rotor models. Both use particles as oscillators to look for generic features that result from this particular style of coupling. Alternatively, some more complex models attempt to replicate specific behaviour of cilia and micro-swimmer by implementing models with driving mechanisms based on their observed motion. This class of models often focuses on determining efficiency of effectiveness of the motion.

Rower model

The rower model is one of the simplest and is used for investigating synchronisation through hydrodynamic coupling, and is reviewed in [181]. Each oscillator is a bead that is driven by a geometrically updating trap [181–185]. The oscillations are usually limited to one-dimension but they can be free to align in two-dimensional plane [186]. The geometric nature of the trap update leads to fixed amplitude oscillations, but the phase and frequency are free to change when interacting together.

At a small scale, pairs of rowers have demonstrated a switch between stable states, one in-phase and the anti-phase [98]. The change in state has repercussions when long lines of

rowers are simulated, with the correlation length increased for driving forces that correspond to cases with pairs in-phase [187]. Further micro-swimmers have been observed to also switch between in-phase and anti-phase motion in their flagella. Rowers have also been used to explore group alignment, of particular interest during the development of cilia when the organelles orient themselves. Long lines of rowers have been used to recreate metachronal waves, a sort of 'Mexican wave' exhibited by carpets of cilia [187]. Further, it has been shown that heterogeneity in the line of the rower, implemented as irregular spacing, increases the robustness of their collective motion [188]. Rowers are not only used to investigate the collective motion of flagella, but are also used to investigate collective behaviour via hydrodynamic interaction more abstractly [189, 190]. The hydrodynamic nature of the coupling allows control of the system coupling through position and alignment, a useful feature for designing and controlling systems of oscillators.

Rotor model

The rotor model is slightly more complex than the rower model. The oscillator is still a particle, but its trajectory is now some orbit in two-dimensional or three-dimensional space [138]. There is usually some flexibility or compliance in the precise path the rotor follows, in part because it increases the strength of pair-wise coordination [146, 193–195] and when modelling biological oscillators, imperfect repetition is a reasonable assumption [196]. The trajectories travelled by the rotor usually maximise one of two features. Either they use the simplest path possible or try and maximise the realism and use a trajectory based on the motion of biological swimmers [146, 153]. The benefit of the simple case is the same as the rower case, so the observations should be fairly generic. These simple cases have been able to reproduce both in-phase and anti-phase coordination between pairs [197], as well as showing that a change in drag dependence can switch between these states [198]. Further the basic force profile demonstrated a collective increase in fluid transport for pairs of rotors [199]. Conversely, hydrodynamic coupling is more directly linked to the organism's motion when experimentally based trajectories are implemented. Rotors based on the trajectory of *Volvox* flagellum have demonstrated in-phase motion and phase-locking [158]. Similarly rotors based on *Chlamydomonas* swimming have synchronised anti-phase, and metachronal waves in cilia carpets [153, 196].

Other models

There are many other models, of varying complexity used to model hydrodynamic oscillators. Some examples are shown in figures 2.3(d,e,f,g,h). In some cases the models build upon

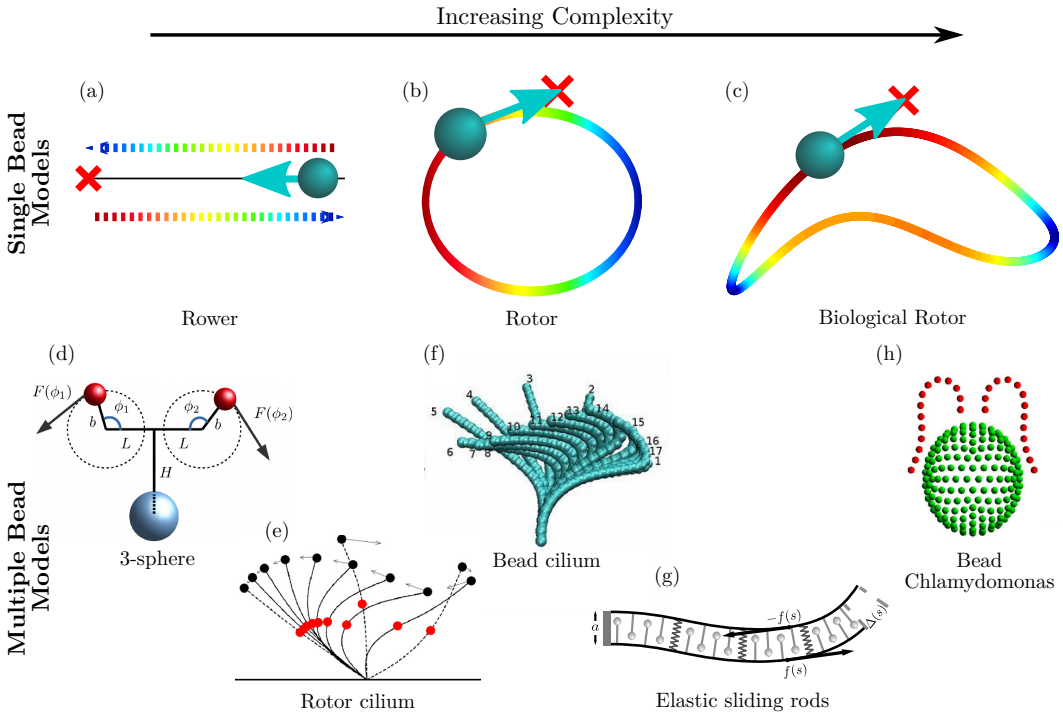

Fig. 2.3 Examples of some oscillators designed for low Reynolds' number regimes. (a) The rower model, where the oscillator is a sphere driven by a geometrically updating force (b) Simple rotors driven on circular orbits, usually with some flexibility in the trajectory or velocity variability. (c) Biological rotors are driven along trajectories based on experimental data. The shape of the trajectory is derived from the centre of drag of a particular flagellum. (d) 3-sphere model, a simple representation for a microswimmer using a combination of rotors; adapted from [138]. (e) Several rotors with different trajectories representing a cilium; adapted from [191]. (f) A cilium constructed from beads or spheres. The beads are linked elastically and driven to replicate a cilium's stroke, adapted from [165]. (g) An example of the sliding elastic rod model; adapted from [192]. The internal dynamics are chosen to replicate the motion of cilia. (h) A *Chlamydomonas* built up from many different particles, the red move to swim and the green are static; adapted from [164].

the rotor and rower models by combining spheres [164, 200]. This would include the 3-sphere model, and the bead flagella models where a chain of particles are linked by elastic forces [201–204]. The paddle model, elastic rod model, and cantilever model, by contrast are not related to spheres in any case but the extreme far-field. More complex models often study features of a given system. This is a response to the detail required to create these models, which often precludes general applications. Several models have been applied to studying the motion of *Paramecium* cilia [160, 165]. An extension to slender body theory has recreated the *Paramecium's* stroke and exhibited metachronal waves when simulated in large arrays [160]. The efficiency and robustness of *Paramecium's* motion has also been inferred using other rod models [24, 205]. Concurrently the flagella motion of *Chlamydomonas* has been studied in the same way, using filaments and resistive force theory to replicate its motion [155, 206, 207].

A heavily researched topic is the implied benefit of cilia beating for fluid transport, given its ubiquity in nature [206, 24]. This work usually focuses on the efficiency and robustness of the motion. In terms of efficiency, there are two types considered: the energy required to produce the motion, and how quickly the fluid/load transport occurs. The circumstances of the ciliated organisms vary, and so does the relative importance of the efficiencies and robustness. For single cell organisms, there main energy expenditure is swimming, and the energy efficiency of the beat is critical to their survival [24]. For mammals it is far more important that the motion is robust and imperturbable.

Chapter 3

Hydrodynamic coupling

3.1 Fluid flow encompasses different disciplines and scales

Fluid flow underpins many natural and technical processes. It is responsible for the spread of nutrients through blood, and leads to the spread of food and energy throughout the globe via ocean and atmospheric streams [208, 209]. Fluid motion is described by the Navier-Stokes equation, a differential expression for the flow field [210, 211]. It includes both the viscous and inertial components of fluid flow. Consequently it applies to systems as diverse as lava flow and bacterial swimming which are dominated by viscous forces, to the inertia centred regime in which mammals and fish swim [150, 212]. Some systems can span the entire spectrum, the vascular system for example [209]. When one particular effect dominates the motion, either inertial or viscous, it is possible to reduce the problem [210, 211]. Without these simplification it is incredibly difficult to advance, even with modern computing. This chapter is concerned with the situation where viscous forces dominate the motion, and will cover the development of the Navier-Stokes equation to the simpler Stokes equation before introducing some fundamental solutions to the simplified equations.

3.2 Navier-Stokes equation

The velocity field of an incompressible fluid $\boldsymbol{u}(\boldsymbol{r},t)$, at position $\boldsymbol{r}$ and time t, is governed by the Navier-Stokes equation [210],

$$\rho\left(\frac{\partial \boldsymbol{u}}{\partial t}+\boldsymbol{u}\cdot\overrightarrow{\nabla}\boldsymbol{u}\right)=-\overrightarrow{\nabla}P+\eta\nabla^2\boldsymbol{u}+\boldsymbol{F}. \tag{3.1}$$

The density of the fluid is ρ, and the viscosity is η. The fluid pressure field is $P(\boldsymbol{r},t)$, while $\boldsymbol{F}(\boldsymbol{r},t)$ is the contribution from all external forces and includes the effect of gravity.

In many situations, including this work, fluids are assumed to be incompressible. The standard form for incompressibility condition stems from the conservation of mass equation,

$$\frac{\partial \rho}{\partial t} + \overrightarrow{\nabla} \cdot (\rho \boldsymbol{u}) = 0. \tag{3.2}$$

When the fluid is incompressible the density is a constant, and so the equation simplifies to,

$$\overrightarrow{\nabla} \cdot \boldsymbol{u} = 0. \tag{3.3}$$

3.3 Stokes Equation

3.3.1 Reynolds' number

The Reynolds' number is a measure for the ratio of inertial forces to viscous forces [210]. It depends on the characteristic length scale of the system L, characteristic velocity U, as well as the density and viscosity, ρ and η. Specifically the Reynolds' number Re is,

$$Re = \frac{UL\rho}{\eta}. \tag{3.4}$$

The Reynolds' number is small when a fluid is highly viscous, i.e. ηs is large. Alternatively the particle could be very small or light, with any combination L, U, and ρ very small. When Re is very small the Navier-Stokes equation, see 3.1, can be simplified to the Stokes' equation; a derivation of which is demonstrated in the following section. The consequence of low Re is the loss of inertial terms, and the governing equation becomes linear and instantaneous as well as reversible in time and space. This dramatically changes the net effect of reciprocal motion, i.e. a cycle constitutes a set of configurations that are actuated forward and then in reverse to return to the initial position. In the low Reynolds' regime the speed of passing through the different configurations are irrelevant, and without this there is no net change from performing reciprocal motion. This result is often referred to as the Scallop Theorem, referring to Purcell's famous example of an animal unable to swim at low Reynolds' number [1].

For humans with a $L \approx 10^0$m, $U \approx 10^0 - 10^1 \mathrm{m}/s$ and water with density and viscosity $\rho \approx 10^3$ and $\eta \approx 10^{-3}$, the Re$\approx 10^6 - 10^7$. Our lives exist where inertial forces determine behaviour. For *E. coli* that have $L \approx 2 \times 10^{-6}$m and $U \approx 50 \times 10^{-6} \mathrm{m}/s$ in water, the Reynolds number is $\approx 10^{-4}$ and viscosity shapes their lives [213]. Even more extreme values occur

in lava domes, which due to their high viscosity can have a Reynolds number as small as 10^{-10} [212].

3.3.2 Deriving Stokes' equation

The Navier-Stokes equations reduces to the Stokes equations in the low Reynolds' number regime. Converting the Navier-Stokes equation in 3.1 to dimensionless units results in,

$$\frac{UL\rho}{\eta}\left(\frac{\partial \tilde{\boldsymbol{u}}}{\partial \tilde{t}} + \tilde{\boldsymbol{u}} \cdot \overrightarrow{\nabla}\tilde{\boldsymbol{u}}\right) = -\overrightarrow{\nabla}P_c + \nabla^2\tilde{\boldsymbol{u}} + \tilde{F}. \tag{3.5}$$

The tilde notation is to distinguish between the dimensionless case. In this form the dependence of the inertial terms of the Re is explicit. Assuming $Re \ll 1$, and reintroducing units results in the expression for Stokes' equation,

$$\eta\nabla^2\boldsymbol{u} - \overrightarrow{\nabla}P = -F. \tag{3.6}$$

There is no time dependence in the above equation, as a consequence the flow updates instantaneously. The flow can be determined without information of the system at any other time. The linearity of the equation is responsible for the time irreversibility associated with creeping flow.

3.4 Oseen tensor

In this section we are interested in the simplest solution for Stokes equations. The flow field resulting from a point force will be introduced, but first the drag force on a sphere is discussed. The drag force a sphere experiences due to a flow is,

$$\boldsymbol{F} = \gamma\boldsymbol{v}. \tag{3.7}$$

For a sphere with radius a, the equation can be solved analytically with no slip boundary conditions, resulting in $\gamma = 6\pi\eta a$ [210]. This is called Stokes drag coefficient.

To calculate the flow field $\boldsymbol{u}(\boldsymbol{r})$ generated by a particle, the force exerted by the particle is assumed to be a point force,

$$\boldsymbol{F}_\rho(\boldsymbol{r}) = \boldsymbol{F}\delta(\boldsymbol{r}), \tag{3.8}$$

where the particle is assumed to be at the origin. The force density is $\boldsymbol{F}_\rho$ and $\boldsymbol{F}$ the total force. The linearity of Stokes' equation (3.6) implies the solution for the velocity field will

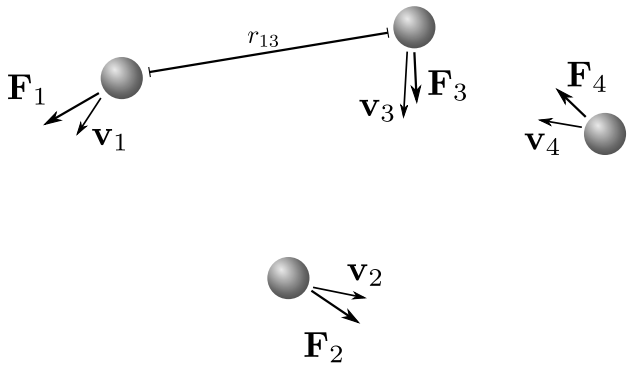

Fig. 3.1 The particles are coupled through a viscous fluid. When far from any boundary, the interaction between point forces is described by the Oseen tensor. The coupling is entirely dependent on the relative position and distance between the different particles, $\hat{\mathbf{r}}_{ij}$ and r_{ij}. As a consequence of the interaction, the particles do not move directly parallel to the force that is being applied.

depend linearly on the force applied. Hence $\boldsymbol{u}(\boldsymbol{r})$ is expressed as,

$$\boldsymbol{u}(\boldsymbol{r}) = \mathbb{G}(\boldsymbol{r}) \cdot \boldsymbol{F}, \tag{3.9}$$

where $\mathbb{G}(\boldsymbol{r})$ is an appropriate tensor. $\mathbb{G}(\boldsymbol{r})$ can be solved for in several ways [214], including using Fourier transforms see Appendix A. The result is the 3x3 Oseen matrix,

$$\mathbb{G}(\boldsymbol{r}) = \frac{1}{8\pi\eta r}\left(\mathbb{I} + \hat{\boldsymbol{r}} \otimes \hat{\boldsymbol{r}}\right), \tag{3.10}$$

where $\mathbb{I}$ is the identity matrix in 3-dimensions, r is the distance from the particle and $\hat{\boldsymbol{r}}$ the associated unit vector. The flow field generated by a point force is called a Stokeslet.

The linearity of the Stokes equation (3.6) allows the flow field of N particles to be calculated using superposition. In general, the superposition of Stokeslets can be written as,

$$\boldsymbol{u}_i = \sum_{j=1}^{N} \boldsymbol{\mu}_{i,j} \cdot \boldsymbol{F}_j, \tag{3.11}$$

with the velocity of the ith particle $\boldsymbol{u}_i$ depending on the sum of the forces on the others $\boldsymbol{F}_j$. $\boldsymbol{\mu}$ is called the mobility matrix. It is a second rank tensor, i.e. a NxN array of $\boldsymbol{\mu}_{i,j}$. The mobility matrix is replaced by $\boldsymbol{H}$ the Oseen tensor for the special case where particles are in an unbounded fluid. The tensor is found by superimposing the solution for a pair of

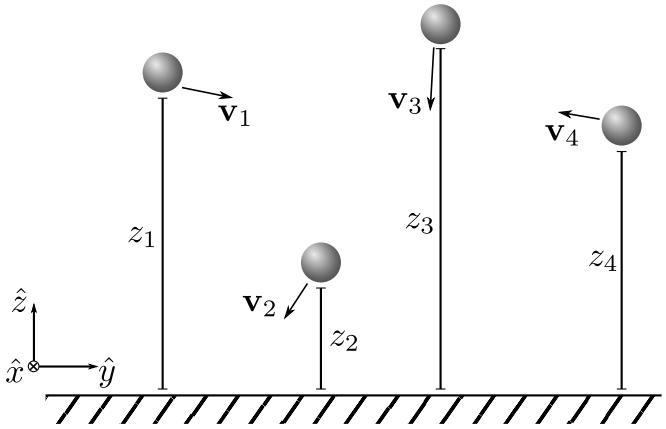

Fig. 3.2 Particles near a no-slip boundary experience higher drag, and their coupling is heavily dependent on their height above the surface z_i. Near the boundary the coupling strength decays quickly, but far from the boundary the interaction is similar to that of the Oseen tensor.

particles [214, 211], see equation (3.10), and takes the form,

$$\boldsymbol{H}_{ij} = \begin{cases} \frac{1}{\gamma}\boldsymbol{I}, & i = j, \\ \frac{1}{\gamma}\frac{3a}{4r_{i,j}}\left(\boldsymbol{I} + \hat{\boldsymbol{r}}_{ij} \otimes \hat{\boldsymbol{r}}_{ij}\right), & i \neq j. \end{cases} \tag{3.12}$$

where the distance between two particles is $r_{i,j} = |\boldsymbol{r}_j - \boldsymbol{r}_j|$ and the associated unit vector $\hat{\boldsymbol{r}}_{ij}$. The diagonal terms are given by the Stokes drag, which assumed a point force. To neglect the particle size and meet this assumption the particles must be far from one another ($r_{i,j} \gg a$).

The Oseen tensor is used for most simulations and theoretical calculations of small systems in this thesis. It avoids unnecessary complexity and minimises the parameters describing the system. The tensor has a slow decay rate ($1/r$) which leads to long range interaction. No system truly exists in an infinite medium, and for systems with large numbers of particles this approximation becomes increasingly unrealistic. Instead for systems with more particles the Blake tensor is used. This tensor has a faster decay rate and is discussed in the following section.

3.5 Blake tensor

Near a solid boundary the solution for a point force can be developed using the method of images [215]. The image flows are chosen to ensure the flow at the boundary is zero. The solution is named for Blake who first derived it. The diagonal terms of the tensor, i.e. the

drag a bead experiences corrected for the wall's presence, is,

$$\boldsymbol{\mu}_{ii}^{B} = \frac{1}{6\pi\eta a}\left(\begin{bmatrix}1&0&0\\0&1&0\\0&0&1\end{bmatrix} - \frac{9}{16}\frac{a}{h}\begin{bmatrix}1&0&0\\0&1&0\\0&0&2\end{bmatrix} + h.o.t\right), \tag{3.13}$$

where h is the height above the wall. It has been assumed that the height is constant, i.e. the particle moves in a plane parallel to the wall.

The off-diagonal terms of the Blake tensor are a combination of Stokeslet flows $\boldsymbol{G}^{Os}$ (Oseen tensors), a stresslet and rotlet $\boldsymbol{G}^{St}$ (Stokeslet doublet), and a source doublet $\boldsymbol{G}^{So}$ [211].

$$\boldsymbol{\mu}_{ij}^{B} = \boldsymbol{G}^{Os}(\boldsymbol{r}_i - \mathbf{r}_j) - \boldsymbol{G}^{Os}(\boldsymbol{r}_i - \bar{\boldsymbol{r}}_j) + 2h^2\boldsymbol{G}^{So}(\boldsymbol{r}_i - \bar{\boldsymbol{r}}_j) - 2h\boldsymbol{G}^{St}(\boldsymbol{r}_i - \bar{\boldsymbol{r}}_j). \tag{3.14}$$

The position of the jth rower is $\boldsymbol{r}_j = (x_j, y_j, h)$. The image rower position is marked by $\bar{\boldsymbol{r}}_j = (x_j, y_j, -h)$. The expressions for each of the Green's functions is as follows,

$$\boldsymbol{G}^{Os}(\boldsymbol{r}) = \frac{1}{8\pi\eta}\frac{1}{r}\left(\boldsymbol{I} + \frac{\boldsymbol{r}\otimes\boldsymbol{r}}{r^2}\right), \tag{3.15}$$

$$\boldsymbol{G}^{So}_{\lambda\nu}(\boldsymbol{r}) = \frac{1}{8\pi\eta}(1-2\delta_{\nu 3})\frac{\partial}{\partial r_\nu}\left(\frac{r_\lambda}{r^3}\right), \tag{3.16}$$

$$\boldsymbol{G}^{St}_{\lambda\nu}(\boldsymbol{r}) = (1-2\delta_{\nu 3})\frac{\partial}{\partial r_\nu}G^{Os}_{\lambda 3}(\boldsymbol{r}) \tag{3.17}$$

The decay rate of the Blake tensor depends on the height above the boundary. Increasing h decreases the contribution from the image terms, with the Blake tensor equivalent to the Oseen in the limit $h \to \infty$. In this regime the tensor decays as $1/r$. At the other extreme where h is very small the interaction decays very quickly. This becomes apparent when considering the xx coupling between two particles,

$$\mu_{ij}^{B,xx} = \frac{1}{8\pi\eta}\left(\frac{1}{r_R} + \frac{\Delta x^2}{r_R^3} - \frac{1}{\sqrt{r_R^2+4h^2}} - \frac{\Delta x^2+2h^2}{(r_R^2+4h^2)^{3/2}} + \frac{6h^2\Delta x^2}{(r_R^2+4h^2)^{5/2}}\right). \tag{3.18}$$

The distance between the two particles is r_R and the distance to the image particle is $r_I = \sqrt{r_R^2+4h^2}$. The particles are separated by some distance along x labelled Δx. Assuming the separation and force are aligned along x, i.e. $r_R = \Delta x$, and assuming the particles are close to the wall $h \ll r$ then the coupling is approximately,

$$\mu_{ij}^{B,xx} \approx \frac{3h^2}{2\pi\eta r_R^3} + \mathscr{O}\left(\frac{h^4}{r_R^5}\right). \tag{3.19}$$

The approximation employed truncates the function using the first order Taylor series. In this regime the coupling decays as $1/r^3$, much faster than in the "bulk" Oseen case.

The effect is even more extreme when considering coupling perpendicular to the application of the force. Assuming the force is applied along x and the particles are separated by a distance r_R in y, i.e. $\Delta x = 0$, then the near wall Blake coupling is

$$\mu_{ij}^{B,xx} = \frac{1}{8\pi\eta}\left(\frac{1}{r_R} - \frac{1}{\sqrt{r_R^2+4h^2}} - \frac{2h^2}{(r_R^2+4h^2)^{3/2}}\right) \approx 0 + \mathscr{O}\left(\frac{h^4}{r_R^5}\right). \tag{3.20}$$

At the other extreme when $h \to \infty$ the Blake tensor converges to the Oseen, the solution calculated with no boundary,

$$\mu_{ij}^{B,xx} \approx \frac{1}{8\pi\eta}\left(\frac{1}{r_R} + \mathscr{O}(h^{-1})\right) \to \frac{1}{\gamma}\frac{3a}{4r_R}, \quad \text{as } h \to \infty. \tag{3.21}$$

Consequently the orientation of the particles movement has increasing importance when decreasing the height above the no-slip boundary.

In this thesis the Blake tensor is used to couple large systems of rowers. This avoids problems with cumulative forces that grow unbounded with the system size.

3.6 Zeta tensor

To emulate the change in decay rate of the interaction, I developed a tensor based on the 'bulk' case. The new tensor has a more direct method of adjusting the interaction range. I call this tensor the "zeta tensor", referring to the new parameter that I introduced. The tensor is inspired by hydrodynamic tensors, but it is not a solution to Stokes' equation. Specifically the tensor has the same form as the Oseen tensor with an added parameter ζ that defines the decay rate of the interaction,

$$\boldsymbol{H}_{ij} = \begin{cases} \mathbf{I}/\gamma & : i = j \\ \frac{3}{4\gamma}\left(\frac{a}{r_{ij}}\right)^{\zeta}\left[\mathbf{I} + \hat{\mathbf{r}}_{ij}\hat{\mathbf{r}}_{ij}\right] & : i \neq j \end{cases}, \tag{3.22}$$

as before $\gamma = 6\pi\eta a$ is the drag, and $\hat{\mathbf{r}}_{ij}$ and r_{ij} are the direction and distance between rowers. To remain within sensible regimes the parameter ζ is restricted to the interval $[1,3]$. Unlike the Blake tensor, it is immediately apparent in the Zeta-tensor how quickly the interaction decays. However, this new form does not mimic the increasing sensitivity to orientation that the Blake has when the distance from the wall is small. This is demonstrated in figure 3.3.

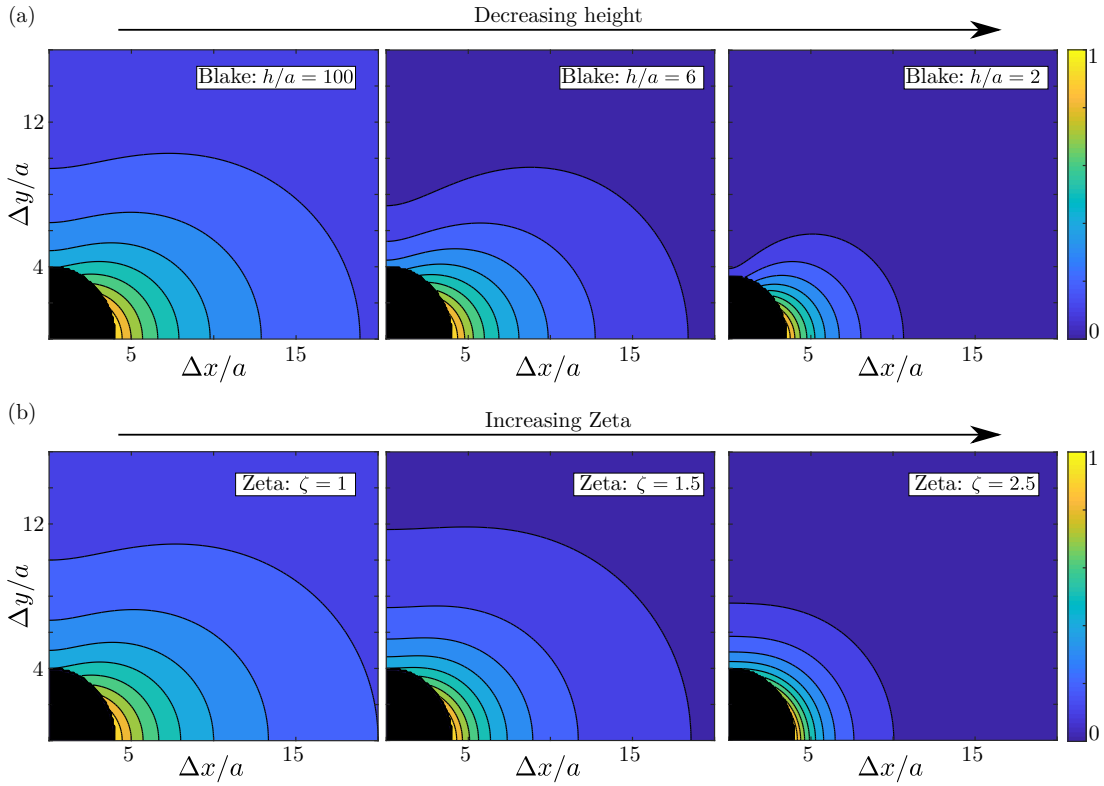

Fig. 3.3 The Zeta tensor can be used in proxy for the Blake tensor when varying the height above a boundary. In the Zeta tensor, the interaction decay rate is a direct input. (a) The decay of the coupling strength in x for the Blake tensor as the height is decreased. The coupling strength is normalised by the maximum in each case, to ease comparison. (b) The decay of the interaction strength in x for the Zeta tensor when increasing ζ. There is not the same orientation dependence in the Zeta case, with slower decay when Δy is increased. This can be minimised by rotating the oscillation direction in the Blake case.

The decay of the coupling strength for the Zeta tensor is shown in 3.3(b), with similar Blake cases in (a). The Zeta tensor has a similar landscape, but with a different decay rate when changing ζ. In the Blake examples, the interaction along y decays much faster near the wall. It is possible to minimise this difference by adjusting the direction of the oscillations.

The Zeta-tensor is used exclusively in chapter 8. The system is small in this case, but controlling the range of the interaction is crucial for the formation of the particular state explored in that chapter.

Chapter 4

Implementation of numerical methods and data analysis

4.1 Implementing the rower model in simulation

The rower model is highly simplified, and so represents the dynamics of the hydrodynamic oscillators in a coarse fashion [181]. In the model each oscillator is represented by a bead, though biological flagella involve slender filaments [150, 216]. In the far-field, i.e. for large separation distances, the flow field resulting from a filament should approach that of a sphere [181, 217]. Moreover a hard sphere does not require many assumptions regarding its internal dynamics, where as slender filament does [165, 218–220]. These include the flexibility of slender cylinder, how the filament is driven and if and how any noise is applied to the driving mechanism. The trajectory for rowers is also simplified, usually restricted to one degree of freedom. The justification for this assumption is the presence of a cell wall from which flagella protrude [181]. The wall suppresses the flow perpendicular to the wall [215], and as a consequence it is reasonable to restrict the oscillations to one dimension that is parallel to the wall [217]. Beyond simplifying the dynamics, this approximation relaxes the restrictions on the driving force that result from the oscillator trajectory. The magnitude of the force can be set arbitrarily with position in the rower model, where as two-dimensional trajectories must balance the relative forces along the two directions to maintain the desired orbit [221].

The oscillations of the rower model are created by a geometrically updated driving potential. The potential must be either strictly increasing or decreasing, depending on whether the trap is attractive or repulsive. The switch is geometric. i.e. position based. When a bead passes a given threshold the driving potential is updated (flipped) and the

rower reverses its direction. This criteria is used to enforce the strictly increasing/decreasing requirement on the driving potential, and so regularises the model [182]. For example, for a rower driven by a square root potential the switch prevents it from reaching the vertex of the potential where the force would diverge. Further, more specific detail regarding the implementation of driving potentials is discussed in section 4.1.1.

4.1.1 Driving forces

Attractive traps

The rower is assumed to oscillate along a direction, say x, driven by a potential trap that is updated geometrically. The shape of the potential contains in a coarse-grained fashion the degrees of freedom of the complex cilium shapes and activity, and the far-field fluid dynamics can be matched to a given biological system [181]. While the potential in the model can be any strictly increasing function, I predominantly focus on a simple power law with kx_r^{α}; k is the trap strength and x_r the distance relative to the vertex of the trap. Details of the model are represented in figure 4.1, with aspects of the power law potentials covered in 4.1(b). The position update behind the oscillations is illustrated in figure 4.1(a). Once a rower passes a certain threshold x_s the trap is reflected and the bead reverses direction, with the threshold measured relative to the vertex. The reflection axis is chosen to create oscillations with amplitude A. The period of the oscillation $2\tau_0$ is set by the driving potential and the drag in the fluid γ.

The pair-wise behaviour of rowers is dependent on the shape of the driving potential [98]. When the rowers accelerate into the traps, i.e. $\alpha < 1$ and have negative curvature, they are known to move in-phase and will tend to the same point in their cycle. Conversely, when they decelerate into the traps, $\alpha > 1$, the rowers will move anti-phase and be half a period out of step with each other.

Repulsive traps

Oscillations can also be created by repelling the rower from a trap and including a geometric update similar to the attractive case. In this case the particles are repelled from the trap, and once they pass a threshold the trap position is updated to reverse the rower's direction. A schematic of a particle in the repelling traps in shown in figure 4.2(a). Similar to the attractive potentials, it is often useful to measure the particle position relative to the trap vertex x_r and the update point depends on an offset x_s that is also measured relative to the vertex. However, in this case the trap updates when the rower exceeds a distance $A + x_s$ relative to the vertex. The swap to repulsion also switches the sign of a potentials curvature, so rowers in traps with

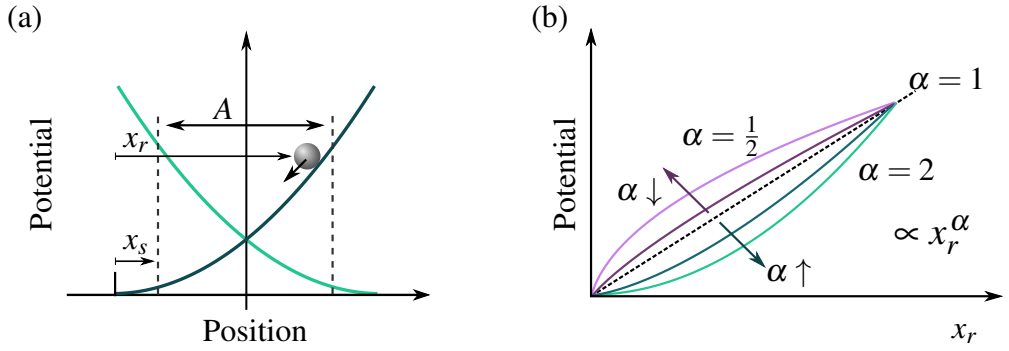

Fig. 4.1 Rower are driven by a geometrically updating trap, resulting in free phase and a frequency depending on the fluid drag. (a) The bead is driven along a strictly increasing potential. Once it reaches the threshold x_s, the trap is reflected and the direction of the bead reversed. The switching trap results in oscillations with an amplitude A. It is often simpler to specify a rower's position through its position relative to the trap vertex x_r. (b) The most common driving potential used is a simple power law, $\propto x_r^{\alpha}$. The trap has negative curvature when $\alpha < 1$, and positive when $\alpha > 1$.

$\alpha > 1$ accelerate into the trap and $\alpha < 1$ decelerate. It was shown in [98] that this leads to a swap in the steady state of the rower pair.

4.1.2 Noise implementation

At the scales considered, Brownian noise comes into play [98]. Thermal fluctuations on each bead result from the random forces applied by the fluid molecules. This noise is included using the Ermack-McCammon method to emulate Brownian dynamics [222]. The drag of the each particle depends on the position, and so the noise is multiplicative. The implementation of the noise affects the Fokker-Planck equation associated with the original Langevin, with a drift correction required in some cases [223, 224]. However, in this case it is unnecessary as the noise is implemented using the Ito convention. The Ito convention refers to the case where the position dependent aspect of the noise is evaluated at the beginning of the discretised time interval. Labelling the noise on ith particle as f_i, the mean and variance of the noise is,

$$\langle f_i(t)\rangle = 0, \qquad \langle f_i(t) f_j(t')\rangle = 2k_B T H_{ij}^{-1}\delta(t-t'). \tag{4.1}$$

The variance depends on the hydrodynamic tensor H_{ij}^{-1} as well as the temperature T and Boltzmann's constant k_B. For an isolated particle, the noise is white with the Stokes' drag coefficient scaling the size of the fluctuations.

The method for evaluating the noise is unchanged from the original work by Loïc Damet [225]. The hydrodynamic tensor is evaluated at the start of the time interval and a

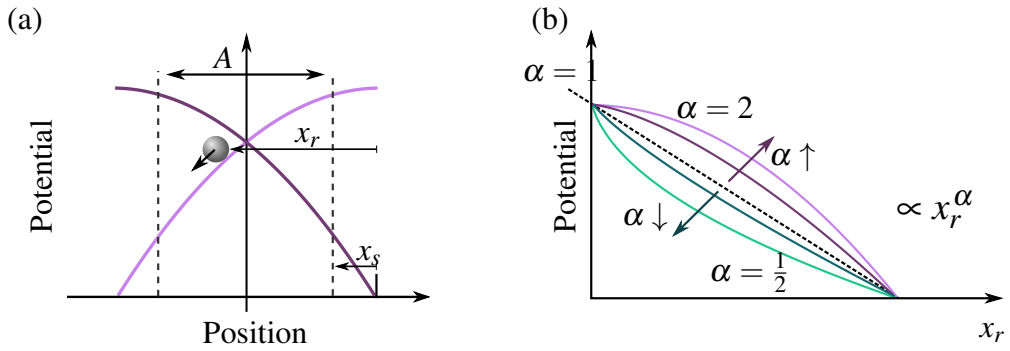

Fig. 4.2 Inverting the driving potentials leads to repulsive forces. (a) The position to the vertex is x_r, but now the particle moves away from the vertex. Similarly the switch point now occurs at $A + x_s$, with x_s ensuring the bead does not stagnate. (b) When using power laws, the switch to repulsive traps changes the curvature associated with a given potential. In this case $\alpha > 1$ has negative curvature and the particles accelerate into the trap, and $\alpha < 1$ has positive curvature.

Cholesky decomposition calculated. The decomposition uses functions inbuilt to the GNU scientific library GSL. The resulting tensor is then combined with the white noise to update the rower position.

4.1.3 The Langevin equation

To simulate the rowers, each rower is updated using the following equation,

$$\dot{\boldsymbol{r}}_i = \sum_{j=1}^{N} \boldsymbol{H}_{ij} \cdot \left(\boldsymbol{F}(\boldsymbol{r}_j) + \boldsymbol{f}_j \right). \tag{4.2}$$

There are a total of N rowers in the system, which are coupled through the tensor $\boldsymbol{H}_{ij}$. The different forms of the interaction used were discussed in chapter 3. The rowers are driven by the potentials defined in section 4.1.1. The value of the driving force $\boldsymbol{F}$ from the potential depends on the current position of the rower. The noise term is $\boldsymbol{f}_i$, where the distribution spread depends on the coupling tensor. See section 4.1.2 for more details.

4.1.4 Dimensionless units

The equation governing the rowers can be made dimensionless. Time and position are expressed in terms of the semi-period τ_0 and oscillation amplitude A, as the oscillations are the defining behaviour for rowers. Stokes' drag coefficient is an appropriate parameter when expressing the tensors I use in a dimensionless manner. Consequently the Langevin

equation (4.2) is written as,

$$\frac{d\tilde{\boldsymbol{x}}_i}{d\tilde{t}} = \sum_{j=1}^{N} \tilde{\boldsymbol{H}}_{ij} \cdot \left(\frac{\tau_0 \langle F \rangle_t}{\gamma A} \tilde{\boldsymbol{F}}(\boldsymbol{r}_j) + \frac{\tau_0}{\gamma A} \boldsymbol{f}_j \right), \tag{4.3}$$

where the tilde indicates the equivalent dimensionless quantities from the earlier equation. The trap force is expressed in terms of the time averaged force $\langle F \rangle_t$, which can also be expressed in terms of the earlier parameters. This results in two dimensionless parameters for the system: the dimensionless noise ξ and velocity parameter $\tilde{V}$. ξ is defined using the spread of the noise, while $\tilde{V}$ is from direct inspection of the above expression. They are defined as,

$$\begin{aligned} \tilde{V} &= \frac{\tau_0 \langle F \rangle_t}{A\gamma}, & \xi &= 2k_B T \frac{\gamma}{\tau_0} \left(\frac{\tau_0}{\gamma A} \right)^2 \\ &= 1, & &= \frac{2k_B T}{A \langle F \rangle_t}, \end{aligned} \tag{4.4}$$

where the relation between time average force with A, γ, and τ_0 has been used to simplify both expressions. When altering the trap shape, the average force over the duration of the trap $\langle F \rangle_t$ is kept constant by maintaining a constant τ_0. The semi-period τ_0 is kept constant by adjusting the trap strength k for changes in the trap shape,

$$k = \frac{\gamma}{\tau_0 \alpha} \frac{1}{2-\alpha} \left[(A + x_s)^{2-\alpha} - x_s^{2-\alpha} \right], \tag{4.5}$$

which was derived in [98]. Maintaining a constant $\langle F \rangle_t$ means ξ is unchanged as the trap shape α is varied.

4.2 Defining and measuring observables

4.2.1 Natural Phase Gauge

The natural phase ϕ is defined as phase with a constant velocity for non-interacting oscillators. Natural phase is also referred to as the asymptotic phase, and is the often used because it is useful when applying phase reduction theory [62]. The linear nature of the phase removes any variation that stems from motion inherent to the oscillator, i.e. the motion observed in an individual oscillator not experiencing any interaction forces. Without the intrinsic variations, any small changes stemming from the coupling between oscillators become clear. In this way the measurements of phase focus on the behaviour I am interested in.

Natural phase has been used previously to study hydrodynamic oscillators, with Uchida and Golestanian applying it to rotors [193]. To transform to the natural phase, the same process as described in [91] is used. This approach uses the definition of natural phase to find the transformation,

$$\frac{d\phi}{dx_r} = \frac{d\phi}{dt}\frac{dt}{dx_r} \tag{4.6}$$

$$= -\frac{2\pi}{2\tau_0}\left|\frac{\gamma}{F(x_r)}\right|. \tag{4.7}$$

π/τ_0 is the constant phase velocity for an isolated rower, with τ_0 the time between successive trap updates i.e. the semi-period. The natural phase was chosen to be strictly increasing for attractive potentials. The transformation between ϕ and x_r is found by integrating the expression in 4.7. Given the prevalence of power law driving potentials in this work, it is useful to directly state the transformation between phase and position for this case,

$$\phi(x) = (N_s+1)\pi + C_0 - \frac{\gamma\pi}{k\alpha\tau_0}\frac{1}{2-\alpha}x_r^{2-\alpha}, \tag{4.8}$$

$$C_0 = \frac{\gamma\pi}{k\alpha\tau_0}\frac{x_s^{2-\alpha}}{2-\alpha} = \frac{\pi x_s^{2-\alpha}}{(A+x_s)^{2-\alpha}-x_s^{2-\alpha}}. \tag{4.9}$$

The parameters defining the driving potential α, x_s, τ_0, and A, are explained in section 4.1.1. The counter N_s enumerates the number of trap updates that have taken place, which distinguishes between cases with $x_t > 0$ and $x_t < 0$. The constant C_0 ensures the switch point x_s is at $n\pi$, with $\phi \in [0,\pi)$ for $x_t > 0$ (rower moving right) and $\phi \in [\pi, 2\pi)$ for $x_t < 0$ (rower moving left). The initial N_s is chosen to be consistent with $\phi \in [\pi, 2\pi)$ for $x_t < 0$.

4.2.2 Synchronisation Order Parameters

There are number of ways to define synchronisation. Depending on what is of interest, the measurement of coordination is updated. There are two classes of coordinated states that were measured. The first is an in-phase or a splay state (i.e. anti-phase behaviour in a pair). The in-phase state is where all oscillators are at the same point in their cycle, while the splay has the oscillators equally spaced throughout. The second coordinated state is a phase-locked state. This state is more generic, and focuses on any consistent phase-difference across the population. Examples of these states are illustrated in figure 4.3.

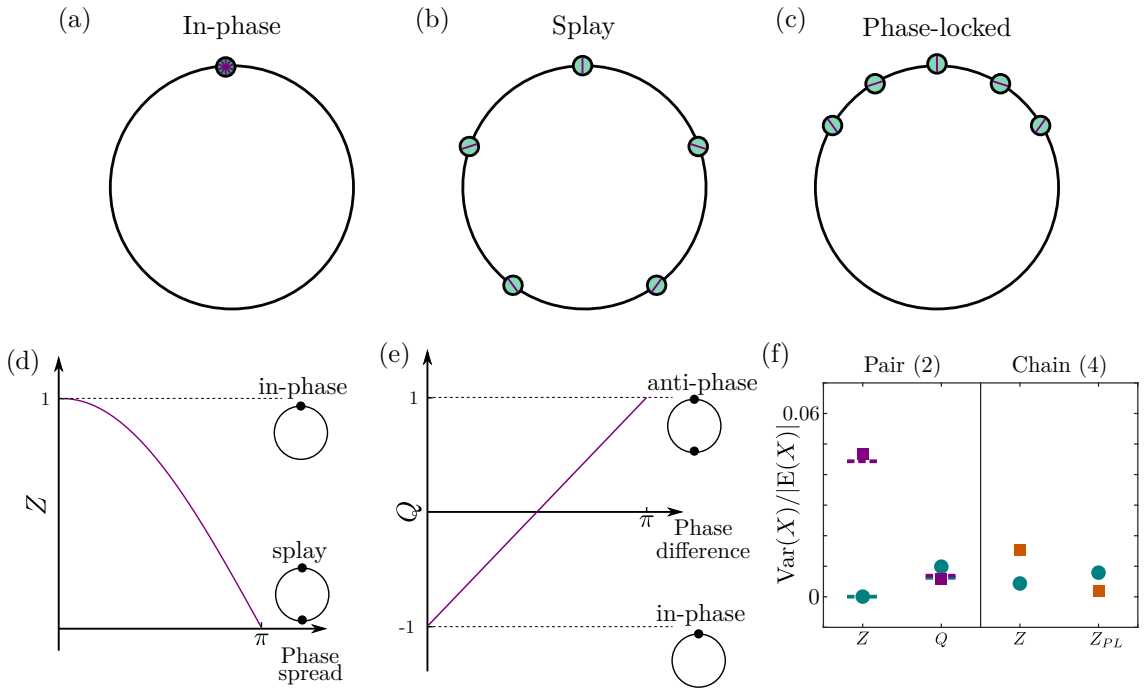

Fig. 4.3 Examples of different styles of coordinated motion. (a) The in-phase state has all oscillators at the same point in their cycle. (b) The splay state (or anti-phase state for two oscillators), as the oscillators equally spaced throughout phase space. (c) Phase-locked oscillators have an equal phase difference between sequential oscillators. (d,e) The difference between Q and Z measures for a pair of oscillators. While Q responds linearly to changes in phase, Z can be easily scaled to larger systems. (f) Comparing the sensitivity of the order parameters for a pair and a chain of four rowers. Empirical values are marked by: purple squares (anti-phase state), green circles (in-phase) and orange squares (phase-locked). The lines indicate the theoretical value for the measured spread of phase. The noise is similar for all cases but the phase-locked state, with $\xi \approx 9.7 \times 10^{-4}$. The phase-locked state was less stable, and to avoid including periods where synchrony was lost the noise was lower $\xi = 5.8 \times 10^{-5}$.

In-phase or anti-phase measures

The in-phase and anti-phase states can be measured by considering the phase or using the trap orientation. Earlier work with rowers measured the coordination of the system with Q, the average time a pair of rowers spend travelling in the same direction between trap updates,

$$Q(k) = \frac{-1}{s_{k+1} - s_k} \int_{s_k}^{s_{k+1}} \sigma_{t1}(t)\sigma_{t2}(t)\, dt, \tag{4.10}$$

where s_k is the time of the kth switch, and $\sigma_t(t)$ is the trap direction of the ith rower at time t. When the rowers are anti-phase $Q(k) = 1$, and when in-phase $Q(k) = 1$. The Q measure has a linear response to change in phase difference, but it isn't simple to extend to larger systems with more than two rowers.

Having developed a phase viewpoint for rowers, the spread of the phase is a natural measure for their coordination. There are several measures of spread for circular variables, with the simplest,

$$Z(t) = \left| \frac{1}{N} \sum_{j=1}^{N} \exp[i\phi_j(t)] \right|. \tag{4.11}$$

The phase is ϕ_j, which is averaged over the N oscillators. While this measure isn't linear for a pair of oscillators, see figure 4.3(d), it is easy to extend it to larger systems. Further it is a popular measure in the literature for Kuramoto oscillators and other simple phase oscillators.

Phase-locking measures

The phase-locked state has a consistent delay between oscillators. The in-phase state discussed above is the special case with no delay between oscillators, and the splay another special state where the delay distributes the oscillators throughout one cycle. To measure the more generic form of phase-locking, the spread of phase difference between pairs is calculated,

$$Z_{PL} = \frac{1}{N-1} \left| \sum_{j=1}^{N-1} \exp[i(\phi_{j+1} - \phi_j)] \right|. \tag{4.12}$$

This is a similar measure to the Z for the in-phase state, but for the phase-locking measure the oscillators must be labelled in some sensible sequence.

Proportion of time spent phase-locked

The fraction of time spent near synchronisation after some initial transient state is another measure used to assess if the state is phase-locked. To determine what would be considered

as near synchronisation, the average phase difference ψ_T is measured using,

$$r\exp(\psi_T) = \sum_{i=1}^{N} \exp(\phi_{i,1} - \phi_{i,2}). \tag{4.13}$$

This is an estimate of phase difference even when slips are occurring, as each slip contributes 0 to the average. This leaves the points where the phase difference settles as the main non-zero contribution. A slip stopped midway gives some contribution, but this is only meaningful for very short time intervals.

The proportion of time spent either in-synchrony or anti-synchrony t_R relative to the average phase difference ψ_T is,

$$t_S = \frac{1}{t_{tot}} \int_0^{t_{tot}} |\phi_{i,1} - \phi_{i,2} - \psi_T| < S_T \, dt + \frac{1}{t_{tot}} \int_0^{t_{tot}} |\phi_{i,1} - \phi_{i,2} - \pi - \psi_T| < S_T \, dt. \tag{4.14}$$

The total time interval is t_{tot}, and S_T the threshold for being near synchronisation; S_T is chosen by examining the fluctuations in the phase difference of an isolated pair at a given noise level. The time spent near synchrony has an inherent non-zero value due to drift through the synchronisation region. Assuming that the simulation length is longer than the drift time $1/(f_d - f_0)$, the expected proportion of time spent in the synchronisation region due to drift is,

$$t_0 = 4\frac{S_T}{2\pi}. \tag{4.15}$$

The time required to exceed the drift time diverges if the two oscillators have the same frequency. Consequently t_T is inappropriate to use for identical oscillators, or those very similar in frequency.

A pair is considered synchronised for the duration of the simulation if the time they spend near synchronisation exceeds half of the time unaccounted for by drift. This means the synchronisation threshold is,

$$t_T = \frac{1}{2}(t_0 + 1). \tag{4.16}$$

Comparing the order parameters

I compare the order parameters Z, Q, and Z_{PL} for a pair of rowers and a chain of four. The measures are compared using the ratio of the variance with the mean, sometimes called the Fano factor [226, 227]. The pair values were calculated analytically as well as empirically for both in-phase and anti-phase motion. In the chain case only empirical values were measured. This revealed that Z was the best parameter for measuring the in-phase state, but Q is more

accurate at determining the anti-phase state and Z_{PL} has a lower value when measuring the phase-locked state.

When considering a pair of rowers, Z and Q can be expressed in terms of the phase difference. For Q the phase difference represents the proportion of time spent with traps misaligned, consequently,

$$Q = 2\frac{\psi}{2\pi} - 1, \tag{4.17}$$

where $\psi = \phi_2 - \phi_1$ is the phase difference. Z can be simplified, which results in a cosine expression for the order parameter,

$$\begin{aligned} Z &= \left| \frac{1}{2} \left(\exp[i\phi_1] + \exp[i\phi_2] \right) \right| \\ &= \frac{1}{4}\sqrt{(1+\cos\psi)^2 + \sin^2\psi} \\ &= \left| \cos\left(\frac{\psi}{2}\right) \right|. \end{aligned} \tag{4.18}$$

Assuming that the phase difference follows a normal distribution with a variance σ_ψ, the ratio of the variance and the expected value can be calculated using the moments of the distribution [228]. To do so, Z was approximated by its Taylor series. In the in-phase case fourth order terms were required for a non-zero variance, but for the anti-phase only first order terms were necessary. This revealed the various dependencies on σ_ψ, with,

$$\left.\frac{\mathrm{Var}(Z)}{\mathrm{E}(Z)}\right|_{IP} = \frac{12\sigma_\psi^4}{384 - 48\sigma_\psi^2 + 3\sigma_\psi^4}, \quad \left.\frac{\mathrm{Var}(Z)}{\mathrm{E}(Z)}\right|_{AP} = \sqrt{\frac{\pi}{8}}\sigma_\psi(1 - 2/\pi), \tag{4.19}$$

$$\left.\frac{\mathrm{Var}(Q)}{\mathrm{E}(Q)}\right|_{IP} = -\frac{4}{\pi^2}\sigma_\psi^2 \frac{1-2/\pi}{\pi/2 - \sigma_\psi\sqrt{2/\pi}}, \quad \left.\frac{\mathrm{Var}(Q)}{\mathrm{E}(Q)}\right|_{AP} = \frac{4}{\pi^2}\sigma_\psi^2 \frac{1-2/\pi}{\pi/2 - \sigma_\psi\sqrt{2/\pi}}. \tag{4.20}$$

For a distribution near in-phase Z is proportional to σ_ψ^4, and it is the best measure. However, near anti-phase $Z \propto \sigma_\psi$ while $Q \propto \sigma_\psi^2$, and the Q measure is better.

The theoretical values for the variance mean ratio are compared in figure 4.3(f). The dashed lines mark the theoretical values, with purple marking anti-phase results and green the in-phase. The empirical values are indicated by the circle and square markers. It shows, as expected, the Z measure is best for measuring the in-phase state but Q is more useful for the anti-phase. The empirical values for a chain of four rowers is also included for comparison. In this case the Z parameter is still the best measure for the in-phase state, see the green circles. The phase-locked state is better perceived by Z_{PL}, with the measurements for phase-locking shown by the orange markers. The phase-locked state was measured at a

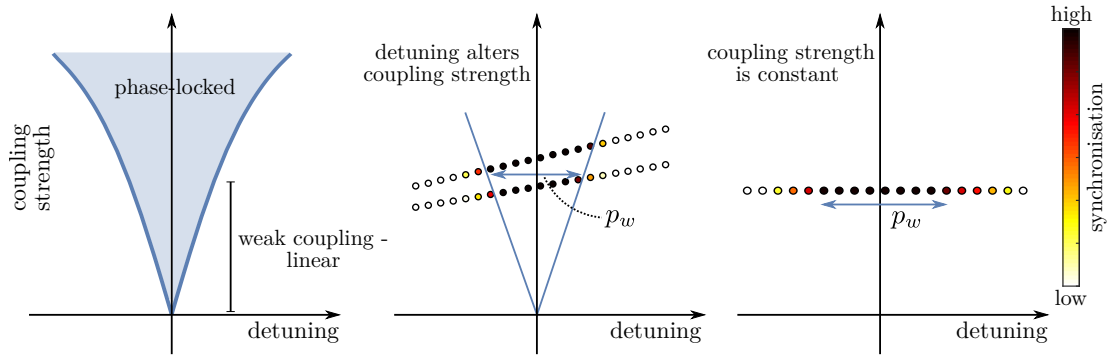

Fig. 4.4 The width of the Arnold tongue for a specific value of weak coupling is a measure for synchronisation strength. (a) The Arnold tongue is the region of detuning in which the two oscillators still synchronise. At low strength coupling the phase-locking region increases linearly. (b) When the coupling strength varies as the oscillators are detuned, the plateau width is found by fitting two straight lines and interpolating for a specific value. (c) If the coupling strength is independent of detuning, the plateau width is measured directly.

lower noise level because it is more sensitive to noise. Consequently the orange and green markers should not be compared.

4.2.3 Parameters for synchronisation strength

Relaxation time near a fixed point

A possible measure for synchronisation strength is how quickly the system reaches the equilibrium state. One approach to measuring this time scale is to measure the relaxation time of the phase difference ψ auto-correlation. This gives an indication of how quickly the system 'forgets' its initial conditions. In the systems considered here the autocorrelation of the phase difference with moderate noise is calculated to determine the relaxation time t_r. To find the relaxation time an exponential is fit to the autocorrelation,

$$\langle \psi_i(t)\psi_i(t+\Delta t)\rangle = \Psi_0 \exp\left(-\frac{\Delta t}{t_r}\right). \tag{4.21}$$

The decay rate of the exponential gives the relaxation time. For simplicity, the auto-correlation is calculated after the system has reached the steady state and noise is applied. The range about the steady state that is sampled depends on the magnitude of the noise applied.

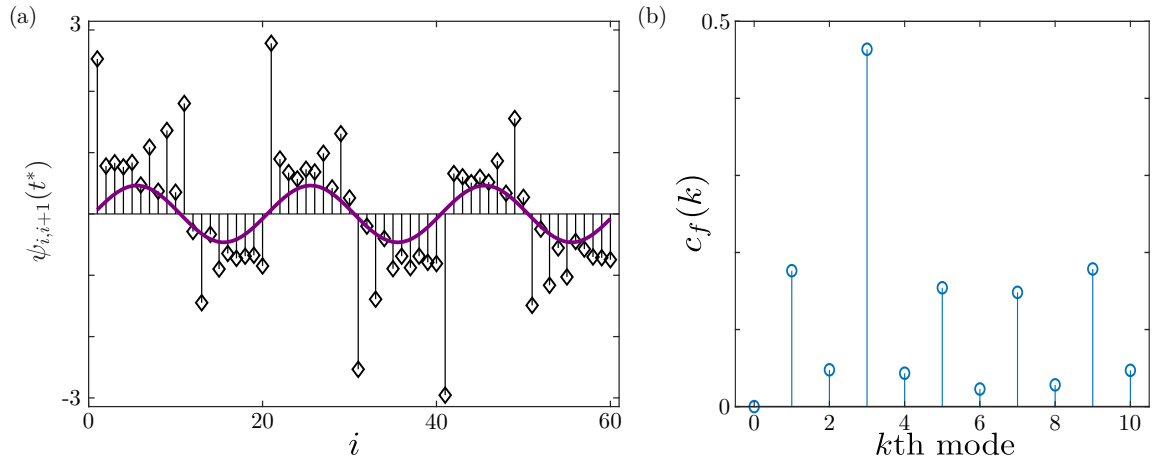

Fig. 4.5 Fourier modes are used to classify dominant features in the phase profile. (a) The phase difference between neighbouring rowers in a chain (black diamonds) overlaid with the dominant Fourier mode (purple line). (b) The initial coefficients of the Fourier series. The 3rd mode clearly has a larger contribution.

Width of Arnold Tongue

The Arnold tongue refers to the region in which two detuned oscillators phase-lock, see figure 4.4(a). The range of detuning in which this occurs depends on the coupling strength between them. For weak coupling in my system, the range of detuning value depends linearly on the coupling strength. This is not always the case, for a pendulum with an oscillating fulcrum, which is governed by the Mathieu equation, the Arnold tongues are not necessarily linear in the weak coupling regime [229, 230].

The width of the Arnold tongue can be used to compare the coupling in different systems. To compare like with like, the width is measured in the linear weak coupling regime. This avoids difficulties with different non-linear responses with strong coupling. The width can be measured directly when the detuning and coupling strength vary independently, see figure 4.4(c). The plateau measures the range of states that are found to have high levels of synchronisation. The precise definition of high synchronisation can vary depending on system specifics. In some cases the coupling varies with the detuning, see figure 4.4(b). In this case, the phase-locking is measured for two similar levels of coupling and the Arnold tongue fitted. The fit includes the two boundary results and the origin. The plateau width is then interpolated using the fit. Note the initial values for the coupling strength are chosen to be similar to the desired interpolation value.

4.2.4 Determining features in the phase front

To classify systematically the regular features in the phase of a rower chain a Fourier transform is applied to the phase difference. This provides a snapshot of the dominant features in the phase profile at a given time. I am only interested in large features that occur over some distance, and so usually discard any Fourier modes that are smaller than three rowers in scale; $N/(2k) > 3$, where k is the number of the Fourier mode and N the total number of rowers. The largest Fourier coefficient should correspond to the overall structure of the phase profile. An example of this process is shown in figure 4.5. The original phase profile is shown in figure 4.5(a) by the black diamonds, the dominant Fourier mode is overlaid as the purple line. The coefficients of the lowest Fourier modes are shown in figure 4.5(b).

4.3 Code details

The simulations are written in either C++ or CUDA. The C++ code was originally written by Loic Damet as used in [225] with alterations made by Nicolas Bruot. It is Nicolas' code that I have worked on, adding extensions to simulate specific effects. The CUDA code is all my original work.

4.3.1 C++ code

Geometry changes The original code only allowed either line or ring configurations for the rowers. In both cases they were equally spaced, with the space between sequential traps set to d. Now the code is extended to a further two new 2-dimensional configurations. The first included a second line of rowers translated perpendicularly from the first line, with the spacing labelled d_v see figure 4.6(b). The second configuration is a square lattice, see figure 4.6(c). The distance between neighbouring trap pairs is the same along rows and across rows, $d_h = d_v$.

Frequency spread An option for heterogeneous frequencies in the rower populations was implemented. To vary the frequencies, the trap strength of each rower is scaled by a random factor, with the ith scaled by $k_s(i)$. The set $\{k_s(i)\}$ is drawn from a normal distribution $\mathcal{N}(1,\Delta f)$. By scaling the trap strength, the mean of the frequency distribution is the natural frequency of unaltered trap strength f_0. The spread of the distribution is varied through Δf, with the spread of the frequency distribution $f_0\Delta f$.

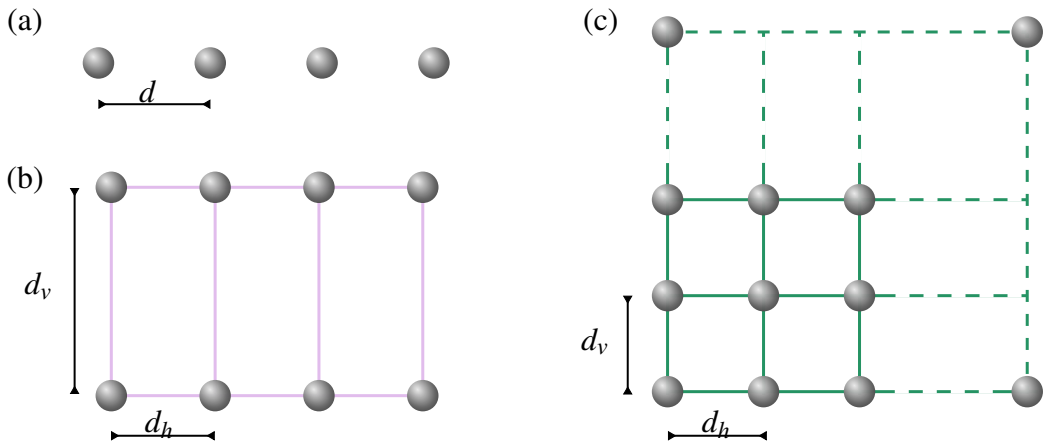

Fig. 4.6 Possible layouts for rowers using the C++ implementation of the code. (a) The original code placed a chain of B rowers, with the trap centres of each pair separated by a distance d. (b) The rowers can be placed in two rows, a simple 2-dimensional configuration. The system is now described by the horizontal distance between neighbouring pairs d_h, and the vertical distance between pairs d_v. (c) An alternative 2-dimensional layout where the rowers are placed in a square lattice, i.e. $d_v = d_h$.

Tensors The Blake tensor for a particle moving in a plane is now a simulation option. The movement plane is parallel to the no-slip boundary. Similar to the original code, the tensor is implemented only in two-dimensions. In the Blake case there is now a parameter for the height above the boundary h, which remains constant throughout the simulation. The reduction to two dimensions reduces the memory usage and increases the speed of the Cholesky decomposition. The Cholesky decomposition is required for the Brownian noise in the Ermack-McCammon algorithm [222]. The two-dimensional tensor is equivalent to the case where the particles are strongly trapped within the plane.

In the case with constant height, the Green's functions in equation (3.14) can be simplified. Consequently the Blake tensor is implemented with the following form for $\boldsymbol{G}^{Os}$, $\boldsymbol{G}^{St}$, and $\boldsymbol{G}^{So}$,

$$\boldsymbol{G}^{Os}(\boldsymbol{r}) = \frac{1}{8\pi\eta}\frac{1}{r}\left(\boldsymbol{I} + \frac{\boldsymbol{r}\otimes\boldsymbol{r}}{r^2}\right), \tag{4.22}$$

$$\boldsymbol{G}^{So}(\boldsymbol{r}) = \frac{1}{8\pi\eta}\frac{1}{r^3}\left(\boldsymbol{I} - 3\frac{\boldsymbol{r}\otimes\boldsymbol{r}}{r^2}\right), \tag{4.23}$$

$$\boldsymbol{G}^{St}(\boldsymbol{r}) = \frac{\Delta z}{8\pi\eta}\frac{1}{r^3}\left(\boldsymbol{I} - 3\frac{\boldsymbol{r}\otimes\boldsymbol{r}}{r^2}\right). \tag{4.24}$$

The system is is two-dimensions, and so $\boldsymbol{r}_i = (x_i, y_i)$. In the Stokeslet doublet the Δz refers to the difference in height above the boundary. For constant height h, the difference in height between the image and real rowers is $2h$.

External signal At various points the susceptibility of rower systems to the influence of an external signal was explored. It is always a square wave, with some frequency f_e. The signal is included in two ways; a force each rower experiences, or as an external flow field that manifests as an external velocity field for the rowers. The type of the external signal affects its implementation. If the signal is a force each particle experiences, the Langevin equation (4.2) becomes,

$$\frac{d\boldsymbol{x}_i}{dt} = \sum_{j=1}^{N} \boldsymbol{H}_{ij}^{-1} \cdot \left(\boldsymbol{F}_j(x) + \boldsymbol{F}_{ext}(t) + \boldsymbol{f}_j\right), \tag{4.25}$$

with the external force $\boldsymbol{F}_{ext}(t)$. In the case of an external velocity flow, the rower's equation of motion is instead,

$$\frac{d\boldsymbol{x}_i}{dt} = \sum_{j=1}^{N} \boldsymbol{H}_{ij}^{-1} \cdot \left(\boldsymbol{F}_j(x) + \boldsymbol{f}_j\right) + \boldsymbol{V}_{ext}(t). \tag{4.26}$$

Here the external velocity is $\boldsymbol{V}_{ext}(t)$. To create the square wave structure, the force or velocity switches direction every N_f frames, i.e. $N_f \delta t$ is the half-period of the external signal.

4.3.2 CUDA details

Tensors The Oseen and Blake tensors are implemented in two-dimensional co-ordinates, the same as for the C++ code. In the case of the Blake, the particles were assumed to be at a constant height above the boundary. The limitation to two-dimensions reduces the memory required for mobility tensor and the multiplicative term in the noise calculation.

Periodic boundary conditions To create periodic boundary conditions image rowers are placed around the original rower configuration. Rowers will then interact with the closest version of another rower, i.e. the original or one of its images if it is closer. The trapped nature of the rowers simplifies the determination of which is closer, the original or some image, because the average position of the rowers (and hence images) is static. Consequently a matrix $\boldsymbol{M}_{PB}$ that encodes the appropriate wrapping for each pair can be calculated at initialisation. Using this matrix, the minimum distance between any two rowers is,

$$\boldsymbol{r}_{ij} = \boldsymbol{r}_i - \boldsymbol{r}_j - \boldsymbol{M}_{PB}(i, j). \tag{4.27}$$

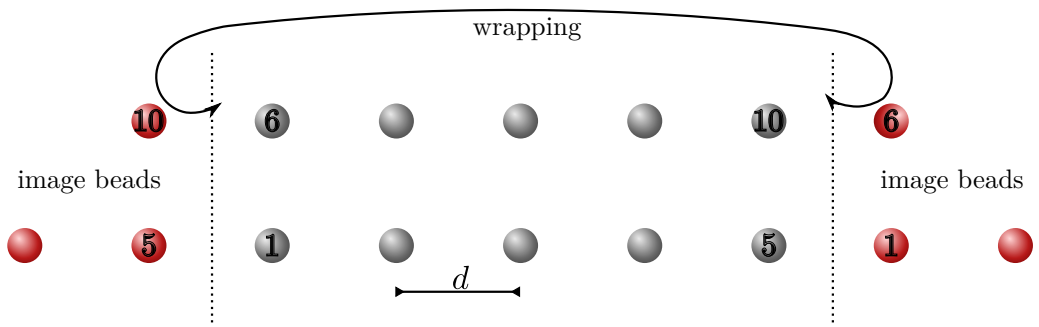

Fig. 4.7 Periodic boundaries use image rowers to remove edge effects. When calculating the distance between rowers, the minimum of the set of distances involving the original rower and all the associated images is chosen. Here the image rowers are indicated by switching to red colouring. Due to the fixed nature of the trap centres, the minimum set of distances and the associated transformations can be calculated once at initiation and then reused throughout the simulation.

An example of wrapping is shown in figure 4.7. In this example $M_{PB}(1,5) = -5d$ and $M_{PB}(5,1) = 5d$.

Periodic boundary conditions require a system large enough that an element does not interact with itself. This can be problematic with Oseen tensor, and its long range interaction. To avoid problems with the interaction range, periodic boundary conditions are only implemented with the Blake tensor (see section 3.5) and $h/d < 1$.

Rower position geometry The rowers can be placed in several configurations. Similar to the C++ code, the rowers can be equally spaced along a line or in a square lattice. A further two 2-dimensional lattices configurations were implemented: a triangular lattice with six nearest neighbour, and a hexagonal lattice with 3 nearest neighbours.

The chain layout has a further extension in which some heterogeneity is introduced into the trap spacing. In the C++ code the trap spacing is always equal, in the CUDA code it is possible to include some additional separation every N_g rowers.

Noise The noise for the CUDA implementation is included using the same approach as the original code. The noise is multiplicative, with the Cholesky decomposition of the hydrodynamic tensor capturing the correlation from hydrodynamic forces. The noise is calculated at the start of the simulation interval, i.e. using the Ito convection, and no drift correction is required. The Cholesky decomposition was calculated using functions from the cusolverDn library.

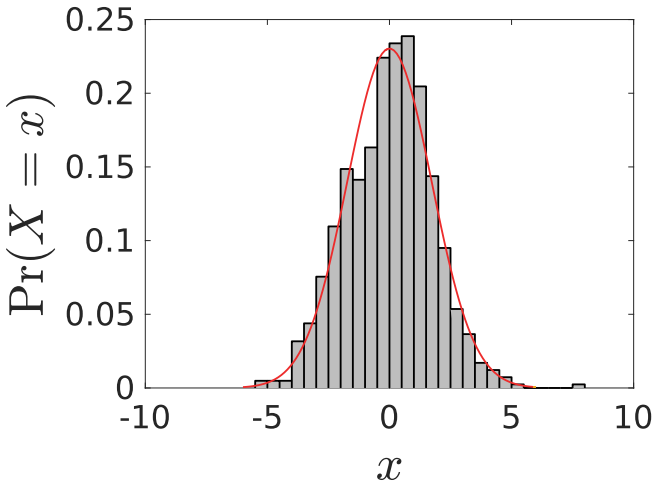

Fig. 4.8 Test case of random data generated by the CUDA code. The histogram is the data produced by the code, the red curve is the theoretical distribution it is drawn from.

For the random noise generation, the curand_kernel library was used to generate random numbers. The noise was randomly seeded using the time at initialisation. For longer experiments, the initial term for the sequence is reset every 100,000 steps. This prevents the code from slowing, which occurs when accessing random numbers very deep in the PRNG sequence. The new sequence initialisation term adds four times the number of particles to their previous sequence initialisation term. At initiation the sequence tag of the *i*th particle is *i*.

4.3.3 Strengths and weaknesses of the CUDA implementation

Benefits of the CUDA code

The key benefit of the CUDA code is the reduction in simulation time for large systems. This is due to the intrinsic parallelisation that takes place when calculating on the GPU. Large systems of rowers are a good candidate for parallelisation, as the hydrodynamic tensor can be constructed in parallel. This has been shown to increase the simulation speed by two orders of magnitude for large systems, see figure 4.9. The increase in system size potentially expands the range of geometries that can investigated. Either because huge systems can be approximated by periodic boundary conditions and a large array that is newly accessible, or because changes in geometry are less likely to yield differences in small arrays.

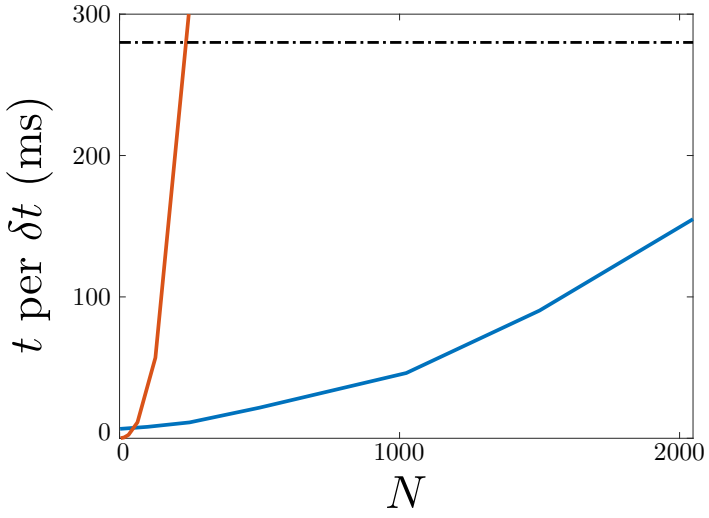

Fig. 4.9 The benefit of the CUDA code is the computation time for large systems. The time to calculate a time step in milliseconds is plotted a simple version of the C++ (red line) and CUDA codes (blue line). The dashed black line is an artificial limit, it is the calculation time per step which can simulate 30s over a 24 hour period using a step size of 10^{-4}s, i.e. 300,000 time steps can be simulated in a 24 hour period. It was chosen as the time at which simulations were too inefficient to execute.

Limitations stemming from the shift to CUDA

The transition to CUDA does lead to some constraints. Memory usage for large matrices is a limiting factor for the very large cases. This could be circumvented through a sparse implementation for the mobility matrix. The advantage of the sparse notation would be particularly useful for cases that have fast decay, e.g. the system is near a boundary. The CUDA implementation necessitates the shift to the Blake tensor in order to suppress the long range nature of 'bulk' hydrodynamic interactions. Without the suppression, the sum of interacting forces is unbounded. This causes difficulty in large systems, which is the focus of the CUDA implementation.

An unavoidable outcome of implementing large systems is the increase in transient time. The large systems of rowers often have more complex potential landscape, which can necessitate longer simulations and more seeds. The nature of the GPU hardware also lends itself to floating point calculations rather than double type, which can lead to a reduction in accuracy due to increased machine error.

Improvements to the CUDA

The limitations associated with the memory can be avoided through a change in format. The move towards a sparse format for the matrices and the Cholesky decomposition would decrease the memory required for a given simulation. The more sparse the matrix, the greater

the benefits. Consequently the sparse notation would be most when the interactions are short range.

To improve the versatility of the CUDA code a direct method for creating the initial conditions could be introduced. Currently the initial conditions for the CUDA code draw the position of each rower from a uniform distribution. Introducing a further input file that would specify the initial conditions would be valuable if aiming to search for specific behaviour. Some interesting states are known to be highly dependent on initial conditions, and are unlikely to occur by chance. In the context of non-identical oscillators, the code would also benefit from a change in the distribution that determines the heterogeneous frequencies. Currently it is Gaussian, which leads to non-physical negative frequencies with large variance. This could be amended by switching to a log-normal distribution for the frequency distribution.

4.3.4 Computer requirements

The C++ code was compiled using C++11, and uses the gsl library. The CUDA code was compiled using CUDA V7.5.17, and uses the cusolverDn, curand and cuda_runtime libraries. The computer is running Ubuntu 14.04, and the graphics card a GeForce STX 750 with 1Gb memory.

Chapter 5

An analytical framework for "mean interaction"

5.1 Context for the application of the "mean interaction"

In this chapter I apply the phase reduction method to the rower model, a new framework in which to interpret rower behaviour. The benefit of which is the rowers being expressed as a dynamical non-linear system. The new continuous expression ties into broader work involving Kuramoto oscillators and other general phase oscillations. Further the new expression for the rower interaction rigorously explains the change in stable behaviour of rower pairs. When applied to larger systems, it becomes possible to determine the equilibrium solutions. The prediction of the steady state means it is now possible to design rower configurations to exhibit specific behaviour, which might inform research into engineering functional collective filament dynamics in artificial systems. The work here is adapted from my work in [2].

Aspects of the pair-wise interaction between rowers can be understood through an iterative map involving a simplified driving force, and through the eigenstates of the coupling tensor [98, 189]. Both approaches have captured the shift from in-phase and anti-phase behaviour as the driving force is varied, and are reviewed in [181]. It is not feasible to extend the iterative map to systems of many rowers, but the eigenstate approach can be applied to larger collections of rowers. Through this lens the equilibrium behaviour of rowers in rings or chains was discussed in terms of eigenstate growth and decay between switches [189]. This culminated in predicting the steady state of planar arrays when varying their positions and alignment [190].

To apply the new technique in this chapter, first the rower's position is related to its natural phase. This is covered in section 5.2.1, before the interaction between two rowers

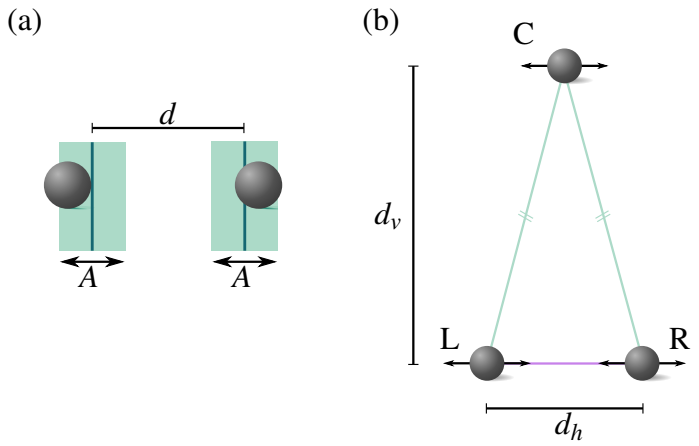

Fig. 5.1 The distance between the rowers is approximated by the distance between their trap centres. (a) For a pair of rowers, the separation between them is approximated by d the distance between the trap centres. (b) Three rowers centres of the vertices of an isosceles triangle. The triangle has a base length d_h and a height d_v.

is averaged to determine the mean pair-wise interaction in section 5.2.2. The results of the averaging is verified by replicating in simulation the predicted shift in stability of fixed points observed in power laws and in a driving force more similar to those in biological systems, section 5.2.3. This is followed by a direct comparison of the simulation relaxation time of a pair with the theoretical prediction, section 5.4. Finally this technique is applied to a new system of three rowers to demonstrate its predictive ability in section 5.5. The results are then reviewed in section 5.6, which also includes some further extensions that could take advantage of this new framework.

5.2 Procedure to calculate the mean interaction

To calculate the mean interaction, I followed directly the steps laid out in [91]. First the transformation between position and natural phase is determined. The relationship is then inverted to express position in terms of phase, which allows the force to expressed in terms of phase rather than position. The evolution of the phase can be determined in a similar way, this time the velocity of bead is converted to phase velocity. The “mean” interaction is calculated by averaging the interaction in terms of phase over one period. This assumes that the interaction between the oscillators is small, and that the phase difference is about constant over this time scale. This results in an interaction that depends on the phase difference. The entire process is referred to as phase reduction [4, 62]. It is an indispensable tool when considering weakly coupled limit cycle oscillators. An early example of this technique can

be found in [231], and the process continues to be updated and expanded [232, 233]. A more recent review of the technique can be found in [62].

5.2.1 Natural phase

To calculate the average interaction between rowers I first transform into the natural phase frame. This transformation is often used to link Josephson junctions to Kuramoto phase oscillators, but it is not restricted to such cases [66, 91, 193]. The natural phase is a frame where the velocity is constant for an uncoupled rower. The natural phase accounts for any variations in velocity due to the driving force, but not for velocity changes stemming from coupling between oscillators. The transformation also reduces the parameters describing the place a rower is at in its cycle to just the phase ϕ, rather than its position and the trap direction.

The relationship between phase and position can be determined using the velocity in terms of x as determined by equation (4.2) with the Oseen tensor used for the coupling. I approximate by dropping the noise and only considering the direction of oscillation x. Equations (4.2) and (3.12) then simplify to:

$$\frac{dx_i}{dt} = \sum_{j=1}^{N} H_{ij}^{x} F_j(x), \tag{5.1}$$

$$H_{ij}^{x} = \begin{cases} 1/\gamma & : i = j \\ \frac{1}{\gamma}\frac{3a}{4r_{ij}}\left[1 + \frac{(x_i - x_j)^2}{r_{ij}^2}\right] & : i \neq j \end{cases}. \tag{5.2}$$

The hydrodynamic coupling in the x direction is H_{ij}^{x} and the trap force along this direction $F_j(x)$. To simplify future calculations, I approximate the distance between rowers (r_{ij}) by the distance between their trap centres ($r_{ij}^{(t)}$). The hydrodynamic coupling for a given pair is constant under this approximation, which I label μ_{ij},

$$\mu_{ij} = \begin{cases} 1/\gamma & : i = j \\ \frac{1}{\gamma}\frac{3a}{4r_{ij}^{(t)}}\left[1 + \left(\frac{x_{ij}^{(t)}}{r_{ij}^{(t)}}\right)^2\right] & : i \neq j \end{cases}. \tag{5.3}$$

$x_{ij}^{(t)}$ is used to indicate the trap separation in the x direction. This approximation assumes the oscillation amplitude is small, i.e. $A \ll r_{ij}^{(t)}$. For a pair such as in 5.1(a), $r_{ij}^{(t)}$ is d, for the isosceles layout in 5.1(b) it is either d_h or $(d_h^2/4 + d_v^2)^{1/2}$.

The reparametrisation of position to the natural phase transforms a rower into a moving reference frame. For an uncoupled rower in this frame the phase velocity is constant. To determine the transformation to this frame I consider a single rower, and relate its phase to position using the chain rule,

$$\begin{aligned}\frac{d\phi}{dx_r} &= \frac{d\phi}{dt}\frac{dt}{dx_r} \\ &= -\frac{\pi}{\tau_0}\left|\frac{\gamma}{F(x)}\right|, \qquad (5.4)\end{aligned}$$

$$\frac{d\phi}{dt} = \Omega = \frac{\pi}{\tau_0}. \qquad (5.5)$$

Ω is the constant phase velocity for an isolated rower, which I defined using τ_0 the time between successive trap updates of a single rower i.e. the semi-period. I choose the natural phase to be strictly increasing. It is easier to relate the phase to position using the position relative to the trap vertex $x_r = |x - x_t|$, which is strictly decreasing with time. Given a specific trap force, the transformation between the natural phase and the position coordinates can be calculated by integrating equation (5.4). This transformation between phase and position is used to express the driving force in terms of phase, and so include interactions between rowers in the phase velocity. This is expanded upon in the following section.

5.2.2 Mean Interaction

When including interactions between rowers in the evolution of the natural phase, the interaction can be approximated by its average effect over a period. This is in keeping with the process described in [91]. This approach has two key benefits: the interaction is explicitly dependent on the differences between rowers, and the interaction becomes continuous. This allows the system to be analysed in terms of fixed points and stability using standard techniques. This is a far more tractable problem than previous approaches [98, 189].

The approximation relies on weak coupling between the rowers resulting in two timescales in the system [6, 230]. This requires that the perturbations of the phase from the trap force are small, i.e. the variations in the trap force are small compared to its average. Furthermore the hydrodynamic coupling must also be weak i.e. μ_{ij} is small, which is true in the far field I am considering. The weak coupling was confirmed empirically by comparing the synchronisation time with the period of the oscillations, which for low curvature systems has the appropriately long time scales for the synchronisation time. For complete details on how I calculated the average interaction see Appendix B, which includes the full derivation of the phase evolution and examples for specific potentials. A similar process involving

perturbation analysis can be found in [6], and includes higher order terms of the relevant coupling parameter. The final expression for the phase derivative is,

$$\frac{d\phi_i}{dt} = \Omega + \sum_{i \neq j} \mu_{ij} G_I[\phi_i - \phi_j], \tag{5.6}$$

$$G_I[\psi] = \frac{1}{2\pi} \int_0^{2\pi} \left.\frac{d\phi}{dx_r}\right|_{x(\vartheta+\psi)} \left.\frac{dx_r}{dx}\right|_{x(\vartheta+\psi)} F[x(\vartheta)]\, d\vartheta. \tag{5.7}$$

$G_I[\psi]$ is defined as the mean of the interaction function in the natural phase frame, where the variable ϑ is a dummy used for the averaging. This expression is generic and applies to any potential, assuming the phase/position inverse exists i.e. the potential is monotonically increasing.

When considering the evolution of the phase difference for a single pair of rowers, the even component of the interaction is the same regardless if the rower is leading or trailing ($G_{even}[\psi] = G_{even}[-\psi]$). Defining the odd component of $G_I[\psi]$ as $G_{odd}[\psi]$, the phase difference changes as,

$$\begin{aligned} \frac{d\psi}{dt} &= \frac{d\phi_1}{dt} - \frac{d\phi_2}{dt} \\ &= \mu_{12} \left(G_I[\psi] - G_I[-\psi]\right) \equiv 2\mu_{12}\, G_{odd}[\psi], \end{aligned} \tag{5.8}$$

where $\mu_{12} = \mu_{21}$ and $\psi = \phi_1 - \phi_2$. Calculating the effective interaction by transforming to the natural phase gauge and taking the average over a period uses equivalent steps to those taken in [193]. It is remarkable that in doing so the expression used for the interaction is no longer discontinuous. This converts the complex configuration and history-dependent interactions of a rower pair to a simple one-dimensional non-linear system. The fixed points of the system and their stability can be investigated from this perspective, where before it was interpreted in terms of eigenstates of the hydrodynamic tensor and their decay rate [189, 190].

5.2.3 The power law potentials

The mean interaction for power law potentials can be calculated analytically, with details in B.2. The resulting expression $G_I[\psi]$ depends on two variables p and C_0,

$$p = \frac{1-\alpha}{2-\alpha}, \qquad C_0 = \frac{\pi x_s^{2-\alpha}}{(A+x_s)^{2-\alpha} - x_s^{2-\alpha}}. \tag{5.9}$$

The parameter p depends exclusively on the trap shape α. The p interval $(0, \frac{1}{2})$ corresponds to $0 < \alpha < 1$ and negative curvature, while $p \in \mathscr{R} \backslash [0,1)$ to $\alpha > 1$ and for positive curvature.

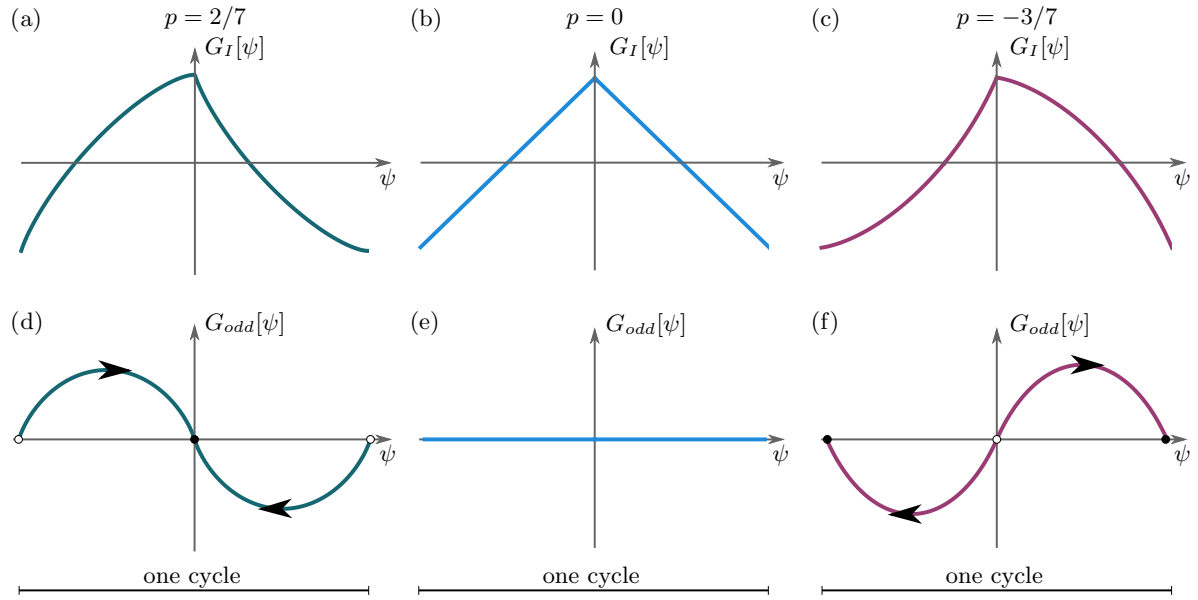

Fig. 5.2 The average pair interaction captures the shift from the in-phase behaviour to the anti-phase as the trapping potential changes shape. (a) The average interaction for $p = 2/7$ ($\alpha = 0.6$) indicates that when a rower lags behind ($\psi < 0$) it experiences a greater force than the rower in front ($\psi > 0$). (d) Focuses on the odd component of the interaction. It confirms that a rower that falls behind will catch the leading rower, and highlights the stability of the in-phase fixed point. (b) The average interaction for $p = 0$ ($\alpha = 1$), i.e. a linear driving potential. (e) In this case the interaction function is even and the rowers don't coordinate. (c) The behaviour reverses, with the leading rower experiencing the greater force when $p = -3/7$ ($\alpha = 1.3$). (f) The odd function has been reflected in the horizontal axis, which leads to the fixed points swapping stability.

$\alpha = 2$ is the special case where p diverges. The divergence stems from the calculation of phase-position transformation which involves $\int x_r^{1-\alpha} dx_r$ that assumed $\alpha \neq 2$. Considering the case $\alpha = 2$ separately, the integral still has a solution and it is still possible to solve for $G_I[\psi]$. C_0 ensures the switch point of the trap corresponds to $\phi = n\pi$. It depends on the amplitude and switch point, so in some way quantifies the variation of the force within the trap. A higher value corresponds to a potential with more similar forces and hence weaker coordination.

Examples of the interaction are shown in figure 5.2. In figure 5.2(a) $p = 2/7$ ($\alpha = 0.6$), and the curvature is negative. The interaction shows that when a rower lags behind another ($\psi < 0$), it experiences a force greater than the rower ahead. This is confirmed in 5.2(d), where the odd component of the interaction is plotted. The discrepancy in the force leads to the lagging rower catching the leading rower, and so in-phase motion $\psi = 0$ is stable. Figure 5.2(b) is the special case where $p = 0$ and the trap potential is linear. In this case the average interaction is an even function, emphasised in figure 5.2(e), and rowers experience the same force regardless if they lead or trail. Consequently there is no impetus to synchronise the rowers, as explored experimentally in [98]. In 5.2(c) $p = -3/7$ ($\alpha = 1.3$) and the trap has positive curvature. The average interaction in this case shows the leading rower experiencing greater force than the lagging rower. This exacerbates the separation between the rowers and pushes the system towards anti-phase. Figure 5.2(f) confirms the stability of the anti-phase point. In calculating the average interaction I have accounted for the known shift between anti-phase and in-phase behaviour when varying the shape of a power law potential.

Next I go further and quantify the coupling strength associated with a given potential.

5.3 Analytical relaxation time near the steady state

To quantify the coupling strength of a given potential I use the relaxation time. Capturing the synchronisation strength increases the utility of the mean interaction approach. At this stage it is useful to express the mean interaction in terms of its Fourier series. This is a simple way to separate the odd and even contributions, and accelerates any calculations. The series will converge, because the averaging process ensured the interaction function is continuous. A side benefit of this is that it ties back to more generic work with Kuramoto oscillators and other general oscillators [6, 63, 66].

The sine coefficients s_k are calculated using the dimensionless form of G_I, and so the evolution of the phase difference is expressed as,

$$\frac{d\psi}{dt} = \frac{2\gamma\mu_{12}}{\tau_0}\sum_{k=1}^{\infty} s_k \sin(k\psi), \tag{5.10}$$

$$s_k = \frac{\tau_0}{\gamma\pi}\int_{-\pi}^{\pi} G_I[\psi]\,\sin(k\psi)\,d\psi. \tag{5.11}$$

This is similar to the Adler equation, and when truncated to first order terms, i.e. s_1, it is the equation [4]. The even sine terms s_{2k} were zero across all the cases I investigated. Any driving potential with a moderate s_2 term would be of interest, because I believe it is the most likely case to exhibit phase-locking where $\psi \neq n\pi$. I find that the first few non-zero terms are enough to capture the details of the system.

To calculate the relaxation time I assume that the system is near the phase difference steady state solution. I then linearise the system, which leads to an exponential solution. Assuming the in-phase point is stable then,

$$\frac{d\psi}{dt} = \frac{2\gamma\mu_{12}}{\tau_0}(s_1\sin(\psi) + s_3\sin(3\psi) + ...) \tag{5.12}$$

$$\approx \frac{2\gamma\mu_{12}}{\tau_0}(s_1 + 3s_3 + ...)\,\psi, \tag{5.13}$$

$$\psi = \psi_0 \exp[-t/t_r], \tag{5.14}$$

$$t_r(2n-1) = -\frac{\tau_0}{2\gamma\mu_{12}}\left(\sum_{i=1}^{n}(2i-1)s_i\right)^{-1}. \tag{5.15}$$

The relaxation time $t_r(2n-1)$ varies with the number of terms included in the sine series. For the anti-phase point,

$$\frac{d\psi}{dt} \approx -\frac{2\gamma\mu_{12}}{\tau_0}(s_1 + 3s_3 + ...)(\psi - \pi), \tag{5.16}$$

$$t_r(2n-1) = \frac{\tau_0}{2\gamma\mu_{12}}\left(\sum_{i=1}^{n}(2i-1)s_i\right)^{-1}. \tag{5.17}$$

Including more terms increases the accuracy close to the fixed point but also limits the region in which it is applicable, due to restrictions when linearising. It was assumed that $\sin(k\psi) \approx k\psi$ during linearisation, which completely breaks down when $k\psi > \pi/2$. For this reason keeping to a minimal number of terms is often more robust than including many additional terms. The first order relaxation time of the power law potentials is displayed in figure 5.3(a): it diverges when $p \to 0$ reflecting the increasing difficulty to synchronise as

the driving potential becomes more linear. The relaxation time also becomes longer as C_0 is increased, reflecting that for large x_s the forces don't vary particularly within the trap.

5.4 Verification of relaxation time

5.4.1 Power law potentials

I verified the analytical relaxation time by comparing with the relaxation time in simulation. A pair of rowers as described in chapter 4 are simulated. The average force over the duration of the trap $\langle F \rangle_t$ is kept constant by maintaining a constant τ_0. The semi-period τ_0 is maintained by adjusting the trap strength k for changes in the trap shape, $\alpha \in [0.5, 1.5]$. See section 4.1.4 for details. Keeping $\langle F \rangle_t$ constant means ξ is unchanged as α changes, where I set $\tau/(A\gamma) = 1.09\,\mathrm{pN}^{-1}$ and calculated k accordingly. Unless stated otherwise $\xi = 9.70 \times 10^{-4}$. Using the trap amplitude as the characteristic distance, the switch point $x_s/A = \frac{1}{31}$, bead radius $a/A = 0.56$, and trap separation $d/A = 10$. I used a time step $dt/(2\tau_0) = \frac{1}{490}$, i.e. 490 frames per period, and each simulation lasted 400 cycles. To begin the rower position is drawn from a uniform distribution ($x \in U[-A/2, A/2]$) and the trap randomly oriented. Once the pair reaches equilibrium the relaxation time is calculated using the autocorrelation of the phase difference. I measure the relaxation time by fitting an exponential to the autocorrelation and recording the rate of decay, see section 4.2.3. The simulations are repeated 20 times with different initial conditions. The extreme outliers are then removed before calculating the mean and standard deviation of t_r; extreme outliers occasionally occur in weakly coupled cases, and are defined as being far outside the interquartile range, $t_r < Q_1 - 3(Q_3 - Q_1)$ or $t_r > Q_3 - 3(Q_3 - Q_1)$ with Q_1 and Q_3 the first and third quartiles.

The comparison between the simulated and analytical Fourier series relaxation times are shown in figures 5.3(b,c). The trap shape is varied in (c), and the simulated results closely follow the Fourier series approximation. The inset focuses on changes as the number of Fourier terms in the linearisation is increased. In both the plot and the inset the first order term is the solid line, the third is the dashed, and the fifth the dot-dashed. The simulation measurements for relaxation time are marked with the grey error bars. The bars mark the confidence interval $\bar{t}_r \pm t_{(0.025),(n-1)} S(t_r)/\sqrt{n}$, where $t_{(0.025),(n-1)}$ is drawn from the t-distribution, $S(t_r)$ is the measured standard deviation, and the number of trials is 20, $n = 20$. The trap separation is set to $d/A = 10$, to ensure the hydrodynamic coupling is approximately constant throughout the cycle, i.e. $H^x_{12} \approx \mu_{12}$. The relationship between rower separation and relaxation time is explored in more detail in figure 5.3(b). The top panel (green lines) with $p = 0.17$ has the pair moving in-phase, and the rowers are expected to have

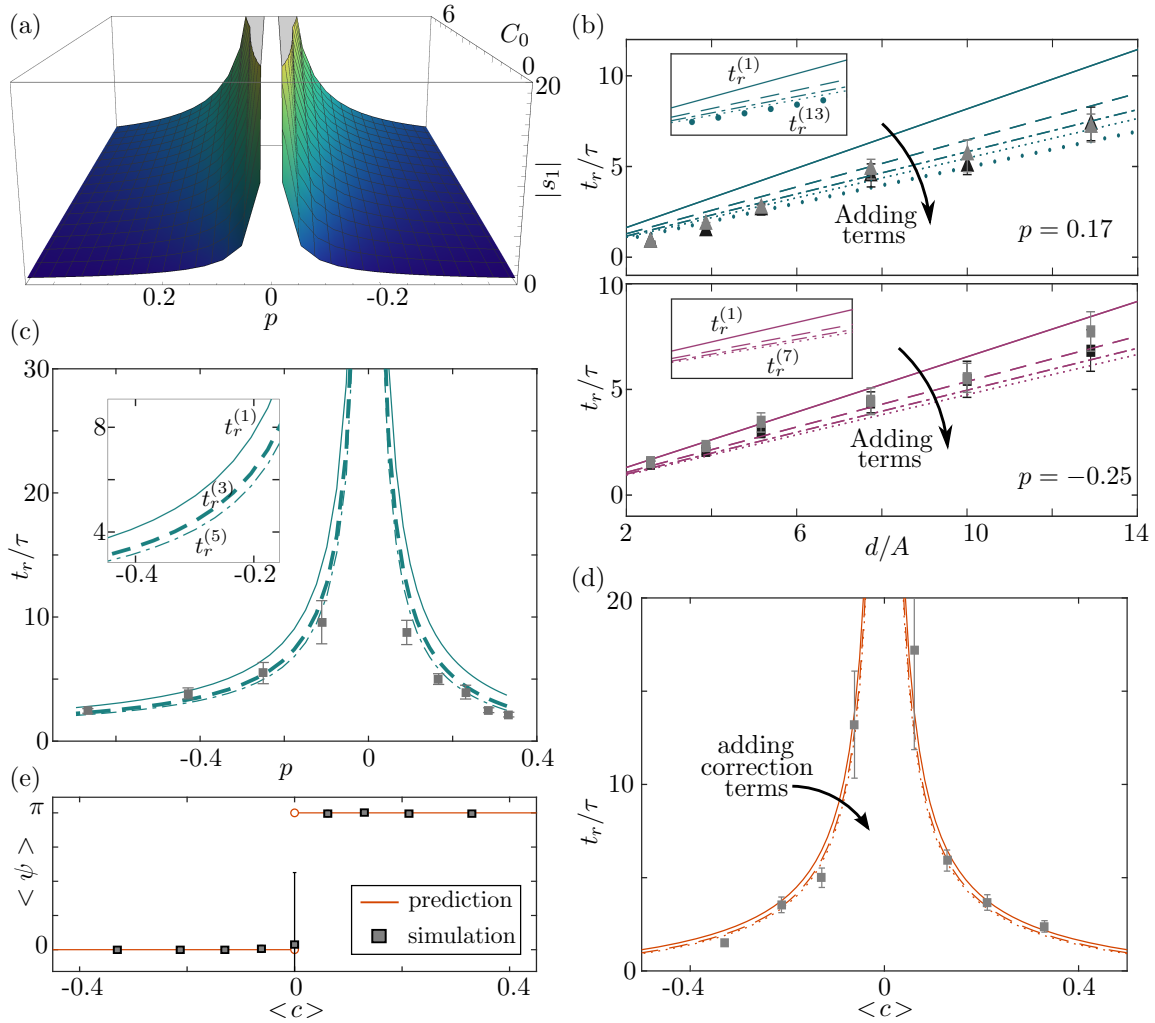

Fig. 5.3 The strength of the pair coupling is measured with the relaxation time; the time is determined by linearising the Fourier series of the average interaction. (a) The magnitude of the first sine coefficient as predicted by the average interaction. Along with the hydrodynamic coupling, the sine coefficient determines the relaxation time for a pair of rowers. (b) The theoretical relaxation time with distance, the green compares the in-phase case $p = 0.17$, and the purple the anti-phase $p = -0.25$. For small distances adding terms improves the in-phase approximation but the anti-phase fit deteriorates. This discrepancy disappears at large d, and is likely due to a breakdown of the fixed distance assumption for the hydrodynamic coupling. In each case the effect of noise is touched upon, with high noise in grey ($\xi = 1.93 \times 10^{-3}$) and low noise in black ($\xi = 9.70 \times 10^{-4}$). Often the higher noise case is better captured by lower order approximations, because increasing the order also decreases the region where they are valid. The insets zoom in on the analytical results, with the convention that $t_r^{(1)}$, $t_r^{(3)}$, $t_r^{(5)}$, and $t_r^{(7)}$ correspond to solid, dashed, dot-dashed, and dotted lines. For the in-phase case $t_r^{(13)}$ is also included, the line with large dots, to coincide with the strongly coupled cases at low d/A. (c) The predicted relaxation time is compared with the simulated results when the trap shape is changed. The inset emphasises the decreasing effect of adding correction term, using the same convention as (b) but only considering up to $t_r^{(5)}$. I set $d/A = 10$ when changing the trap shape, to justify the approximating the hydrodynamic coupling as a constant. (d) The predicted relaxation time is as accurate when considering the more complex cubic potential. In this case the change in trap shape is captured by the change in average curvature $<c>$. (e) The change in stable behaviour is predicted by the mean interaction, with the predicted fixed point (orange curve) coinciding with the average phase difference $<\psi>$ of simulations (grey squares).

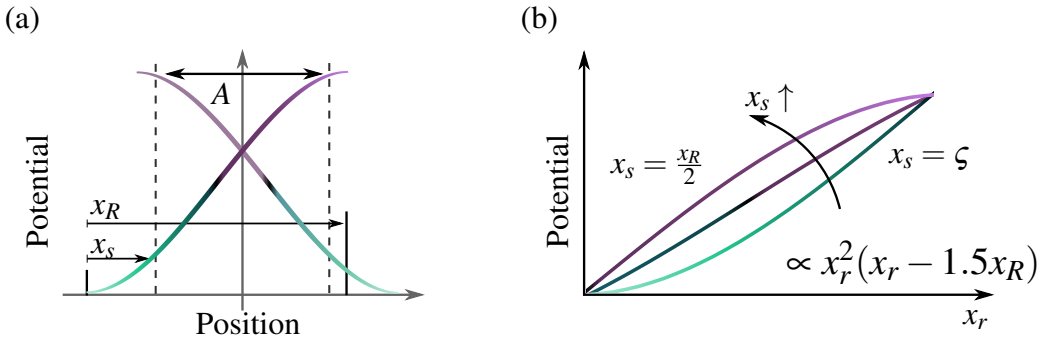

Fig. 5.4 Cubic potentials with a mixture of curvature are more similar to the force profile of a *Chlamydomonas* flagellum's centre of drag. (a) It is the only extension to power law potentials I consider, with a mixture of positive (marked in green) and negative (purple) curvature, i.e. near a non-stationary point of inflection. The switch point x_s is measured relative to the local minimum, and x_R is the distance between the minimum and maximum. (b) The composition of the curvature is varied by adjusting x_s.

a constant separation throughout a period. The grey and black markers represent different noise levels, grey-$\xi = 1.93 \times 10^{-3}$, black-$\xi = 9.70 \times 10^{-4}$. Higher noise results are often better represented by t_r with fewer terms. Including more terms restricts the region about the fixed point in which the measure is valid. The restriction results from the linearisation in section 5.3. In the bottom panel (purple lines) $p = -0.25$ and the rowers are synchronising in anti-phase. When moving anti-phase the distance between rowers varies through the cycle, and for small separation the approximation $H_{12}^x = \mu_{12}$ is poor. In this case I find the simulation relaxation time is higher than would be expected at small separation. The mismatch between simulation and analytical relaxation time is exacerbated by including additional terms. At larger separation the results are more akin to the in-phase case, with lower noise cases better represented by t_r with more terms than the higher noise.

5.4.2 *Chlamydomonas* style cubic potential

The mean interaction can be calculated for any monotonic potential. I also consider a cubic potential, which has periods of both acceleration and deceleration. This is a more realistic description, as living organisms will exhibit both styles of motion. For example, when resistive force theory is used to approximate *Chlamydomonas* flagella, the projection of the driving potential parallel to the cell body appears as cubic-like, see supplementary material of [98]. For consistency all the parameters of the cubic potential, including the average force, are the same as in the power law case. The noise is set to an intermediate value of

the two previously used, $\xi = 1.45 \times 10^{-3}$. In this case the trap shape is varied through the switch point x_s, not α, see figure 5.4. To ensure a mixture of curvature in each trap I set $x_R = 2(A+\varsigma)$ and $x_s \in [\varsigma, x_R/2]$. The small offset $\varsigma = 0.03A$ is included to prevent the rower stagnating at the extremes, i.e. where the driving force is zero.

The analytical expression for $G_I[\psi]$ in the cubic case also exists and can be found in B.3, but it and the associated parameters lack a natural interpretation. Instead I will consider the average curvature of the potential $<c>$,

$$\begin{aligned} <c> &= -\frac{1}{A}\int_{A+x_s}^{x_s} \frac{d^2U}{dx^2}\,dx \\ &= -k(A+2x_s-x_R). \end{aligned} \tag{5.18}$$

The relaxation time is plotted against the average curvature in 5.3(d). The theoretical values from $G_I[\psi]$ are shown by the orange lines, with the same style convention as in 5.3(c). The results from simulation are marked with grey squares. The agreement between the simulation and Fourier series relaxation time is as high for the more complex, cubic case as it is for the power law.

The fixed point as predicted by the average interaction also coincides with the equilibrium behaviour seen in simulation. The average phase difference (grey squares) and the phase difference of the stable fixed point (orange line) are plotted against $<c>$ in 5.3(e). The two are in agreement for all $<c>$. At $<c>=0$ the average interaction has no stable fixed point and the simulated rowers do not synchronise, reflected in the large error bars.

Previously the equilibrium behaviour for a potential derived from the *Chlamydomonas* swimming stroke could only be corroborated using simulation, and the synchronisation strength inferred through sensitivity to noise. Now with the average interaction I can predict the behaviour and the relaxation time of the potential. The relaxation time quantifies the synchronisation strength of different potentials, and can be used to compare driving forces. In this way it is possible to probe the sensitivity of a potential to small changes in shape.

5.5 The mean interaction as a predictive tool

The new approach of calculating an average interaction simplifies the interaction between a pair of rowers to a one-dimensional nonlinear equation. Including additional rowers increases the dimension of the system of equations. If restricted to a particular driving force, i.e. a particular Fourier series, I can explore the effect of varying the coupling between different rowers. In this way I can search for desired or interesting behaviour and then design the rower

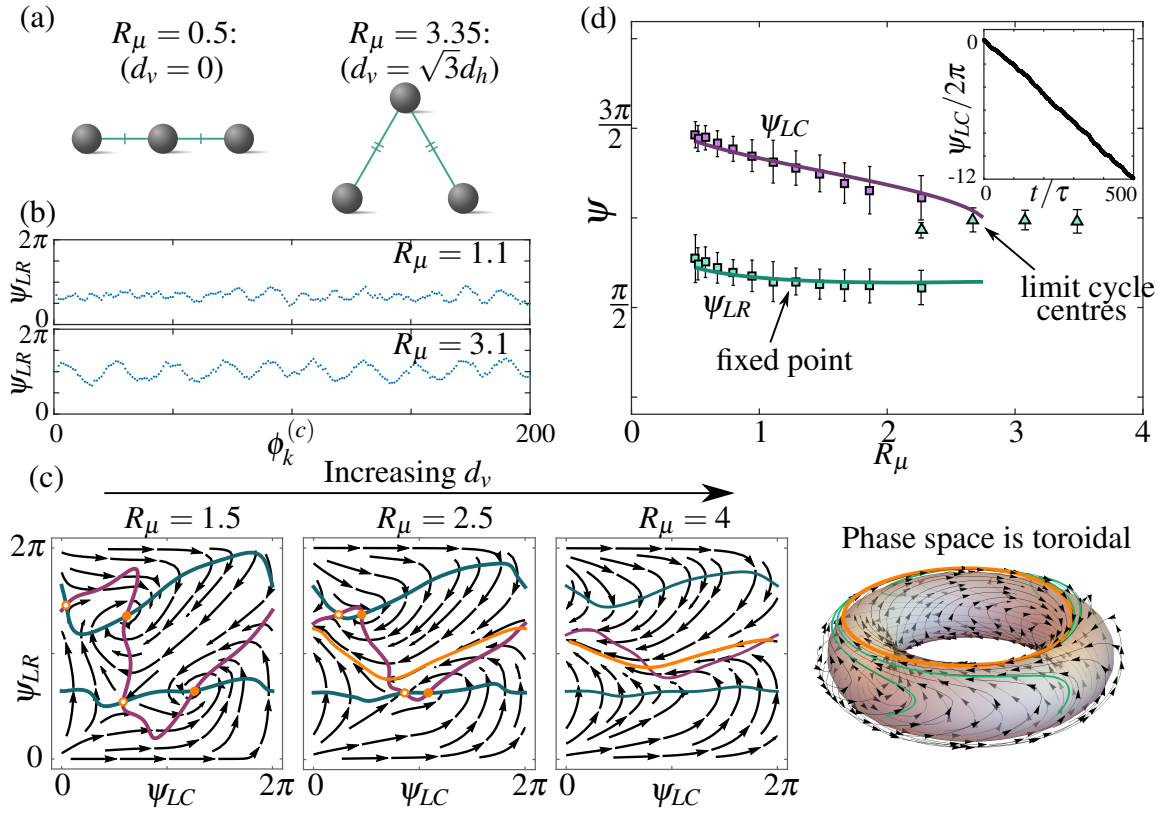

Fig. 5.5 The average interaction is also applicable to larger systems and can be used to predict behaviour or design control systems. (a) I investigated the specific case where rowers are placed in an isosceles configuration. The vertical distance d_v between the central rower (C) and the left and right rowers (L,R) can be adjusted to control the ratio of coupling between the left and right and the coupling with the centre $R_\mu = \mu_{LR}/\mu_{LC}$. (b) Poincaré sections of simulations reveal a limit cycle centred on π for $R_\mu = 3.1$, and a stable fixed point near $\psi_{LR} = 2$ for $R_\mu = 1.1$. (c) The phase portraits show a saddle-node bifurcation as R_μ is increased. The phase space bounded, as it is toroidal, and so a stable limit cycle emerges during the destruction of the stable fixed point. (d) Simulation measures of the stable state is consistent with the predictions from the phase portraits. The simulation results for the fixed points are shown by square markers, with green and purple distinguishing between ψ_{LR} and ψ_{LC}. For the limit cycle the mean of ψ_{LC} is irrelevant, because ψ_{LC} continues to grow in time (see inset). The mean of the cycle for ψ_{LR} is marked with green triangles, where the error bars are calculated using the standard deviation of the each cycles midpoint. Near $R_\mu = 2.2$ both the limit cycle and phase-locked state were observed, when plotted each behaviour was considered separately. The analytical results for the fixed point are marked by the green and purple lines.

layout to achieve the necessary coupling. This extends the use of the average interaction beyond just understanding the synchronisation between rower pairs to a predictive tool for designing systems of rowers.

I focus here on the three rower case, which has three pair combinations and so three different coupling strengths. To reduce this, I assumed the coupling was symmetric between two of the pairs. An isosceles triangle layout is a simple geometry that would lead to this sort of dynamic, represented in figure 5.5(a). In this system the dynamics depend on a single parameter R_μ, the ratio between the unique pair coupling μ_{LR} and the symmetric coupling $\mu_{LC} = \mu_{RC}$. I can tailor the system for any value by varying d_v, the vertical distance between the central rower (C) and the left and right rowers (L,R), demonstrated in figure 5.5(a). I used the Fourier series derived from a power law potential with $p = -0.25$ and $C_0 = 0.21$.

The evolution of the phase difference between the left-right pair, ψ_{LR}, and left-centre pair, ψ_{LC}, can be calculated by extending equation (5.6) to three rowers, i.e $i, j \in \{1,2,3\}$. Using these equations the phase portraits of the system for a given R_μ can be plotted, examples of which are shown in figure 5.5(c). The nullclines are marked by purple and green curves, with the fixed points indicated by orange points; unstable are empty and stable points are filled circles. If a stable limit cycle exists it is also marked in orange, but is a curve. The portraits show the saddle-node bifurcation that occurs when the coupling with rower C decreases. The phase space is toroidal and must be bounded, so a stable limit cycle forms as the fixed points 'mask' and then annihilate one another. Examples of the two stable behaviours are shown using Poincaré sections in figure 5.5(b). ψ_{LR} is plotted at each point rower C completes a cycle, i.e. phase of rower C $\phi^{(c)} = 2\pi$. The same parameters as in section 5.4.1 are used, but the noise is decreased to emphasise the limit cycle behaviour, $\xi = 4.85 \times 10^{-4}$.

The rowers are phase-locked at the fixed points, the predicted shift in phase difference is compared to simulation in figure 5.5(d). The curves are the predicted values and the markers the results of simulation. The colour indicates the pair being considered, green for ψ_{LR} and purple for ψ_{LC}. The marker changes from a square to triangle when the simulations are displaying a limit cycle. The centre of the limit cycle is calculated by finding the midpoint of each cycle and averaging them. It is meaningless to average ψ_{LC} for the limit cycle because it continually grows, see the inset. At $R_\mu = 2.4$ both the limit cycle behaviour and the phase-locked state were observed. The two behaviours were considered separately and both results shown, hence the presence of the square and triangle markers. This aligns with the predictions from the phase portraits, which show a region of coexistence between the phase-locked state $< \psi_{LR} > \approx 2$ and the stable limit cycle centred at $< \psi_{LR} > = \pi$.

The phase portraits derived using the average interaction are a highly effective predictive tool for rower systems. Here I focused on a given driving force for a three rower system,

where one rower was designed to have equal coupling with the other two. The phase portraits predicted a shift from a fixed point with a set phase difference to a limit cycle. Of particular interest was the overlap of the regions where each state is stable, revealing a region of bistability. This approach is not limited to the case discussed here, but can be applied to any system with an arbitrary number of rowers. It is only limited by the ability to visualise and understand the phase space.

5.6 Reviewing the outcomes of the “mean interaction” framework

I have shown that the mean interaction between a pair of geometrically updated oscillators captures their synchronisation properties. The structure of the average interaction’s odd component accounts for the switch between in-phase and anti-phase behaviour when the trap shape is changed. This explanation involving a one-dimensional non linear system is more rigorous than other attempts. Previously the change from in-phase to anti-phase behaviour was interpreted as a preference for the decay or growth of an eigenstate between trap updates. While this does capture the change, there is no obvious method to interpret different levels of the decay rate in terms of synchronisation strength. In contrast this new approach captures the change in the steady state, and measures the coupling strength by predicting the relaxation time. This allows direct comparison of the synchronisation strength of different potentials. Further, it ties rower systems to the larger body of work involving bifurcations and fixed point analysis, which was previously inaccessible

The mean interaction technique can be applied to any monotonically increasing driving potential. Here I included a cubic potential with varying levels of positive and negative curvature. The mixture of slow and fast regions is more similar to the potentials based on resistive force theory applied to actual flagella. Through the mean interaction it is again possible to predict the equilibrium behaviour and relaxation time of these more complex potentials. As this analysis can be applied to any potential, it is possible to explore the sensitivity of the steady state and relaxation time to changes in the interaction.

The benefits of the mean interaction framework become even more apparent when applied to larger systems of rowers. With more rowers, more diverse behaviour can be exhibited. In this case the trap potential is no longer the only defining feature of the equilibrium state. The coupling relative to other rowers, the direct consequence of their physical positions, also has a key role in determining the type of behaviour. The mean interaction can be used to explore both the relative coupling as well as the effect of the trapping potential. The separation of the

hydrodynamic coupling and the trap means the average interaction can be used as a predictive technique. The relative coupling can be varied to find specific behaviour, and then the rower configuration can be designed to produce the desired outcome. This can be of assistance when building blocks of rowers that are sensitive to changes of a single, control rower. The mean interaction approach is not limited to identical oscillators, and can be used to explore the effect of detuning oscillators. This underpins the work in the following chapter, which investigates the difference in coupling strength between oscillators with the entrainment of oscillators with an external signal.

Chapter 6

Susceptibility to an external signal

6.1 Justification for applying external flows

Oscillatory systems are often probed through the application of an external signal. In the context of hydrodynamic systems, the external signal usually takes the form of an external flow [234–237]. For biological systems, they are often applied to either probe a particular cell's behaviour or to align and organise the system beforehand. This is prevalent when growing cells, which often experience flow *in vivo*. The basal body at the base of a motile cilium is directional. Basal bodies have been shown to align under external flows in both *Xenopus* larvae and mouse brain cilia [167, 235]. Aligning the basal bodies leads to an increase in alignment of the cilia motion. To better understand the underlying mechanics of a flagellum, external flows are applied to *Chlamydomonas* [238, 239]. This can be to determine the load response and the effect of fluid viscosity as in [239], or it can to be infer the coupling strength between the flagellum themselves [238].

Applying external flows is a non-invasive way to test a living hydrodynamic oscillator directly. I use the rowers to explore the similarities between synchronisation with an external flow, and synchronisation between oscillators. I find that for pair interactions, the underlying driving force is a critical factor for the synchronisation strength. The same dependence is not observed for an external flow. The differences between the external flow and the coupling between oscillators becomes more pronounced when extended to larger systems. Longer chains become more difficult to synchronise with an external force, but large groups of oscillators spend more time coordinated with one another than small groups. The different responses to the driving force and population size make it impossible to naively equate the synchronisation between an external flow with the coupling between oscillators.

Before demonstrating the differences between oscillators coupling and the coupling of an external signal with an oscillator, the two systems are introduced in detail in section 6.2.

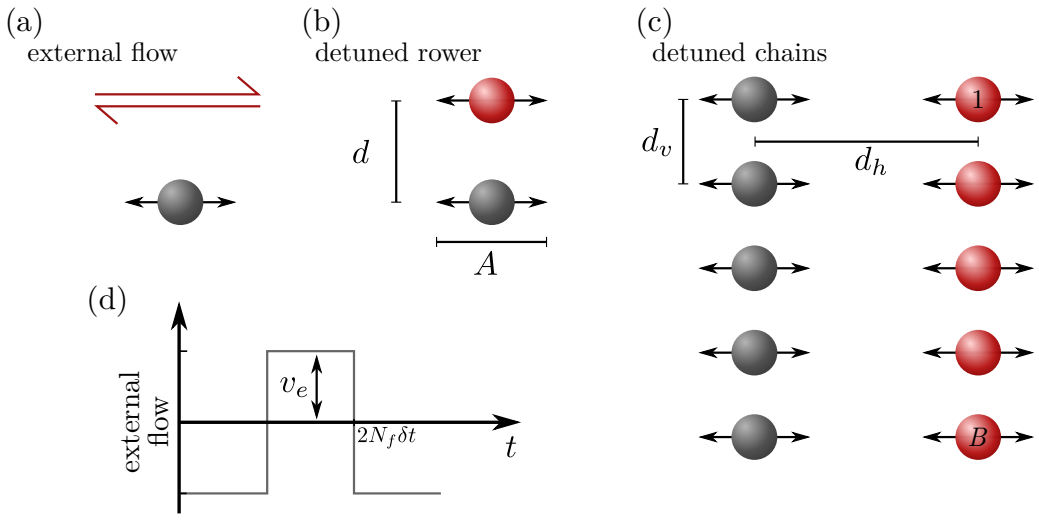

Fig. 6.1 Comparing synchronisation between rowers with the phase-locking between a rower and external flow. (a) A rower with an oscillating external flow applied. (d) The flow has a square wave structure with amplitude v_e and period $2N_f\delta t$. (b) The pair of rowers are separated by a distance d perpendicular to their direction of oscillation. The red rower is detuned by scaling its trap strength. (c) Rower chains consist of a B equally spaced rowers, with the spacing perpendicular to their direction of oscillation d_v. The chain can either be placed in an external flow parallel to the oscillations, or a second detuned chain (red) can be placed a distance d_h away.

Pairs of coupled rowers are introduced in section 6.2.1, before discussing larger systems with two chains of rowers. The equivalent set up for an external signal is explained in section 6.2.2. The theoretical Arnold's tongues are calculated for the rower pairs, and single rower signal system in section 6.3. The differences between the coupling styles is first analysed in this context. This is supplemented in section 6.5, which includes estimates for driving potential based on biological data. Extending beyond this, the more complex case with many rowers is then discussed in section 6.6. The chapter is concluded in section 6.7, where some possible future directions are also included.

6.2 Configuring the signal and rower systems

6.2.1 Rower-rower set up

Rower pairs

The rowers are driven by repulsive traps, which are described in section 4.1.1. In the repulsive case, driving potentials with $\alpha > 1$ lead to in-phase behaviour and $\alpha < 1$ lead to anti-phase.

To explore the effect of curvature on the coordination, both the trap shape α and switch point x_s are varied, with $\alpha \in [0.2, 1.95]$ and $x_s/a \in [0.17, 0.57]$. The rowers oscillate in x but are separated in y, to minimise variation in the distance between them throughout a cycle, shown in figure 6.1. To test the strength of the coupling between the rowers, the frequency of the first rower is detuned, marked as a red bead in 6.1(b). To detune the rower, the trap strength is scaled by f_d/f_0 the ratio of the new detuned frequency f_d and the unperturbed frequency of the second (grey) rower f_0. The noise as defined in section 4.1.4 was set to $\xi = 4.34 \cdot 10^{-4}$ using the average force of the non-detuned rower $\langle F \rangle_t = 2.05$pN; associated with the semi-period $\tau_0 = 0.11$s. The step size for the simulations is $\delta t = 9.1 \cdot 10^{-4}\,\tau_0$ and length $270\tau_0$.

The rowers are coupled using the Oseen tensor, see section 3.4. The distance d between the rowers is chosen to produce weak coupling but maintain clear phase-locking. Specifically $d/a = 9.14$ or 11.43.

Pairs of rower chains

The larger system considered is a chain or line of rowers. They are spaced equally from one another perpendicular to their direction of oscillation, see figure 6.1(c). Similar to the pair case, the rowers are driven by repulsive potential but here I limit my focus to $\alpha = 2$ and $x_s/a = 0.57$. The two groups are detuned, with one chain made up of rowers with frequency f_0 and the other with rowers with frequency f_d. The number of rowers in a chain is varied from $B \in [2, 30]$. The distance between neighbouring rowers within a chain is $d_v/a = 6.86$. The distance between nearest neighbours across the chains is $d_h/a = 54.86$. This ensures the coupling between the groups is weak when compared to the internal chain coupling. The noise is set to $\xi = 5.13 \cdot 10^{-4}$ with the average force of the unaltered rowers $\langle F \rangle_t = 1.74$pN and the semi-period $\tau_0 = 0.125$s. The noise was chosen so as not to overwhelm the weak interaction between the chains, but above zero to avoid persisting in a locally stable configuration. The simulations were repeated 10 times with a random seed for both noise, as well as initial position and trap orientation. Each simulation had a time step $\delta t = 7.8 \cdot 10^{-4}\,\tau_0$ and length $234\tau_0$.

The rowers are coupled through the Blake tensor, but far from the wall $h = 80\,\mu$m; see section 3.5 for details. The Blake tensor was chosen to avoid problems in larger systems, as large numbers of rowers coupled through the Oseen tensor can escape their traps. They escape due to the total interaction having no upper limit as additional rowers are included.

This stems from the unbounded nature of the harmonic series,

$$\sum_{i=1}^{\infty} \frac{1}{n} \to \infty, \tag{6.1}$$

representing a breakdown in the 'infinite' fluid assumption underlying the Oseen tensor.

6.2.2 External signal

Single rower

The implementation of the external signal is discussed in section 4.3.1, with the rower motion in the presence of the signal governed by equation (4.26). An illustration of the signal-rower system set up is shown in figure 6.1(a). The external signal is applied as an oscillating flow aligned to the rower's oscillation. The flow is described by a square wave that switches direction every N_f frames, resulting in a half-period $N_f \delta t$. To minimise the disparities between the signal-rower coupling (SR) and rower-rower coupling (RR), the amplitude of the external flow v_e is set using the time averaged force driving a rower $\langle F \rangle_t$,

$$v_e = \boldsymbol{H}_{12} \langle F \rangle_t \tag{6.2}$$

$$= \boldsymbol{H}_{12} \frac{\gamma A}{N_f \delta t} = \gamma \boldsymbol{H}_{12} 2 A f_e. \tag{6.3}$$

The expression for the average force is found from the dimensionless parameter $\tilde{V}$ defined in equation (4.4), and depends on the frequency of the flow f_e. It is often simpler in this case to express $\langle F \rangle_t$ in terms of a rowers frequency instead of the period, because detuning is expressed in terms of frequency.

The rower itself is driven by the same potential as the non-detuned rower discussed in section 6.2.1. The rower will experience drag described by the Oseen tensor while being driven by a repulsive trap with $\alpha \in [0.2, 1.95]$ and $x_s/a \in [0.17, 0.57]$. To be consistent across the different simulations, the non-detuned rower was unaltered when comparing rower pairs with an external flow. Consequently the rower has an average force $\langle F \rangle_t = 2.05$pN, with the semi-period $\tau_0 = 0.11$s. When altering the trap shape, τ_0 was maintained by adjusting the trap strength, this process is discussed in section 4.4. The noise in the single rower simulation is set to $\xi = 4.34 \cdot 10^{-4}$, the same as the rower pair. Similarly the step size is $\delta t = 9.1 \cdot 10^{-4}\, \tau_0$ and simulation length $270\tau_0$.

Chain of rowers

External flows are also applied to groups of rowers in a chain configuration. The rowers are spaced equally along a line perpendicular to their oscillations direction, see the grey rowers in figure 6.1(c). Specifically the rowers are separated by either $d/a = 4.57$, 6.86, or 13.71. Each rower is driven by a repulsive trap with $\alpha = 2$ and $x_s/a = 0.57$. The external flow is set to $v_e = 5\mu\text{m}/s$ with each rower experiencing an average driving force $\langle F \rangle_t = 1.74\text{pN}$ and semi-period $\tau_0 = 0.125\text{s}$. To decrease computation time there is no noise in the system, with the external velocity expected to disrupt the chain caught in a minimally stable configuration. The chains are also reseeded and run 10 times, with the time step and simulation length identical as the pair of rower chains, $\delta t = 7.8 \cdot 10^{-4}\,\tau_0$ and $234\,\tau_0$.

External flow or external force

An external flow is applied in this chapter to align with work occurring within the group and others [238, 240]. However the method of applying the external signal is important in the context of low Reynolds' number regimes, stemming from the instantaneous nature of the governing equations. Applying an external force to a rower is also felt by the neighbouring rowers. Consequently there are differences between placing rowers under external flow and driving a rower with the geometrically updating force and an additional time dependent force. A lattice of rowers undergoing either a external force or an external flow is explored in Appendix D, where it is found that larger lattices can be easier to entrain when driven by an external force. The same effect is not observed when an external flow is applied.

6.3 Using phase reduction to find the Arnold tongue

6.3.1 Signal-Rower Arnold tongue

The phase difference between a rower and the external flow can be expressed as an autonomous system by applying the same process as in chapter 5. The details of the adaptation of this technique to include an external signal are shown in Appendix C. To distinguish from the detuned rower case, the phase difference with the signal is labelled ψ_S and the averaged

interaction function $G_S[\psi_S]$. The evolution of the phase is,

$$\frac{d\psi_S}{dt} = \Delta\Omega_S + \frac{\gamma v_e \Omega_0}{\pi |F(x_s)|} G_S[\psi], \tag{6.4}$$

$$G_S[\psi] = \begin{cases} \frac{C_0^{-p}}{p+1}\left[C_0^{p+1} + (\pi + C_0)^{p+1} - 2(C_0 - \psi_S)^{p+1}\right], & -\pi < \psi_S \leq 0 \\ \frac{C_0^{-p}}{p+1}\left[2(\pi + C_0 - \psi_S)^{p+1} - C_0^{p+1} - (\pi + C_0)^{p+1}\right], & 0 < \psi_S \leq \pi \end{cases} . \tag{6.5}$$

The natural phase velocity of the bead is Ω_0, and is the difference between the external flow and the rower $\Delta\Omega_S = \Omega_0 - 2\pi f_e$. The interaction function is determined using the same dimensionless parameters as the power law interaction in chapter 5, where C_0 and p are stated explicitly in equation 5.9. The term $|F(x_s)|$ is the magnitude of the driving force at x_s. The rower can be phase-locked if there exists a fixed point for the phase difference, i.e. if a solution exists for

$$\frac{d\psi_S}{dt} = 0. \tag{6.6}$$

Solving for fixed points (see appendix C), the formula for the boundary of phase-locked region is,

$$v_e = \frac{2|f_-|(p+1)}{(2-\alpha)} \left[(A + x_s)^{2-\alpha} - x_s^{2-\alpha}\right]^{1/(2-\alpha)} \left|(1 + C_0/\pi)^{p+1} - (C_0/\pi)^{p+1}\right|, \tag{6.7}$$

where the frequency difference is indicated by $f_- = \Delta\Omega_S/(2\pi)$. The phase locking region is linear with the phase difference. Non-linearities would occur if higher order terms were included when approximating the interaction [36, 241]. The method for doing so is in its infancy, since strong coupling often violates the assumptions leading to the phase approximation.

To explore the effect of altering the driving force on the synchronisation strength, the plateau width for the signal-rower Arnold tongues p_S is measured for a given external flow. The frequency range is considered in terms of f_0, i.e. f_-/f_0. The strength of the external flow is set as $v_e = 2\mu m/\text{s}$, in terms of the average rower velocity $v_e/(2Af_0) = 0.071$. This sets the applied velocity below the minimum velocity produced by the driving potential. The driving potentials are varied using both β and x_s, the effect of which is shown in figure 6.2(b). Generally the magnitude of the curvature decreases as x_s increases, but the effect is more pronounced for higher curvature potentials i.e. increasing $|\beta - 1|$. The plateau width does not vary much when the trap is changed, staying near $p_S = 0.17$. The width does increase slowly as the trap curvature increases, but not dramatically.

6.3.2 Rower-Rower Arnold tongue

The interaction between detuned rowers has the same structure as the dimensionless version calculated for identical rowers in chapter 5. The contribution from each rower, however, is different in the detuned case. The equation governing the phase difference between a pair of detuned rowers is,

$$\frac{d\psi}{dt} = \Delta\Omega_R + \gamma\mu \left[\frac{k_0}{\tau_d k_d} G_{ID}[\psi] - \frac{k_d}{\tau_0 k_0} G_{ID}[-\psi] \right], \tag{6.8}$$

$$G_{ID}[\psi] = \frac{\tau_0}{\gamma} G_I[\psi]. \tag{6.9}$$

The frequency difference between the detuned and unaltered rower is $\Delta\Omega_R = \Omega_d - \Omega_0 = 2\pi(f_d - f_0)$. The dimensionless interaction function G_{ID} has the same structure as G_I in equation B.13. The relative magnitude of the contribution depends on the detuning, i.e. scaling of the coupling strength applied to each term. Expressing the interaction function as a Fourier series, $G_{ID}[\psi]$ is,

$$G_{ID}[\psi] = \sum_{n=1}^{\infty} c_n \cos(n\psi) + s_n \sin(n\psi). \tag{6.10}$$

Approximating the interaction to its first order terms, the equation for the phase difference becomes,

$$\frac{d\psi}{dt} = 2\pi f_- \left(1 - \frac{\gamma\mu c_1}{\pi} \cos(\psi) + \frac{\gamma\mu s_1}{\pi} \frac{f_+}{f_-} \sin(\psi) \right), \tag{6.11}$$

where $f_- = f_d - f_0$ and $f_+ = f_d + f_0$. The detuning range for which a solution exists for the fixed point is,

$$\left| \frac{f_-}{f_+} \right| = \frac{|\tilde{\mu} s_1/\pi|}{\sqrt{1 - \tilde{\mu}^2 c_1^2/\pi^2}}, \tag{6.12}$$

where $\tilde{\mu}$ is the dimensionless Oseen interaction $\gamma\mu^{xx}$. The derivation for this region are expanded upon in appendix C. The detuning f_-/f_+ increases linearly for weak coupling, but then broadens as $\tilde{\mu}$ increases. At very large coupling this expression predicts infinite phase-locking range, demonstrating that when $\tilde{\mu}$ is large enough that it is no longer valid to apply the averaging process.

To explore the effect of curvature on the synchronisation strength, the width of the synchronisation region p_R is calculated. To match the signal-rower case, the plateau is reported in terms of f_0, with f_-/f_+ converted to f_-/f_0. Similarly the coupling strength is measured in terms of average velocity applied by the detuned rower $\mu_{12}^{xx}\langle F \rangle_t = 2\mu \mathrm{m}/s$, which occurs around $d/a \sim 10$. Figure 6.2(a) is a contour plot of p_R for $\beta \in [0.2, 1.9]$ and

$x_s/a \in [0.17, 0.57]$. The plateau shrinks to zero when the traps become linear $\beta \to 1$, and the curvature is decreased to zero. This is consistent with earlier work, where rowers did not synchronise when driven by linear traps [98]. p_R increases as $|\beta - 1|$ grows, with a sharper increase for $\beta > 1$. The reason for this isn't obvious, but could be due to traps with $\beta < 1$ being more sensitive to movements in the switch point. They drop in curvature much faster when x_s is increased than traps with $\beta > 1$.

6.4 Comparing the coupling strength

The two systems vary in their sensitivity to changes in the driving potential. The difference in the plateau widths is shown in figures 6.2(c) and 6.2(d). Figure 6.2(c) is the theoretical difference using the first order approximation. The plateaus measured for the simulated systems is shown in figure 6.2(d). The intensity of the colour indicates the magnitude of the difference, with pink shades indicating the rower-rower system has a broader synchronisation region and green shades indicating the signal-rower system has the wider plateau. Near $\beta = 1$ the signal-rower system has much stronger synchronisation, but the width of p_R quickly outstrips p_S as the trap curvature is increased. The increased sensitivity of the rower-rower system to driving potential is most likely due to the feedback between the two rowers. In the signal-rower case, the rower must match the frequency of the external flow which remains unaltered. In contrast, both rowers interact with one another and so would be expected to depend on the driving potential. The different sensitivity to changes in the driving potential means careful consideration is necessary when equating the entrainment of an oscillator with the synchronisation between a pair of oscillators.

6.5 Biological estimates

Flagella motion is intricate and it is difficult to quantify how their beat motion differs, without even considering whether that difference is important. In this section I use potentials calculated from real flagella, with the hope that the compression process would suppress excess complexity [98, 181, 182, 217]. The types of flagella that were analysed were *Chlamydomonas*, quadri-flagellates, cilia from mouse brain epithelia, and human airways cilia. Differences between the profiles were assessed in terms of the relative susceptibility to external flows compared to their ability to synchronise. This could be one way to tease out whether an apparent change to flagellum's motion results in a different collective behaviour, or if it in fact changes little regarding the coordination.

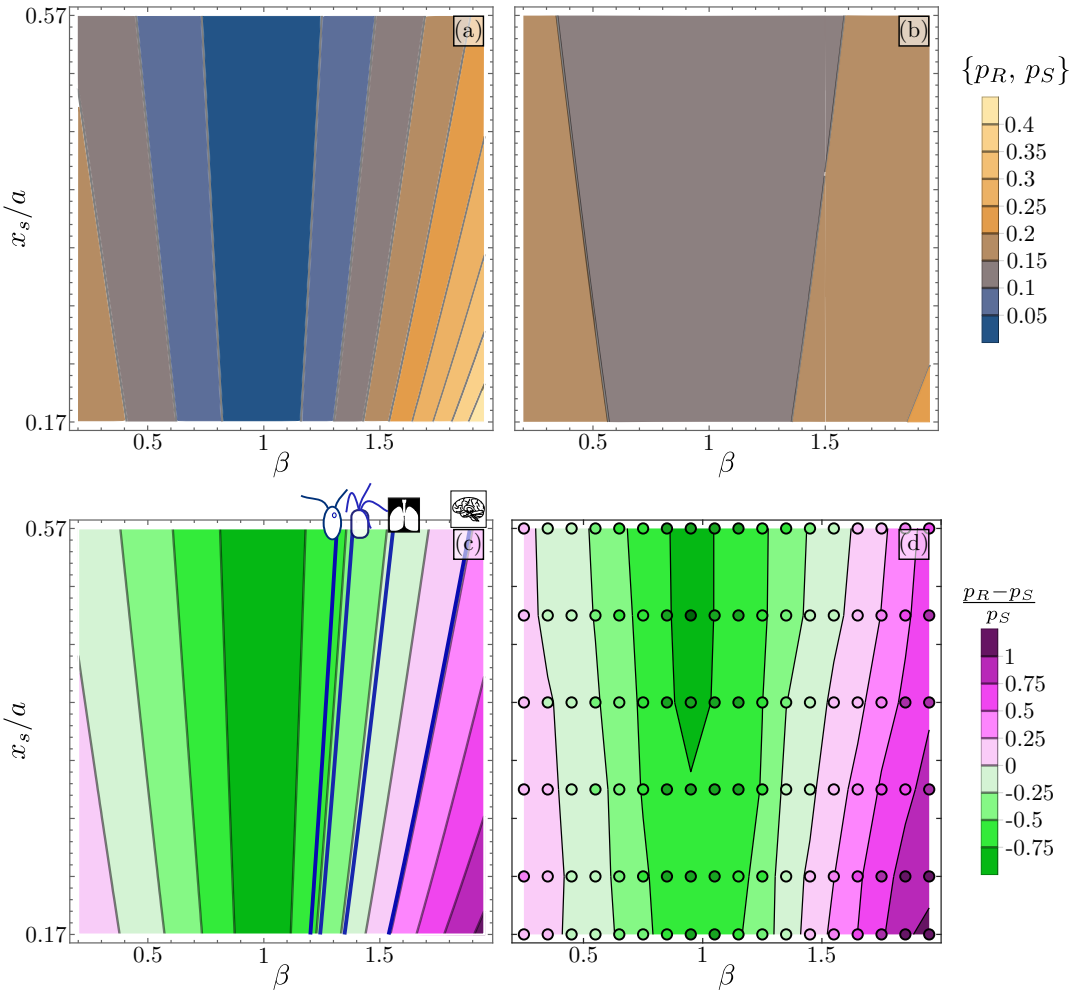

Fig. 6.2 Increasing the curvature of the driving potential leads to stronger coupling between oscillators than with an external signal. (a) The plateau for detuned rowers p_R increases as the trap deviates from linear $\beta \neq 1$. (b) The plateau when a rower is under external flow p_S, with $v_e = 2\,\mu\text{m}/s$. There is little change in the plateau as the driving potential is changed. (c) The difference in plateaus $(p_R - p_S)/p_S$ emphasises the different dependence on curvature. The green regions are when p_S is larger, with the vividness an indication of magnitude. p_R is wider for the purple tones. Cubic force profiles were fit to the motion of *Chlamydomonas* flagella and quadri-flagellated alga, as were airways and mouse brain cilia; details of the fitted force profiles are in Appendix C. The average relative coupling strengths calculated for these potentials are marked by blue lines, and labelled with cartoon cells, lungs or a brain symbol. The single cell organisms show higher susceptibility to an external signal, but mouse brain cilia appear to be sensitive to synchronisation between oscillators. The airways results indicate stronger coupling between oscillators compared to the alga, but examining the spread of the results indicates that it is too large to draw conclusions at this stage. (d) The simulation results for the plateau widths, with markers the raw data and the fitted contours underlaid. The observed coupling strengths are consistent with the theoretical result using the first order approximation.

The details of the compression process are in Appendix C.2. The essence of the procedure is as follows: The flagella are tracked and the centre of drag calculated using resistive force theory. The central axis is defined for the orbit of the centre of drag, and the position data projected onto the axis. The magnitude of the force associated with each point is unchanged, but the sign is now determined by which side of the central axis it appeared. Cubic force curves are then fit to the resulting position and force data. Nicola Pellicciotta tracked the flagella, and the centre of drag calculated using code written by Luigi Feriani. The code was based on the work published in [162]. Regarding the source videos, Kirsty Wan kindly provided us the videos of *Chlamydomonas* and the quadri flagellates which are available at [152, 163]. Lechtreck also generously provided some videos of mouse brain cilia [242], while one other mouse video is from Nicola Pelliciotta that is included in a paper under review [240]. The videos of human airways cilia were provided by Luigi Feriani and available from [243].

Chlamydomonas

Cubic polynomials were fit to force profiles derived from the motion of *Chlamydomonas* flagella. The fits and the process that was developed to compress the flagella motion into a one-dimensional rower trajectory are discussed in Appendix C.2. An example of the trajectory for the centre of drag is shown in figure 6.3(a). The relative difference in the plateaus was calculated for both the left and right flagellum,

$$\left(\frac{p_R - p_S}{p_S}\right)_{Ch,L} = -0.54, \qquad \left(\frac{p_R - p_S}{p_S}\right)_{Ch,R} = -0.56. \tag{6.13}$$

To position them in the context of the power law potentials, the relative plateau difference is used. The cubic potential does not diverge at a vertex, as such the marker for the mean plateau difference measured for *Chlamydomonas* is placed on the $\beta > 1$ half of the map, see figure 6.2(c). This would indicate that the *Chlamydomonas* flagellum are more likely to entrain with an external signal, and are not particularly sensitive neighbouring oscillators.

Quadri-flagellates

Algae exist with more than two flagella. The centre of drag and the associated trajectories of a quadri-flagellated algae were also calculated. The same process was used as for *Chlamydomonas*, as the trajectories had a similar elliptical orbit see figure 6.3(b). Full details of the fit are included in Appendix C.2. The difference in plateau strength was determined for both the “gallop” gait and the “trot” gait. When trotting the alga exhibit breaststroke motion by

pairing its flagella, but when galloping all four flagella perform their own stroke [163]. The plateau difference was measured for a flagellum trotting and also for a flagellum galloping,

$$\left(\frac{p_R - p_S}{p_S}\right)_{tr} = -0.53, \quad \left(\frac{p_R - p_S}{p_S}\right)_{gal} = -0.38. \tag{6.14}$$

The values for the gallop and left trot are similar to those measured for *Chlamydomonas*, and the mean difference is marked on the contour map in figure 6.2(c)

Mouse brain cilium

The trajectories of the epithelial cilia, including those in the mouse brain, are converted to rowers using an approach similar to the elliptical *Chlamydomonas* orbits. However, the trajectories of the centre of the drag of epithelial cilia are crescent shaped rather than elliptical, see figures 6.3(c) and 6.3(d). Consequently instead of fitting with an ellipse, the trajectories are fit with a second order Fourier series. To then convert to a one-dimensional path, the points are projected onto the central line. This allows the more complex paths of the epithelial cilia to be compressed into a rower style. Further details on the calculation and projection to the central curve are included in Appendix C.2.

The plateau difference was calculated for three different trajectories, two filmed *in vivo* and one *in vitro*. To distinguish the cases, the *in vivo* are labelled $M.vv$ and the *in vitro* $M.vt$,

$$\left(\frac{p_R - p_S}{p_S}\right)_{M.vv1} = 0.10, \quad \left(\frac{p_R - p_S}{p_S}\right)_{M.vv2} = 0.38, \quad \left(\frac{p_R - p_S}{p_S}\right)_{M.vt} = 0.23. \tag{6.15}$$

On average the plateaus indicate stronger coupling between oscillators than with an external flow, counter to the *Chlamydomonas* case. This is illustrated in figure 6.2(c) where the line marking the average brain plateau is inside the pink region.

The compression to a one dimensional oscillation requires a certain level of approximation. Beyond the assumption the cilium can be reduced to a bead, the approach assumes the rowers are aligned at all times with the possibility of moving in opposite directions. This would correspond to being near in-phase or anti-phase at all times. Further the approach ignores any anisotropy in the coupling that would be introduced by the presence of the cell wall. It may be possible to only consider the contribution that is aligned with the cell wall, but currently there are problems arising from differences in the amplitude for the power and recovery stroke.

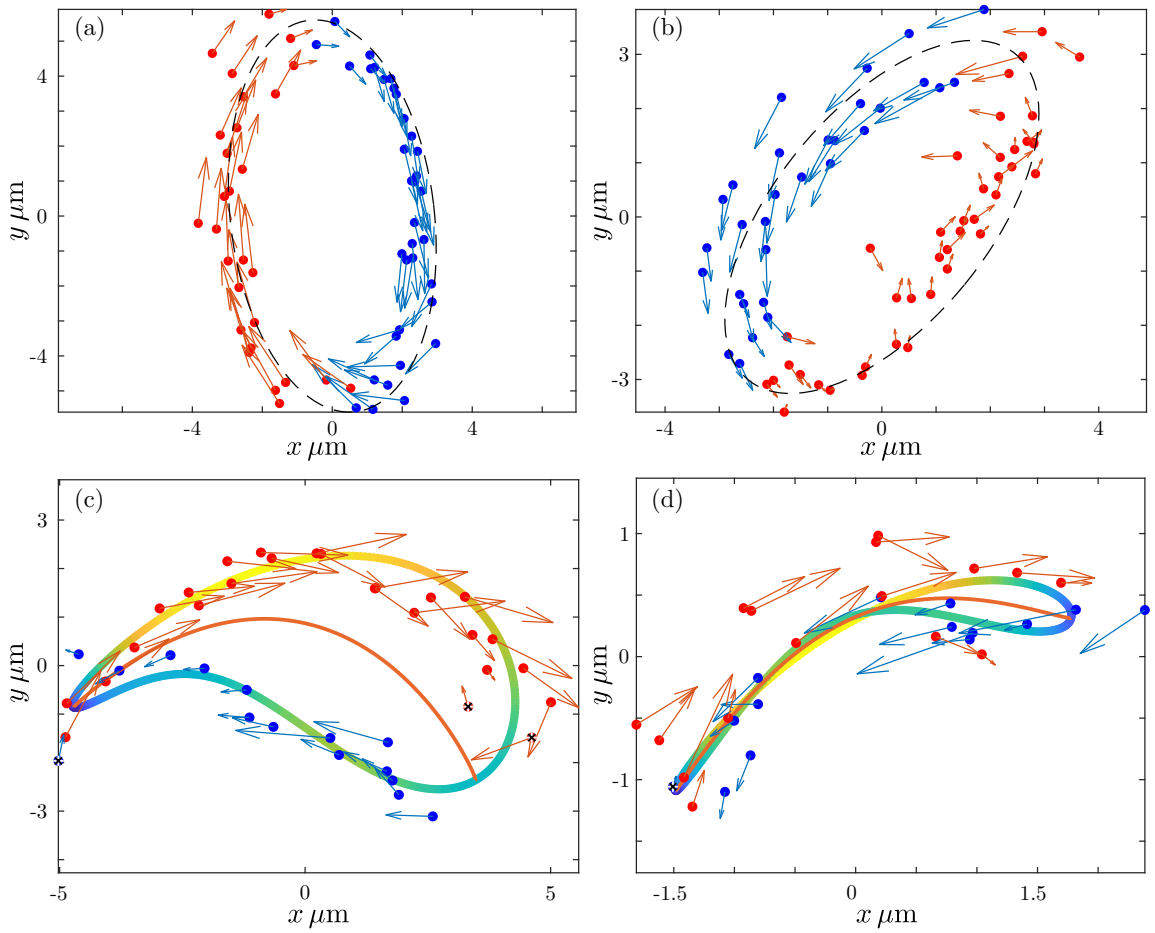

Fig. 6.3 Examples of rower trajectories fit to the motion of living cilia. (a) Tracking the centre of drag of a *Chlamydomonas* flagellum. The net force applied by the flagellum is indicated by the arrow. To convert to one-dimensional rowers, forces right of the major axis (blue) are set as negative and force left of the axis (red) are positive. (b) The same for a quadri-flagellated algae performing the gallop gait. Both algae have an approximately ellipsoidal trajectory, the same is not observed of cilia found in the mouse brains and human airways. (c) The trajectory mapped out by the centre of drag of a mouse brain cilium. In this case the trajectory in x and y are fit with second order Fourier series, where x is parallel to the cell wall and y is perpendicular. (d) The trajectory for a human airways cilium fit with the second order Fourier series. The trajectories in these cases are much more elongated, with the stretching occurring parallel to the epithelial surface.

Human airways cilium

The force profiles for the human airways cilia were calculated using the second order Fourier series in the same way as the mouse cilia. An example of the airways crescent trajectory is plotted in figure 6.3(d). The difference in plateau width was calculated for four different cilium, with the derived profiles and trajectories included in Appendix C.2. The plateaus were calculated as,

$$\begin{aligned} \left(\frac{p_R - p_S}{p_S}\right)_{H1} &= -0.55, \quad \left(\frac{p_R - p_S}{p_S}\right)_{H2} = 0.17, \\ \left(\frac{p_R - p_S}{p_S}\right)_{H3} &= -0.59^*, \quad \left(\frac{p_R - p_S}{p_S}\right)_{H4} = 0.13. \end{aligned} \tag{6.16}$$

The value for $H3$ is marked with a star to indicate the first order approximation was particularly poor, with the second order terms comparable to the first. The approximate value when higher order terms are included is -0.34. The range of observed values is much broader. Some broadening is expected because of the high density of the cilia in the airways, which makes tracking a cilium difficult. This is reflected by the reduced number of measurements drawn from a video, which then increases the variability in the trajectory and the plateau measurements. For completeness the average plateau difference for airways is also included in figure 6.2(c), with a lungs symbol used to indicate the airways value.

Collating the data for different types of flagella

The results from the different species are compiled in figure 6.4. The difference in the plateau widths are grouped as single cell or epithelium cilia in figure 6.4(a). It indicates that for the single cell flagella studied, the susceptibility to an external flow is greater than the oscillator coupling strength. The mouse brain cilia in contrast appear to have stronger coupling between oscillators. For the airways case there is some evidence of stronger coupling, but the broad spread of the results inhibits drawing firm conclusions. To link back to the theoretical work involving simple power laws the range of the plateaus for the different species are included on the earlier contour map in figure 6.4(b). To simplify the image the coloured region of the contours have been removed and the algae are represented by green bands, the brain range by the pink region, and the results of the airways by the blue band. Consistent differences also appear in the elongation of the tracked trajectories. To have the same width measure across the different shaped trajectories the area traced out is divided by the amplitude. This width is plotted against the amplitude in figure 6.4(c). To give an indication of the elongation reference lines are included and labelled with rectangle reflecting the ratio between length

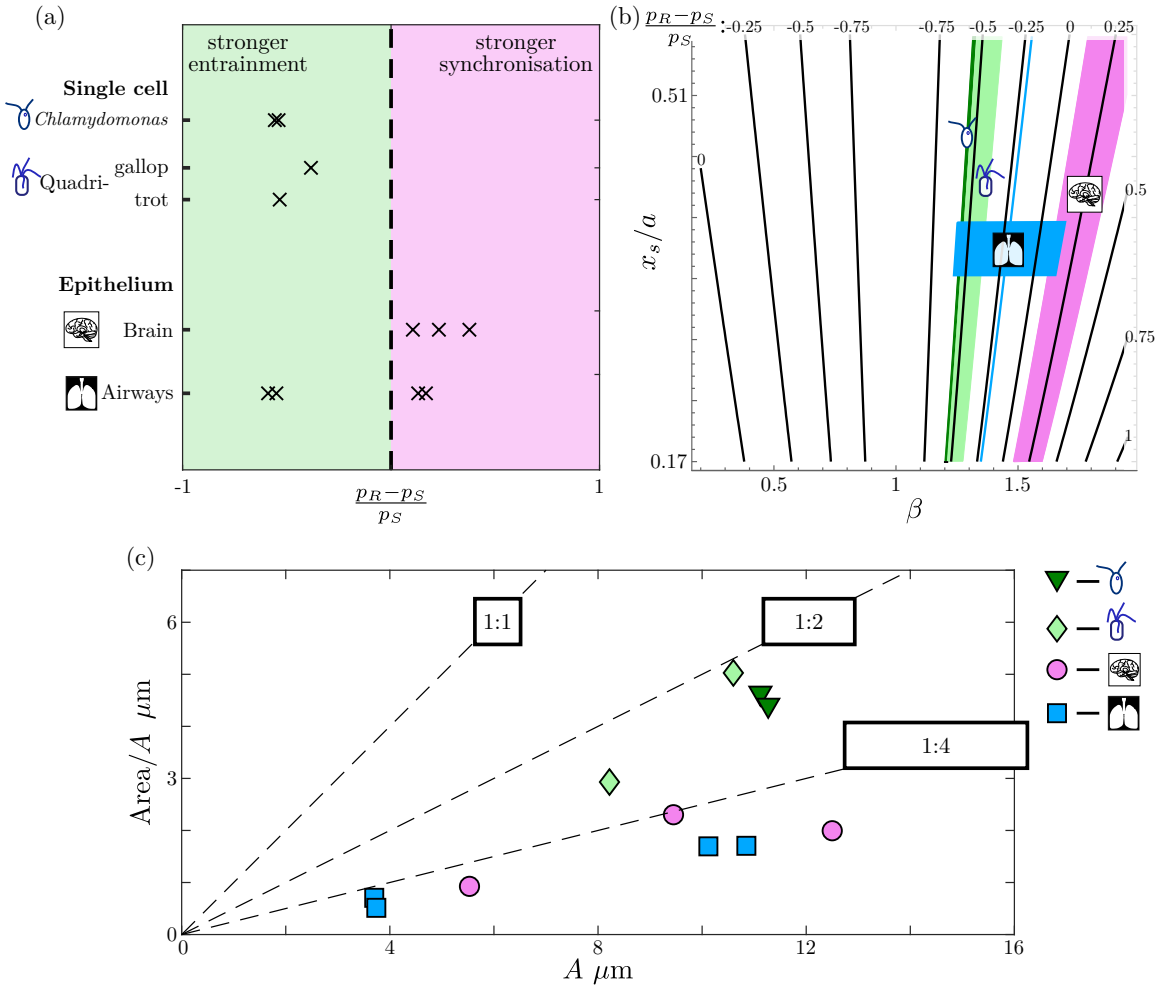

Fig. 6.4 Tracking flagella indicates epithelial cilia exhibit a different stroke style to single cell algae like *Chlamydomonas*. The algae are more easier to entrain, while coupling between oscillators is stronger in brain cilia. (a) The difference in oscillator coupling p_R when compared with the entrainment susceptibility p_S for the different species. The difference for *Chlamydomonas* and quadri-flagellates indicates they are more susceptible to entrainment. The epithelial cilia by contrast appear to have stronger coupling between oscillators. The airways results are clustered either with the brain cilia with strong oscillator coupling and near the algae. The high density of airways cilia causes difficulty when tracking a single cilium, which is most likely responsible for the increased spread. (b) The range of observed plateaus are combined with the theoretical values predicted by simple power laws. The range *Chlamydomonas* is dark green with a bi-flagellated marker. Similarly the quadri-flagellates are marked by light green and a marker with four flagella. The range of values seen in mouse brain cilia is marked in pink with a brain marker. To avoid confusion with the broad range of values, the mean of the airways is marked with a blue line, and the range indicated by the blue strip and a lungs symbol. (c) Comparing how elongation of the different trajectories. To measure the width of the trajectories the ratio of area with amplitude is used, which can be applied to any trajectory shape. The dashed lines indicate specific ratio, with the labels demonstrating the elongation. The algae trajectories (green markers) have approximately 1:2 ratio between their amplitude and width, with a slightly lower value consistent with an oval. The paths mapped out by the epithelial cilia (brain-pink and airways-blue) are much narrow with a ratio of 1:4.

Table 6.1 The number of rowers removed to avoid edge effects.

	Chain length, B										
	1	2	3	4	6	8	10	15	20	30	40
No. rowers	0	0	0	0	0	3	3	5	6	10	10

and width. The algae markers are dark green triangles and light green diamonds. They fall near the 1:2 ratio, and would be consistent with an oval trajectory with the minor and major axes related by a similar ratio. The trajectories mapped out by the epithelial cilia are much more elongated than those describing the algae. The brain and airways markers (pink circles and blue squares) all fall below the 1:4 ratio. This may only reflect the added impediment of a cell wall, but could be indicative of a change in flagella stroke that leads to increased coupling between cilia.

6.6 Coupling for a chain of rowers

6.6.1 Edge effects for a chain

Extending to larger systems introduces edge effects into the system. Rowers at the limits of the chain have fewer close neighbours than those located closer to the centre. For large enough chains the absence of neighbours leads to a reduction in frequency and only transient phase-locking occurs. To avoid unnecessary extra spread in the frequency distribution of the rower chain, the edge rowers are not considered when measuring the phase-locking. A broader frequency distribution leads to a smearing at the onset of phase-locking, making measurements of the plateau width more difficult.

The rowers excluded due to edge effects are determined using the chain with the strongest coupling $d/a = 4.57$ with no external flow. The set of removed rowers is then maintained across all the different chain cases, both external flow and detuned, to avoid changes due to the choice of excluded rowers. Examples of the exclusion region for $B = 6$, 10, and 30 are shown in figure 6.5. The cut off region, marked by the dotted orange line, is selected such that rowers with average frequency lower than the central rowers are not included. To confirm the cut off choice, the residual frequency using the average of the selected rower is plotted. The choice is rejected if the central residuals show a positive bias. The cut off values used are listed in table 6.1

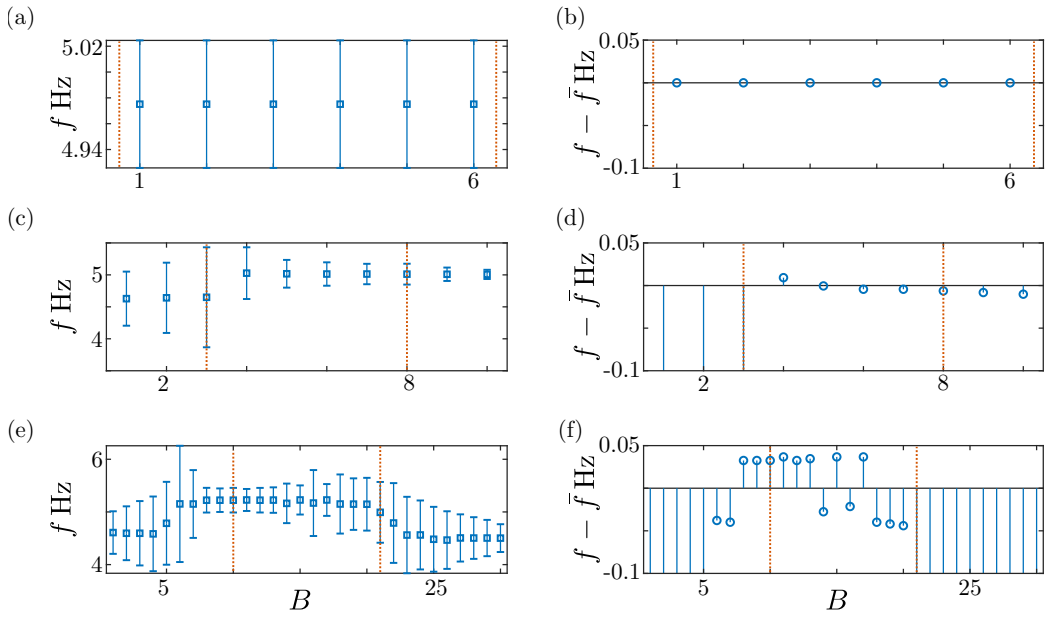

Fig. 6.5 Excluding rowers on the edge of the chain to avoid smearing at the boundary of phase-locking. (a,b) The observed frequency of the rowers f and variations around the mean excluding the edges $f - \bar{f}$ for $B = 6$. The orange line marks the point at which the edge cut off begins, which for chains smaller than $B = 6$ is beyond the chain edge. (c,d,e,f) The same for chains of length $B = 10$ and 30. The fluctuations are much larger in the longer lattice than in the small case, even restricting to only the central rowers.

6.6.2 A chain of rowers under external flow

The phase-locking is measured using the proportion of time spent near synchronisation. The details of the measure are included in section 4.2.2. The system is defined as near synchronisation if the phase difference is within 0.45 of the average or offset by π, i.e.

$$t_S = \frac{1}{t_{tot}} \int_0^{t_{tot}} |\phi_i - \phi_S - \psi_T| < 0.45\, dt + \frac{1}{t_{tot}} \int_0^{t_{tot}} |\phi_i - \phi_S - \pi - \psi_T| < 0.45\, dt. \quad (6.17)$$

The minimum expected value to drift from the threshold at 0.45 is $t_0 = 0.29$. The chain is considered phase-locked when the average time spent near the synchronisation across the chain is above $0.5(t_0 + 1)$, i.e. more than half the time unaccounted for by drift is spent phase-locked.

The plateau width is used to compare the coupling strength as the chain length is increased, see section 4.2.3 for details. An example for a single seed is shown in figure 6.6(a). The range of frequencies that the will phase-lock decreases as B increases. The average plateau width for different d is plotted in figure 6.6(b). The trend of decreasing plateau width persists across the different cases. The error bars are the larger of: the standard deviation of p_S and the resolution of the simulated detuning 0.107. The lowest density case with the weakest coupling between the rowers (purple circle - $d/a = 13.17$) has the smallest reduction in plateau width, and the low width is reached earliest. In contrast the high density case with strong coupling (green square - $d/a = 4.57$) has the greatest drop in p_S and has reductions in p_S for a larger number of rowers. This indicates the more rowers that are interacting, the more difficult it is to entrain them to an external flow. I believe this may be due to the increase in frequency spread observed when the chain length is increased. If the spread is large enough, it may not phase-lock with the signal and then disrupt the others. Another possibility is the signal pushing the rowers towards being perfectly in-phase. This in turn will accelerate them via the reduction in drag. The new frequency may be beyond what the original signal can entrain.

6.6.3 A pair of rower chains

The synchronisation between the detuned chains of rowers is also measured using the time spent phase-locked. To measure this time, the phase-difference between the nearest neighbours across the chains is considered rather than using the external signal phase,

$$t_S = \frac{1}{t_{tot}} \int_0^{t_{tot}} |\phi_{i,1} - \phi_{i,2} - \psi_T| < 0.45\, dt + \frac{1}{t_{tot}} \int_0^{t_{tot}} |\phi_{i,1} - \phi_{i,2} - \pi - \psi_T| < 0.45\, dt. \quad (6.18)$$

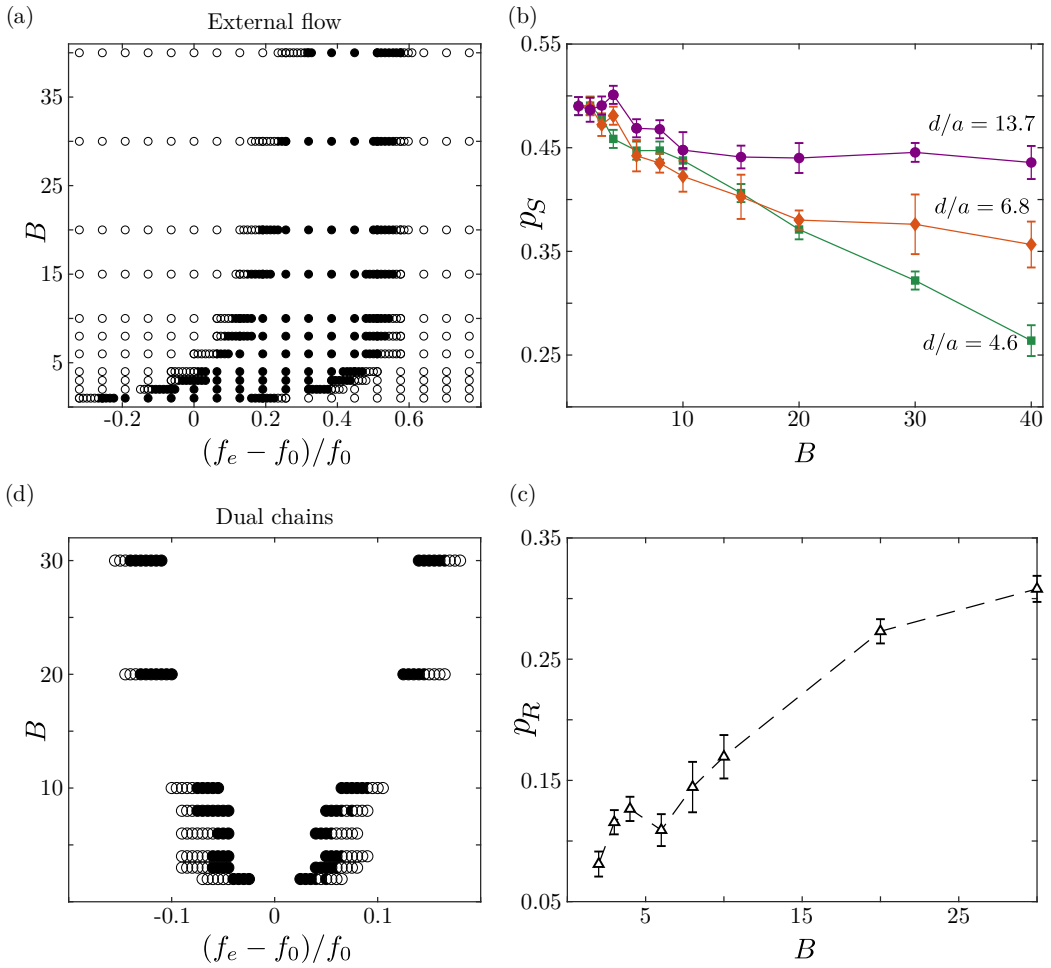

Fig. 6.6 Including further rowers when applying an external flow and for chain pairs has diverging trends for the synchronisation plateau. (a) The range of detuning for which a rower can phase-lock with an external flow decreases as the chain length B increases. A simulation is considered synchronisation if the proportion of time spent synchronised $t_S > 0.64$. (b) Averaging the plateaus over 10 seeds for $d/a = 4.6$, 6.8, and 13.7. When the rowers are close together, the reduction in plateau width p_S is more pronounced. (c) Two chains of rowers increase the detuning range when B is increased. (d) The average plateau width over 10 seeds highlights this trend. In both (c) and (d) the error bars are the maximum of the standard deviation of $p_{(S,R)}$ and the simulation resolution 0.011.

The same threshold of $t_S = 0.64$ is used to determine which states are synchronised, with the average value across the chain tested.

As before the plateau widths for the rower chains p_R are used to infer the coupling strength as the chain length is increased. An example of the plateaus with increasing B is shown in figure 6.6(c). In contrast with the external signal, p_R increases with the chain length. The average over the different seeds is plotted in figure 6.6(d). This highlights the contrasting trend in the rower plateaus, but it does appear to start flattening at very long length. This is expected, as it would be infeasible for the effect to continue indefinitely.

6.7 Summarising the distinctions between oscillator coordination and entrainment

The synchronisation strength between oscillators depends on their individual motion. By contrast, the ability of an external flow to entrain a rower is not very sensitive to the driving potential. Consequently depending on the curvature, the oscillator coupling may be higher than that indicated by the entrainment with an external flow. This demonstrates some nuance is required when extrapolating from one case to the other. Simple approximations of flagella trajectories indicate differences in the stroke can appreciably alter the oscillator coupling strength relative to the external flow. Early results show epithelial cilia are more likely to be strongly coupled, but at this stage difficulties in tracking dense cilia inhibit drawing strong conclusions.

Scaling to larger systems produces diverging trends for oscillator coupling and entrainment under flow. The plateau width expands when additional rowers are included in a pair of oscillator chains. If used as a proxy for synchronisation strength, this would indicate an increase in the oscillator coupling or some emergent phenomena. The same trend is not observed when more rowers are placed in the external flow. The chain of rowers becomes increasingly difficult to entrain when either the density, and hence coupling between the rowers, or the number of rowers is increased. This highlights that a distinction may need to be drawn between multi-ciliated cells and those with only a few flagella.

This is the final chapter that involves the phase reduction. The following chapters are more akin to the chain work in this chapter, and focus on larger arrays of rowers. Specifically the ability to influence subset formation through physical properties, including the spatial position, of the oscillator population.

Chapter 7

Controlling subset formation using mechanisms inspired by starfish larva

7.1 Background information on starfish larva

The simplicity of the rower model means it is predominantly used to investigate general features of emergent coordination. In the previous chapters the focus has been on generic features of oscillator pairs or small systems. Here it is shifted to investigate certain behavioural features, specifically the formation of subsets or clusters in large populations of oscillators. It is demonstrated in this chapter that the formation of the subsets can be controlled through the geometry of the system, or some small alteration to the oscillator. Whereas before the simplicity of the rower model was expected to lead to widely observable behaviour, now it should lead to widely applicable geometries or control mechanisms.

The work in this chapter is inspired by the movement of starfish larva [244]. The larva have a band of cilia around their periphery, which have two swimming styles. One is to swim and the other to feed. Multiple swimming styles is not unique to starfish larva, and are exhibited by other microorganisms including *Paramecium* [245–248]. The different strokes are not always related to nutrient uptake, but can be an evasive response to a detected threat [245, 247]. The feeding stroke for larva in [244] was postulated to be a motion style that promoted vorticity in its surrounding. This would then draw prey inwards. This theory was based on the apparent eddy formation around a larva trapped between two slides. An example of which is shown in figure 7.1(a), with streamline schematics of cilia reversals that could lead to such flows in figures 7.1(b) and 7.1(c). The validity of this conclusion was questioned, as eddies are a known by-product of the changing boundary conditions

when sandwiching a starfish larva between slides [249], however Gilpin *et al.* stand by their conclusions [250].

Ciliary bands in marine larva are often controlled directly by a basic localised nervous system, but the details vary across the species [244, 251, 252]. Furthermore, simpler ciliated microorganisms without a central nervous system still display active motion, with more than one gait available for different contexts [245, 246, 248]. The diverse range of solutions that have evolved to combine feeding and locomotion through ciliary motion raise the question: can hydrodynamic forces play a supporting role in subset formation. To establish whether or not subsets are created through hydrodynamic forces, three different control mechanisms inspired by the larva, are implemented for a chain of rowers; see figure 7.1(d). My results demonstrate that the rower subsets can be encouraged to form at predetermined points by altering particular rowers or adjusting the geometry of the system. Before introducing the control mechanisms that lead to the subset formation, details of the unaltered chain are discussed in section 7.2. The control mechanisms are then presented in section 7.3, and then the different behaviour resulting from each discussed in section 7.4. The likelihood of the different states being observed in covered in section 7.5. The chapter concludes with section 7.6 where the effectiveness of each mechanism is reviewed.

7.2 Configuration to form metachronal waves

7.2.1 Geometric parameters of the rower chain

The starfish larva shows metachronal wave patterns along its cilia. This behaviour has been replicated before in systems of rowers [187]. Taking inspiration from the work in [187], when investigating chains of rowers representing starfish larva I use oscillators with a large amplitude at high density, very near a boundary. Specifically $A/a = 30$, $d/a = 7$, and $h/a = 3$. To allow this dense spacing with large oscillations, the rowers oscillate at 45° off the horizontal with the distance between oscillators measured along the horizontal. The chain itself is 60 rowers long. Periodic boundary conditions are implemented to reproduce the features of the monocilia carpet. Unlike in [187], I do not want to suppress changes in the direction of the metachronal wave. Consequently there is no additional asymmetry in the driving force for this system.

7.2.2 Simulation parameters for starfish modelling

The beads are driven by an attractive square root potential, with $\alpha = 0.5$ and the switch point $x_s/a = 2.5$. This should produce metachronal waves with long correlation length. The trap

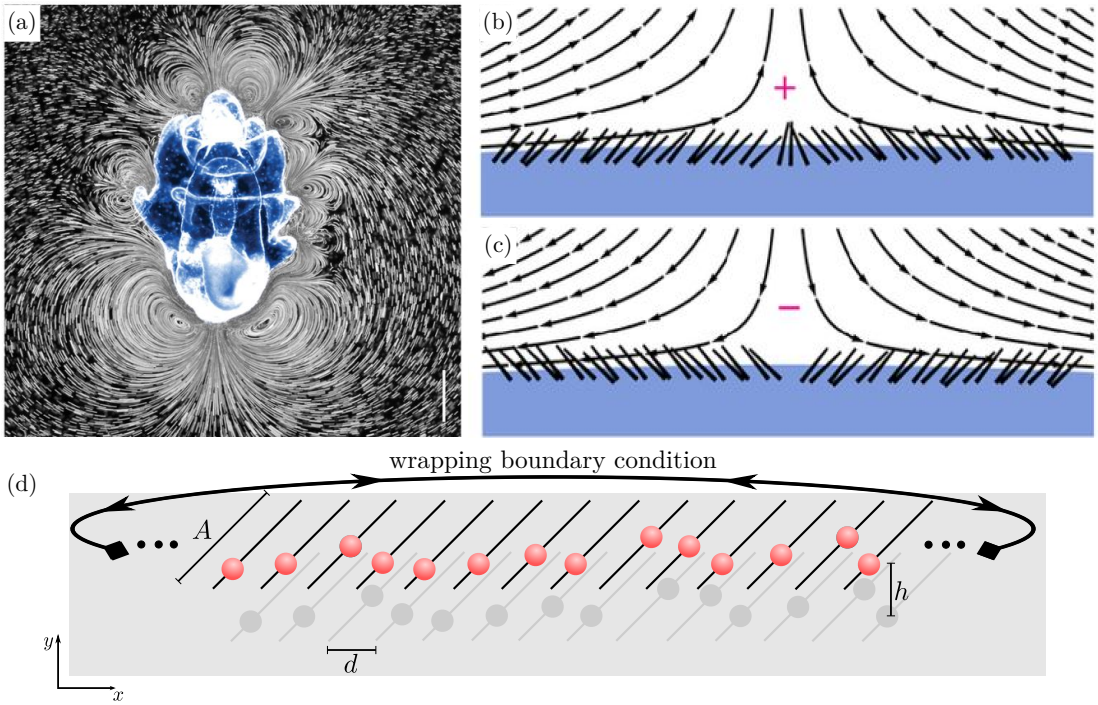

Fig. 7.1 The monocilia carpet of starfish larva is modelled as a chain of rowers. (a) An eight week old starfish larva with tracer particles, adapted from [244]. (b,c) Streamlines for a model flow generated by sign change in the velocity along the surface with illustrative cilia; they are adapted from [244]. (d) The monocilia are modelled as a chain of rowers near a boundary. To replicate the geometry of the larva, periodic boundary conditions are implemented and the rowers wrapped. The amplitude A, height from surface h, and the separation distance d are selected to create a stable metachronal wave.

strength produces a period of 2s, with the step size $2 \cdot 10^{-3}$ cycles and the simulation length 2000 cycles. The starting positions for each simulation are drawn from $\mathscr{U}(-A/2, A/2)$, and the trap randomly oriented. Each case is reinitialised 50 times, with new starting positions in each simulation. The noise is set to $\xi = 3.7 \cdot 10^{-5}$, see section 4.1.4 for details.

7.3 Posited control mechanisms

7.3.1 Shape change to modify hydrodynamic coupling directly

The starfish larva are swapping between two swimming states. It appears that the larva is undergoing some shape change. This can directly change the hydrodynamic coupling between neighbouring groups of cilia. By bending and changing its shape, the larva could alter the orientation and distance between clusters cilia. For example, if cilia were on the outer surface of a $\cup$ shape, then the cilia on the straight sections would not be expected to strongly couple via hydrodynamic forces. This would lead to a reduction in coupling strength. To recreate this affect along a line extra distance separating some rowers is introduced. This is illustrated in figure 7.2(a). The extra distance d_X is introduced regularly between every N_g rowers. Only reduced coupling is considered with $d_X > 0$ in all cases.

7.3.2 Cilia oscillation size

Alternatively the beat of the cilia themselves might alter to change the swimming stroke of the larva. While there are still unanswered questions about the precise process underpinning the different aspect of cilia motion, it is accepted that the amplitude can be varied through some regulation of the dynein activity [253]. Therefore a possible control mechanism stemming from the motion of the cilium is a change in the amplitude.

To investigate the formation of subsets by altering the amplitude I alter the amplitude of regularly spaced rowers. This is illustrated in figure 7.2(b). Every N_g rowers the amplitude is altered by A_X, which can be either positive or negative. The frequency of the rowers is maintained across the entire chain, so a rower with $A_X < 0$ has decreased trap strength. This in turns leads to a reduction in the velocity and coupling strength with the other rowers. Conversely, $A_X > 0$ increases the bead velocity and the coupling strength. This is an additional freedom that is not considered when changing the distance between subsets.

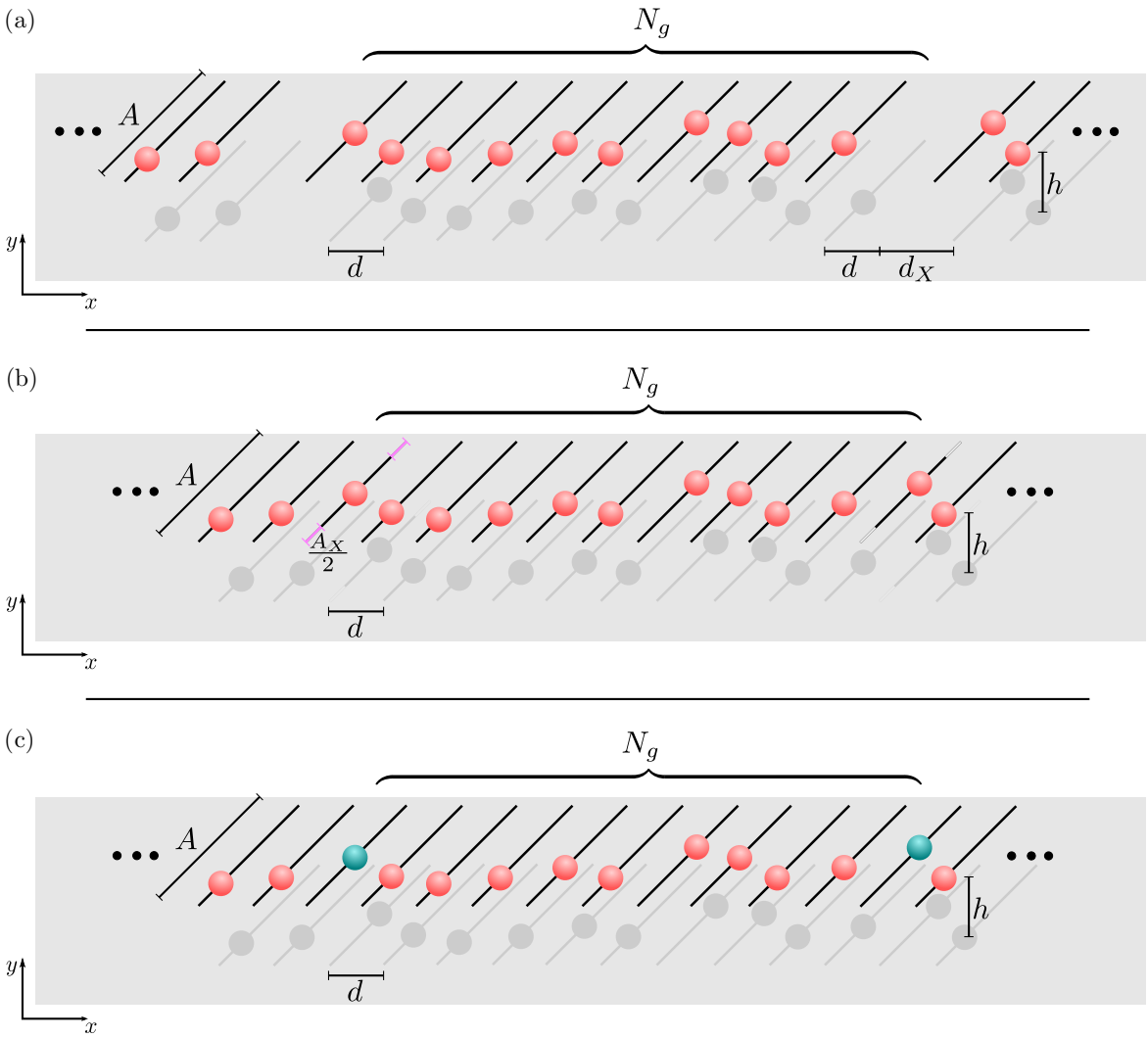

Fig. 7.2 Three possible control mechanisms for the formation of phase-locked subsets. (a) Increasing the distance between groups to encourage the formation of subsets. Each group has N_g constituents, with the additional distance d_X. (b) Regularly adjusting the oscillation amplitude also introduces some structure to promote the formation into subsets. As before there are N_g beads in each subset, with the amplitude of the first changed by A_X. This is indicated by the lilac section. The amplitude change could be an increase or decrease, but in both cases the frequency of the oscillations is kept constant by scaling the trap strength. (c) Alternatively the frequency of every N_gth rower can be altered. The rowers with the frequency change are marked in green for this figure.

7.3.3 Cilia frequency

Another possible effect from regulating the dynein activity or altering the ATP concentration is a change in beat frequency of the cilium. This is implemented in a similar way as the previous options, with the frequency of every N_gth rower scaled by a factor f_X. This is illustrated in figure 7.2(c), with the rowers with altered frequency marked in green. The frequency can be increased or decreased with $f_X > 1$ or $f_X < 1$, which scales the trap strength k to alter the frequency. Consequently this either increases the coupling strength when $f_X > 1$ or decreases the coupling when $f_X < 1$.

7.4 Behaviours resulting from the different mechanisms

The chain of rowers will settle into a phase-locked state if it is undisrupted or the irregularities are small. When the chain is disrupted, either through position, amplitude or frequency, the phase profile of the rower chain develops further structure. Examples of the observed behaviour are shown in figure 7.3. Groups of N_g rowers are formed when additional distance is included between the subsets. The groups can be recognised by the increase in the phase difference, and reversals that occur in the phase profile; a reversal is used to describe the situation where the phase difference changes sign, i.e. in one group the left neighbours lead while in another the right neighbour would be ahead in the cycle. An example of the reversals is shown in figure 7.3(b), where $d_X/d = 16/7$. The phase profile is marked by the black line to emphasise its shape. A reversal appears as a chevron in the phase profile. In this particular case there are three chevrons across the chain, each occurring at the point of disruption. The dotted black lines mark the rowers that have increased separation distance.

Similar phase profiles appear when the amplitude is varied. Initially when the amplitude change is small, the chevrons are sharp like they are in the distance case. However, the placement of the chevrons is not as systematic. Not all reversals occur at the rower with altered amplitude. This is shown in figure 7.3(c). One point of the chevron is at the 20th rower, which is altered. A second reversal in the profile is necessary to maintaining the periodic boundary conditions. This point occurs in what would be expected to be the centre of a subset, around the 55th rower under the current labelling. Changing the amplitude further creates additional differences in the shape of the profile. Where previously the reversals in the phase profile were sharp and the phase difference consistent in size if not direction, now the profile is smoother with the phase difference varying between and in subsets. This is shown in figure 7.3(d), which shows a more sinusoidal pattern than sharp zigzag shown figure 7.3(b).

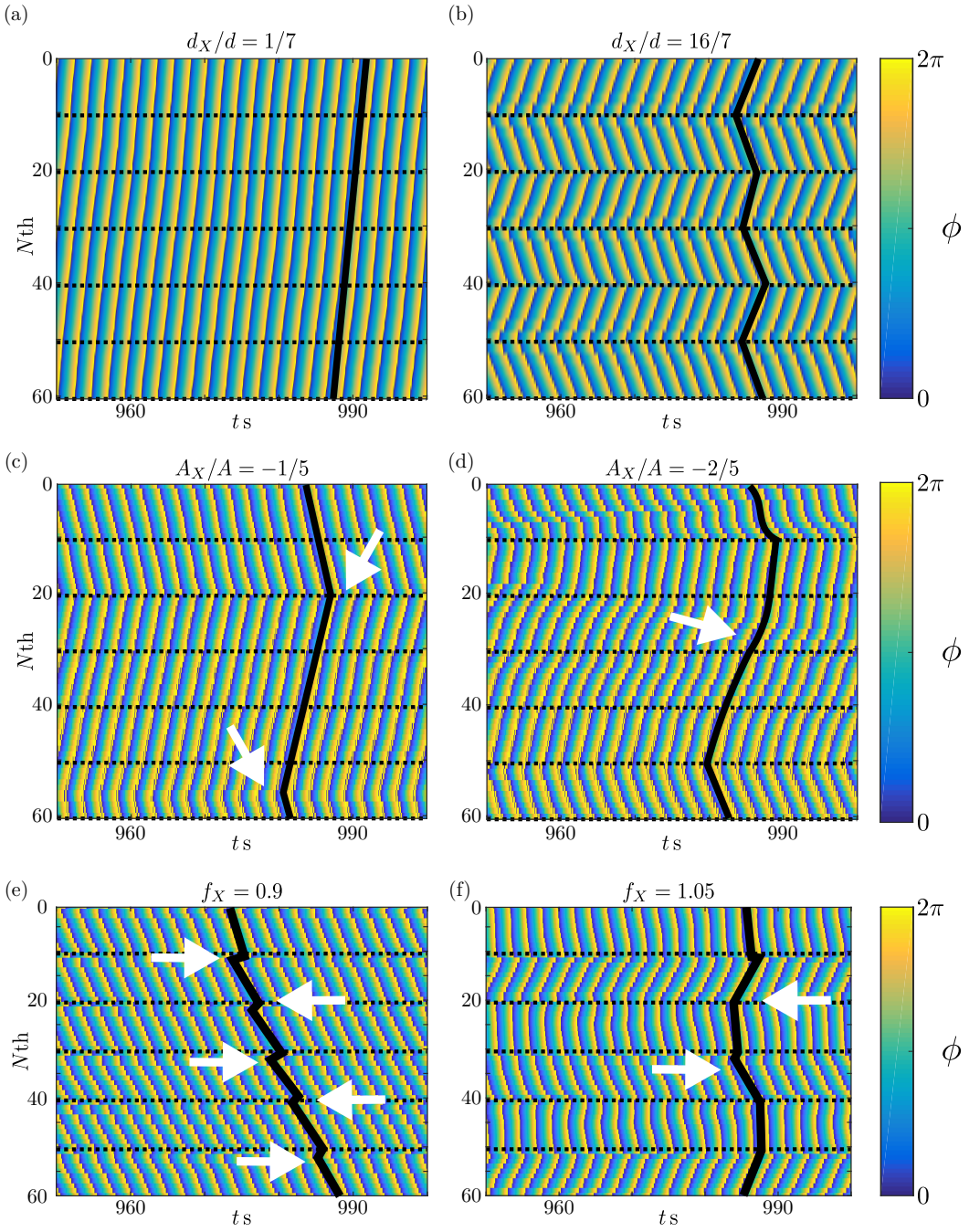

Fig. 7.3 Examples of subset formation with the different control methods. (a) When all the rowers are near one another, the chain settles into one phase-locked state. The colour represents the phase, the black line highlights its structure. (b) Increasing the separation creates subsets, which have can have opposing directions for the phase difference. Similar features are observed in the amplitude cases, but the subsets are less consistent. This can manifest as in (c) where the phase reversal does not occur at the rower with altered amplitude. (d) For larger changes the phase profile becomes smoother. The phase profile generally has a different structure when the frequency is changed. For large differences in frequency the altered rowers do not phase-lock while the rest coordinate around them. This is shown in (e) where each altered rower produces a kink in the profile. When the rowers are only slightly accelerated, they are likely to form subsets in-phase and with alternating subsets phase-locked between them; see (f).

Varying the frequency of the rowers also creates similar subsets, but with a few features unique to the style of disruption. Increasing the frequency of every N_gth rower appropriately appears to stabilise the in-phase subsets. These subsets are seen regularly in the frequency cases, with each in-phase subset separated by a phase-locked subset. An example of such behaviour is plotted in figure 7.3(f). For larger changes the altered rowers do not phase-lock with the others. When the change is a frequency reduction, the other rowers phase-lock with the altered remaining incoherent. This often manifests in the profile as 6 small kinks, see figure 7.3(e). If the altered rowers have a frequency that is too high, the system is unable to stabilise. The asymmetrical effect will most likely stem from the difference in coupling strength, low frequency rowers have lower coupling strength, allowing the remaining rowers to coordinate.

7.5 Consistency of the observed phase profiles

7.5.1 Modelling chevron occurrence using a binomial distribution

The shape profile exhibited is dependent on the initial configuration of the system. The size of the basin of stability for a given behaviour is also important to consider, not just the features that can occur. To that end, the consistency of observing the reversals in the phase profile is modelled using a binomial distribution. The process to measure the chevron formation is discussed in section 4.2.4, and involves measuring the prominence of terms in the Fourier series.

The assumptions underpinning the binomial distribution are useful when considering the number of reversals in the phase profile. First, the requirement that there are only two outcomes is easily met by either the existence or non-existence of a reversal. Second, the independence of each trial is likely to be met if the subsets are large enough. However, if chevron formation is not independent that would be notable on its own. It is the final assumption, the number of trials being fixed that may be a barrier to using the binomial model. This is unlikely to be a problem in the amplitude and distance cases, which generally showed reversals at the point of disruption. The frequency disruption however, has more non-uniformity it its behaviour and is unlikely to meet the assumption. This will become apparent when discussing the frequency results in section 7.5.4.

The probability of chevron occurring p_{ch} is measured by dividing the total number of chevrons observed by the total possible number chevron occurrences; for example, if a maximum of three chevrons can occur in a chain and there are 50 simulations of the chain, then the maximum number of chevrons that can occur is 150. This measure assumes that

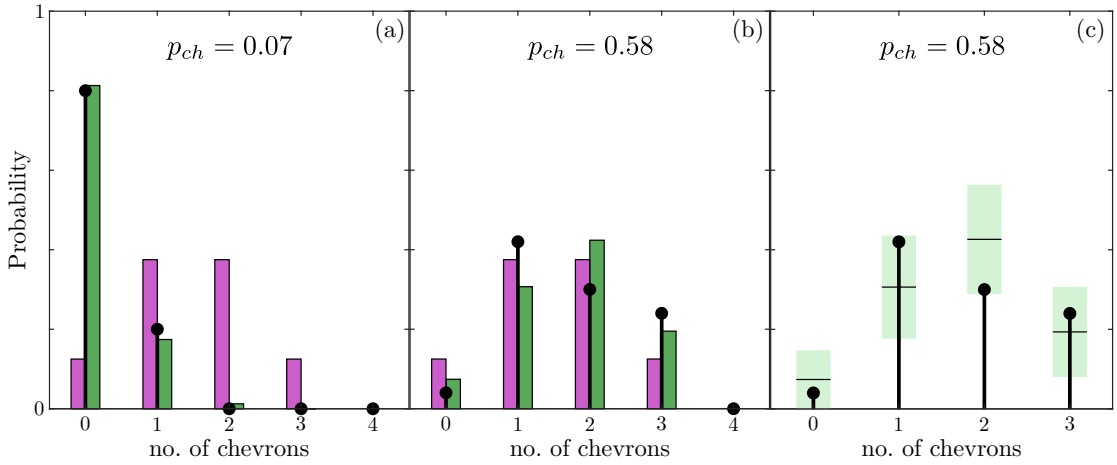

Fig. 7.4 Examples of fitting a binomial distribution to the number of chevrons. (a) An example when $p_{ch} = 0.07$, i.e. the probability is low. The observed data is shown by the black stems, and two theoretical distributions shown in green and purple. The green is the binomial distribution for $p_{ch} = 0.07$, the value measured from simulation, and the purple distribution is the random case where $p_{ch} = 0.5$. (b) An example where the p_{ch} is midway between the extremes of 0 and 1, specifically the probability is measured as $p_{ch} = 0.58$. Again the green distribution has a probability equal to the measured value, and the purple has random chance. The observed values don't align as closely with the theoretical distribution. The variability of binomial distributions depends on p_{ch}, with the peak at $p_{ch} = 0.5$. (c) 95% confidence intervals for observed frequency when $p_{ch} = 0.58$. Every value observed lies within the confidence interval. The ranges are correlated, and the observed values are likely to fall mostly outside the intervals or all within.

each chevron forms independently in the chain. Binomial distributions with random change ($p_{ch} = 0.5$) and the measured chevron probability are plotted in figure 7.4. An example where observed probability is small is shown in figure 7.4(a). The random binomial distribution is shown in purple, while the distribution for measured probability is shown in green. The original data is indicated by the black circles. The green distribution clearly aligns with the simulated data. In figure 7.4(b) the same colour convention applies, but this time the probability of observing a chevron is much higher. At first glance it appears the data (black circles) does not align well with the green distribution, but binomial data exhibits the greatest variability near $p = 0.5$. To demonstrate this effect, the range of observed probability for a given number of chevrons is shown in figure 7.4(c). The green bands given an indication of the variation that can be observed, with 1000 random data set generated from a binomial distribution with $p_{ch} = 0.58$ and the appropriate number of trials. The horizontal lines mark the mean value observed, which aligns with the theoretical value. The green bands are the 90% confidence interval the generated data. The simulated chain data is again the black circular markers, all of which fall within the confidence bands.

7.5.2 Extra distance

The subsets formed exclusively in groups of N_g rowers separated by the additional distance d_X. This implies the number of chevrons that can occur in any one chain is three; the periodic boundary conditions mandate that the phase difference wraps, consequently each $\bigwedge$ shape in the chevron has a corresponding $\bigvee$. The maximum number of chevrons fixes the number of trials in the binomial modelling. Initially there are no subsets and I expect the probability of a chevron occurring to be 0. At the opposite extreme, once the groups are far enough apart they should decouple completely and the probability of a reversal should be random, i.e. 1/2. It is in the intermediate regime that a maximum in chevron probability is observed. This indicates that there is a choice of distances in which the chance of creating subsets with opposing directions is preferred.

The observed probability for the number of chevrons in a chain is shown in figure 7.5. The distribution of the results are plotted in figure 7.5(a), with the random case ($p_{ch} = 0.5$) overlaid as diamond markers. Initially when $d_X = 0$ chevrons are never observed, but as d_X is increased they become more common. Of particular interest are the cases where $d_X = 8/7$ and $16/7$, where the number of cases with chevrons exceeds what would be expected by chance. This is corroborated in figure 7.5(b), where the probability of observing a chevron p_{ch} is plotted against d_X. The markers left uncoloured do not have enough evidence to assume some preference for either chevrons or no chevrons (two-tailed; $p > 0.05$). The purple and green markers are for cases that do exhibit some preference, with the two categorised by

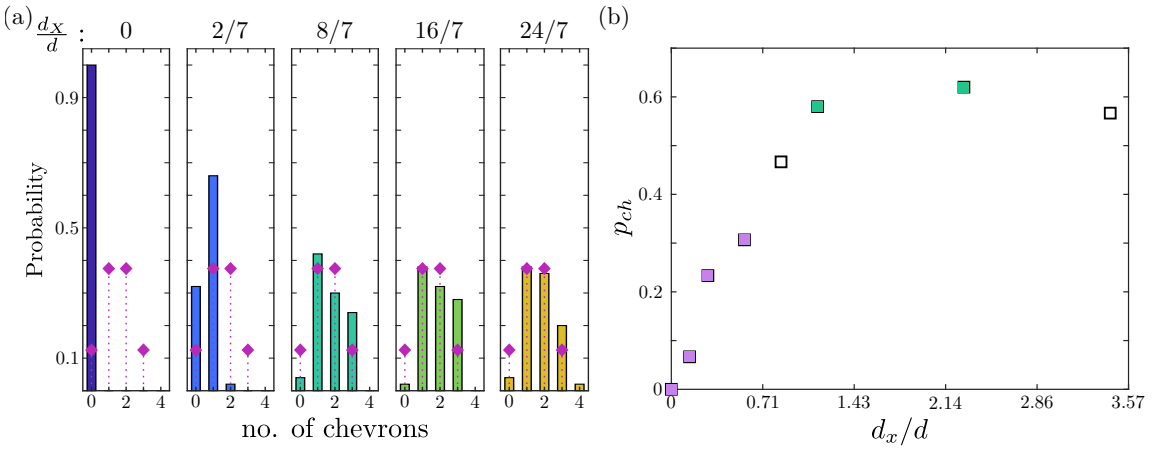

Fig. 7.5 Increasing the spacing between chain segments improves the chances of a chevron appearing. Assuming a binomial distribution, there exists a regime where the chance of a chevron occurring is higher than 50%. (a) The number of chevrons observed in each chain for different spacing, with the no preference case of $p_{succ} = 0.5$ overlaid as purple diamonds for reference. When there is an additional 8μm$-16\,\mu$m of separation, there are more three chevron cases than would be expected by chance. (b) The probability of observing a chevron as the separation is changed. The coloured markers are the cases where some preference for chevrons was demonstrated (two-tailed; p<0.05). The purple markers are for cases with a reduced chance of a chevron occurring, and the green are the cases where the number of chevrons exceeds what would be expected by chance.

inspection. Purple markers indicate states that have a decreased probability of chevrons, and green a better than random chance.

7.5.3 Changing oscillation amplitude

The changes in amplitude lead to some chevrons occurring in the centre of an expected subset. This undermines the assumption that there are three trials, because the reversals are no longer restricted to the N_gth rowers. Instead three options are considered, with the maximum number of chevrons in any one chain n_s assumed to be either 3, 4, or 6. The case where $n_s = 3$ is to mimic the previous case for distance, $n_s = 4$ is the maximum number of clear chevrons observed, and $n_s = 6$ assumes a chevron can appear at the amplitude altered rowers or half way between them. The distributions for the number of observed chevrons is shown in figure 7.6(a). Here the overlaid diamond markers are the expected number of observations by random chance when there are 4 possible locations for a chevron. Across the different cases, there is never an abundance of chevrons appearing, with normally one chevron the most likely outcome. When the amplitude is greatly reduced, i.e. $A_X/A = -0.6$, the distribution most closely resembles what would be expected for $p_{ch} = 0.5$, but still demonstrates a skew towards one reversal. The probability of a chevron assuming the different number of chevron

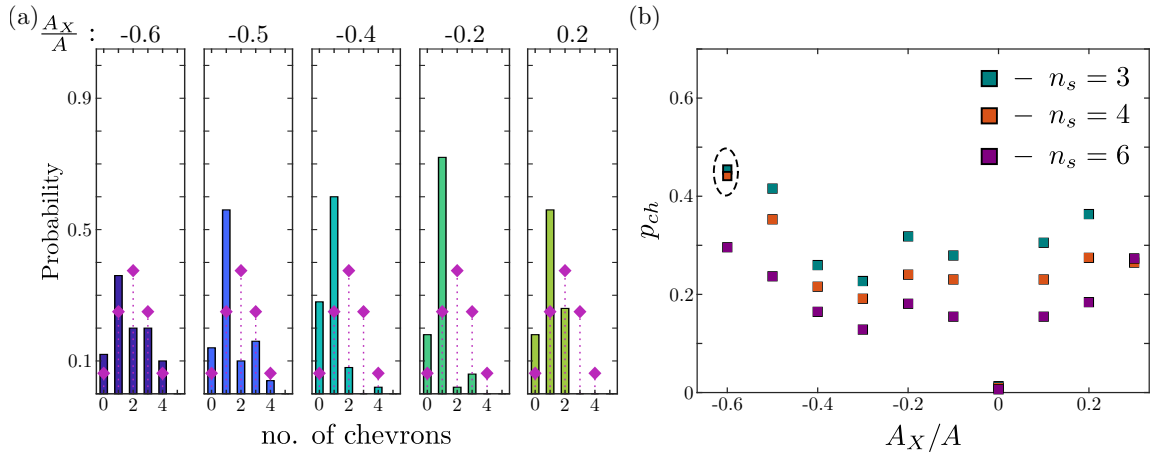

Fig. 7.6 Introducing heterogeneity in the chain through a change oscillation amplitude can lead to phase-locked subsets forming. (a) The probability distribution of the number of chevrons forming for increasing A_X. There is an increase in the number cases with more than three chevrons, revealing a decrease in control over the structure of the subsets. The overlaid distribution in this case is $Bi\,(4, 0.5)$. (b) The probability of success as A_X is varied. There are three choices for the maximum number of chevrons possible in any given chain n_s. The green markers are for $n_s = 3$ to be consistent with the extra distance cases where switches only occur at the point of disruption. The orange markers are for $n_s = 4$, the maximum number of switches observed, and the purple $n_s = 6$ that assumes two switches can occur between oscillators with altered amplitude. The two circles markers are the two cases where the results could reasonably be drawn from $Bi \sim (n_s, 0.5)$. Increasing n_s lowers the probability of success, but for each case the estimated probability of a chevron never exceeds 0.5.

locations is show in figure 7.6(b). The green markers are for 3 locations, the orange for 4, and purple when $n_s = 6$. Unsurprisingly increasing the number of trials reduces the observed probability. Regardless of the trial number, none of the changes in amplitude demonstrates a preference beyond that of chance for chevron formation. Further the only case that has apparent random chevron occurrence is $A_X/A = -0.6$.

7.5.4 Frequency alterations to regularly spaced rowers

The structure in the phase profile is often less regular when the frequency is strongly altered every N_g rowers. When the frequency is lowered, the detuned rowers fail to phase-lock but the remaining rowers synchronise. This appears as sixth order term in the Fourier series, and is a lack of coordination rather than the appearance of six chevrons. An example can be seen in figure 7.7(a). The case where $f_X = 0.95$ is clearly bimodal centred on 0 or 6 chevrons, and is in demonstrably not well represented by a bimodal distribution. The the other extreme when the adjusted frequency it too large the chain doesn't stabilise, and the most prominent Fourier term also doesn't correspond to a stable chevron state. This manifests as a flattening of the distribution as seen when $f_X = 1.1$ in figure 7.7(a). Nonetheless the probability of observing a chevron is calculated assuming that a total of six can appear, see figure 7.7(b). Despite the irregularity in doing so, a strong positive skew in the distribution would still be expected to produce an uptick in the probability. This does not appear when plotting the probability against the detuning level.

7.6 Interpreting the effect of the different control mechanisms

Each of the mechanisms was chosen because it alters the coupling between the rowers, and has some basis in what is feasible for a ciliated mircoorganism to exhibit. The inclusion of additional separation displayed the greatest control over the exact grouping of the rowers. Most likely the result of not only the neighbouring rowers have decreased coupling, but all the rowers in a given subset having weaker coupling with the other subgroups. In contrast, altering aspects of the oscillation produced subgroups with a wider range of phase differences, and in the case of frequency demonstrated that in-phase subsets can be stabilised. However, for both the amplitude and frequency alterations the resulting subsets were less consistent and often occurred over a smaller parameter window. All three mechanisms demonstrate the formation of subsets can be engineered, and previously unstable states can become preferable under the appropriate conditions.

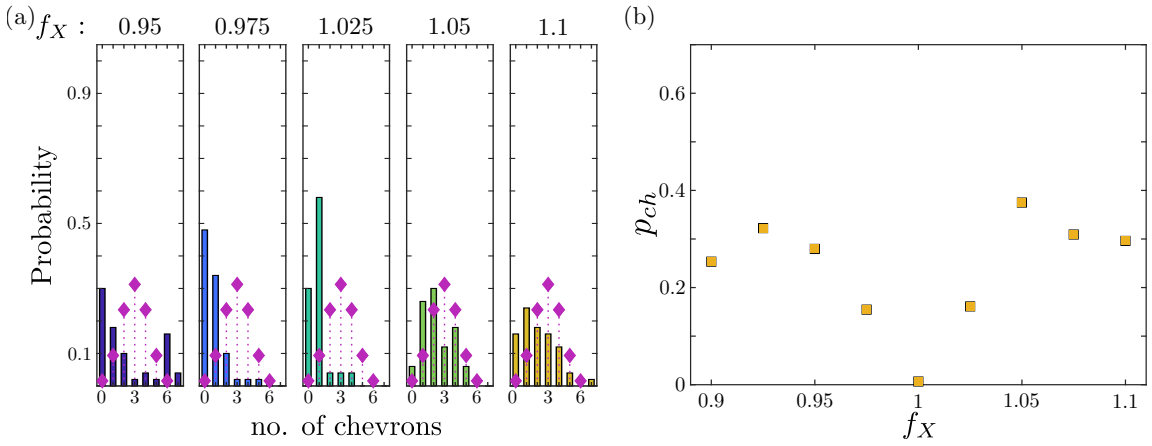

Fig. 7.7 Altering the frequency of specific rowers doesn't lead to the same chevron formation. (a) The probability distribution of the dominant Fourier mode. The distribution for $Bi \sim (6, 0.5)$ is marked by the purple diamonds. Large detuning values either lead to an unstable phase profile or remain incoherent while the remaining rower synchronise. This undermines the binomial assumption. The incoherent rowers lead to bimodal results, and the unstable profile often appears more like a uniform distribution because it lacks a sensible measurement time point. (b) Despite these problems, the binomial probability is calculated and plotted against the detuning f_X. The binomial probability may be valid for small values of detuning, but a high probability of chevron formation is never observed.

The results here suggest that for starfish larva a change in shape could assist in grouping subsets of cilia. Shape change would decrease the coupling between cilia in a similar way as increasing the spacing between rowers. The separation spacing demonstrated the most control over the location of the subsets, which would be important for vortex formation. Additionally, decreasing the coupling this way led to the sharpest chevron formation. This indicates that cell shape and potential changes in this shape could assist subset formation that stems from hydrodynamic coupling, though it is still contentious whether vortices are appearing around a larva. Further investigation would likely shift focus to *Paramecium*, which is not as controversial and has no central nervous system.

The focus of this chapter was on the control of subsets inspired by a specific living organism. In the following chapter the focus is on demonstrating a more abstract state, which in my system can be controlled through the spatial geometry of the oscillators.

Chapter 8

Chimera states in small arrays of rowers

8.1 Context for the chimera state

A "chimera state" is a state with simultaneous incoherent and coherent subsets, and is receiving increasing amounts of interest. It has been observed in phase, amplitude and chaotic oscillators, using a variety of different models including Ginzburg-Landau, Kuramoto, Lorenz, Stuart-Landau, and FitzHugh-Nagumo oscillators [100, 75, 142, 112, 140]. The coupling structures that lead to the formation of these states include uniform, nonlocal, and time-delayed interactions [76, 75, 254]. Though once thought to be a theoretical anomaly, it has now been observed experimentally [255, 256, 23]. The systems involved vary in terms of scale and in oscillator type, with optical, chemical, and mechanical oscillators all exhibiting the chimera state [257, 255, 256, 258, 112, 141, 23, 259]. The state is being related to a range of natural phenomena [260, 261, 41, 99, 262]. It has been linked to many biological systems that involve complex and often competing interactions, from internal processes such as epilepsy and heart fibrillation, to ecological predator and prey systems [263, 86, 137, 99, 69, 263, 264].

Chimera-like features have been noted in another minimal model inspired by ciliated tissue, where the oscillators were heterogeneous [265]. In this chapter, I use the rower model to produce chimera behaviour. The hydrodynamic tensor between the rowers allows the coupling to be varied through position. A direct consequence of the coupling being well understood and based on fundamental physical principles. The position dependence allows control over the emergence of subsets by varying array geometries, which changes the layout of identical rowers. The numerical simulations show that for an appropriate interaction range and rower spacing, synchronised and incoherent populations coexist. For long range interaction, rowers all oscillate in-phase together, but when the range is restricted phase-locked states are observed. I find that in an intermediate range, chimera states develop with the

synchronised population's geometry depending on the system layout. The different states are considered in the context of the Oseen eigenmodes, which are derived from the fundamental interaction between rowers [266, 189]. The chimera state appears as a combination of different modes and its emergence can be predicted by considering appropriate combinations of the normal mode relaxation rates. Alternatively, the chimera states can be interpreted using the mean interaction of each subset, emphasising the parallels with the behaviour of systems involving uniformly coupled Kuramoto phase oscillators [76, 114]. This work is adapted published work in [3].

The chapter begins by discussing the configuration of the system and how this allows control of the coupling in section 8.2. This is followed by an explanation of the measured applied to the sub-populations as well as some details on the curvature and the orientation dependence of the coupling and the corresponding effects on the noise in sections 8.3 and 8.4. The behaviours exhibited by the system as the geometry of the system is altered are illustrated in section 8.5, before they are characterised in terms of tensor eigenstates and the average coupling in section 8.6. Before concluding in section 8.8, the apparent stability of the state in this system is briefly discussed in section 8.7.

8.2 The geometry of the rower arrays

In this chapter the driving potential is an attractive square root potential $kx_r^{1/2}$, see Fig. 8.1(a). The exponent of the power law was chosen to guarantee in-phase synchronisation between pairs of rowers. The y position of the rowers is maintained by a harmonic trap, which depending on the row has a minimum at 0 or d_R. These traps restrict the rower oscillations to one-dimension, along the x-axis.

The Zeta-tensor, as described in section 3.6, is used to allow direct control of the interaction range. The parameter ζ is introduced by the tensor and is a simple control for the interaction range. It takes some value between $[1,3]$. The interval of ζ creates an interaction decay rate somewhere between being far from any impediment ($\zeta = 1$) and being near a no-slip boundary ($\zeta = 3$). The tensor allows the coupling between the rowers to be altered in two ways. Changing ζ from 1 to 3 increases the decay of the interaction, so the rowers no longer interact over a long range but only with their close neighbours. The second way to adjust the coupling is to vary the distance between rowers. The rowers are arranged to encourage separation into two subsets, with the eight beads placed in two rows as shown in Fig. 8.1(b). To alter the coupling through position, the distance between the rows d_R is varied.

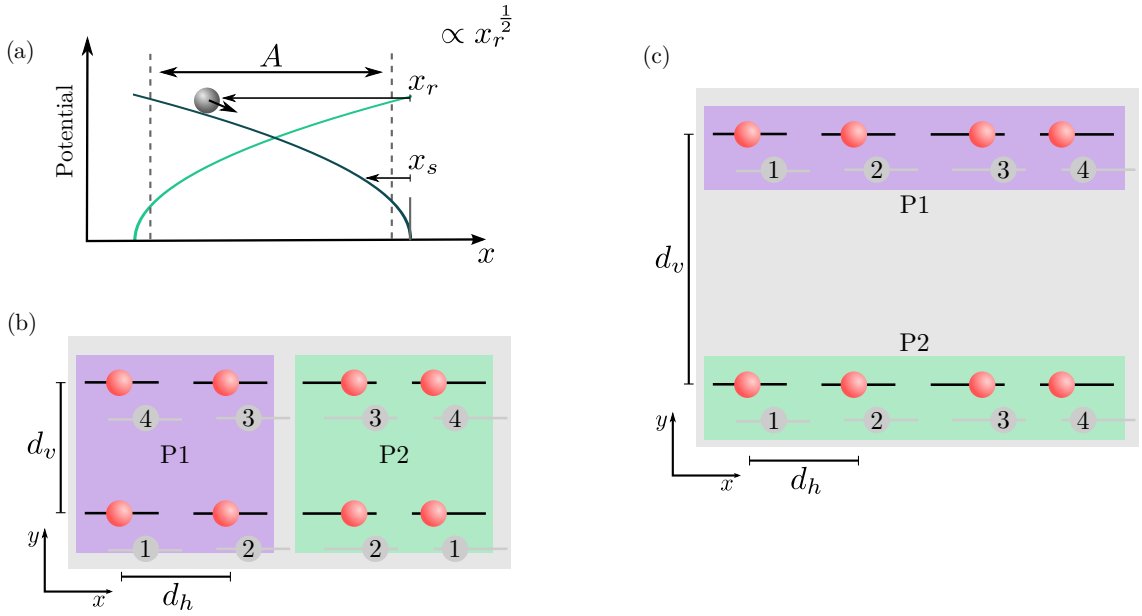

Fig. 8.1 Rowers are a simple model for non-uniform oscillators that interact at low Reynolds' number. (a) Beads are driven by a power law potential, $kx_r^{1/2}$, where x_r is the distance relative to the trap vertex. Once a rower is x_s from its vertex, the trap switches (dark to light green potential in diagram). To create a chimera state I focus on systems of eight beads. (b)-(c) Beads are placed in two rows. Within a row, the trap centres are spaced d_h apart. The two rows are separated by d_v. Depending on the spacing and interaction, the dynamics of the rowers tend to divide into block or chain populations. The block is shown in (b), the chain is shown in (c). The two populations are labelled P1 and P2, with purple and green rectangles marking the appropriate subset. The rowers are numbered in the block or chain configuration to ensure the central beads are always indexed 2 and 3.

8.3 Measuring synchronisation in each population

The positions of the rowers oscillate in the system. Using the natural phase frame captures the oscillations in a single parameter. The transformation from position to phase is described in equation (4.8) when $\alpha = 1/2$. The phase is used to determine two phase order parameters similar to those in section 4.2.2. Here they are calculated over two subsets rather than the whole population, with the index p distinguishing between the two subsets,

$$Z^{(p)}(t) = \frac{1}{N_p}\sum_{j=1}^{N_p} \exp[i\phi_j^{(p)}(t)], \tag{8.1}$$

$$Z_{PL}^{(p)}(t) = \frac{1}{N_p - 1}\sum_{j=1}^{N_p-1} \exp[i(\phi_{j+1}^{(p)}(t) - \phi_j^{(p)}(t))]. \tag{8.2}$$

The phase $\phi_j^{(p)}$ is the phase of jth in the pth population and N_p is the size of the population. $Z^{(p)}$ is a measure of a population's mean phase, and $Z_{PL}^{(p)}$ the measure for mean phase-difference. The magnitudes of $Z^{(p)}$ and $Z_{PL}^{(p)}$ gauge the coherence of a population, with $|Z_{PL}^{(p)}|$ measuring the variability in the phase-difference between neighbours and $|Z^{(p)}|$ measuring how in-phase the rowers are in each population. The population is incoherent when $|Z_{PL}| \approx 0$, and phase-locked (constant phase-difference) when $|Z_{PL}| \approx 1$. $|Z| \approx 1$ corresponds to the specific case when the phase-difference is zero, but $|Z| \approx 0$ occurs for both incoherent and splay states; the splay state for four rowers is $\phi_{i+1}^{(p)}(t) - \phi_i^{(p)}(t) = \frac{\pi}{2}$. I use both measures to classify the system.

8.4 Noise and curvature details

The simulation parameters are chosen to produce strong interactions between the rowers. I chose high negative curvature, as defined in [98], and low noise. This ensures strong in-phase synchronisation between a pair of rowers, so any departure from this state is the result of additional rowers. The curvature depends on the force at the beginning and end of the trap, F_b and F_e, as well as the average force F_0. Explicitly $c = -2(F_e - F_b)/F_0$, with $F_b = -k/2\,(A+\delta)^{-1/2}$ and $F_e = -k/2\,\delta^{-1/2}$. I set $A/\delta = 31$, which results in a curvature of $c = -0.7$ for the trap potential.

Here the dimensionless noise is defined in slightly different way than section 4.1.4. The adaptation is to account for differences between the x and y directions. I define the noise strength ξ_0 in a similar way as in [98] where noise and synchronisation was also investigated. I also include the dimensionless quantity D_0. This term scales the trap strength to maintain a

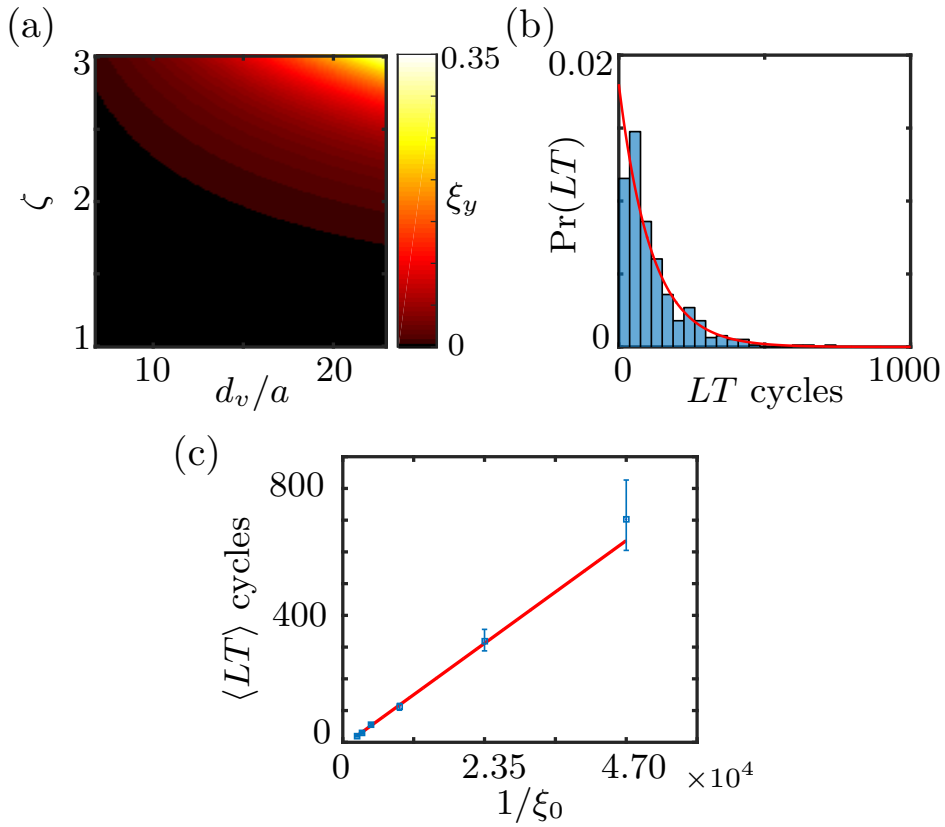

Fig. 8.2 The low noise level $\xi_0 = 2.13 \times 10^{-5}$ generally doesn't impede the interaction in y, and produces chimera states with a long lifetime. (a) The map of dimensionless noise scaled by the interaction in y, ξ_y, for varying ζ and d_R/a when $\xi_0 = 2.13 \times 10^{-5}$. For the most part the noise is small $\xi_y < 0.1$, with $\xi_y \approx 0.1$ the bright red. (b) The histogram of the simulated lifetime LT measurements, with the fitted distribution shown in red, when $\xi_0 = 1.06 \times 10^{-4}$. (c) The relationship between average lifetime $< LT >$ and $1/\xi_0$ is linear when $\zeta = 1.6$ and $d_R/a = 9.1$. The error bars indicate the 95% confidence interval for the mean, determined using the pivotal quantity for an exponential distribution. The fit suggests the block chimera state is stable when noise is not present.

given period for a chain of four rowers moving in-phase when the coupling range is varied by ζ[1]. I relate the noise to D_0, the temperature T and average trap force F_0 by,

$$\xi_0 = \frac{2k_BT}{AD_0F_0}, \qquad F_0 = \frac{1}{2}(F_e + F_b), \tag{8.3}$$

with A the amplitude of the oscillations and k_B the Boltzmann constant. The coupling is anisotropic in the system, due to its dependence on the direction of oscillation and the geometry of the system. I compare the noise to the interaction forces along x and y by scaling it using the nearest neighbour coupling in each direction. The scaled noises for x and y, ξ_x and ξ_y are related to ξ by,

$$\xi_x = \frac{2}{3}\left(\frac{d}{a}\right)^{\zeta}\xi, \qquad \xi_y = \frac{4}{3}\left(\frac{d_R}{a}\right)^{\zeta}\xi. \tag{8.4}$$

I set the ratio d/a = 6.86, and $d_R/a \in [6.86, 22.86]$, which results in $d_R/d \in [1, 3.33]$. The dimensionless trap strength is $D_0k\tau/(\gamma a^{3/2}) = 3.28$, where τ is the period of a single chain of four rowers moving in-phase, and $\delta/a = 0.057$. Unless stated otherwise, the noise is $\xi_0 = 2.13 \times 10^{-5}$, i.e. the noise is small when compared with the neighbouring interaction in x, with $\max(\xi_x) = 4.58 \times 10^{-3}$. The range of ξ_x lies within the expected synchronised region in [98] when the results are rescaled appropriately. This noise should not prevent the rowers coordinating with their neighbours along x. The coupling strength of vertically opposite rowers has a wider range, as both d_R and ζ vary, see Fig. 8.2(a). While the noise is initially small with $\xi_y \approx 10^{-4}$, for larger d_R/a and ζ the noise could prevent coordination between the rows with $\xi_y \approx 10^{-1}$. For the most part ξ_y is small and the rower interaction along y exceeds the noise.

8.5 Observing three different synchronisation states

The interaction range ζ and row spacing d_R determine the rowers behaviour. There are three states observed: in-phase, chimera, and phase-locked. The chimera state has two sub-categories chimera-block and chimera-chain, depending on the subset geometry. Fig. 8.3 shows some examples of these behaviours. When the interaction is long ranged with ζ near one, there is no separation into subsets as all the rowers oscillate in-phase. The synchronisation of the rowers when $\zeta = 1.1$ and $d_R/a = 8$ is shown in Fig. 8.3(a) and 8.3(b).

[1] $D_0 = 1 + \frac{3}{2}\left(\frac{a}{d}\right)^{\zeta}\Lambda$, where Λ is the largest eigenvalue of $(\boldsymbol{I} + \hat{\mathbf{r}}_{ij}^{(c)}\hat{\mathbf{r}}_{ij}^{(c)})$ when $\hat{\mathbf{r}}_{ij}^{(c)}$ is the distance between rowers in a chain. It was assumed the rowers were spaced parallel to their oscillation direction. I limit the chain to four rowers. The formula is an adaptation of relaxation time in equation (5) of [189].

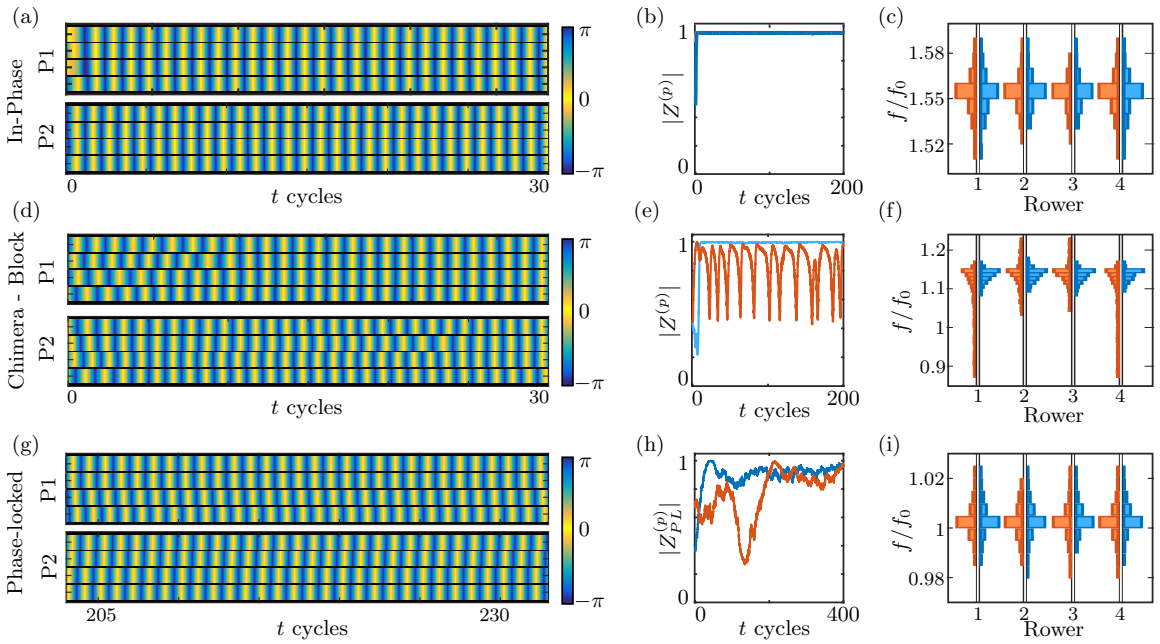

Fig. 8.3 The chimera state forms in the intermediate range between in-phase motion and phase-locked states. (a)-(b) The phase and order of an in-phase state, where $d_R/a = 8$ and $\zeta = 1.1$. The rowers start from a random position, but both populations (P1-blue and P2-orange) quickly form and maintain the in-phase state with $|Z^{(p)}| = 1$. (c) The frequency distributions are similar for both populations when in-phase. The distributions are horizontal, contrasting the 'same' rower in each population, i.e. same number or relative position. For each rower the distribution is scaled by f_0, the frequency of a rower without interaction. (d)-(f) Only one population can coordinate when $d_R/a = 10.29$ and $\zeta = 1.6$. Defects develop in pairs of rowers from the second population P2, preventing in-phase motion. The defects result in apparent 'breathing' in the orange curve of the order parameter and a tail developing in the frequency distribution. The skew is responsible for the drop in mean frequency, behaviour associated with the chimera state. (g)-(i) For a sufficiently short interaction range the phase-locked state occurs, $d_R/a = 21.71$ and $\zeta = 3$. The total strength of the interacting forces are smaller for short ranged interactions, so the rowers are slow to settle into the phase-locked state.

It appears as vertical bands in the phase in 8.3(a) and the convergence to one in 8.3(b). When the interaction is short ranged the oscillators settle into phase-locked states. This appears as diagonal bands in the phase and $|Z_{PL}| \approx 1$, see Fig. 8.3(g) and 8.3(h) where $\zeta = 3$ and $d_R/a = 21.71$. The total interaction $\sum_{i \neq j} H_{ij}^x$ tends to be weaker in these cases, and so the rowers take longer to become coordinated. The chimera state occurs in the intermediate range between the in-phase and phase-locked states. In this state, one population is in-phase, whilst the other is unable to settle with defects developing whenever it approaches in-phase. This causes $|Z|$ to rise and fall in the incoherent population.The phase defects in the chimera state when $\zeta = 1.6$ and $d_R/a = 10.28$ are shown in Fig. 8.3(d) and (e). The defects create the apparent 'breathing' in the order parameter $|Z|$ of the unsynchronised population. The frequency distributions of phase-locked and in-phase states are symmetric, but the distribution of incoherent rowers develops a tail, see Fig. 8.3(c), 8.3(f) and 8.3(g). This leads to a reduction in mean frequency for the unsynchronised population in the chimera state.

When noise is present the subsets do swap roles, but as the noise decreases the chimera intervals last for longer periods. When comfortably within the chimera-block region, see the circle marker in Fig. 8.5(a) and 8.5(c), the lifetime of the state increases linearly with $1/\xi$, see Fig. 8.2. Though the lifetime of the chain state increases with decreasing noise, it also exhibits chaotic characteristics. This makes it difficult to make definitive claims concerning the long term behaviour. Since I am interested in a physical system with noise, I classify the chimera state by considering 40 cycle intervals. When more than half the intervals measure one population remaining synchronised whilst the other fluctuates, the state is labelled as a chimera. The states are classified as block or chain by comparing $|Z|$ for both configuration, it is then categorised as the geometry that measures a different spread in $|Z|$ for each population.

8.6 Interpretations of the chimera state

8.6.1 Decay of the eigenstate projection

The eigenstate approach focuses on the interval between updates, and infers the long term behaviour from successive updates suppressing or promoting different behaviours.

The behaviour of rower ensembles can be understood qualitatively from their fundamental interaction by projecting onto appropriate eigenstates. Previously this technique has been applied to rings of rowers [189], and two rows of rowers with varying oscillation direction [190]. A similar approach has also been used to understand synchronisation in quantum oscillators coupled through dissipation [267, 268]. Following the procedure in Ref. [189], where the

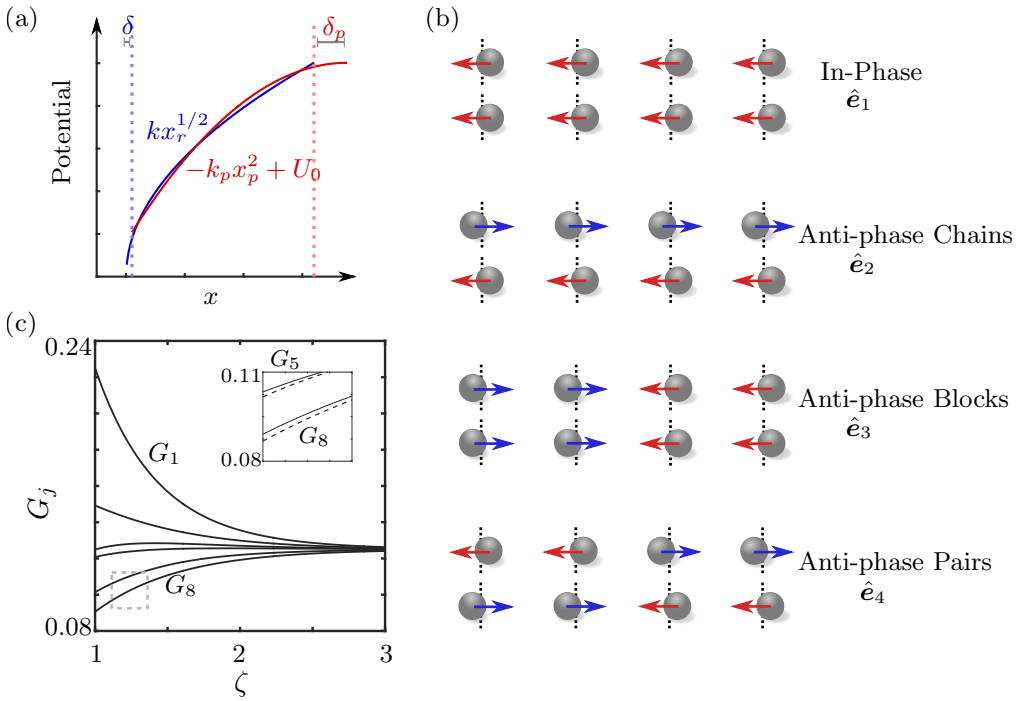

Fig. 8.4 The growth rate of the interaction tensor's eigenstates G_j when the trap potential is parabolic. (a) Approximating the original $x^{1/2}$ potential with a negative parabola that maintains the curvature. The original potential is shown in blue, the new parabolic potential is in red. The parabola has been translated by U_0 to highlight the similarity to $kx_r^{1/2}$, but the force is unaffected by this value. (b) Representations of four eigenstates states. In-phase motion or $\hat{\boldsymbol{e}}_1$ grows the fastest, followed by $\hat{\boldsymbol{e}}_2$ anti-phase chain population, $\hat{\boldsymbol{e}}_3$ anti-phase block populations, and $\hat{\boldsymbol{e}}_4$ anti-phase pairs. (c) The growth rate of the different eigenstates assuming the rowers are either phase-locked or in the chimera state, i.e. $n_t = 5$, with $d_R/a = 10.29$. The growth rate is indexed by descending size, so G_1 is the fastest rate and G_8 the slowest. The difference between G_5 and G_6, and G_7 and G_8 is minimal, so only one of each pair is considered when classifying the states. These states are shown in the inset, which is a closer view of the dashed section in the lower left corner.

distance between the rowers r_{ij} is approximated by the distance between their trap centres (a function of d and d_R) and noise is neglected, the system configuration at each time can be projected onto the eigenvectors of the interaction tensor. To express the trap force in terms of the projection the potential needs to be parabolic. Earlier work in Ref. [98] showed rower synchronisation is governed by the curvature of the potential. Consequently I use a negative parabolic potential with the same curvature as the earlier square root form to calculate the eigenmodes, i.e. the potential $-k_p x_p^2$ with $\delta_p/a = 0.37$, see Fig. 8.4(a). To match the $x_r^{1/2}$ potential, the parabolic trap strength is set by $k_p = k(\sqrt{A+\delta} - \sqrt{\delta})/((A+\delta_p)^2 - \delta_p^2)$. In shifting to the new potential, the distance is now measured relative to the turning point of the parabola. The new potential means $h_j = \hat{\boldsymbol{e}}_j \cdot \boldsymbol{r}$, the projection of the rower positions onto the jth eigenvector, obeys,

$$h_j(t) - (\hat{\boldsymbol{e}}_j \cdot \boldsymbol{s}) - \tau_j \frac{d}{dt} h_j(t) = 0, \tag{8.5}$$

$$\tau_j = \frac{\gamma/(2k_p)}{1 + \frac{3}{4}(a/d)^{\zeta}\lambda_j}, \tag{8.6}$$

where λ_j is the eigenvalue associated with the vector, $\boldsymbol{s}$ the trap position vector, and k_p the trap strength for the parabolic potential. This expression only holds between trap updates, i.e. $\boldsymbol{s}$ is constant.

Employing a similar argument as that in Ref. [189], but focused on divergence, predicts that the observed state will be the fastest diverging state: because the state that diverges fastest experiences the greatest growth between trap updates. Using the approximation of a parabolic potential, the growth rate of the jth mode over one switch G_j is,

$$G_j = \frac{\exp\left[t_s/(n_t\tau_j)\right] - 1}{\sum_{k=1}^{N}\{\exp[t_s/(n_t\tau_k)] - 1\}}. \tag{8.7}$$

The growth is measured over the median time between any two switches t_s/n_t, with t_s the time between a rower's switches and n_t the median number of traps expected to update over this period. The switch time is interpolated from the simulation results, as are the number of switches. When in-phase $n_t = 1$, and for the chimera and phase-locked states $n_t = 5$. Each state will be diverging, but the system prefers the state which diverges the quickest. The index j orders the states by their rate of divergence, G_1 is the fastest growth while G_8 is the slowest. The four states fastest to diverge are in-phase, anti-phase chain, anti-phase block, and anti-phase pairs. Representations of these four states are shown in Fig. 8.4(b).

The growth rates when $n_t = 5$ are plotted against the interaction range ζ for the different states in Fig. 8.4(c). These growth rates were used when classifying the different regions

for the behaviour. The general trend when ζ increases is for the states to converge to equal representation (1/8). The inset zooms in on G_5, G_6, G_7, and G_8. The difference between G_5 and G_6 (and G_7 and G_8) is small, as such there are only six states well separated. I classify the regions using the well separated states G_1, G_2, G_3, G_4, G_5, and G_7.

8.6.2 Mean coupling strength for a population

The observed chimera state, particularly the rise and fall in incoherent population mentioned in the results section, is reminiscent of the 'breathing' seen in populations of Kuramoto phase oscillators [76, 114]. The Kuramoto populations are uniformly coupled, suggesting the mean population forces encapsulate the chimera behaviour. To parallel this work, I consider the difference between the mean coupling within each subset M,

$$M = \frac{\mu - \nu}{\mu + \nu}, \tag{8.8}$$

$$\mu = \sum_{\substack{j \neq 1 \\ j \in P_1}} H^x_{1j}, \quad \nu = \sum_{j \in P_2} H^x_{1j}, \tag{8.9}$$

where μ is the sum of forces parallel along x within a population acting on a bead labelled as number one in Fig 8.1. The mean cross population force ν is the sum of forces on the same rower exerted by the other population. Selecting populations with the chain or block geometry is supported by the divergence rate of eigenstates with the same symmetry. Using the mean interaction I find the results are reconcilable with the Kuramoto oscillators, and the transition from block to chain subsets can be predicted.

In-phase behaviour is expected when M is small, and the cross-population forces are comparable to intra-population, i.e. $\zeta \approx 1$ and forces are long-range. In contrast, the mean interaction becomes a poor approximation for the dynamics when the interactions are short range. This is more problematic for the chain configuration, where the difference between maximum and minimum spacing is larger. The effect of varying ζ and d_R on M is shown in Fig. 8.5(c) and 8.5(d). The expected shift from block to chain is at the cusp in the M curves. It occurs when the chain population sum μ_C exceeds the block μ_B. The chain population's enhanced sensitivity to ζ is also apparent, seen as the section of high M when d_R increases and $3 > \zeta > 2$. Simulation results are overlaid on the map of M in Fig. 8.5(d). The different markers in Fig. 8.5(d) correspond to the in-phase, chimera, and phase-locked states. The chain-chimera states are marked with a plus. A mixture of chimera and in-phase is recorded when over half the simulation registers in-phase motion but there is an interval of chimera behaviour, and shown by the empty squares. If the simulation doesn't measure consistently

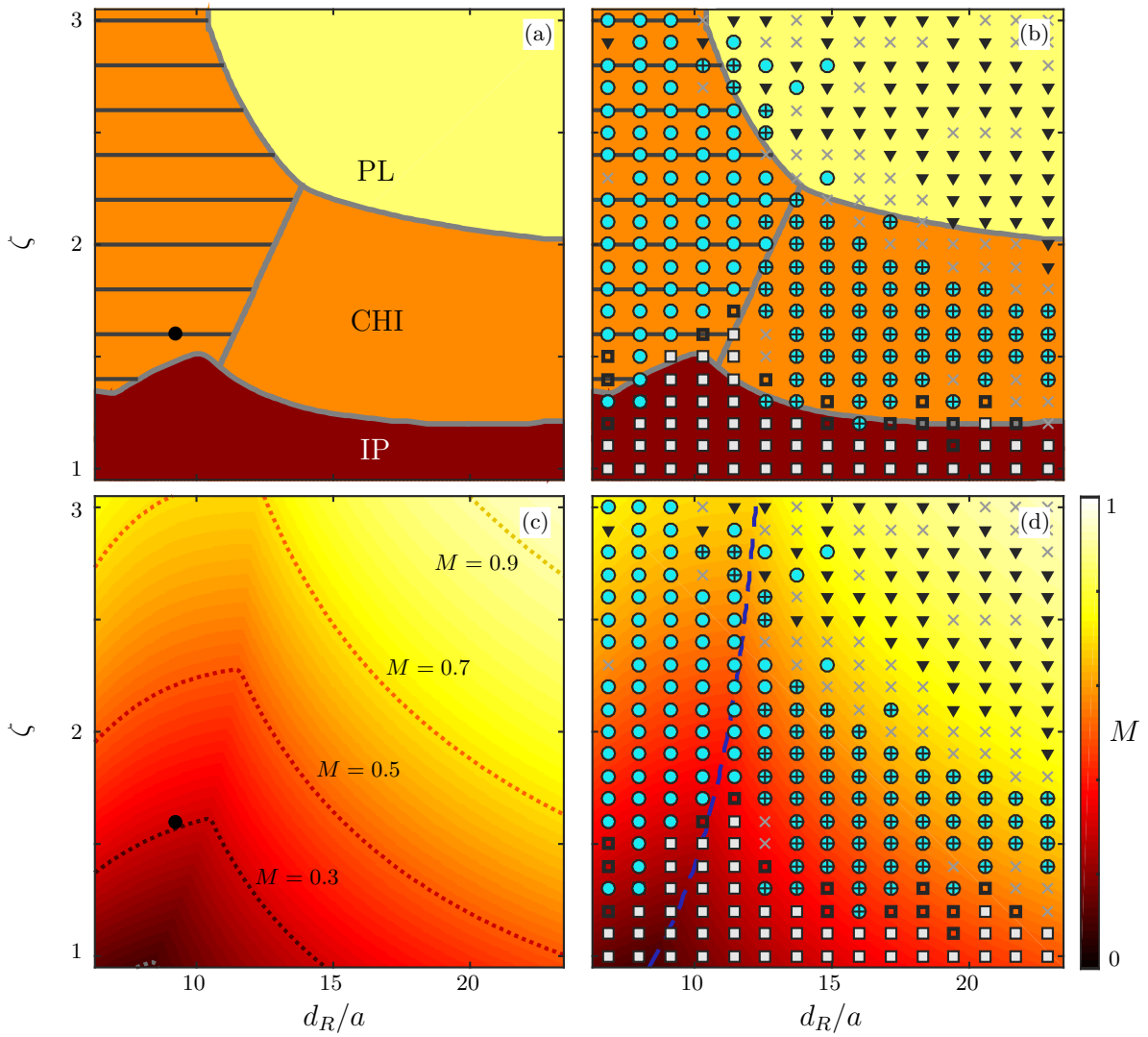

Fig. 8.5 Regions for the different states can be classified using the growth rate, or the difference between intra- and cross- population forces. (a),(b) The classification of the different regions using the eigenmode growth rates G_j: the in-phase region (burgundy), phase-locked region (yellow), and the chimera region between (orange). The in-phase state is observed when the growth rate of the in-phase eigenmode G_1 outstrips the others. I define the in-phase section by $G_4 < 0.125$ and $G_2 - G_4 > 0.012$, which ensures the growth rates of the other states are small; G_j are indexed in descending size. Phase-locking occurs when all the growth rates converge. The region where the rates have coalesced is defined by the faster growth rates being similarly spaced to the slower, more closely spaced states, $G_1 - G_2 < G_5 - G_7$ and $G_1 - G_3 < G_4 - G_7$. The stripes mark when the block formation is preferred to the chain. This region is defined by $G_2 - G_3 < G_4 - G_5$, i.e. using the slower states to determine when the difference in growth between chain and block states is small. (c),(d) The colour indicates the difference in population forces, $M = (\mu - \nu)/(\mu + \nu)$. Lines for $M = 0.3$, 0.5, 0.7,and 0.9 are plotted and labelled. The cusp in the lines indicates where the rowers swap from preferring block configuration to chain. The cusp is marked by a dashed line in (d), i.e. the expected transition point from block to chain. (b),(d) The results of simulation are superimposed over the different regions. White squares, cyan circles, and black triangles mark in-phase, chimera, and phase-locked states. A grey cross indicates the state could not be classified, whilst an open squares mark a mixture of in-phase and chimera behaviour. To distinguish the chain-chimera, a plus is added to the cyan circle. The lifetime stability for the block-chimera was measured at the dark point in (a) and (c), where $\zeta = 1.6$ and $d_R/a = 9.14$.

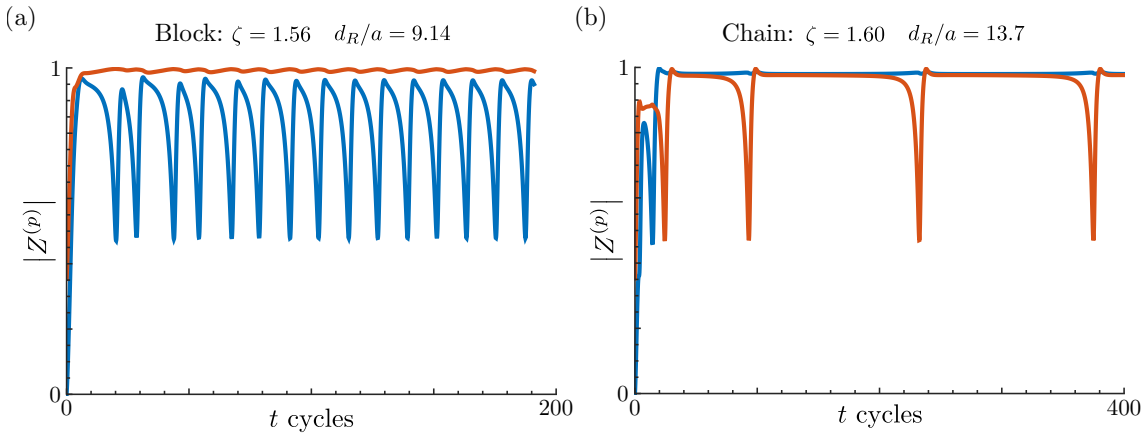

Fig. 8.6 Recreating the simulated chimera state by numerically solving the 7 phase difference equations determined using the "mean" interaction function from chapter 5. (a) An example of the block chimera state, where $\zeta = 1.56$ and $d_R/a = 9.14$. The time scale of the peaks appears similar to that of simulation. (b) A chain chimera example, with $\zeta = 1.6$ and $d_R = 13.7$. The dips appear to occur over a longer time scale. This may be due to the truncation of the Fourier series representing the interaction function. In simulation the chain state was observed to be sensitive to changes, including in initial conditions, temperature, and time step. When solving, the interaction function was truncated at 25 non zero terms, and the initial condition randomly selected to be far from in-phase, with the set $\{\psi_{ij}\}$ set to $\{-\pi, 0, \pi, -\pi, 0, \pi, \pi/2\}$.

high levels of $|Z_{PL}|$ in either population then it isn't classified and is marked by a grey cross. The cusp in M occurs on the navy line. The chain states begin to be observed when $\mu_C > \mu_B$. More generally, the chimera state is recorded when $0.7 > M > 0.4$. The upper bound results from the shortened interaction range, whilst the lower bound is consistent with Ref. [114]. There is no direct correspondent for the phase lag from the Kuramoto model, but the boundary near 0.4 is in accord with a moderate range of phase lag. For small d_R the intra-population forces are more uniform, so the map of M best captures results that occur in this range. In particular the dark patch where $M < 0.25$, when $6.8 < d_R/a < 11.5$, captures the transition from in-phase to block chimera behaviour.

8.7 Coexistence of two stable states

The chimera state can be reproduced using the "mean" interaction function from chapter 5 to reduce the system to 7 non-linear equations. Examples of chimera states found by solving these equations are shown in figure 8.6. While these equations can be propagated numerically to create a chimera path, it is difficult to visualise the phase space. To reduce the dimensions of the system to something more easily pictured, the phase space of a single

chain of rowers is used. Graphical representation of their phase space revealed a sub-critical pitchfork bifurcation for the in-phase state, see Appendix E. The onset of the bifurcation can cause the stable state to be 'masked' by its neighbouring unstable states, creating a limit cycle. It is the coexistence of this limit cycle and the stable in-phase state that I believe corresponds to the chimera state in the two chains.

The existence of two stable states is an explanation for the relative robustness of this chimera state. In many reported chimera states the state is unstable or transient. Here the chimera persists for weak noise. At high noise it swaps between the two symmetric solutions too often to be distinguishable, rather than collapsing to in-phase state.

8.8 Overview of the chimera state with hydrodynamic coupling

I found the chimera state using simulations of a simple model for non-uniform oscillators with a hydrodynamic interaction. The resulting states can be interpreted using the eigenmodes of the interaction tensor, and their associated growth rates. Specifically the chimera state appears when the faster growth rates have converged, but not with the slower states. The faster states converging means combination of these states are not suppressed, and the system separates into two subsets. This gives rise to the synchronised and incoherent subsets expected of the chimera state. Alternatively, the system can be analysed by assuming the existence of two subsets and considering their mean interaction. This simple approach links the rower chimera state results to chimera states in Kuramoto oscillators. Additionally, the mean interaction predicts the shift in preferred population geometry from block to chain by comparing the intra-population forces for each geometry. In contrast to the eigenmodes whose growth rates suggest which eigenstates govern the chimera, the mean interaction is a simple indicator of which geometry is preferred.

In conclusion, I have simulated the chimera state using a simple, minimal model for non-linear oscillators interacting at low Reynolds' number. I would expect this to emerge in experimental observations of the chimera state in oscillators with hydrodynamic coupling, and it may play a part in understanding collective dynamics of motile cilia.

Chapter 9

Review and looking to the future

Synchronisation is most often an aid or hindrance to a system, it is rarely considered to be an incidental property. In the scope of hydrodynamic coupling, coordination is important for fluid transport in many biological system, either in terms of transport through the fluid or transporting the fluid. A complete understanding of the role of hydrodynamic coupling in these systems is still being developed, with most studies yet to account for multiple stable waveforms in flagella and focussing on a single set motion. Further there are opportunities stemming from the position dependent nature of the coupling, to physically exhibit a range of more abstract states that are the focus of research from a more theoretical perspective. In this thesis I have linked a generic type of hydrodynamic oscillator to the broader context of phase oscillators. Additionally I have shown the phase dependence of the hydrodynamic interaction can be used as a control mechanism for subset formation in populations of oscillators.

A broad overview of synchronisation behaviour is covered in chapter 2. There is a focus on phase oscillators, which are an important generic class of oscillators and the context in which I later link rowers. The importance of synchronisation in systems with viscous hydrodynamic coupling is also reviewed, with emphasis placed on swimming micro-organisms and epithelial cilia. This review is complemented by chapter 3, where analytical expressions hydrodynamic coupling tensor for common boundary conditions are introduced. These tensors are position dependent, leading to the ability to control oscillator coupling via a physical property of the system, This is an important theme throughout my work, where the coupling between oscillators is controlled either through their style of motion of their geometric configuration.

The work in this thesis can be broken into two parts. The first involves the application of the phase reduction framework to the rower model. In chapter 5 I implemented a phase reduction on identical rowers. The results of which were verified using the known change in anti-phase and in-phase behaviour, as well as the relaxation time. Critically, applying

the phase reduction opens the rower model to being analysed in the context of non-linear dynamical systems techniques. The approach was then adapted for detuned oscillators in chapter 6. The focus here was the difference between mutual synchronisation between oscillators as opposed to oscillator entrainment. The underlying dynamics of the oscillators were critical when determining the inter-oscillator dynamics. The same sensitivity was not found for entraining the oscillator. Furthermore, diverging trends were found when increasing the system size, where large groups of rowers are more able to entrain one another but less susceptible to external flows. These chapters focus on the development of the mean interaction framework for rower, which separates the hydrodynamic coupling term from the principal trajectory of the oscillator. The outcome is an ability to predict the coordination of small systems, be they identical or detuned. This combined with the control provided through the spatial dependence of the coupling allows the configuration of small systems to be designed for a specific outcome.

The other part of this work involves larger arrays of rowers. The size of the system prohibits predictions using the mean interaction. However the formation of subgroups can still be controlled through the position and fundamental characteristics of the oscillators. In chapter 7 the control mechanisms of the subsets are inspired by a specific biological organism, the starfish larva. The modifications to the oscillators had some level of success controlling the subset formation, but it was the geometric changes motivated by the larva's shape changes that demonstrated the most control of the geometry of the subsets. In contrast, the chimera state investigated in chapter 8 was informed by abstract theoretical work involving Kuramoto oscillators. The ability to control the interaction range through a physical mechanism meant rower arrays are a prime candidate for realising this incongruous state. In both cases it is the hydrodynamic coupling that allows the unique level of control of the subset through its physical position.

9.1 Limitations of the techniques applied

Employing phase reduction comes with its own set of limitations. It is reliant upon the assumption of weak coupling and requires changes in the phase difference to occur over time scales longer than one period. This may not be true for biological organisms with a dense cilia carpet. Consequently higher order effect observed *in vitro* will never be reproduced using this framework. There are efforts to include correction to the phase reduction model being developed by the theoretical community, but accounting for the loss of amplitude can never be fully recovered.

The one-dimensional nature of rower oscillations suppresses a certain level of complexity. This could have important implications when applying an external flow. The one-dimensional nature of the oscillations means there can never be any variability in the coupling with the external flow that depends on the rowers position. This would become important when applying a flow to groups of oscillators. Intermittent periods of relatively strong and weak coupling between oscillators could occur if they were moving in and out of alignment with the flow. The restriction of the oscillators to one dimension also requires a certain loss of functionality when converting biological trajectories into oscillators. Variation in the motion of cilium can be captured at least in part by other models, for example as compliance in the rotor orbit. However there is no equivalent mechanism for the rower model, with the driving potential of the rower unaffected and unvaried over time or by additional oscillators. This is a mild example of a much larger problem faced by generic, simple oscillator models of flagella. Namely how to capture the complex and emergent nature of the flagellum, which can often exhibit multiple stable waveforms. How these waveforms emerge from the individual constituents of the flagella is not a factor in the simple models. Consequently they cannot replicate the formation of waveforms nor can they address how one specific waveform would affect the emergent waveform of another flagellum.

This work has benefited from the control over the coupling structure through the presence of a no-slip boundary. The range of different surfaces that can be implemented in simulation is limited. Stemming from the restriction in the ability to determine the analytical expression for the coupling. Recently some progress was made for a Stokeslet near a corner, but more complex and curved surfaces are still out of reach [269]. This restricts the ability to mimic and understand the effect of shape changes seen in organisms like the starfish. It also represents a missing control mechanism in systems of oscillators coupled through hydrodynamic forces. A change in boundary could mitigate unwanted synchronisation in small systems, or to implement some irregular but interesting coupling structure that is of interest to the theoretical, phase oscillator community.

9.2 Further developments stemming from this work

9.2.1 Biologically inspired control mechanisms

The immediate steps following this work are to quantify the shape changes in the starfish larva. This would lead to some estimation in the change in coupling strength, and would assess whether the changes required to produce subsets are accessible for the larva. Assuming the conformation change is within range, this could motive a study into the shape and

conformation across the different multi-flagellated species. To separate the role of shape change and neuronal control, simpler organisms would be a useful starting point. *Paramecium* would be an obvious candidate, though the cell has a stiff elastic membrane that may prohibit the required level of shape change. The generic style of the coupling also means there may be archaeal organisms that could be studied. Some archaea have flagella-like protuberances, but the underlying structure of it is different. These archaeal flagella are used to swim by some organisms. Further, this work also raises questions concerning thinning in cilia carpets that can occur with trauma [168]. Injuries that leading to sections of "dead" cilia could lead to the local synchrony being maintained in subsets, while the whole is no longer able to.

Force profiles derived from flagella

A range of species motion was considered when approximating flagella with a rower force profile. This revealed a change in geometry between the path tracked out single cell flagellum and epithelial cilium. At this point only a few flagella have been tracked per species, and given the high level of simplification further data is required to confidently draw conclusions. A useful starting point would be to compare *Chlamydomonas* and *Volvox* cells. In both cases the flagella can be confidently tracked without problems stemming from high cilia density. *Chlamydomonas* flagella are coupling through the basal body and through the fluid, with increasing amounts of evidence that their basal coupling is necessary for synchronisation. In *Volvox* colonies the sole source of coupling is the fluid. Consequently comparing the two species would be a useful system to test approximations of flagella dynamics and the resulting sensitivity to flow and other oscillators.

The epithelial cilia also bear further investigation, given their change in trajectory geometry. The elongated trajectory for the centre of drag is likely to result from the presence of the cell wall, but whether the altered trajectory leads to differences coupling is an open question. Further the current method used to approximate the flagella does not account for any anisotropy in the coupling. This is not the case near the cell wall, with the flow resulting from motion parallel to the wall decaying slower than the flow perpendicular to the surface. Updating the rower profile approximation to include the anisotropic effects may reveal a strong change in coupling between oscillators.

9.2.2 Further developing the rower model in the context of phase oscillators

The result of the phase reduction applied in chapter 5 is a direct link between rowers and the broader context of phase oscillators. Due to the fundamental understanding of the coupling

mechanism, i.e. hydrodynamic forces, systems of rowers are ideally placed to actualise abstract states that have been investigated theoretically. One possibility would be exhibiting chaos in a small array of oscillators. Bick *et al.* demonstrated that four globally coupled Daido oscillators behave chaotically in the appropriate regime [115]; Daido oscillator refers to a Kuramoto style oscillator with higher order trigonometric coupling terms. The effective interaction between rowers can be tailored through their driving potential. Expressing this interaction has a Fourier series and by comparing with the coupling functions studied in [115], it should be possible to design driving potentials that mimic the form by Bick *et al.* Simulation could then confirm that an array of these oscillators exhibit chaotic behaviour, with the roadmap for demonstrating the state is not transient laid out in [115]. Assuming the state appears when simulated, the system is small enough to be realised experimentally. This would be a the first example of chaos in rower systems, and a rare example of chaos in the low Reynolds' number regime. Another possibility would be to build upon the chimera result. The block and chain states can be produced by numerically solving the phase equations using the "mean" interaction framework. Consequently the sensitivity of the state to its initial conditions and its stability could be further examined from this perspective. The success when reproducing the chimera state using the phase reduced interaction also motivates a replication of the control mechanisms discussed in chapter 7. In this case the system of equations would need to scale up to 60, however it would further confirm the utility of the framework.

The control over the coupling structure through position and the oscillator coupling function via the driving potential establish the rower model as good candidate for exhibiting theoretically studied states. This would be of interest to theoretical audience that investigates phase oscillator, they are excited by new and novel systems in which to test their results. For those studying hydrodynamic coupling, the rower systems are exciting as they expand the potential behaviours that can be attributed to this style of coupling.

9.2.3 Questions related to large arrays of rowers

Concurrently, the phase reduction expands the range of techniques that can be applied to rower systems. Of particular interest are mean-field techniques, as the analytical study of large systems of rowers is currently a obstacle. One classic approach to study oscillators in the mean-field is to employ the Ott-Antonsen ansatz [46, 270]. The ansatz assumes the form of the Fourier series describing the phase probability density; the Fourier components relate to the Daido order parameters. The coefficients allow the time evolution of the order parameter to be evaluated. While the original assumes there is no noise and global coupling, recent research has been tackling how to expand its applicability [79, 271]. This has been in

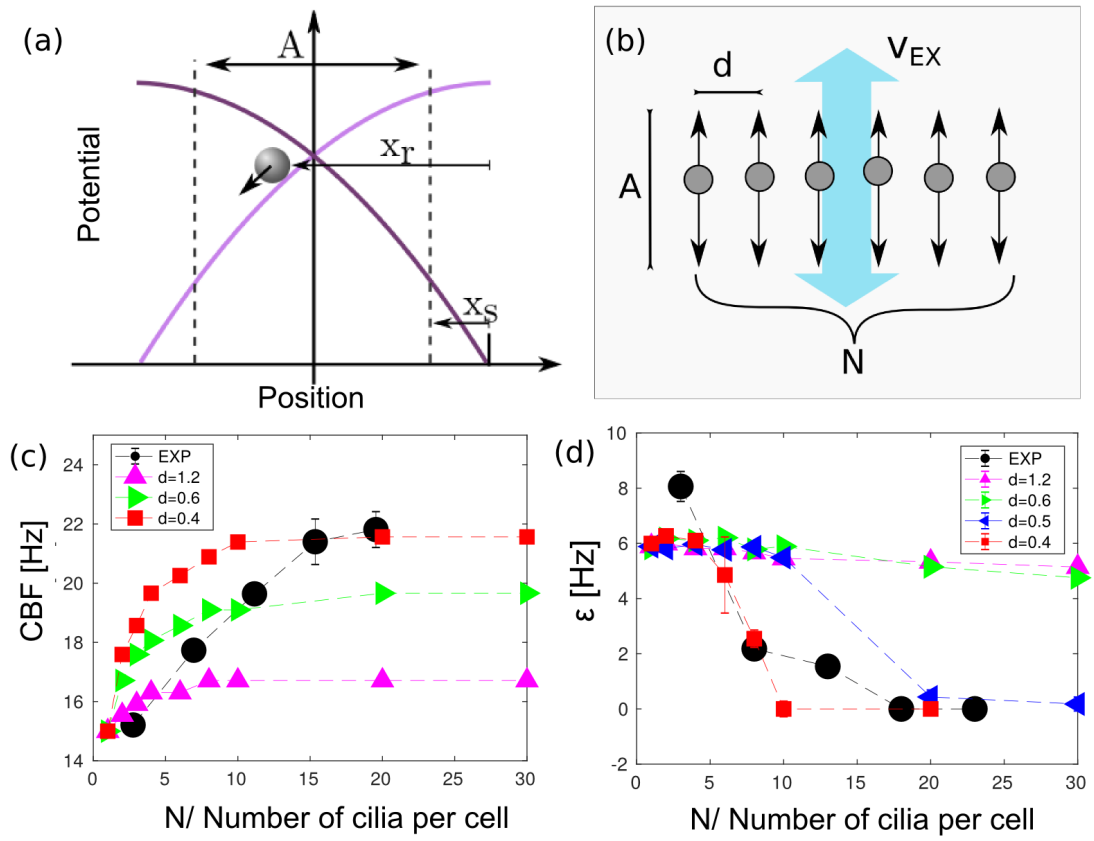

Fig. 9.1 The same trends in frequency and susceptibility to external flows are observed in multi-ciliated cells; adapted from [240]. (a) The trend in the ciliated cells is compared with rowers driven by repulsive traps. (b) The oscillators experience an oscillator flow that is parallel to their direction of motion. (c) The median frequency of cilia increases with the number of cilia in the cell (the black markers). This same trend is seen in simulated rowers, with the magnitude of the increase depending on the coupling strength between them (coloured markers). (d) The susceptibility to an external flow decreases with the cilia number (black markers). This is consistent with the behaviour of rowers (coloured markers).

part motivated by biological systems, where stochastic effects can play a critical role and the coupling structure is often irregular.

Transient or meta-stable states are neglected when considering systems through the perspective of the mean-field. Further they are ill-equipped for non-autonomous systems with some time varying input. These sort of problems can still be addressed through numerical simulation and creative thought. One such problem question motivated by the work in this thesis is the change in entrainment susceptibility when the system size increases. The same effect was recorded in our group in experiments on multi-flagellated cells, see figure 9.1. The susceptibility, as measured through the width of the phase-locking range with the external flow, of the cilia decreases with the number of cilia per cell. A deeper understanding of

this effect could be found by further investigation of rower entrainment in the presence of neighbours. This could ask questions concerning the susceptibility and the driving potential. It was established that the driving potential is critical to determining the coupling strength between oscillators. Consequently the driving potential would be an important consideration for the resulting entrainment range reduction observed larger systems with coupling between oscillators. Alternatively the entrainment can be probed in smaller systems by perturbing a single a rower and quantifying the effect of including one additional oscillator that is immune to the external signal. This route could reveal unexpected states or configurations in which the susceptibility is enhanced rather than inhibited by additional oscillators.

9.3 Looking to the horizon

Coordination and collective behaviour in systems with hydrodynamic coupling is an expansive area of research. At this stage the focus has been on oscillators with one mode of motion that may include some flexibility in the precise trajectory, with some work dabbling in recreating waveforms through internal coupling. My work has reaffirmed the connection between an oscillator in this specific area with a broader class in the study of synchronisation, while also taking advantage of opportunities to control the coupling strength and structure through the style of coupling. The oscillator used here have a single style of motion that results from there underlying mechanics, as is the standard in hydrodynamic models. In truth most real incarnations of oscillators have several styles of motion. Moreover artificial swimmers would like to mimic the versatility seen in biological flagella. The research into the emergence of flagella waveforms is still in its infancy, with questions remaining as to how emergent forms can coexist, switch and interact with one another. Answering these type of question will be critical to building our understanding of systems which rely on coordination between cilia, and will build on the current work involving simpler oscillators. Further, as devices and sensors continue to be miniaturised, more components will be required to function at a scale where viscous forces reign. Deepening our understanding of collective motion resulting from viscous forces will become more important for increasing efficiency and avoiding unintended consequences.

Appendix A

Deriving the Oseen tensor using Fourier transforms

To derive the Oseen matrix I follow the work in [214]. Highlights of the process are also included in [211], which also includes additional detail regarding higher order corrections and the Blake tensor. The process begins with the Stokes equations,

$$-\nabla p(\boldsymbol{r}) + \eta \nabla^2 \boldsymbol{u}(\boldsymbol{r}) = -\boldsymbol{F}\delta(\boldsymbol{r}), \tag{A.1}$$

$$\nabla \cdot \boldsymbol{u} = 0, \tag{A.2}$$

and the boundary condition: $|\boldsymbol{u}(\boldsymbol{r})| \to 0$ as $r \to \infty$. The same notation as in section 3.4 has been used for consistency. While any constant flow can be applied as a boundary condition, they relate to the zero case through a change of reference frame. Taking the divergence of A.1 and using the result of A.2 results in an expression for the pressure in terms of the force,

$$\nabla^2 p(\boldsymbol{r}) = \nabla \cdot \boldsymbol{F}\delta(\boldsymbol{r}). \tag{A.3}$$

The next step is to apply the Fourier transform to the above equation. The process simplifies the derivatives and results in an expression for $\hat{p}$ the Fourier transform of the pressure field in terms of the wave vector $\boldsymbol{k}$.

$$-k^2 \hat{p}(\boldsymbol{k}) = i\boldsymbol{k} \cdot \boldsymbol{F}\hat{p}(\boldsymbol{k}) \tag{A.4}$$

$$\hat{p}(\boldsymbol{k}) = -\frac{i\boldsymbol{k} \cdot \boldsymbol{F}}{k^2}. \tag{A.5}$$

Repeating the same process with equation A.1 and substituting in $\hat{p}$ results in a similar expression for the Fourier transform of the velocity $\hat{\boldsymbol{u}}$,

$$\hat{\boldsymbol{u}}(\boldsymbol{k}) = \frac{1}{\eta k^2}\left(\boldsymbol{F} - \boldsymbol{k}\frac{(\boldsymbol{k}\cdot\boldsymbol{F})}{k^2}\right). \tag{A.6}$$

To proceed it is useful to consider the fundamental solutions of the harmonic and biharmonic functions,

$$\nabla^2\left(\frac{1}{4\pi r}\right) = -\delta(\boldsymbol{r}), \tag{A.7}$$

$$\nabla^4\left(\frac{r}{8\pi}\right) = -\delta(\boldsymbol{r}). \tag{A.8}$$

Calculating the Fourier transform of the above results in functions with the correct k decay,

$$-k^2\mathscr{F}\left(\frac{1}{4\pi r}\right) = -1, \tag{A.9}$$

$$k^4\mathscr{F}\left(\frac{r}{8\pi}\right) = -1. \tag{A.10}$$

Additional effects of the $\boldsymbol{k}$ can be included by considering the derivatives and taking advantage of identities involving Fourier transform. The important cases here are,

$$\mathscr{F}\left(\nabla\frac{1}{4\pi r}\right) = -i\frac{\boldsymbol{k}}{k^2}, \tag{A.11}$$

$$\mathscr{F}\left(\frac{1}{4\pi r}\right) = \frac{1}{k^2}, \quad \mathscr{F}\left(\nabla\otimes\nabla\frac{r}{8\pi}\right) = \frac{\boldsymbol{k}\otimes\boldsymbol{k}}{k^4} \tag{A.12}$$

Comparison of (first equation) with the expression for the pressure field, and comparison of (second set of equation) with the expression for the velocity tensor reveals,

$$\boldsymbol{P}(\boldsymbol{r}) = \nabla\frac{1}{4\pi r} = \frac{1}{4\pi}\frac{\boldsymbol{r}}{r^3}, \tag{A.13}$$

$$\begin{aligned}\boldsymbol{G}(\boldsymbol{r}) &= \frac{1}{4\pi\eta r}\boldsymbol{I} - \nabla\otimes\nabla\frac{r}{8\pi\eta} \\ &= \frac{1}{8\pi\eta r}\left(\boldsymbol{I} + \frac{\boldsymbol{r}\otimes\boldsymbol{r}}{r^2}\right).\end{aligned} \tag{A.14}$$

$\boldsymbol{P}(\boldsymbol{r})$ is the vector field associated with the pressure, and $\boldsymbol{G}(\boldsymbol{r})$ is the tensor for the velocity field, with

$$p(\boldsymbol{r}) = \boldsymbol{P}(\boldsymbol{r})\cdot\boldsymbol{F}, \qquad \boldsymbol{u}(\boldsymbol{r}) = \boldsymbol{G}(\boldsymbol{r})\cdot\boldsymbol{F}. \tag{A.15}$$

Appendix B

Calculating the mean phase interaction for identical oscillators

B.1 Calculating phase response curves for generic potentials

Deriving the expression for the evolution of the natural phase from the x velocity. The steps for finding this technique are taken from [91]. Further depth regarding this technique, the appropriate timescales and perturbation analysis for weakly coupled nonlinear oscillators can be found in [4] and [6], while the ideas behind the method of averaging for oscillators can be found in [230]. Using the chain rule, the phase velocity that includes interaction with other oscillators can be related to the velocity from equation (5.1),

$$\frac{d\phi_i}{dt} = \frac{d\phi_i}{dx_r}\frac{dx_r}{dx_i}\frac{dx_i}{dt} \tag{B.1}$$

$$= \frac{d\phi_i}{dx_r}\frac{dx_r}{dx_i}\sum_{j=1}^{N} H_{ij}^{x} F(x_j) \tag{B.2}$$

$$= \frac{d\phi_i}{dx_r}\frac{dx_r}{dx_i}\left[\frac{1}{\gamma}F(x_i) + \sum_{i\neq j} H_{ij}^{x} F(x_j)\right]. \tag{B.3}$$

Approximating the distance between rowers using the separation between their trap centres removes the time dependence from the hydrodynamic coupling, and the tensor becomes constant. The same approach has been used in [98, 182]. The elements of this new tensor are

labelled with μ_{ij} and explicitly defined in equation (5.3). The phase velocity is then,

$$\frac{d\phi_i}{dt} \approx \frac{d\phi_i}{dx_r}\frac{dx_r}{dx_i}\frac{1}{\gamma}F(x_i) + \sum_{i\neq j}\mu_{ij}\frac{d\phi_i}{dx_r}\frac{dx_r}{dx_i}F(x_j). \tag{B.4}$$

The Oseen tensor assumes far field interaction for a sphere, i.e. $d > a$, ensuring weak coupling with μ_{ij} small. The perturbations in the trap force from the mean should also be small to ensure the coupling is appropriately weak. This was determined empirically by comparing the synchronisation time to the oscillator period. The weak coupling allows the interaction to be approximated by its average over one period.

$$\frac{d\phi_i}{dt} \approx \frac{d\phi_i}{dx_r}\frac{dx_r}{dx_i}\frac{1}{\gamma}F(x_i) + \sum_{i\neq j}\mu_{ij}G_I[\phi_i-\phi_j], \tag{B.5}$$

$$\begin{aligned} G_I[\phi_i-\phi_j] &= \frac{1}{2\pi}\int_0^{2\pi}\left.\frac{d\phi}{dx_r}\right|_{x(\phi_i+\vartheta)}\left.\frac{dx_r}{dx}\right|_{x(\phi_i+\vartheta)}F[x(\phi_j+\vartheta)]\,d\vartheta \\ &= \frac{1}{2\pi}\int_0^{2\pi}\left.\frac{d\phi}{dx_r}\right|_{x(\phi_i-\phi_j+\vartheta)}\left.\frac{dx_r}{dx}\right|_{x(\phi_i-\phi_j+\vartheta)}F[x(\vartheta)]\,d\vartheta. \end{aligned} \tag{B.6}$$

This process is phase reduction theory [4, 62, 91], and has long been applied to weakly interacting oscillators [231, 232]. To simplify the purely self-interacting component (only i dependent), the explicit expression for $\frac{d\phi_i}{dx_r}$ is substituted into the equation,

$$\begin{aligned} \frac{d\phi_i}{dt} &= -\Omega\left|\frac{\gamma}{F(x_i)}\right|\frac{dx_r}{dx_i}\frac{F(x_i)}{\gamma} + \sum_{i\neq j}\mu_{ij}G_I[\phi_i-\phi_j] \\ &= \Omega + \sum_{i\neq j}\mu_{ij}G_I[\phi_i-\phi_j], \end{aligned} \tag{B.7}$$

$$\left|\frac{\gamma}{F(x_i)}\right|\frac{F(x_i)}{\gamma} = \begin{cases} -1 & : x_t < 0 \\ 1 & : x_t > 0 \end{cases}, \qquad \frac{dx_r}{dx} = \begin{cases} 1 & : x_t < 0 \\ -1 & : x_t > 0 \end{cases}. \tag{B.8}$$

The natural phase has a constant velocity when $\mu_{ij} = 0$, but this is no longer true when the rowers interact.

B.2 The mean interaction function for power law potentials

Solving for the specific case where the force $F(x)$ is a power law, the phase and position are related by,

$$\phi(x) = (N_s+1)\pi + C_0 - \frac{\gamma\pi}{k\alpha\tau_0}\frac{1}{2-\alpha}x_r^{2-\alpha}, \tag{B.9}$$

$$C_0 = \frac{\gamma\pi}{k\alpha\tau_0}\frac{x_s^{2-\alpha}}{2-\alpha} = \frac{\pi x_s^{2-\alpha}}{(A+x_s)^{2-\alpha}-x_s^{2-\alpha}}. \tag{B.10}$$

The counter N_s enumerates the number of trap updates that have taken place, which distinguishes between cases with $x_t > 0$ and $x_t < 0$. The constant C_0 ensures the switch point x_s is at $n\pi$, with $\phi \in [0,\pi)$ for $x_t > 0$ (rower moving right) and $\phi \in [\pi, 2\pi)$ for $x_t < 0$ (rower moving left). The initial N_s is chosen to be consistent with $\phi \in [\pi, 2\pi)$ for $x_t < 0$.

The trap force in terms of the natural phase is,

$$F(x(\phi)) = \begin{cases} k\alpha C_1^{\frac{\alpha-1}{2-\alpha}}(\pi - C_0 - \phi)^{\frac{\alpha-1}{2-\alpha}}, & 0 < \phi < \pi \\ -k\alpha C_1^{\frac{\alpha-1}{2-\alpha}}(2\pi - C_0 - \phi)^{\frac{\alpha-1}{2-\alpha}}, & \pi < \phi < 2\pi \end{cases}, \tag{B.11}$$

$$C_1 = \frac{k\alpha\tau_0(2-\alpha)}{\gamma\pi}. \tag{B.12}$$

The constant C_1 is the negative of the coefficient of x_r in equation B.9, and is defined to increase the readability of the expression. For this particular force, the expression for $G_I[\psi]$ can be solved for analytically. In doing so the integral separates into four pieces, two of which are unique, and so $G_I[\psi]$ has four terms for each case,

$$G_I[\psi] = \begin{cases} \frac{\gamma}{\tau_0}\big(g[\psi+\pi, \psi+\pi+C_0] - g[\psi+\pi, \pi+C_0] + g[\psi, \psi+\pi+C_0] - g[\psi, C_0]\big), & \psi \in [-\pi, 0) \\ \frac{\gamma}{\tau_0}\big(g[\psi, \pi+C_0] - g[\psi, \psi+C_0] + g[\psi-\pi, C_0] - g[\psi-\pi, \psi+C_0]\big), & \psi \in [0, \pi) \end{cases}, \tag{B.13}$$

$$g[x,y] = \frac{x^p(-y)^{1-p}}{p-1}\,{}_2F_1[1-p, -p; 2-p, y/x], \qquad p = \frac{1-\alpha}{2-\alpha}. \tag{B.14}$$

${}_2F_1$ is the ordinary hypergeometric function. The average interaction depends on the phase difference and two parameters describing the driving potential, p and C_0. The parameter p depends exclusively on the trap shape α.

B.3 Phase response curves for cubic potentials with mixed curvature

This particular potential is also exactly solvable. The transformation to ϕ is,

$$\phi = \frac{1}{b_0}\log\left(\frac{x_R - x_r}{x_r}\right) - \phi_0, \tag{B.15}$$

$$b_0 = \frac{1}{\pi}\log\left|\frac{1 - x_R/x_s}{1 - x_R/(A + x_s)}\right|, \quad \phi_0 = \frac{1}{b_0}\log\left|\frac{x_R - x_s}{x_s}\right| - (N_s + 1)\pi. \tag{B.16}$$

ϕ_0 shifts the phase such that ϕ is a multiple of π when the rower reverses direction. N_s is a counter that follows the same convention as before, with the switch point x_s at $n\pi$ and $\phi \in [\pi, 2\pi)$ for $x_t < 0$. In the cubic case, the force defined in terms of the natural phase is,

$$F(x(\phi)) = \begin{cases} kx_r^2 \frac{\exp[b_0(\phi+\phi_0)]}{(1+\exp[b_0(\phi+\phi_0)])^2}, & 0 < \phi < \pi \\ -kx_r^2 \frac{\exp[b_0(\phi-\pi+\phi_0)]}{(1+\exp[b_0(\phi-\pi+\phi_0)])^2}, & \pi < \phi < 2\pi \end{cases}. \tag{B.17}$$

The average interaction function can be expressed in terms of both b_0 and ϕ_0, and the phase difference ψ. The explicit form of the function does not provide further insight beyond the Fourier coefficients. Similarly the parameters b_0 and ϕ_0 lack natural interpretations. For completeness the average interaction is,

$$G_I[\psi] = \begin{cases} \frac{\gamma}{\tau_0}\Big(g[e^{b_0(\psi+\pi)}, e^{b_0\phi_0}] - g[e^{b_0(\psi+\pi)}, e^{b_0(\phi_0-\psi)}] \\ \qquad + g[e^{b_0\psi}, e^{b_0(\pi+\phi_0)}] - g[e^{b_0\psi}, e^{b_0(\phi_0-\psi)}]\Big), & \psi \in [-\pi, 0) \\ \frac{\gamma}{\tau_0}\Big(g[e^{b_0\psi}, e^{b_0(\pi-\psi+\phi_0)}] + g[e^{b_0(\psi-\pi)}, e^{b_0(\pi-\psi+\phi_0)}] \\ \qquad - g[e^{b_0\psi}, e^{b_0\phi_0}] - g[e^{b_0(\psi-\pi)}, e^{b_0(\pi+\phi_0)}]\Big), & \psi \in [0, \pi) \end{cases}, \tag{B.18}$$

$$g[x, y] = \frac{1}{b_0 x}\frac{1}{1+y}\left[(x-1)^2 + (y+1)(\log y - b_0\phi_0) + (x^2-1)(1+y)\log(1+y)\right]. \tag{B.19}$$

Appendix C

Applying the phase reduction to detuned oscillators

C.1 Arnold tongues for two oscillator systems

C.1.1 The Arnold tongue for two rowers driven by power law potentials

The two oscillators are not identical in this case, instead one rower has been detuned by scaling the trap strength. Detuning through trap strength doesn't introduce any difference in the phase-position transformation. The transformation depends exclusively on the trap shape, switch point and amplitude. Consequently the phase position transformation for power laws in equation (4.8) still holds. The force in terms of the phase does depend on which rower is being considered. The dependence stems from the trap strength, and so is a coefficient for the general trap structure $F_g(\phi_i)$,

$$F_n(x(\phi_n)) = k_n F_g(\phi_n) \tag{C.1}$$

$$= k_n \begin{cases} \alpha C_1^{-p}(\pi - C_0 - \phi_n)^{-p},\ 0 < \phi < \pi \\ -\alpha C_1^{-p}(2\pi - C_0 - \phi_n)^{-p},\ \pi < \phi < 2\pi \end{cases}, \tag{C.2}$$

$$C_1 = \frac{\pi}{(A + x_s)^{2-\alpha} - x_s^{2-\alpha}}, \quad C_0 = C_1 x_s^{2-\alpha}, \quad p = \frac{1-\alpha}{2-\alpha}. \tag{C.3}$$

The subscript n differentiates between the trap strength for the detuned rower k_d and the unaltered rower k_0. C_0 and p are the same dimensionless parameters used to describe the power law mean interaction in section 5.2.3. Applying the same technique introduced in

chapter 5, the time derivative of the phase can be calculated,

$$\frac{d\phi_n}{dt} = \Omega_n + \left(\frac{d\phi}{dx_r}\frac{dx_r}{dx}\right)\Big|_{\phi_n} \mu_{nn'} F_{n'}(x(\phi_{n'})) \tag{C.4}$$

$$\approx \Omega_n + \frac{\tilde{\mu}_{nn'}}{\gamma}\frac{1}{2\pi}\int_0^{2\pi}\left(\frac{d\phi}{dx_r}\frac{dx_r}{dx}\right)\Big|_{\psi_{nn'}+\theta} F_{n'}(x(\theta))\,d\theta \tag{C.5}$$

$$= \Omega_n + \frac{k_{n'}}{k_n}\tilde{\mu}_{nn'}\Omega_n\frac{1}{\pi}G_{ID}[\psi_{nn'}], \tag{C.6}$$

$$G_{ID}[\psi] = \frac{1}{2}\int_0^{2\pi}\left(\frac{dx_r}{dx}\right)\Big|_{(\psi+\theta)}\left|\frac{1}{F_g(\psi_\theta)}\right| F_g(\theta)\,d\theta. \tag{C.7}$$

In the expression above, the phase velocity of each bead is Ω_n, and the dimensionless hydrodynamic coupling term between them $\tilde{\mu}_{nn'} = \gamma\mu_{nn'}$. For $n = n'$, $\mu_{nn} = 1$ and with only a single pair being considered the subscript notation is now dropped at this point. The evolution of the phase difference can be determined using the phase derivatives, leading to the following expression,

$$\frac{d\psi}{dt} = \Delta\Omega_R + \tilde{\mu}\left(\frac{k_0}{k_d}\frac{\Omega_d}{\pi}G_{ID}[\psi] - \frac{k_d}{k_0}\frac{\Omega_0}{\pi}G_{ID}[-\psi]\right). \tag{C.8}$$

where I have set $\psi = \phi_d - \phi_0$ and $\Delta\Omega_R = \Omega_d - \Omega_0$. To find an expression for the detuning range, the dimensionless interaction function G_{ID} is approximated by truncating the function to its first order Fourier terms. The expression is further simplified by utilising the fact the frequency of each bead is proportional to the trap strength $f_n \propto k_n$,

$$\frac{d\psi}{dt} = \Delta\Omega_R + 2\tilde{\mu}\left[(f_d + f_0)s_1\sin(\psi) - (f_d - f_0)c_1\cos(\psi)\right], \tag{C.9}$$

$$G_{ID}[\psi] \approx c_1\cos(\psi) + s_1\sin(\psi). \tag{C.10}$$

Switching to considering the difference and sum of the frequencies, $f_+ = f_d + f_0$ and $f_- = f_d - f_0$. The evolution of the phase difference is,

$$\frac{d\psi}{dt} = 2\pi f_-\left(1 - \frac{\tilde{\mu}c_1}{\pi}\cos(\psi) + \frac{\tilde{\mu}s_1}{\pi}\frac{f_+}{f_-}\sin(\psi)\right). \tag{C.11}$$

The system has fixed points when $\frac{d\psi}{dt} = 0$. Consequently the rowers can phase lock for,

$$\left|\frac{f_-}{f_+}\right| < \frac{|\tilde{\mu}s_1/\pi|}{\sqrt{1 - \tilde{\mu}^2 c_1^2/\pi^2}}. \tag{C.12}$$

C.1.2 The Arnold tongue for a square external signal and a rower driven by power law potentials

$$\frac{dx}{dt} = \frac{1}{\gamma}F(x) + v_e(t). \tag{C.13}$$

The rower is driven by a power law, and so the same position-phase transformation as in the previous section is used. There is no external flow applied when determining the phase-position transformation.

$$\frac{d\phi_0}{dt} = \frac{d\phi_0}{dx_r}\frac{dx_r}{dx}\frac{dx}{dt} \tag{C.14}$$

$$= \Omega_0 + \Omega_0 \left|\frac{\gamma}{F(x)}\right| v_e(t). \tag{C.15}$$

The external velocity is a square wave, and so the time of the signal can be converted to a phase ϕ_S that is proportional to t. In this format the external signal is expressed as,

$$v_e(\phi_S) = \begin{cases} v_e, & 0 \le \phi_S < \pi \\ -v_e, & \pi \le \phi_S < 2\pi \end{cases}, \qquad \frac{d\phi_S}{dt} = 2\pi f_e = \Omega_S. \tag{C.16}$$

The frequency of the external signal f_e is detuned in this system, with the rower kept at a constant frequency. Using this expression it possible to express the evolution of the rower phase purely in terms of the two phases ϕ_0 and ϕ_S. The interaction can then be averaged using the phase reduction method, the same technique applied to the two rower case,

$$\frac{d\psi_S}{dt} = \Delta\Omega_S + \Omega_0 \left|\frac{\gamma}{F(x(\phi_0))}\right| v_e(\phi_S) \tag{C.17}$$

$$\approx \Delta\Omega_S + \Omega_0 \gamma v_e G_S[\psi_S], \tag{C.18}$$

$$G_S[\psi_S] = \frac{1}{2\pi}\int_0^{2\pi} \mathrm{sign}(v_e(\theta)) \left|\frac{1}{F(x(\psi_S+\theta))}\right| \left|\frac{dx_r}{dx}\right|_{(\psi_S+\theta)} d\theta. \tag{C.19}$$

To distinguish the phase difference with respect to the external signal the subscript S is added to the appropriate parameters: the phase difference $\psi_S = \phi_0 - \phi_S$, the difference in phase velocity $\Delta\Omega_S = 2\pi(f_0 - f_e)$, and the averaged interaction $G_S[\psi_S]$. The interaction here isn't dimensionless, but instead has units of force^{-1}. The phase-locked state is a fixed point of the system. Fixed points satisfy $\frac{d\psi_S}{dt} = 0$, for which solutions exist,

$$\gamma v_e \mathrm{Min}[G_S(\psi_S)] \le \frac{f_0 - f_e}{f_0} \le \gamma v_e \mathrm{Max}[G_S(\psi_S)]. \tag{C.20}$$

$G_S[\psi_S]$ can be calculated explicitly in the power law case. The expression for the force in terms of phase is stated in equation (C.5), with the trap strength k_u, and the phase-position transformation is defined in equation (4.8). Evaluating the integral results in,

$$G_S[\psi_S] = \begin{cases} \frac{C_0^{-p}}{p+1}\left[C_0^{p+1} + (\pi + C_0)^{p+1} - 2(C_0 - \psi_S)^{p+1}\right], & -\pi < \psi_S \leq 0 \\ \frac{C_0^{-p}}{p+1}\left[2(\pi + C_0 - \psi_S)^{p+1} - C_0^{p+1} - (\pi + C_0)^{p+1}\right], & 0 < \psi_S \leq \pi \end{cases} . \quad \text{(C.21)}$$

Deriving the function reveals it is monotonic within the defined domains, consequently the maximum and minimum occur at the limits, i.e. $\psi_S = 0, \pi$. The phase-locking domain for the power law is,

$$\left|\frac{f_0 - f_S}{f_0}\right| \leq \gamma v_e |G_S(\pi)|. \quad \text{(C.22)}$$

C.2 Phase response curves for fitted biological data

C.2.1 Force functions derived from *Chlamydomonas* data

The dimensionless phase interaction $G_{ID}[\psi]$ can be calculated for any strictly increasing driving potential. This includes force profiles that describe the motion of *Chlamydomonas* flagella. Here I layout how I convert the motion of a flagellum into a one-dimensional force profile appropriate for a rower. The original video was provided by Kirsty Wan, and is included as supplementary material in [152]. The cilium were tracked by Nicola Pellicciotta using software developed by Luigi Feriani.

The first step of the conversion is to approximate the cilium with a stokeslet, which is placed on the centre of drag. The software follows the steps laid out in [162]. The centre of drag of the cilium is the average of the positions of the finite elements the flagella is divided into, weighted by their local contributions to the viscous drag obtained via resistive force theory. Examples of the average trajectories are shown in figures C.1(a) and C.1(b). Nicola tracked both the left and right flagella of the *Chlamydomonas*. The second step of the conversion is to split the motion into to groups, to mimic the positive and negative directions when compressed into one-dimension. To group the data and ellipse is fit to the trajectory, and the major axis is used to separate the data. In figure C.1(a) the major axis marked as a black line, and the points are either red or blue to indicate the groups. The third, and penultimate, step of the conversion is to calculate the 'relative position' of the data points. For rowers the relative position describes the distance from the trap, here instead the relative position is measured along the direction of the major axis with the reference points the maximum and minimum values observed. The final step is fit force profile that depends

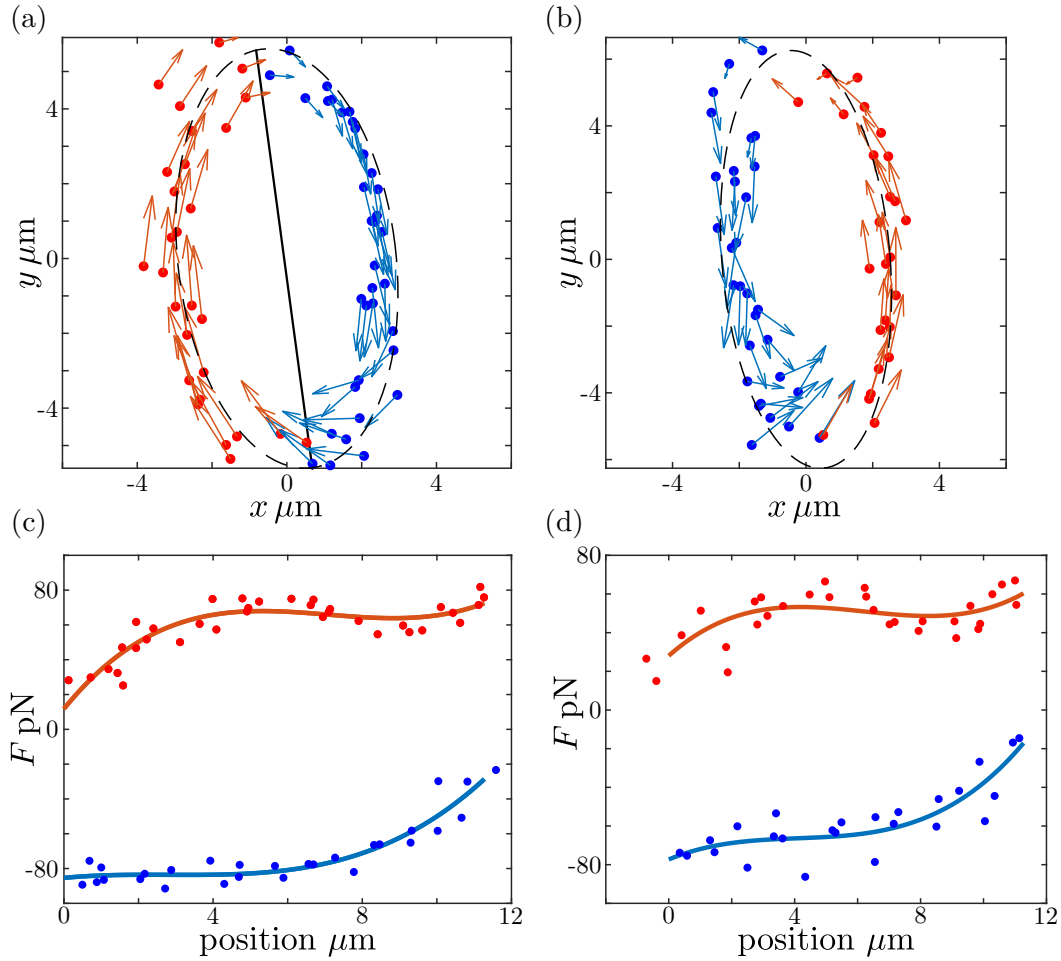

Fig. C.1 Converting trajectories of *Chlamydomonas* flagella into rower force profiles. (a,b) The trajectories of the left and right flagella. The points are grouped using the major axis of the fitted ellipse. Values on the inside half are blue and set as negative, while points on the outside are red and assigned a positive value. (c,d) The force profiles fit to the centre of drag trajectories. To position the points, the distance parallel to the major axis is used. The position here is equivalent to the distance relative to the trap for rowers, and is strictly decreasing following the trajectory. Consequently the position of the blue points is measured relative to the bottom of the ellipse, and the red points from the top.

on the relative position. When fitting, the magnitude of the force is equivalent to the observed value with the sign ascribed by the grouping. Plots of the force profiles for the left and right flagella are shown in figures C.1(c) and C.1(d). The points are the observed values, and the curves the fitted force profiles. The fit takes the form of a cubic polynomial. Stated explicitly the forces for the left (L) and right (R) flagella are,

$$F_L = \begin{cases} 0.0915d_r^3 - 0.7468d_r^2 + 1.9472d_r - 85.222, & F < 0 \\ 0.1873d_r^3 - 3.9336d_r^2 + 25.7968d_r + 13.8413, & F > 0 \end{cases} \tag{C.23}$$

$$F_R = \begin{cases} 0.1212d_r^3 - 1.4902d_r^2 + 6.7439d_r - 77.2897, & F < 0 \\ 0.1397d_r^3 - 2.6061d_r^2 + 14.4851d_r + 28.054, & F > 0 \end{cases} \tag{C.24}$$

The function describing the force for the left flagella is F_L and the amplitude $A = 11.12\mu$m. The force on the right is F_R and the corresponding amplitude $A = 11.27\mu$m. The amplitude is calculated using the average range of the observed points in each group.

To be consistent with the work with power law potentials the external flow strength is,

$$v_{e,Ch} = \frac{v_e}{2Af_R} \cdot 2A_{Ch}f_{Ch}. \tag{C.25}$$

A, f_R, and v_e are the parameters for the power law case, while f_{Ch} is the frequency for the left or right flagella of *Chlamydomonas*. This can be calculated in terms of γ using the force function and amplitude given.

C.2.2 Force functions derived from quadri-flagellated algae

The data from quadri-flagellated data is compressed into a force profile appropriate for a rower via the same method as the *Chlamydomonas*. The conversion is applied to the algae in both the trot and gallop gaits. The videos were provided by Kirsty Wan, and are available in the supplementary material of [163]. The flagella were tracked by Nicola Pellicciotta using the same software developed by Luigi Feriani. The tracked trajectories and the fitted force functions are shown in figure C.2. Figure C.2(a) is a flagellum exhibiting the gallop gait,

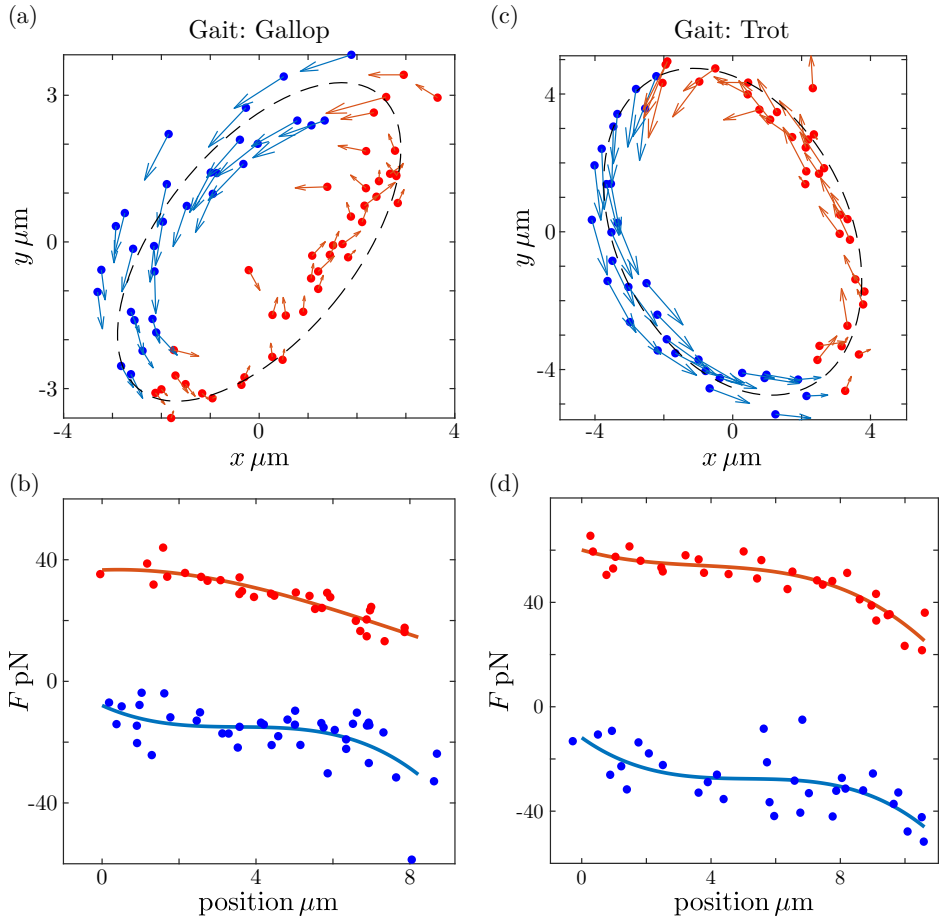

Fig. C.2 Force profiles determined using the motion of quadri-flagellated algae. (a) The trajectory and profile when the algae is in "gallop gait". (b) The force profile is calculated using the same approach as *Chlamydomonas*. (c) The trajectory for a flagellum when alga is exhibiting the trot gait. (c) The force profile calculated for the trot gait.

while figure C.2(c) is the trot gait. The forces for each flagella are,

$$F_{ga} = \begin{cases} -0.1490d_r^3 + 1.5878d_r^2 - 5.7488d_r - 7.9286, & F < 0 \\ 0.0249d_r^3 - 0.5914d_r^2 + 0.4848d_r + 36.6316, & F > 0 \end{cases} \tag{C.26}$$

$$F_{tr} = \begin{cases} -0.1089d_r^3 + 1.6848d_r^2 - 8.845d_r - 11.8437, & F < 0 \\ -0.0724d_r^3 + 0.7921d_r^2 - 3.5468d_r + 60.0766, & F > 0 \end{cases} \tag{C.27}$$

The force for the gallop gait is F_{ga} with the amplitude $A = 8.22\mu$m. The trot force is indicated by F_{tr}, with the corresponding amplitude $A = 10.60\mu$m.

C.2.3 Force profiles derived from mouse brain cilium data

The trajectories of the mouse cilium do not have the same elliptical shape as *Chlamydomonas*. An example of the trajectory seen in mouse brain cilium is shown in figure C.3(a). Instead of fitting the trajectory with an ellipse, second order Fourier series are fit to the x and y data. The result of which is shown in figure C.3(b). The data points are then projected onto the central line of the trajectory. The end points of this line are set using the local minima in the speed calculated with the fitted trajectory. The speed is indicated by the colour of the trajectory in figure C.3(b). If the trajectory has only two minima, they define the end points of the central line. If the trajectory has three minima, the two point are replaced by their midpoint with the two points linked by the slowest trajectory chosen. Alternatively when the trajectory has a strong crescent there are four local minima. In this case the two extremes along the stretched direction are chosen to define the end points of the central line. The data points are projected onto the central line by extending perpendicular rays from each point along the curve. Any data points that are intersected by a ray are placed at the point of origin. The data is grouped as positive and negative forces by considering the change in the projected position and the direction of the force relative to the curve. Force with an angle relative to central axis within the interval $[-\pi/2, \pi/2]$ are considered positive, otherwise they are negative. If the two classifications don't agree, then the point is not included in this fit. An example of the resulting groups are shown in figure C.3(c). The force profile fit is shown in figure C.3(d), where the position is measured from the right end of the curve for positive forces and the left for the negative.

The above process was applied to tracked mouse brain cilia filmed *in vivo* (M.vv) and *in vitro* (M.vt). The tracking was performed by Nicola Pellicciotta using the same software from Luigi Feriani. Nicola Pellicciotta also cultivated the mouse brain cells *in vivo*. Two *in vitro* videos were provided by Lechtreck and are available in [242], which are labelled $M.vt1$ and $M.vt2$. The forces derived from these cilia are,

$$F_{M.vt} = \begin{cases} -0.0782d_r^3 + 0.9900d_r^2 - 3.4113d_r - 0.6593, & F < 0 \\ -0.0560d_r^3 + 0.0432d_r^2 + 1.8470d_r + 1.5787, & F > 0 \end{cases} \tag{C.28}$$

$$F_{M.vv1} = \begin{cases} 0.0059d_r^3 - 0.0662d_r^2 + 0.0819d_r - 0.3073, & F < 0 \\ 0.0013d_r^3 - 0.0263d_r^2 + 0.1611d_r + 0.4440, & F > 0 \end{cases} \tag{C.29}$$

$$F_{M.vv2} = \begin{cases} 0.0012d_r^3 + 0.0065d_r^2 - 0.3286d_r - 0.9662, & F < 0 \\ -0.0060d_r^3 + 0.0772d_r^2 - 0.1291d_r + 1.3765, & F > 0 \end{cases} \tag{C.30}$$

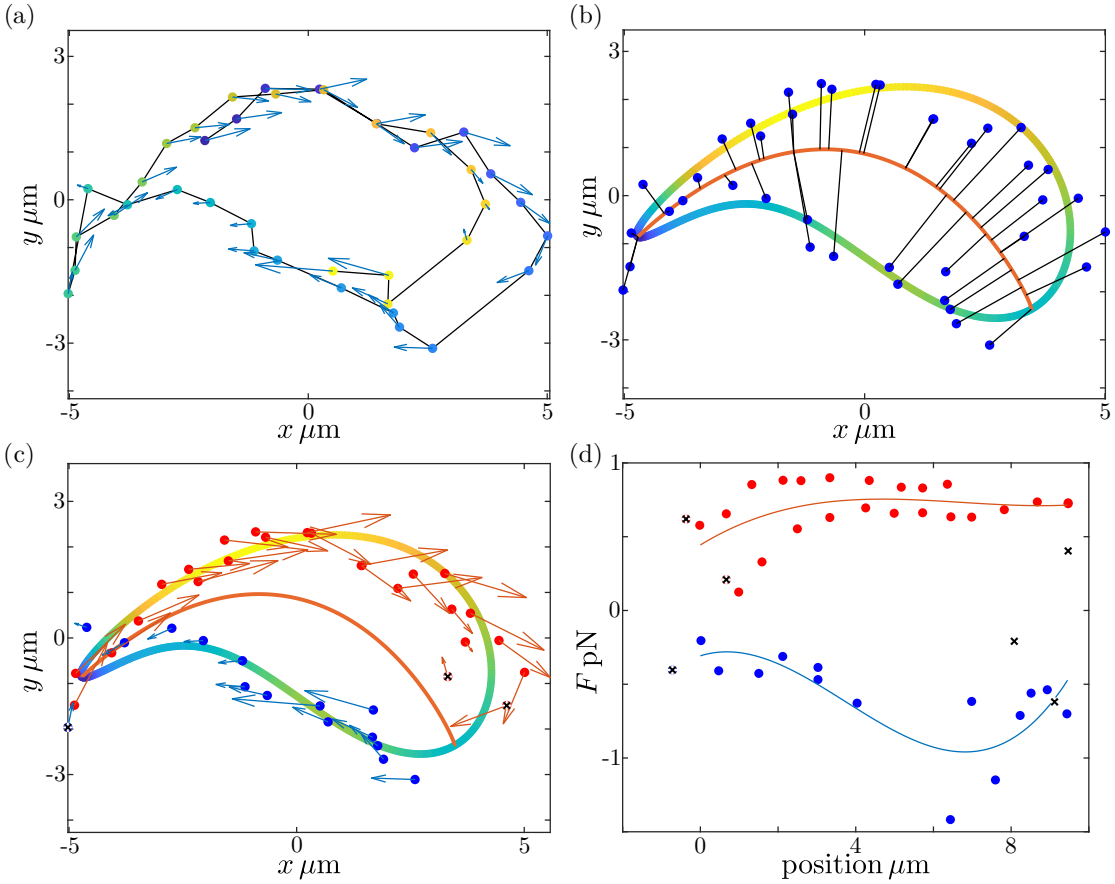

Fig. C.3 Deriving a rower force profile from a centre of drag trajectory taken from a mouse brain cilium. The cilium in this case is observed *in vitro*, with the video sourced from [242]. (a) The original centre of drag trajectory with their associated forces. They are calculated by breaking the flagellum into cylinder elements and averaging their contributions. The trajectory is oriented with respect to the cell wall with x parallel to the wall and y perpendicular. (b) The original trajectory is fit with second order Fourier series, the coloured curve. The data points are then projected onto the centre line of the fit curve. (c) The forces are assigned to be positive (red) or negative (blue) depending on the change in projected position. (d) The force given the position along the trajectory. The position along the trajectory is measured from the left for negative force, and from the right for the positive. This is to align with the shift in trap position of rowers. Cross markers indicate the original direction of the force is inconsistent with the change in projected position. These points are not included when fitting the force profile.

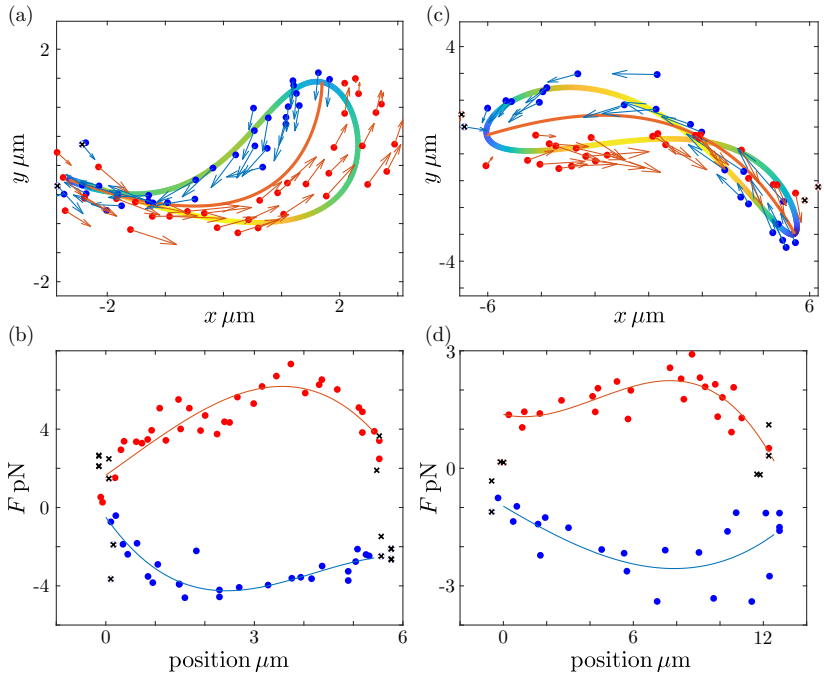

Fig. C.4 Trajectories and force profiles derived using the other mouse cilia. (a) The trajectory of the centre of drag for the *in vivo* video, i.e. $M.vv$. (b) The associated force profile. (c) The trajectory of the second *in vitro* cilium, $M.vv2$. (d) The force profile derived from the trajectory.

The amplitudes associated with the different forces are $A_{M.vt} = 5.53\mu$m, $A_{M.vv1} = 9.45\mu$m, and $A_{M,vv2} = 12.50\mu$m. The grouped data and the fitted profiles for $M.vv2$ and $M.vt1$ cases are plotted in figure C.4.

As in the case with *Chlamydomonas*, the functions $G_{ID}[\psi]$ and $G_S[\psi_S]$ can be calculated numerically using the formula (C.7) and (C.19). To be consistent with the work with power law potentials the external flow strength is,

$$v_{e,MB} = \frac{v_e}{2Af_R} \cdot 2A_{MB}f_{MB}. \tag{C.31}$$

A, f_R, and v_e are the parameters for the power law case, while f_{MB} is the frequency for the mouse brain. This can be calculated in terms of γ using the force profile and amplitude given.

C.2.4 Potential derived from human airways cilium data

The trajectories tracked for the airways cilia have a similar shape to those of the mouse brain cilia. Consequently the potentials are also fit with the second order Fourier series rather than an elliptical orbit. The cells were cultivated and filmed by Maurizio Chioccioli and Luigi Feriani. The original videos are available from [243]. Nicola Pellicciotta tracked the cilia

using the software developed by Luigi Feriani. Four human cilia were tracked, with the associated force profiles,

$$F_{H1} = \begin{cases} 0.0064d_r^3 - 0.0722d_r^2 - 0.1191d_r - 0.9693, & F < 0 \\ 0.0020d_r^3 - 0.0704d_r^2 + 0.5346d_r + 0.2493, & F > 0 \end{cases} \tag{C.32}$$

$$F_{H2} = \begin{cases} -0.0905d_r^3 + 0.5661d_r^2 - 1.2210d_r - 0.3056, & F < 0 \\ 0.0502d_r^3 - 0.4857d_r^2 + 1.3285d_r + 0.8706, & F > 0 \end{cases} \tag{C.33}$$

$$F_{H3} = \begin{cases} -0.1251d_r^3 + 0.7345d_r^2 - 1.2407d_r - 1.4754, & F < 0 \\ -0.1642d_r^3 + 0.4048d_r^2 + 1.2219d_r + 2.2054, & F > 0 \end{cases} \tag{C.34}$$

$$F_{H4} = \begin{cases} 0.0011d_r^3 + 0.0027d_r^2 - 0.1783d_r - 0.0776, & F < 0 \\ 0.0011d_r^3 - 0.0339d_r^2 + 0.2460d_r + 0.1621, & F > 0 \end{cases} \tag{C.35}$$

The amplitudes calculated for the profiles are $A_{H1} = 10.12\mu$m, $A_{H2} = 3.70\mu$m, $A_{H3} = 3.74\mu$m, and $A_{H4} = 10.85\mu$m. The fitted trajectories and profiles for these cases are shown in figure C.5. The magnitude of the external flow is again adapted to be consistent with the new frequency and amplitude

$$v_{e,H} = \frac{v_e}{2Af_R} \cdot 2A_H f_H. \tag{C.36}$$

A, f_R, and v_e are the parameters for the power law case, while f_H is the frequency for the mouse brain. This can be calculated in terms of γ using the force profile and amplitude given.

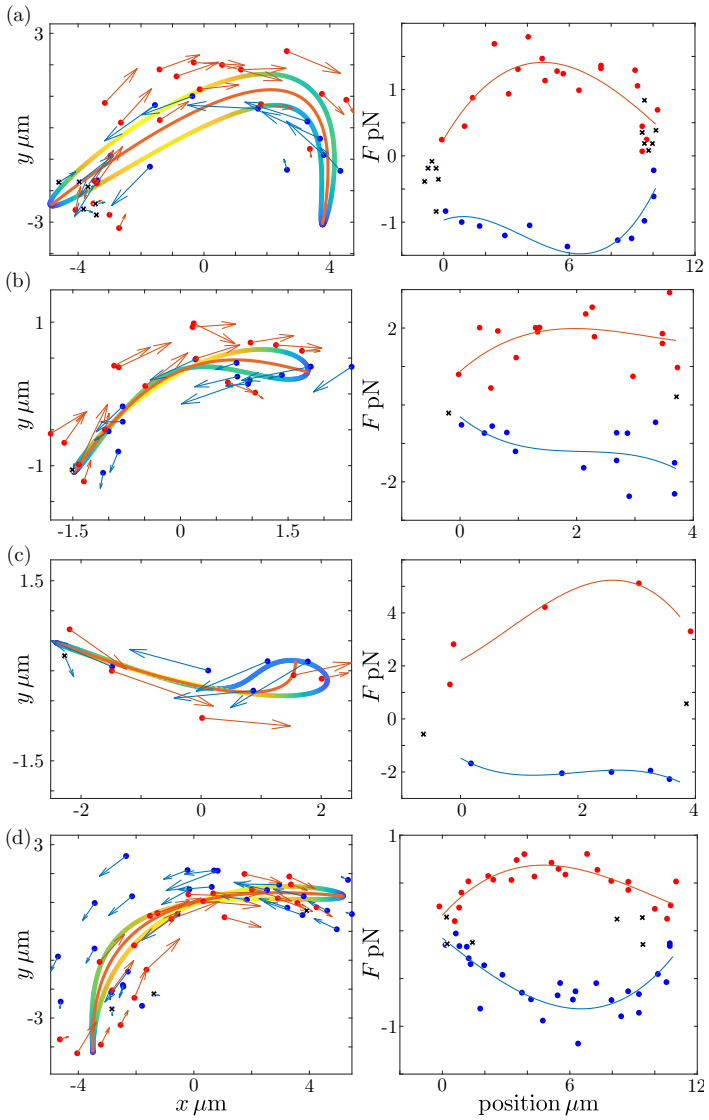

Fig. C.5 Rower force profiles derived from trajectories of the centre of drag describing cilia in human airways. (a) The trajectory for $H1$. (b) The same for $H2$. (c) The trajectory of $H3$. This trajectory and $H2$ have smaller amplitudes. (d) The profile for $H4$.

Appendix D

External signals acting on rower arrays

D.1 Configuration of square rower lattices

The rowers are placed in a square lattice, with the number of rowers B along each side varied. The centre of each trap is separated by d from all its neighbours, see figure D.1. In lattices with more than one bead, i.e. $B > 1$, the rowers have heterogeneous frequencies, drawn from the Gaussian distribution with $\mathcal{N}(f_0, f_0\Delta f)$. The central rower is fixed at the mean of the distribution f_0, because it is used as the measure of lattice phase-locking. This is marked in green in figure D.1(b). In the special case where $B = 1$, the frequency of the central rower is no longer fixed at f_0, instead it too is drawn from a Gaussian distribution. To distinguish this case from the others, the frequency of the rower in the $B = 1$ case is labelled f_1 and the spread of the distribution is $f_0 \cdot \sigma_{f_1}$. The single rower is shown in peach in figure D.1(a) as a reminder of its unique frequency distribution.

In these simulations the Blake tensor is used, to avoid problems with large numbers of rowers interacting. The height was selected to limit the interaction range but not to nearest neighbours, and is $h/d = 3.33$. The lattice spacing is wide, again to avoid large interaction forces, with $d/a = 13.7$.

D.1.1 Implementing the external signal

The external signal is implemented either as a force applied with a square wave structure, or as an external flow felt by the rowers. The two approaches have slightly different implementations, which are discussed in section 4.3.1. The magnitude of the force signal is $F_e/\langle F\rangle_t \in [0, 0.22]$, similarly the magnitude of the external flow is $v_e/(2Af_0) = [0, 0.23]$. The magnitudes of the external signal are kept low to avoid rowers escaping their traps when near the switch point. The frequency of the external signal f_e is set to be above the observed

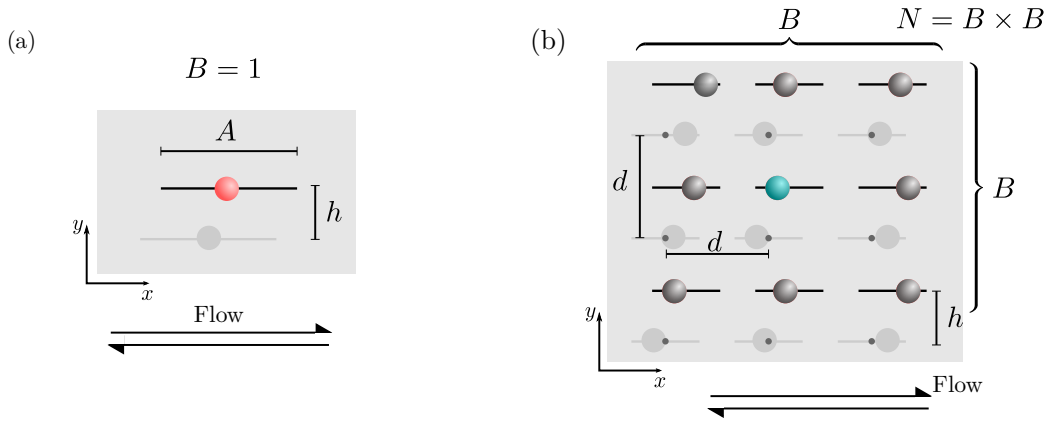

Fig. D.1 The external flow is applied parallel to the direction of oscillation for rowers placed in a square array. (a) The lattice with the single rower has a frequency f_1 drawn from $\mathcal{N}(f_0, \sigma_{f_1})$. The spread of this distribution is chosen to match the observed spread in larger lattices, and is unique to this one rower. (b) In larger arrays, i.e. number of rowers along a side $B > 1$, the rowers are drawn from a similar distribution $\mathcal{N}(f_0, f_0 \cdot \Delta f)$. The central rower, marked in green, is used to measure the phase-locking in the lattice. To reduce the variability in the measure its frequency is fixed to f_0. The trap centres are separated by d in both the x and y directions. In all cases the height above the boundary h is constant, with $h/d = 3.33$.

frequency of a given lattice. The observed frequencies are discussed in depth in section D.4, and the difference between f_e and the observed mean frequency of the central rower $\bar{f}_c$ is $0.184 f_0$.

D.1.2 Simulation parameters for square lattices under external flow

The rowers are driven by harmonic potentials, with a trap strength that ensured the mean period $2\tau_0 = 0.25$s. The simulations were run for $160\tau_0$, with a time step of $8{\cdot}10^{-4}\tau_0$. Each lattice size was run 100 times, with new starting positions and redrawing the frequencies of the non-central rower. The starting position of each bead is drawn from a uniform distribution $\mathcal{U}(-A/2, A/2)$ with $A/a = 1.77$, and the orientation of the trap random. The traps are repulsive, with the switch point at $A + x_s$ and $x_s/a = 0.57$. A small noise term is also included with $\xi = 2.47 \cdot 10^{-4}$, and the average force maintained at $\langle F \rangle_t = 1.8$pN.

To calibrate the frequency of the external flow relative to the measured frequency, 200 simulations were run for lattice with $b > 1$ and no external flow. In these cases the dimensionless spread $\Delta f = 0.12$. Unless stated otherwise the dimensionless spread of the for the single rower is set $\sigma_{f_1} = 0.0411$. This specific value was chosen to coincide with the standard deviation observed in the central rower in the larger lattices. This will be discussed further in

the following section, which focuses on the effects observed in lattices without an external signal.

D.2 Collective effects that are present without an external signal

Rowers often change in frequency when in the presence of other rowers. The use of repulsive traps leads to the in-phase state being preferable. This in turn is associated with an increase in the rower frequency. The spread of the observed frequency distribution is also affected by the lattice size. The two effects are first discussed, and the consequences for such changes in a single bead system are investigated in the next section.

D.2.1 Observed increase in frequency

It has been previously reported and discussed in this thesis that frequency of rowers increases with the number present, see section 6.6 and reference [182]. The mechanism is thought to be the reduction in drag for rowers moving in-phase, and the square lattice should be no different. The frequency of the central rower is important because the detuning between the signal and rower is one of the determining factors of whether phase-locking occurs.

In this particular case the level of synchronisation and the trap strength of the neighbouring rowers has an element of randomness. This is introduced by the Gaussian nature of the intrinsic frequency distribution. The consequence is the measured frequency of the central rower f_m varies between simulation, following some distribution. Information on the measured frequency distributions are shown in figure D.2. The measured frequencies are overlaid with a fitted normal distribution in figure D.2(a). There is a consistent increase in the distribution mean as the lattice size is increased. However, for the $B = 2$ case the data has a skew that precludes the use of a normal distribution. Consequently the centre of $B = 2$ distribution is described by its median rather than the mean.

D.2.2 Reduced impact from Δf

The spread of the measured frequency distribution decreases as the lattice size is increased. This effect is plotted in figure D.2(b). The error bars for the deviation are the 95% confidence interval calculated using a bootstrapping method; re-sample size is 200 and re-sample number is 100000. The larger lattices have the lowest variance resulting from the spread of the intrinsic frequency distribution Δf. This is likely due to an increase in local synchronisation.

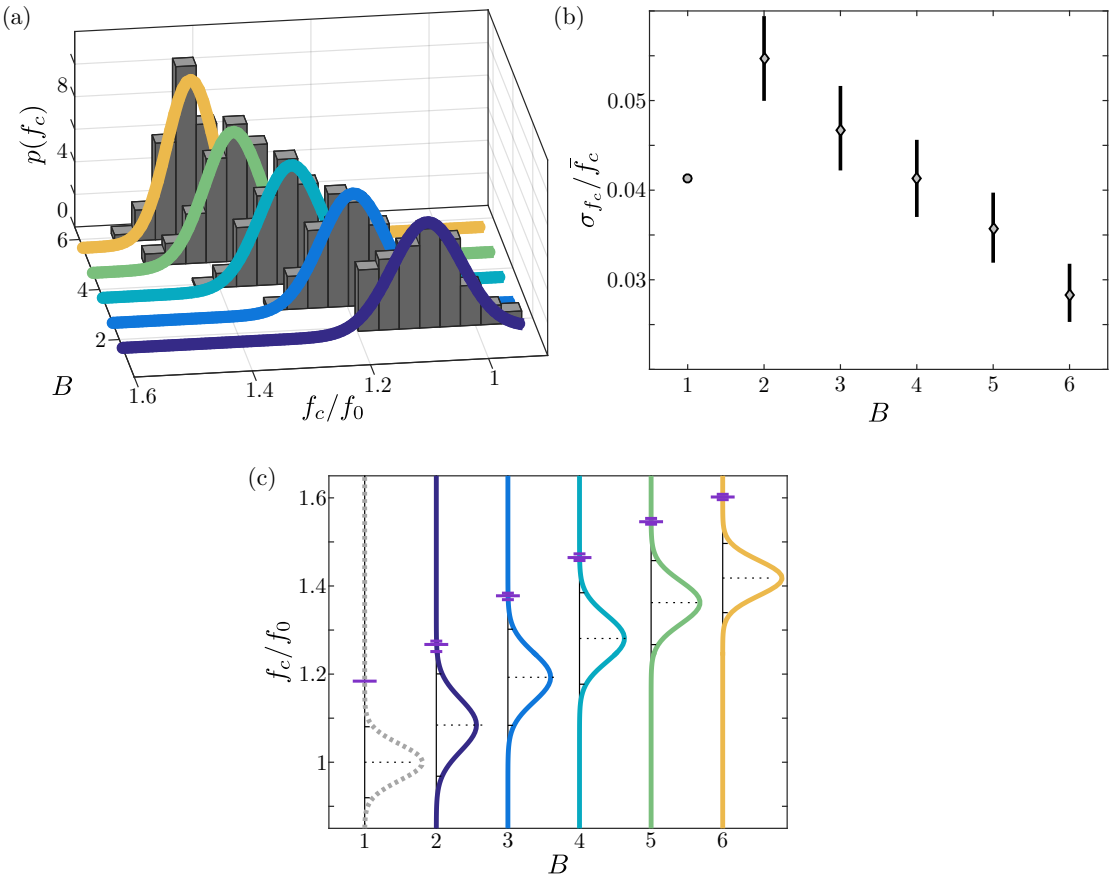

Fig. D.2 Changing the lattice size affects the mean and spread of the unaltered rower in the centre. (a) Distributions of the measured frequency for the central rower f_c as the lattice size is increased. Each distribution is a collection of 200 different simulations where no external signal was applied. The curves are fitted Gaussian distributions to the underlying data. In all cases but $B = 2$ the normal fit seems reasonable. (b) Focusing on the dimensionless spread of the distributions $\sigma_{f_c}/\bar{f}_c$, the trend is a decrease in spread as the lattice size B is increased; the spread is measured in terms of the mean frequency $\bar{f}_c$. The case where $B = 1$ is the special case where the spread is input directly, and was set to be average of the difference lattices. (c) The frequency of the external signal f_e is set relative to the mean of $\bar{f}_c$. The fitted distributions are shown for the different lattices, with the horizontal bars indicating f_e.

The rowers near enough in frequency to phase-lock will form a coherent subset that the central rower couples with, while the remaining rowers are incoherent. Low sampling from the intrinsic distribution should increase the variability in the coherent population size, resulting in larger spread in the observed frequency distribution. The effect of low sampling is ameliorated by increasing the lattice size, and the resulting distributions have lower spread.

D.3 Phase-locking a single bead with random frequency

It has been discussed in chapter 6 that the coupling strength determines the detuning range i.e. interval of frequency difference, that leads to phase-locking. The effect of introducing a distribution to the frequency should lead to some smearing in the transition. Assuming the external signal frequency f_e is above the mean of the rower frequency distribution, then a rower with a frequency slightly above the mean will phase-lock at lower coupling. Conversely if the rower is assigned by chance a frequency below the mean it becomes more difficult to synchronise. This is corroborated in figure D.3(a), which shows the proportion of states that phase-locked when increasing external force. The rower is considered entrained if fewer than 6 phase slips occur after the initial transient period, specifically over the final 67 cycles of the simulation. The results shown are for $\sigma_{f_1} = 0, 0.0132, 0.0263, 0.0394$ and 0.0658, shown as the transition from blue to purple. All the cases pass the midpoint of 0.5 at the same point, with the transition becoming increasingly sharp as the spread is decreased. The midpoint and transition rate as given by the sigmoid fit are shown in figures D.3(b) and D.3(c), which further highlight in constant nature of the midpoint and smearing with spread.

To measure the onset of phase-locking a generic sigmoid function was fit, which took the form,

$$\frac{1}{1+\exp[-(F_e - F_{mp})/\tau_l]}. \tag{D.1}$$

The midpoint of the transition occurs at F_{mp}, with the transition rate capture by τ_l. However, the underlying normal distribution and the constant recorded midpoint value suggest that a sigmoid based of the cumulative distribution function of a normal distribution should be fit,

$$\frac{1}{2}\left[1+\operatorname{erf}\left(\frac{F_e/\langle F\rangle_t - F_{mp}}{\sqrt{2}\sigma_{f_c}/\bar{f}_c}\right)\right]. \tag{D.2}$$

The benefit of this choice is the phase-locking transition rate is already defined a priori by the standard deviation of the frequency distribution. In the notation for the central rower the dimensionless standard deviation is $\sigma_{f_c}/\bar{f}_c$. The midpoint of the transition is F_{mp}, which is dimensionless given the magnitude of the external force F_e is measured relative to the

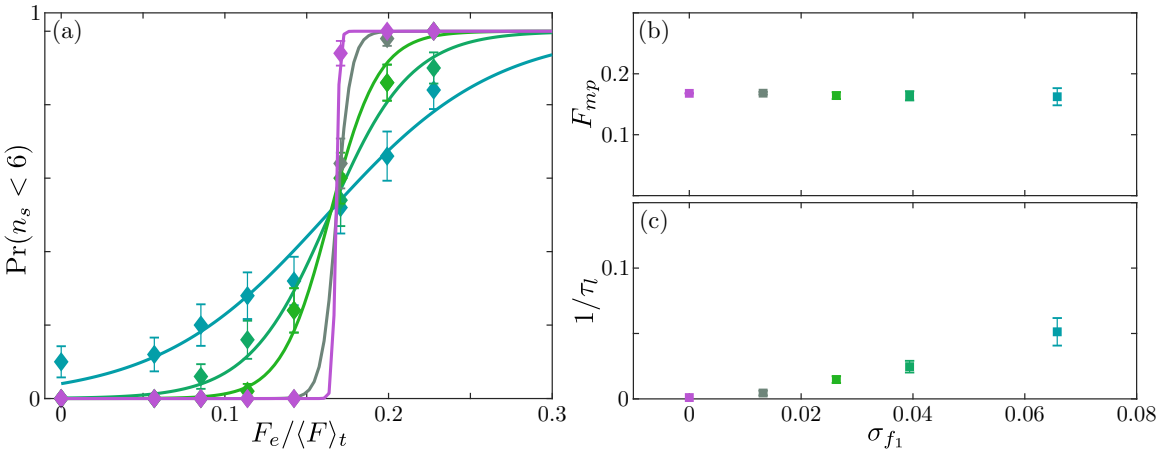

Fig. D.3 The spread of the frequency distribution does not shift the signal strength that lock half of the cases, only the transition rate. (a) The onset of phase-locking as the spread of the single rower frequency f_1 varies; $\sigma_{f_1} = 0, 0.0132, 0.0263, 0.0394$ and 0.0658. Each case is fit with a generic sigmoid with the form of equation (D.1). (b) The midpoint of the fitted curves is constant as the spread is varied. (c) The transition rate in contrast varies approximately linear with the underlying. Consequently future phase-locking curves will be fit with a normal cumulative distribution function form of a sigmoid curve.

average trap force $\langle F\rangle_t$. This is the form of the sigmoid which will be used through out the rest of this work.

D.4 Frequency of the external signal for square lattices

The external flow is set relative to the mean frequency observed for the central rower $\bar{f}_c$ when no external flow is applied. The mean frequency (or median when $B = 2$) for each lattice is calculated for 200 simulations run with no external flow. To have a consistent approach for calculating a confidence interval $\bar{f}_c$, bootstrap resampling is performed. The resulting limits on $\bar{f}_c$ are reported in table D.1. The desired difference between f_e and $\bar{f}_c$ is also reported in the table, as are the resulting values for $\bar{f}_c$ given the initial interval. Simulations are run for all three options of f_e, with the different results providing an estimate for the error resulting from the initial uncertainty in $\bar{f}_c$.

D.5 Phase-locking of the lattices

The force required for phase-locking to occur decreases as the size of the lattice is increased. This is demonstrated in figure D.4. The observed probability of the the system being phase-locked is plotted against the magnitude of the external force in figure D.4(a). The sigmoid

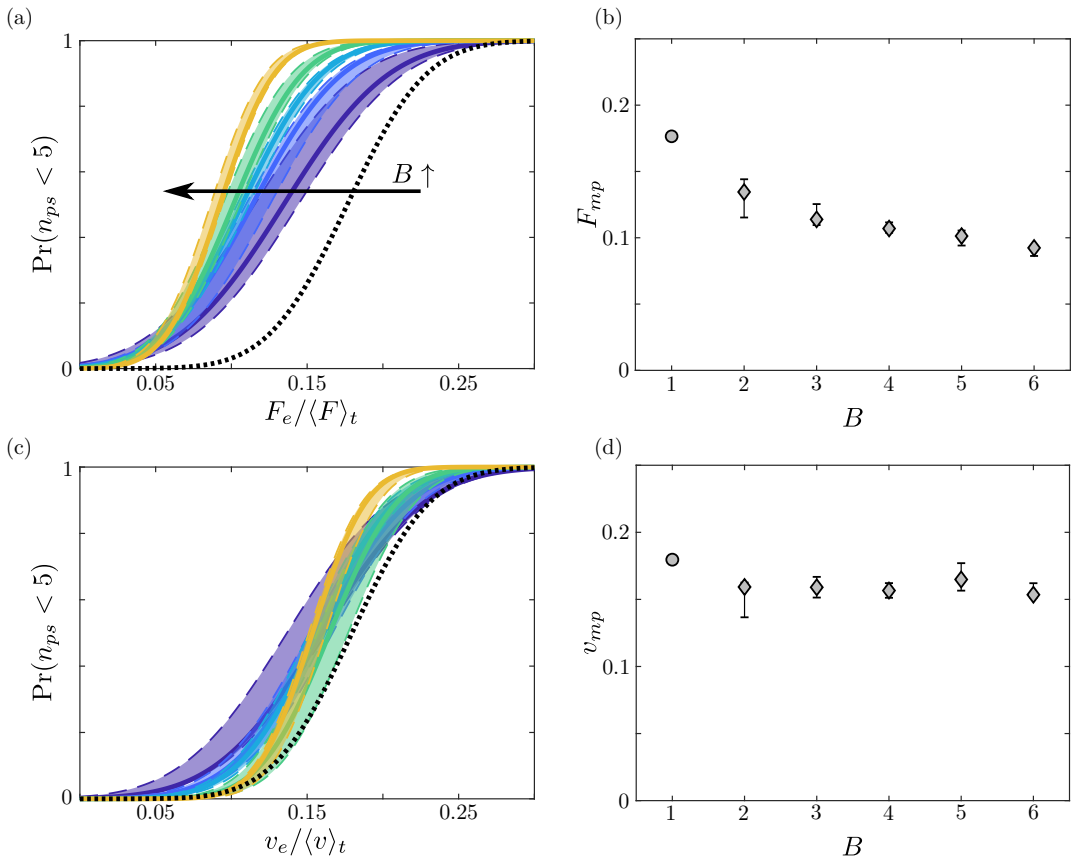

Fig. D.4 Whether the lattice size affects the synchronisation behaviour depends on the method in which the external signal is applied. (a) The onset of phase-locking the external signal is implemented as a force. The colour indicates the size of the lattice, with blue to yellow corresponding to changes from $B = 2$ to $B = 6$. The special case where $B = 1$ marked by the black dotted line. The sigmoid function is the cumulative distribution function for a normal distribution. (b) The force midpoint of the phase-locking sigmoid F_{mp} is plotted against the lattice size. It demonstrates the reduction in phase-locking force is greatest for small lattice sizes with only small changes for the large lattices. The same behaviour is not observed when the external signal is applied as an external flow. (c) The onset of phase-locking as the external velocity $v_e/\langle v\rangle_t$ is increased. There is no obvious translation of the curves when B is increased. (d) The velocity midpoint v_{mp} confirms that lack of translation, with no shift in the midpoint when the lattice size is varied. The midpoint for both the force and velocity of the $B = 1$ case if very similar, indicating that the change is not due to a variation in the magnitude of the signal.

Table D.1 Observed average frequency for the central rower in a lattice with increasing size

B	Mean central frequency $\bar{f}_c/f_0$				External frequency f_e/f_0		
	Low	Average	High	$(f_e-\bar{f}_c)/f_0$	Low	Average	High
2	1.0664	1.0827	1.0913	+0.1843	1.2507	1.2670	1.2755
3	1.1848	1.1928	1.2001	+0.1843	1.3691	1.3771	1.3845
4	1.2736	1.2809	1.2882	+0.1843	1.4579	1.4652	1.4725
5	1.3558	1.3623	1.3693	+0.1843	1.5401	1.5466	1.5536
6	1.4122	1.4180	1.4232	+0.1843	1.5965	1.6024	1.6075

functions are fit to the three different values of f_e for each lattice, with the two extremes marked by dashed line, the internal region coloured, and the results for the average f_e marked by the solid line. The different colours distinguish between the size of the lattice. The transition from dark blue, to green, to yellow corresponds to $B = 2 \rightarrow 6$. The fit for the $B = 1$ case, where the reference rower is drawn from a distribution is shown as the dotted black line. The midpoint on each curve is shifting to the left, indicating the force required to synchronise 50% of the cases is dropping. The drop is greatest when the lattice is small, with the size of the effect decreasing for large lattices. This is underscored in figure D.4(b), where the midpoint is plotted against B.

The same effect does not appear when the external signal is implemented as an external fluid flow. The onset of phase-locking as the velocity of the external flow $v_e/\langle v\rangle_t$ is increased is shown in figure D.4(c). There is no translation in the phase-locking sigmoid when the lattice size is increased. This is confirmed in figure D.4(d), where the velocity midpoint v_{mp} of the fits is plotted against B. There is a small change when switching from the special case of $B = 1$ which has the spread in frequency directly introduced, but no other changes when B is increased. The midpoint for the force and velocity applications is the same when compared for $B = 1$, demonstrating that the change in behaviour is not due to a difference in the magnitude of the external signal.

The different responses to the force and external flow signals stems from the hydrodynamic interaction. The external flow is experienced by all the oscillators, but does not involve the rowers applying a force to the fluid. Consequently it affects the limiting behaviour of the flow field, but isn't directly involved in the coupling between the oscillators. Applying a force to each of the oscillator however, does lead to the rowers applying a force on the fluid. In this way the force applied to one rower also acts on the others at a reduced value. This would explain the reduction in the force required to phase-lock the oscillators as the lattice size is increased. Further it also accounts for the diminishing returns in larger lattices, where the number of oscillators near the central rower has already been capped. Consequently an

external signal can be amplified by including additional hydro-dynamically coupled oscillator if the signal is applied as a force.

Appendix E

Bifurcations in a chain of rowers with varying interaction range

E.1 Prepatory explanation of what is happening here

The full eight rower system is difficult to visualise and represent graphically. Instead a chain of four rowers is used to analytically explore the effect of reducing the interaction. The chain experiences a pitchfork bifurcation as the interaction range is reduced, the features of which can explain some aspects of the chimera state. The Fourier series describing the mean interaction stemming was calculated for the square root potential was limited to 25 non-zero terms. This series was used to calculate the fixed points, their associated eigenvalues, and the example trajectory. Having too few terms in the Fourier series either doesn't recreate the expected behaviour, or converges too slowly.

E.2 Example trajectories

The single chain of four rowers exhibits three different stable states as the interaction range is reduced. When ζ is near one and the interactions are long range, only the in-phase state is observed. However, once the range is sufficiently reduced a stable limit cycle coexists with the in-phase stable point. An example of such a limit cycle is shown in figure E.1(a). The time in the trajectory is indicated by the colour, with black the initial point trending to yellow as time moves forward. Reducing ζ further, the initially stable point becomes unstable via a pitchfork bifurcation, further details are included in the following section. The limit cycle persists through this process, but the shape of the trajectory now twists about the once stable point, see figure E.1(b). Reducing the interaction further, the limit cycle begins to collapse

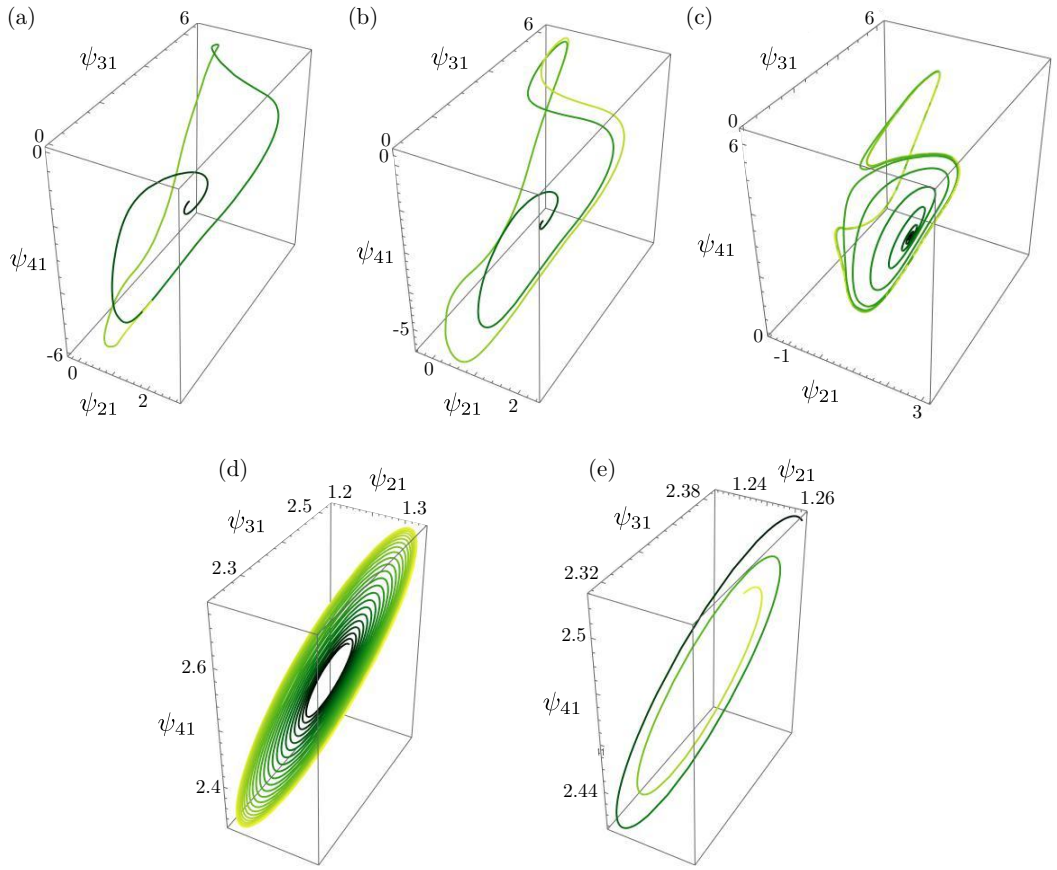

Fig. E.1 The limit cycle appears before being destroyed in a Hopf bifurcation as the interaction range is decreased. (a) The limit first appears when the stable in-phase fixed point is 'masked' by the neighbouring unstable points. This is an example when $\zeta = 1.56$. (b) A trajectory when $\zeta = 1.72$. This is just after the in-phase point has undergone bifurcation with the limit cycle persisting through the process. At this point the limit cycle trajectory twists about the previously stable point. Decreasing the range further, the limit cycle begins to coalesce around the phase-locked state. (c) When $\zeta = 1.9$ the limit cycle still moves through a large sections of phase space, but when $\zeta = 1.94$ as in (d) the limit cycle is restricted to the region about the phase-locking fixed point. (e) After bifurcation when $\zeta = 1.96$ the limit cycle has disappeared and the phase-locked state is now a stable spiral.

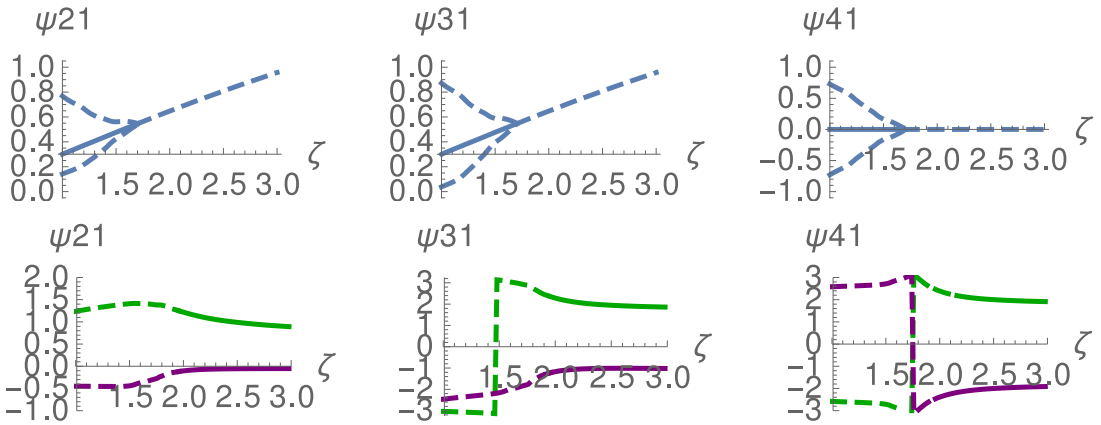

Fig. E.2 Two separate bifurcations occur when the interaction range is restricted. (a) The in-phase fixed point undergoes a subcritical pitchfork bifurcation when the interaction range is decreased. The dashed lines indicate an unstable fixed point, while the solid stipulate the point is stable. The three points converge near $\zeta = 1.7$. (b) The phase-locked state doesn't become stable until $\zeta \approx 2$. I believe this is a Hopf bifurcation, given the absence a limit cycle once the phase-locked state is stable.

onto the phase-locked point. The convergence to the limit cycle also slows during this period, see figuresE.1(c) and E.1(d). Once $\zeta = 1.96$, as in figure E.1(e), the phase-locked point is now stable and the limit cycle is no longer observed. The bifurcations of the mentioned points are expanded upon in the following section.

E.3 Bifurcation of the in-phase and phase-locked states

The system undergoes two bifurcations as the interaction range is reduced. Initially the stable point loses its stability through a sub-critical pitchfork bifurcation. This is shown in figure E.2(a). The three points are shown as the blue lines, with the unstable points marked with the dashed line and the stable with the solid. When the three converge the central stable point is masked. This is what leads to the limit cycle, as there now exists a bounded region which contains no stable point [6]. Increasing ζ further, the three points converge, and the in-phase point is no longer stable. This occurs around $\zeta = 1.75$, and is about the range at which the chain chimera state is no longer observed. The Hopf bifurcation that occurs at the phase-locked point doesn't occur until $\zeta \approx 2$, see figure E.2(b). Unsurprisingly the two chains don't demonstrate the phase-locked behaviour until ζ exceeds this lower limit. Between these two limits the system was unclassified, with no obvious interpretation of the behaviour. Given that the limit cycle is the only stable state in this region, it seems likely that that the two populations were both following a limit cycle. The remaining question

is whether the two chains were so weakly coupled that the two populations are following independent cycles or if the two limit cycles are connected.

References

[1] E. M. Purcell. Life at low Reynolds number. *Am. J. Phys.*, **45**:3–11, 1977.

[2] E. Hamilton and P. Cicuta. Interpreting the synchronisation of driven colloidal oscillators via the mean pair interaction. *New J. Phys.*, 2018.

[3] E. Hamilton, N. Bruot, and P. Cicuta. The chimera state in colloidal phase oscillators with hydrodynamic interaction. *Chaos*, **27**(12):123108, 2017.

[4] M. G. Rosenblum, A. Pikovsky, and J. Kurths. *Synchronization – A universal concept in nonlinear sciences*. Cambridge University Press, Cambridge, 2001.

[5] R. M. McDermott and I. H. Redmount. Coupled classical and quantum oscillators. *arXiv preprints*, 2004.

[6] S. Strogatz. *Nonlinear Dynamics and Chaos: With Applications to Physics, Biology, Chemistry, and Engineering*. Advanced book program. Westview Press, 1994.

[7] L. Glass. Synchronization and rhythmic processes in physiology. *Nature*, **410**(6825):277–284, 2001.

[8] D. Zhang, L. Györgyi, and W. R. Peltier. Deterministic chaos in the belousov–zhabotinsky reaction: Experiments and simulations. *Chaos*, **3**(4):723–745, 1993.

[9] I. R. Epstein and K. Showalter. Nonlinear chemical dynamics: Oscillations, patterns, and chaos. *J. Chem. Phys.*, **100**(31):13132–13147, 1996.

[10] M. Toiya, H. O. González-Ochoa, V. K. Vanag, S. Fraden, and I. R. Epstein. Synchronization of chemical micro-oscillators. *J. Phys. Chem. Lett.*, **1**(8), 2010.

[11] V. Petrov, Q. Ouyang, and H. L. Swinney. Resonant pattern formation in achemical system. *Nature*, **388**:655, 1997.

[12] J. Delgado, N. Li, M. Leda, H. O. González-Ochoa, S. Fraden, and I. R. Epstein. Coupled oscillations in a 1D emulsion of Belousov–Zhabotinsky droplets. *Soft Matter*, **7**:3155–3167, 2011.

[13] S. H. Strogatz and I. Stewart. Coupled oscillators and biological synchronization. *Sci. Am.*, **12**:68–75, 1993.

[14] R. L. Sack, D. Auckley, R. R. Auger, M. A. Carskadon, P. W. Kenneth, M. V. Vitiello, and I. V. Zhdanova. Circadian rhythm sleep disorders: Part I, basic principles, shift work and jet lag disorders. *Sleep*, **30**(11):1460–1483, 2007.

[15] J. Aschoff. Circadian rhythms in man. *Science*, **148**(3676):1427–1432, 1965.

[16] C. R. McClung. Plant circadian rhythms. *Plant Cell*, **18**(4):792–803, 2006.

[17] D. H. Park, D. E. Somers, Y. S. Kim, Y. H. Choy, H. K. Lim, M. S. Soh, H. J. Kim, S. A. Kay, and H. G. Nam. Control of circadian rhythms and photoperiodic flowering by the Arabidopsis GIGANTEA gene. *Science*, **285**(5433):1579–1582, 1999.

[18] A. Samach and G. Coupland. Time measurement and the control of flowering in plants. *Bioessays*, **22**(1):38–47, 2000.

[19] J. Buck and E. Buck. Synchronous fireflies. *Sci. Am.*, **234**(5):74–85, 1976.

[20] B. Ermentrout. An adaptive model for synchrony in the firefly Pteroptyx malaccae. *J. Math. Biol.*, **29**(6):571–585, 1991.

[21] Z. Néda, E. Ravasz, Y. Brechet, T. Vicsek, and A.-L. Barabási. The sound of many hands clapping. *Nature*, **403**:849, 2000.

[22] E. M. Cherry and F. H. Fenton. Visualization of spiral and scroll waves in simulated and experimental cardiac tissue. *New J. Phys.*, **10**(12):125016, 2008.

[23] E. A. Martens, S. Thutupalli, A. Fourrière, and O. Hallatschek. Chimera states in mechanical oscillator networks. *Proc. Natl. Acad. Sci. U.S.A.*, **110**(26):10563–10567, 2013.

[24] H. Guo and E. Kanso. Evaluating efficiency and robustness in cilia design. *Phys. Rev. E*, **93**:033119, 2016.

[25] N. Kolosova, N. Gorenstein, C. M. Kish, and N. Dudareva. Regulation of circadian methyl benzoate emission in diurnally and nocturnally emitting plants. *Plant Cell*, **13**(10):2333–2347, 2001.

[26] R. A. Raguso, R. A. Levin, S. E. Foose, M. W. Holmberg, and L. A. McDade. Fragrance chemistry, nocturnal rhythms and pollination "syndromes" in nicotiana. *Phytochemistry*, **63**(3):265–284, 2003.

[27] P. Dallard, T. Fitzpatrick, A. Flint, A. Low, R. R. Smith, M. Willford, and M. Roche. London Millennium Bridge: Pedestrian-induced lateral vibration. *J. Bridge Eng.*, **6**(6):412–417, 2001.

[28] S. Nakamura and Y. Fujino. Lateral vibration on a pedestrian cable-stayed bridge. *Struct. Eng. Int.*, **12**(4):295–300, 2002.

[29] N. Massad and J. Andersen. Three different ways synchronization can cause contagion in financial markets. *Risks*, **6**(4):104, 2018.

[30] L. S. Junior and I. D. P. Franca. Shocks in financial markets, price expectation, and damped harmonic oscillators. *arXiv preprint arXiv:1103.1992*, 2011.

[31] A. N. Burkitt. A review of the integrate-and-fire neuron model: I. homogeneous synaptic input. *Biol. Cybern.*, **95**(1):1–19, 2006.

[32] R. M. May. Limit cycles in predator-prey communities. *Science*, **177**(4052):900–902, 1972.

[33] B. E. Steinberg, L. Glass, A. Shrier, and G. Bub. The role of heterogeneities and intercellular coupling in wave propagation in cardiac tissue. *Philos. Trans. Royal Soc. A*, **364**(1842):1299–1311, 2006.

[34] G. B. Ermentrout and N. Kopell. Multiple pulse interactions and averaging in systems of coupled neural oscillators. *J. Math. Biol.*, **29**(3):195–217, 1991.

[35] M. C. Mackey and L. Glass. Oscillation and chaos in physiological control systems. *Science*, **197**(4300):287–289, 1977.

[36] K. C. Wedgwood, K. K. Lin, R. Thul, and S. Coombes. Phase-amplitude descriptions of neural oscillator models. *The Journal of Mathematical Neuroscience*, **3**(1):2, 2013.

[37] M. Golubitsky, I. Stewart, P.-L. Buono, and J. Collins. A modular network for legged locomotion. *Physica D*, **115**(1-2):56–72, 1998.

[38] R. E. Mirollo and S. H. Strogatz. Synchronization of pulse-coupled biological oscillators. *SIAM J. Appl. Math.*, **50**(6):1645–1662, 1990.

[39] X. Guardiola, A. Díaz-Guilera, M. Llas, and C. J. Pérez. Synchronization, diversity, and topology of networks of integrate and fire oscillators. *Phys. Rev. E*, **62**:5565–5570, 2000.

[40] C. Van Vreeswijk, L. Abbott, and G. B. Ermentrout. When inhibition not excitation synchronizes neural firing. *J. Comput. Neurosci.*, **1**(4):313–321, 1994.

[41] C. R. Laing and C. C. Chow. Stationary bumps in networks of spiking neurons. *Neural Comput.*, **13**(7):1473–1494, 2001.

[42] M. Timme, F. Wolf, and T. Geisel. Coexistence of regular and irregular dynamics in complex networks of pulse-coupled oscillators. *Phys. Rev. Lett.*, **89**(25):258701, 2002.

[43] Z. Wang and Y. Wang. Pulse-coupled oscillators resilient to stealthy attacks. *IEEE Trans. Signal Process.*, **66**(12):3086–3099, 2018.

[44] J. Borge-Holthoefer, P. Piedrahita, and A. Arenas. Evolving activity cascades on socio-technological networks. *Journal of Computational Social Science*, **1**(1):67–79, 2018.

[45] A. Corral, C. J. Pérez, A. Díaz-Guilera, and A. Arenas. Self-organized criticality and synchronization in a lattice model of integrate-and-fire oscillators. *Phys. Rev. Lett.*, **74**:118–121, 1995.

[46] A. Pikovsky and M. Rosenblum. Dynamics of globally coupled oscillators: Progress and perspectives. *Chaos*, **25**(9):097616, 2015.

[47] G. C. Sethia, A. Sen, and G. L. Johnston. Amplitude-mediated chimera states. *Phys. Rev. E*, **88**:042917, 2013.

[48] A. A. Selivanov, J. Lehnert, T. Dahms, P. Hövel, A. L. Fradkov, and E. Schöll. Adaptive synchronization in delay-coupled networks of stuart-landau oscillators. *Phys. Rev. E*, **85**:016201, 2012.

[49] H. Bi, X. Hu, X. Zhang, Y. Zou, Z. Liu, and S. Guan. Explosive oscillation death in coupled stuart-landau oscillators. *EPL*, **108**(5):50003, 2014.

[50] A. Koseska, E. Volkov, and J. Kurths. Transition from amplitude to oscillation death via turing bifurcation. *Phys. Rev. Lett.*, **111**:024103, 2013.

[51] D. Kondrashov, M. D. Chekroun, and P. Berloff. Multiscale Stuart-Landau emulators: Application to wind-driven ocean gyres. *Fluids*, **3**(1):21, 2018.

[52] P. Le Gal, A. Nadim, and M. Thompson. Hysteresis in the forced stuart–landau equation: Application to vortex shedding from an oscillating cylinder. *J. Fluids Struct.*, **15**(3-4):445–457, 2001.

[53] M. C. Thompson and P. Le Gal. The Stuart–Landau model applied to wake transition revisited. *Eur. J. Mech. B/Fluids*, **23**(1):219–228, 2004.

[54] P. R. Bauer, A. Bonnefont, and K. Krischer. Dissipative solitons and backfiring in the electrooxidation of CO on Pt. *Sci. Rep.*, **5**:16312, 2015.

[55] M. Kantner, E. Schöll, and S. Yanchuk. Delay-induced patterns in a two-dimensional lattice of coupled oscillators. *Sci. Rep.*, **5**:8522, 2015.

[56] B. Hu and C. Zhou. Phase synchronization in coupled nonidentical excitable systems and array-enhanced coherence resonance. *Phys. Rev. E*, **61**:R1001–R1004, 2000.

[57] D. B. Forger, M. E. Jewett, and R. E. Kronauer. A simpler model of the human circadian pacemaker. *J. Biol. Rhythms*, **14**(6):533–538, 1999.

[58] B. Kaplan, I. Gabay, G. Sarafian, and D. Sarafian. Biological applications of the "filtered" van der pol oscillator. *J. Franklin Inst.*, **345**(3):226–232, 2008.

[59] S. Wirkus and R. Rand. The dynamics of two coupled van der Pol oscillators with delay coupling. *Nonlinear Dyn.*, **30**(3):205–221, 2002.

[60] M. Leoni and T. B. Liverpool. Hydrodynamic synchronization of nonlinear oscillators at low Reynolds number. *Phys. Rev. E*, **85**(4):040901, 2012.

[61] J. Rogge and D. Aeyels. Stability of phase locking in a ring of unidirectionally coupled oscillators. *J. Phys. A*, **37**(46):11135, 2004.

[62] H. Nakao. Phase reduction approach to synchronisation of nonlinear oscillators. *Contemp. Phys.*, **57**(2):188–214, 2016.

[63] S. H. Strogatz. From Kuramoto to Crawford: Exploring the onset of synchronization in populations of coupled oscillators. *Physica D*, **143**(1-4):1–20, 2000.

[64] T. Stankovski, T. Pereira, P. V. E. McClintock, and A. Stefanovska. Coupling functions: Universal insights into dynamical interaction mechanisms. *Rev. Mod. Phys.*, **89**:045001, 2017.

[65] D. Wilson and B. Ermentrout. Greater accuracy and broadened applicability of phase reduction using isostable coordinates. *J. Math. Biol.*, **76**(1-2):37–66, 2018.

[66] J. A. Acebrón, L. L. Bonilla, C. J. Pérez Vicente, F. Ritort, and R. Spigler. The Kuramoto model: A simple paradigm for synchronization phenomena. *Rev. Mod. Phys.*, **77**:137–185, 2005.

[67] Z. Zheng, G. Hu, and B. Hu. Phase slips and phase synchronization of coupled oscillators. *Phys. Rev. Lett.*, **81**(24):5318–5321, 1998.

[68] Y. Kim, Y. Ko, and S.-H. Yook. Structural properties of the synchronized cluster on complex networks. *Phys. Rev. E*, **81**(1):011139, 2010.

[69] E. A. Martens, C. R. Laing, and S. H. Strogatz. Solvable model of spiral wave chimeras. *Phys. Rev. Lett.*, **104**:044101, 2010.

[70] E. A. Martens, E. Barreto, S. Strogatz, E. Ott, P. So, and T. Antonsen. Exact results for the kuramoto model with a bimodal frequency distribution. *Phys. Rev. E*, **79**(2):026204, 2009.

[71] J. Gómez-Gardeñes, Y. Moreno, and A. Arenas. Paths to synchronization on complex networks. *Phys. Rev. Lett.*, **98**(3):034101, 2007.

[72] F. A. Rodrigues, T. K. D. Peron, P. Ji, and J. Kurths. The Kuramoto model in complex networks. *Phys. Rep.*, **610**, 2016.

[73] F. Radicchi and H. Meyer-Ortmanns. Reentrant synchronization and pattern formation in pacemaker-entrained Kuramoto oscillators. *Phys. Rev. E*, **74**(2):026203, 2006.

[74] E. Oh, D. S. Lee, B. Kahng, and D. Kim. Synchronization transition of heterogeneously coupled oscillators on scale-free networks. *Phys. Rev. E*, **75**(1):011104, 2007.

[75] D. M. Abrams and S. H. Strogatz. Chimera states for coupled oscillators. *Phys. Rev. Lett.*, **93**:174102, 2004.

[76] D. M. Abrams, R. Mirollo, S. H. Strogatz, and D. A. Wiley. Solvable model for chimera states of coupled oscillators. *Phys. Rev. Lett.*, **101**:084103, 2008.

[77] P. Clusella, A. Politi, and M. Rosenblum. A minimal model of self-consistent partial synchrony. *New J. Phys.*, **18**(9):093037, 2016.

[78] F. D. Smet and D. Aeyels. Partial entrainment in the finite Kuramoto–Sakaguchi model. *Physica D*, **234**(2):81–89, 2007.

[79] K. M. Hannay, D. B. Forger, and V. Booth. Macroscopic models for networks of coupled biological oscillators. *Sci. Adv.*, **4**(8):e1701047, 2018.

[80] H. Hong and S. H. Strogatz. Conformists and contrarians in a Kuramoto model with identical natural frequencies. *arXiv e-prints*, 2011.

[81] E. A. Martens, M. J. Panaggio, and D. M. Abrams. Basins of attraction for chimera states. *New J. Phys.*, **18**(2):022002, 2016.

[82] O'Keeffe Kevin P., Hong Hyunsuk, and Strogatz Steven H. Oscillators that sync and swarm. *Nat. Commun.*, **8**(1):1504, 2017.

[83] E. Tognoli and J. S. Kelso. The metastable brain. *Neuron*, **81**(1):35–48, 2014.

[84] E. Montbrió and D. Pazó. Kuramoto model for excitation-inhibition-based oscillations. *Phys. Rev. Lett.*, **120**:244101, 2018.

[85] K. P. O'Keeffe and S. H. Strogatz. Dynamics of a population of oscillatory and excitable elements. *Phys. Rev. E*, **93**:062203, 2016.

[86] R. G. Andrzejak, C. Rummel, F. Mormann, and K. Schindler. All together now: Analogies between chimera state collapses and epileptic seizures. *Sci. Rep.*, **6**:23000, 2016.

[87] H. Kori, Y. Yamaguchi, and H. Okamura. Accelerating recovery from jet lag: Prediction from a multi-oscillator model and its experimental confirmation in model animals. *Sci. Rep.*, **7**:46702–46702, 2017.

[88] J. Honerkamp. The heart as a system of coupled nonlinear oscillators. *J. Math. Biol.*, **18**(1):69–88, 1983.

[89] Z. Néda, E. Ravasz, T. Vicsek, Y. Brechet, and A.-L. Barabási. Physics of the rhythmic applause. *Phys. Rev. E*, **61**(6):6987, 2000.

[90] K. Wiesenfeld, P. Colet, and S. H. Strogatz. Frequency locking in josephson arrays: Connection with the kuramoto model. *Phys. Rev. E*, **57**:1563–1569, 1998.

[91] J. W. Swift, S. H. Strogatz, and K. Wiesenfeld. Averaging of globally coupled oscillators. *Physica D*, **55**(3):239–250, 1992.

[92] G. Heinrich, M. Ludwig, J. Qian, B. Kubala, and F. Marquardt. Collective dynamics in optomechanical arrays. *Phys. Rev. Lett.*, **107**:043603, 2011.

[93] F. Dorfler and F. Bullo. Synchronization and transient stability in power networks and nonuniform Kuramoto oscillators. *SIAM J. Control Optim.*, **50**(3):1616–1642, 2012.

[94] V. Fioriti, S. Ruzzante, E. Castorini, E. Marchei, and V. Rosato. Stability of a distributed generation network using the Kuramoto models. In R. Setola and S. Geretshuber, editors, *Critical Information Infrastructure Security*, 14–23. Springer Berlin Heidelberg, Berlin, Heidelberg, 2009.

[95] G. V. Osipov, A. S. Pikovsky, M. G. Rosenblum, and J. Kurths. Phase synchronisation effects in a lattice of nonidentical Rossler oscillators. *Phys. Rev. E*, **55**(3), 1997.

[96] H. Shi and W. Li. The application of chaotic oscillator in detecting weak resonant signal of mems resonator. *Rev. Sci. Instrum.*, **88**(5):055003, 2017.

[97] G. Wang, D. Chen, J. Lin, and X. Chen. The application of chaotic oscillators to weak signal detection. *IEEE Trans. Ind. Electron.*, **46**(2):440–444, 1999.

[98] N. Bruot, J. Kotar, F. de Lillo, M. Cosentino Lagomarsino, and P. Cicuta. Driving potential and noise level determine the synchronization state of hydrodynamically coupled oscillators. *Phys. Rev. Lett.*, **109**:164103, 2012.

[99] M. J. Panaggio and D. M. Abrams. Chimera states: Coexistence of coherence and incoherence in networks of coupled oscillators. *Nonlinearity*, **28**(3):R67, 2015.

[100] Y. Kuramoto and D. Battogtokh. Coexistence of coherence and incoherence in nonlocally coupled phase oscillators. *Nonlinear Phenomena in Complex Systems*, **5**(4):380–385, 2002.

[101] D. Dudkowski, J. Grabski, J. Wojewoda, P. Perlikowski, Y. Maistrenko, and T. Kapitaniak. Experimental multistable states for small network of coupled pendula. *Sci. Rep.*, **6**:29833, 2016.

[102] S. Nkomo, M. R. Tinsley, and K. Showalter. Chimera states in populations of nonlocally coupled chemical oscillators. *Phys. Rev. Lett.*, **110**:244102, 2013.

[103] E. Niebur, H. G. Schuster, D. M. Kammen, and C. Koch. Oscillator-phase coupling for different two-dimensional network connectivities. *Phys. Rev. A*, **44**(10):6895, 1991.

[104] A. Arenas, A. Díaz-Guilera, J. Kurths, Y. Moreno, and C. Zhou. Synchronization in complex networks. *Phys. Rep.*, **469**(3):93–153, 2008.

[105] J. L. Rogers and L. T. Wille. Phase transitions in nonlinear oscillator chains. *Phys. Rev. E*, **54**(3):R2193, 1996.

[106] D. Chowdhury and M. C. Cross. Synchronization of oscillators with long-range power law interactions. *Phys. Rev. E*, **82**:016205, 2010.

[107] N. Uchida. Many-body theory of synchronization by long-range interactions. *Phys. Rev. Lett.*, **106**(6):064101, 2011.

[108] S. Gupta, A. Campa, and S. Ruffo. Overdamped dynamics of long-range systems on a one-dimensional lattice: Dominance of the mean-field mode and phase transition. *Phys. Rev. E*, **86**(6):061130, 2012.

[109] P. König, A. K. Engel, and W. Singer. Relation between oscillatory activity and long-range synchronization in cat visual cortex. *Proc. Natl. Acad. Sci. U.S.A.*, **92**(1):290–294, 1995.

[110] S. H. Strogatz. Exploring complex networks. *Nature*, **210**(6825):268–276, 2001.

[111] A. Mishra, S. Saha, D. Ghosh, G. V. Osipov, and S. K. Dana. Traveling chimera pattern in a neuronal network under local gap junctional and nonlocal chemical synaptic interactions. *Opera Med. Physiol.*, (1), 2017.

[112] L. Schmidt, K. Schönleber, K. Krischer, and V. García-Morales. Coexistence of synchrony and incoherence in oscillatory media under nonlinear global coupling. *Chaos*, **24**(1):013102, 2014.

[113] M. Rosenblum and A. Pikovsky. Self-organized quasiperiodicity in oscillator ensembles with global nonlinear coupling. *Phys. Rev. Lett.*, **98**:064101, 2007.

[114] M. J. Panaggio, D. M. Abrams, P. Ashwin, and C. R. Laing. Chimera states in networks of phase oscillators: The case of two small populations. *Phys. Rev. E*, **93**:012218, 2016.

[115] C. Bick, M. Timme, D. Paulikat, D. Rathlev, and P. Ashwin. Chaos in symmetric phase oscillator networks. *Phys. Rev. Lett.*, **107**:244101, 2011.

[116] T. J. Walker. Acoustic synchrony: Two mechanisms in the snowy tree cricket. *Science*, 1969.

[117] D. Gonze, N. Markadieu, and A. Goldbeter. Selection of in-phase or out-of-phase synchronization in a model based on global coupling of cells undergoing metabolic oscillations. *Chaos*, **18**(3):037127, 2008.

[118] B. Novák and J. J. Tyson. Design principles of biochemical oscillators. *Nat. Rev. Mol. Cell Biol.*, **9**:981, 2008.

[119] H. S. Thoke, A. Tobiesen, J. Brewer, P. L. Hansen, R. P. Stock, L. F. Olsen, and L. A. Bagatolli. Tight coupling of metabolic oscillations and intracellular water dynamics in saccharomyces cerevisiae. *PloS one*, **10**(2):1–16, 2015.

[120] S. H. Strogatz and R. E. Mirollo. Collective synchronisation in lattices of non-linear oscillators with randomness. *J. Phys. A*, **21**(13):L699, 1988.

[121] H. Daido. Lower critical dimension for populations of oscillators with randomly distributed frequencies: A renormalization-group analysis. *Phys. Rev. Lett.*, **61**:231–234, 1988.

[122] S. Friedli and Y. Velenik. *Statistical Mechanics of Lattice Systems: A Concrete Mathematical Introduction*. Cambridge University Press, 2017.

[123] P. G. J. Ochab. Synchronization of coupled oscillators in a local one-dimensional kuramoto models. *Acta Phys. Pol. B Proc. Suppl*, **3**:453, 2010.

[124] H. Hajian and A. Banai. Various coupling configurations on the performance of two-dimensional coupled oscillator arrays. *IET Microw. Antenna P.*, **11**(3):426–432, 2016.

[125] H. Hong, H. Park, and M. Y. Choi. Collective synchronization in spatially extended systems of coupled oscillators with random frequencies. *Phys. Rev. E*, **72**:036217, 2005.

[126] K. Kruse and A. Pikovsky. Traveling waves and compactons in phase oscillator lattices . *Chaos*, **18**(3), 2008.

[127] A. Pikovsky and P. Rosenau. Phase compactons. *Physica D*, **218**(1):56–69, 2006.

[128] J. M. Vilar and A. Corral. Synchronization of short-range pulse-coupled oscillators. *arXiv preprint cond-mat/9807403*, 1998.

[129] B.-W. Li and H. Dierckx. Spiral wave chimeras in locally coupled oscillator systems. *Phys. Rev. E*, **93**:020202, 2016.

[130] F. Rogister, K. S. Thornburg, L. Fabiny, M. Möller, and R. Roy. Power-law spatial correlations in arrays of locally coupled lasers. *Phys. Rev. Lett.*, **92**:093905, 2004.

[131] H. H. Lund. Ola—what goes up must fall down: Emergent mexican wave behavior. *Artificial Life and Robotics*, **4**(1):17, 2000.

[132] D. Helbing, I. Farkas, and T. Vicsek. Simulating dynamical features of escape panic. *Nature*, **407**(6803):487, 2000.

[133] E. Bonabeau. Agent-based modeling: Methods and techniques for simulating human systems. *Proc. Natl. Acad. Sci. U.S.A.*, **99**(suppl 3):7280–7287, 2002.

[134] M. Moussaïd, D. Helbing, S. Garnier, A. Johansson, M. Combe, and G. Theraulaz. Experimental study of the behavioural mechanisms underlying self-organization in human crowds. *Proc. R. Soc. London, Ser. B*, rspb–2009, 2009.

[135] D. Helbing, P. Molnár, I. J. Farkas, and K. Bolay. Self-organizing pedestrian movement. *Environ. Plan.*, **28**(3):361–383, 2001.

[136] J. J. Collins and I. Stewart. Hexapodal gaits and coupled nonlinear oscillator models. *Biol. Cybern.*, **68**(4):287–298, 1993.

[137] T. Banerjee, P. S. Dutta, A. Zakharova, and E. Schöll. Chimera patterns induced by distance-dependent power-law coupling in ecological networks. *Phys. Rev. E*, **94**(3), 2016.

[138] N. Uchida, G. Ramin, and R. R. Bennett. Synchronization and collective dynamics of flagella and cilia as hydrodynamically coupled oscillators. *J. Phys. Soc. Jpn.*, **86**(10):101007, 2017.

[139] I. A. Shepelev, A. Zakharova, and T. E. Vadivasova. Chimera regimes in a ring of oscillators with local nonlinear interaction. *Commun. Nonlinear Sci. Numer. Simul.*, **44**:277–283, 2017.

[140] A. Zakharova, M. Kapeller, and E. Schöll. Chimera death: Symmetry breaking in dynamical networks. *Phys. Rev. Lett.*, **112**:154101, 2014.

[141] S. Nkomo, M. R. Tinsley, and K. Showalter. Chimera and chimera-like states in populations of nonlocally coupled homogeneous and heterogeneous chemical oscillators. *Chaos*, **26**(9):094826, 2016.

[142] R. Gopal, V. K. Chandrasekar, A. Venkatesan, and M. Lakshmanan. Observation and characterization of chimera states in coupled dynamical systems with nonlocal coupling. *Phys. Rev. E*, **89**(052914), 2014.

[143] A. Barrat, M. Barthelemy, and A. Vespignani. *Dynamical processes on complex networks*. Cambridge university press, 2008.

[144] T. Banerjee and A. Basu. Active hydrodynamics of synchronization and ordering in moving oscillators. *Phys. Rev. E*, **96**(2):022201, 2017.

[145] G. Taylor. Analysis of the swimming of microscopic organisms. *Proc. R. Soc. Lond. A*, **209**(1099):447–461, 1951.

[146] D. R. Brumley, M. Polin, T. J. Pedley, and R. E. Goldstein. Hydrodynamic synchronization and metachronal waves on the surface of the colonial alga *Volvox carteri*. *Phys. Rev. Lett.*, **109**:268102, 2012.

[147] I. Aranson. The aquatic dance of bacteria. *Physics*, **6**:61, 2013.

[148] E. Lushi, H. Wioland, and R. E. Goldstein. Fluid flows created by swimming bacteria drive self-organization in confined suspensions. *Proc. Natl. Acad. Sci. U.S.A.*, **111**(27):9733–9738, 2014.

[149] S. Basak and A. Raman. Hydrodynamic coupling between micromechanical beams oscillating in viscous fluids. *Phys. Fluids*, **19**(1):017105, 2007.

[150] J. Elgeti, R. G. Winkler, and G. Gompper. Physics of microswimmers—single particle motion and collective behavior: A review. *Rep. Prog. Phys.*, **78**(5):056601, 2015.

[151] R. E. Goldstein. Green algae as model organisms for biological fluid dynamics. *Annu. Rev. Fluid Mech.*, **47**(1):343–375, 2015.

[152] K. Y. Wan and R. E. Goldstein. Rhythmicity, recurrence, and recovery of flagellar beating. *Phys. Rev. Lett.*, **113**(23):238103, 2014.

[153] K. C. Leptos, K. Y. Wan, M. Polin, I. Tuval, A. I. Pesci, and R. E. Goldstein. Antiphase synchronization in a flagellar-dominance mutant of *Chlamydomonas*. *Phys. Rev. Lett.*, **111**:158101, 2013.

[154] C. Battle, C. P. Broedersz, N. Fakhri, V. F. Geyer, J. Howard, C. F. Schmidt, and F. C. MacKintosh. Broken detailed balance at mesoscopic scales in active biological systems. *Science*, **352**(6285):604–607, 2016.

[155] P. Bayly, B. Lewis, E. Ranz, R. Okamoto, R. Pless, and S. Dutcher. Propulsive forces on the flagellum during locomotion of Chlamydomonas reinhardtii. *Biophys. J.*, **100**(11):2716–2725, 2011.

[156] J. S. Guasto, K. A. Johnson, and J. P. Gollub. Oscillatory flows induced by microorganisms swimming in two dimensions. *Phys. Rev. Lett.*, **105**:168102, 2010.

[157] M. Polin, I. Tuval, K. Drescher, J. P. Gollub, and R. E. Goldstein. Chlamydomonas swims with two "gears" in a eukaryotic version of run-and-tumble locomotion. *Science*, **325**(5939):487–490, 2009.

[158] D. R. Brumley, M. Polin, T. J. Pedley, and R. E. Goldstein. Metachronal waves in the flagellar beating of Volvox and their hydrodynamic origin. *J. Royal Soc. Interface*, **12**(108), 2015.

[159] N. Narematsu, R. Quek, K.-H. Chiam, and Y. Iwadate. Ciliary metachronal wave propagation on the compliant surface of Paramecium cells. *Cytoskeleton*, **72**(12):633–646, 2015.

[160] S. Gueron, K. Levit-Gurevich, N. Liron, and J. J. Blum. Cilia internal mechanism and metachronal coordination as the result of hydrodynamical coupling. *Proc. Natl. Acad. Sci. U.S.A.*, **94**(12):6001–6006, 1997.

[161] N. Osterman and A. Vilfan. Finding the ciliary beating pattern with optimal efficiency. *Proc. Natl. Acad. Sci. U.S.A.*, **108**(38):15727–15732, 2011.

[162] D. R. Brumley, K. Y. Wan, M. Polin, and R. E. Goldstein. Flagellar synchronization through direct hydrodynamic interactions. *eLife*, **3**, 2014.

[163] K. Y. Wan and R. E. Goldstein. Coordinated beating of algal flagella is mediated by basal coupling. *Proc. Natl. Acad. Sci. U.S.A.*, **113**(20):E2784–E2793, 2016.

[164] V. F. Geyer, F. Jülicher, J. Howard, and B. M. Friedrich. Cell-body rocking is a dominant mechanism for flagellar synchronization in a swimming alga. *Proc. Natl. Acad. Sci. U.S.A.*, **110**(45):18058–18063, 2013.

[165] J. Elgeti and G. Gompper. Emergence of metachronal waves in cilia arrays. *Proc. Natl. Acad. Sci. U.S.A.*, **110**(12):4470–4475, 2013.

[166] B. M. Friedrich and F. Jülicher. Flagellar synchronization independent of hydrodynamic interactions. *Phys. Rev. Lett.*, **109**:138102, 2012.

[167] R. Faubel, C. Westendorf, E. Bodenschatz, and G. Eichele. Cilia-based flow network in the brain ventricles. *Science*, **353**(6295):176–178, 2016.

[168] A. E. Tilley, M. S. Walters, R. Shaykhiev, and R. G. Crystal. Cilia dysfunction in lung disease. *Annu. Rev. Physiol.*, **77**(1):379–406, 2015.

[169] H. C. Lam, S. M. Cloonan, A. R. Bhashyam, J. A. Haspel, A. Singh, J. F. Sathirapongsasuti, M. Cervo, H. Yao, A. L. Chung, K. Mizumura *et al.* Histone deacetylase 6–mediated selective autophagy regulates COPD-associated cilia dysfunction. *J. Clin. Invest.*, **123**(12):5212–5230, 2013.

[170] M. Kurkowiak, E. Ziętkiewicz, and M. Witt. Recent advances in primary ciliary dyskinesia genetics. *J. Med. Genet.*, **52**(1):1–9, 2014.

[171] W. B. Guggino and B. A. Stanton. New insights into cystic fibrosis: Molecular switches that regulate CFTR. *Nat. Rev. Mol. Cell Biol.*, **7**(6):426–436, 2006.

[172] B. Thomas, A. Rutman, R. A. Hirst, P. Haldar, A. J. Wardlaw, J. Bankart, C. E. Brightling, and C. O'Callaghan. Ciliary dysfunction and ultrastructural abnormalities are features of severe asthma. *J. Allergy Clin. Immunol.*, **126**(4):722–729, 2010.

[173] J. Hessel, J. Heldrich, J. Fuller, M. R. Staudt, S. Radisch, C. Hollmann, B.-G. Harvey, R. J. Kaner, J. Salit, J. Yee-Levin *et al.* Intraflagellar transport gene expression associated with short cilia in smoking and COPD. *PloS one*, **9**(1):e85453, 2014.

[174] S. Sareh, J. Rossiter, A. Conn, K. Drescher, and R. E. Goldstein. Swimming like algae: Biomimetic soft artificial cilia. *J. Royal Soc. Interface*, **10**(78), 2012.

[175] E. Gauger, M. Downton, and H. Stark. Fluid transport at low Reynolds number with magnetically actuated artificial cilia. *Eur. Phys. J. E*, **28**, 2009.

[176] S. Hanasoge, M. Ballard, P. J. Hesketh, and A. Alexeev. Asymmetric motion of magnetically actuated artificial cilia. *Lab Chip*, **17**:3138–3145, 2017.

[177] M. Vilfan, N. Osterman, and A. Vilfan. Magnetically driven omnidirectional artificial microswimmers. *Soft Matter*, **14**:3415–3422, 2018.

[178] R. Dreyfus, J. Baudry, M. L. Roper, M. Fermigier, H. A. Stone, and J. Bibette. Microscopic artificial swimmers. *Nature*, **437**(7060):862–865, 2005.

[179] A. M. Maier, C. Weig, P. Oswald, E. Frey, P. Fischer, and T. Liedl. Magnetic propulsion of microswimmers with dna-based flagellar bundles. *Nano Lett.*, **16**(2):906–910, 2016.

[180] S. Muiños-Landin, K. Ghazi-Zahedi, and F. Cichos. Reinforcement learning of artificial microswimmers. *ArXiv e-prints*, 2018.

[181] N. Bruot and P. Cicuta. Hydrodynamically coupled driven colloidal oscillators as models of motile cilia synchronization and cooperation. *Annu. Rev. Condens. Matter Phys.*, **7**(1), 2016.

[182] J. Kotar, M. Leoni, B. Bassetti, M. C. Lagomarsino, and P. Cicuta. Hydrodynamic synchronization of colloidal oscillators. *Proc. Natl. Acad. Sci. U.S.A.*, **107**(17):7669–7673, 2010.

[183] M. Leoni, B. Bassetti, J. Kotar, P. Cicuta, and M. C. Lagomarsino. Minimal two-sphere model of the generation of fluid flow at low Reynolds numbers. *Phys. Rev. E*, **81**(3):036304, 2010.

[184] Cosentino Lagomarsino, M., Bassetti, B., and Jona, P. Rowers coupled hydrodynamically. Modeling possible mechanisms for the cooperation of cilia. *Eur. Phys. J. B*, **26**(1):81–88, 2002.

[185] M. C. Lagomarsino, P. Jona, and B. Bassetti. Metachronal waves for deterministic switching two-state oscillators with hydrodynamic interaction. *Phys. Rev. E*, **68**:021908, 2003.

[186] N. Bruot and P. Cicuta. Emergence of polar order and cooperativity in hydrodynamically coupled model cilia. *J. Royal Soc. Interface*, **10**(87), 2013.

[187] C. Wollin and H. Stark. Metachronal waves in a chain of rowers with hydrodynamic interactions. *Eur. Phys. J. E*, **34**(4), 2011.

[188] S. Dey, G. Massiera, and E. Pitard. Role of spatial heterogeneity in the collective dynamics of cilia beating in a minimal one-dimensional model. *Phys. Rev. E*, **97**(1):012403, 2018.

[189] G. M. Cicuta, E. Onofri, M. C. Lagomarsino, and P. Cicuta. Patterns of synchronization in the hydrodynamic coupling of active colloids. *Phys. Rev. E*, **85**:016203, 2012.

[190] R. Lhermerout, N. Bruot, G. M. Cicuta, J. Kotar, and P. Cicuta. Collective synchronization states in arrays of driven colloidal oscillators. *New J. Phys.*, **14**(10):105023, 2012.

[191] P. Lenz and A. Ryskin. Collective effects in ciliar arrays. *Phys. Biol.*, **3**(4):285, 2006.

[192] A. Hilfinger, A. K. Chattopadhyay, and F. Jülicher. Nonlinear dynamics of cilia and flagella. *Phys. Rev. E*, **79**:051918, 2009.

[193] N. Uchida and R. Golestanian. Generic conditions for hydrodynamic synchronization. *Phys. Rev. Lett.*, **106**:058104, 2011.

[194] N. Uchida and R. Golestanian. Hydrodynamic synchronization between objects with cyclic rigid trajectories. *Eur. Phys. J. E*, **35**(12):1–14, 2012.

[195] J. Kotar, L. Debono, N. Bruot, S. Box, D. Phillips, S. Simpson, S. Hanna, and P. Cicuta. Optimal hydrodynamic synchronization of colloidal rotors. *Phys. Rev. Lett.*, **111**:228103, 2013.

[196] T. Niedermayer, B. Eckhardt, and P. Lenz. Synchronization, phase locking, and metachronal wave formation in ciliary chains. *Chaos*, **18**(3):037128, 2008.

[197] A. Vilfan and F. Jülicher. Hydrodynamic flow patterns and synchronization of beating cilia. *Phys. Rev. Lett.*, **96**:058102, 2006.

[198] A. Maestro, N. Bruot, J. Kotar, N. Uchida, R. Golestanian, and P. Cicuta. Control of synchronization in models of hydrodynamically coupled motile cilia. *Commun. Phys.*, **1**(1):28, 2018.

[199] Y. Izumida, H. Kori, and U. Seifert. Energetics of synchronization in coupled oscillators rotating on circular trajectories. *Phys. Rev. E*, **94**(5):052221, 2016.

[200] A. Najafi and R. Golestanian. Coherent hydrodynamic coupling for stochastic swimmers . *EPL*, **90**(6):68003, 2010.

[201] R. R. Bennett and R. Golestanian. Phase-dependent forcing and synchronization in the three-sphere model of Chlamydomonas. *New J. Phys.*, **15**:075028, 2013.

[202] R. R. Bennett and R. Golestanian. Emergent run-and-tumble behavior in a simple model of *Chlamydomonas* with intrinsic noise. *Phys. Rev. Lett.*, **110**:148102, 2013.

[203] R. R. Bennett and R. Golestanian. A steering mechanism for phototaxis in Chlamydomonas. *J. Royal Soc. Interface*, **12**(104), 2015.

[204] M. Reichert and H. Stark. Synchronization of rotating helices by hydrodynamic interactions. *Eur. Phys. J. E*, **17**(4):493–500, 2005.

[205] S. Gueron and K. Levit-Gurevich. Energetic considerations of ciliary beating and the advantage of metachronal coordination. *Proc. Natl. Acad. Sci. U.S.A*, **96**(22):12240–12245, 1999.

[206] D. Tam and A. Hosoi. Optimal feeding and swimming gaits of biflagellated organisms. *Proc. Natl. Acad. Sci. U.S.A.*, **108**(3):1001–1006, 2011.

[207] S. Aoyama and R. Kamiya. Cyclical interactions between two outer doublet microtubules in split flagellar axonemes. *Biophys. J*, **89**(5):3261–3268, 2005.

[208] G. R. Bigg. *The Oceans and Climate*. Cambridge University Press, 2 ed., 2003.

[209] A. Quarteroni, M. Tuveri, and A. Veneziani. Computational vascular fluid dynamics: problems, models and methods. *Comput. Vis. Sci.*, **2**(4):163–197, 2000.

[210] T. E. Faber. *Fluid dynamics for physicists*. Cambridge university press, 1995.

[211] M. Manghi, X. Schlagberger, Y.-W. Kim, and R. R. Netz. Hydrodynamic effects in driven soft matter. *Soft Matter*, **2**:653–668, 2006.

[212] R. W. Griffiths. The dynamics of lava flows. *Annu. Rev. Fluid Mech.*, **32**(1):477–518, 2000.

[213] S. Chattopadhyay, R. Moldovan, C. Yeung, and X. Wu. Swimming efficiency of bacterium escherichiacoli. *Proc. Natl. Acad. Sci. U.S.A.*, **103**(37):13712–13717, 2006.

[214] M. Lisicki. Four approaches to hydrodynamic green's functions–the oseen tensors. *arXiv preprint arXiv:1312.6231*, 2013.

[215] J. Blake and A. Chwang. Fundamental singularities of viscous flow. *J. Eng. Math.*, **8**(1):23–29, 1974.

[216] Rosenbaum Joel L. and Witman George B. Intraflagellar transport. *Nat. Rev. Mol. Cell Biol.*, **3**:813, 2002.

[217] N. Bruot. *Hydrodynamic coupling and synchronization of colloidal oscillators*. Ph.D. thesis, University of Cambridge, 2014.

[218] S. Camalet and F. Jülicher. Generic aspects of axonemal beating. *New J. Phys.*, **2**(1):24, 2000.

[219] R. Ma, G. S. Klindt, I. H. Riedel-Kruse, F. Jülicher, and B. M. Friedrich. Active phase and amplitude fluctuations of flagellar beating. *Phys. Rev. Lett.*, **113**, 2014.

[220] F. K. W., V. Jyothish, and S. A. S. Evidence for a self-organized compliant mechanism for the spontaneous steady beating of cilia. *Cytoskeleton*, **74**(7):260–280.

[221] L. Feriani. *Understanding the collective dynamics of motile cilia in human airways*. Ph.D. thesis, University of Cambridge, https://doi.org/10.17863/CAM.35709, 2019.

[222] D. L. Ermak and J. A. McCammon. Brownian dynamics with hydrodynamic interactions. *J. Chem. Phys.*, **69**(4):1352–1360, 1978.

[223] A. W. C. Lau and T. C. Lubensky. State-dependent diffusion: Thermodynamic consistency and its path integral formulation. *Phys. Rev. E*, **76**:011123, 2007.

[224] C. Gardiner. *Handbook of stochastic methods for physics, chemistry, and the natural sciences*. London: Springer, 3 ed., 2004.

[225] L. Damet, G. M. Cicuta, J. Kotar, M. C. Lagomarsino, and P. Cicuta. Hydrodynamically synchronized states in active colloidal arrays. *Soft Matter*, **8**:8672–8678, 2012.

[226] U. Fano. Ionization yield of radiations. ii. the fluctuations of the number of ions. *Phys. Rev.*, **72**:26–29, 1947.

[227] I. V. Afanasieva. Study of distortions in statistics of counts in ccd observations using the fano factor. *Astrophys. Bull.*, **71**(3):366–370, 2016.

[228] A. Papoulis. *Probability, random variables, and stochastic processes / Athanasios Papoulis.* McGraw-Hill series in electrical engineering. Communications and signal processing. McGraw-Hill, New York ; London, 3rd ed. ed., 1991.

[229] I. Kovacic, R. Rand, and S. M. Sah. Mathieu's equation and its generalizations: overview of stability charts and their features. *Appl. Mech. Rev.*, **70**(2):020802, 2018.

[230] R. Grimshaw. *Nonlinear ordinary differential equations*. Applied mathematics and engineering science texts ; 2. Blackwell Scientific, Oxford, 1990.

[231] G. B. Ermentrout and N. Kopell. Frequency plateaus in a chain of weakly coupled oscillators, i. *SIAM J. Math. Anal.*, **15**(2):215–237, 1984.

[232] P. J. Thomas and B. Lindner. Asymptotic phase for stochastic oscillators. *Phys. Rev. Lett.*, **113**:254101, 2014.

[233] S. Shirasaka, W. Kurebayashi, and H. Nakao. Phase-amplitude reduction of transient dynamics far from attractors for limit-cycling systems. *Chaos*, **27**(2):023119, 2017.

[234] K. Taira and H. Nakao. Phase-response analysis of synchronization for periodic flows. *J. Fluid Mech.*, **846**, 2018.

[235] B. Guirao and J.-F. Joanny. Spontaneous creation of macroscopic flow and metachronal waves in an array of cilia. *Biophys. J.*, **92**(6):1900–1917, 2007.

[236] N. Bruot, L. Damet, J. Kotar, P. Cicuta, and M. C. Lagomarsino. Noise and synchronization of a single active colloid. *Phys. Rev. Lett.*, **107**, 2011.

[237] B. Mitchell, R. Jacobs, J. Li, S. Chien, and C. Kintner. A positive feedback mechanism governs the polarity and motion of motile cilia. *Nature*, **447**(7140):97, 2007.

[238] G. Quaranta, M. Aubin-Tam, and D. Tam. Hydrodynamics versus intracellular coupling in the synchronization of eukaryotic flagella. *Phys. Rev. Lett.*, **115**(23):238101, 2015.

[239] G. S. Klindt, C. Ruloff, C. Wagner, and B. M. Friedrich. Load response of the flagellar beat. *Phys. Rev. Lett.*, **117**(25):258101, 2016.

[240] N. Pellicciotta, E. Hamilton, J. Kotar, M. Faucourt, N. Spassky, and P. Cicuta. Synchronisation of mammalian motile cilia with hydrodynamic forces. *Submitted*.

[241] M. Rosenblum and A. Pikovsky. Numerical phase reduction beyond the first order approximation. *Chaos*, **29**(1):011105, 2019.

[242] K.-F. Lechtreck, P. Delmotte, M. L. Robinson, M. J. Sanderson, and G. B. Witman. Mutations in hydin impair ciliary motility in mice. *J Cell Biol*, **180**(3):633–643, 2008.

[243] M. Chioccioli, L. Feriani, Q. Nguyen, J. Kotar, S. D. Dell, V. Mennella, I. Amirav, and P. Cicuta. Quantitative high speed video profiling discriminates between variants of primary ciliary dyskinesia. *Am. J. Resp. Crit. Care Med.*, 2019.

[244] W. Gilpin, V. N. Prakash, and M. Prakash. Vortex arrays and ciliary tangles underlie the feeding–swimming trade-off in starfish larvae. *Nat. Phys.*, **13**:380, 2016.

[245] A. Hamel, C. Fisch, L. Combettes, P. Dupuis-Williams, and C. N. Baroud. Transitions between three swimming gaits in paramecium escape. *Proc. Natl. Acad. Sci. U.S.A.*, **108**(18):7290–7295, 2011.

[246] I. Jung, T. R. Powers, and J. M. Valles Jr. Evidence for two extremes of ciliary motor response in a single swimming microorganism. *Biophysic. J.*, **106**(1):106–113, 2014.

[247] E. Lauga. Emergency cell swimming. *Proc. Natl. Acad. Sci. U.S.A.*, **108**(19):7655–7656, 2011.

[248] H. Machemer. The swimming cell and its world: Structures and mechanisms of orientation in protists. *Eur. J. Protistol.*, **37**(1):3–14, 2001.

[249] G. von Dassow, R. Emlet, and D. Grünbaum. Boundary effects on currents around ciliated larvae. *Nat. Phys.*, **13**(6):520, 2017.

[250] W. Gilpin, V. N. Prakash, and M. Prakash. Reply to 'boundary effects on currents around ciliated larvae'. *Nat. Phys.*, **13**(6):521, 2017.

[251] T. C. Lacalli, T. H. J. Gilmour, and J. E. West. Ciliary band innervation in the bipinnaria larva of pisaster ochraceus. *Philos. Trans. R. Soc. Lond., B, Biol. Sci.*, **330**(1258):371–390, 1990.

[252] K. A. Yankura, C. S. Koechlein, A. F. Cryan, A. Cheatle, and V. F. Hinman. Gene regulatory network for neurogenesis in a sea star embryo connects broad neural specification and localized patterning. *Proc. Natl. Acad. Sci. U.S.A.*, **110**(21):8591–8596, 2013.

[253] C. J. Brokaw. Thinking about flagellar oscillation. *Cell Motil. Cytoskel.*, **66**(8):425–436, 2009.

[254] G. C. Sethia, A. Sen, and F. M. Atay. Clustered chimera states in delay-coupled oscillator systems. *Phys. Rev. Lett.*, **100**(144102), 2008.

[255] A. M. Hagerstrom, T. E. Murphy, R. Roy, P. Hövel, I. Omelchenko, and E. Schöll. Experimental observation of chimeras in coupled-map lattices. *Nat. Phys.*, **8**(9):658–661, 2012.

[256] M. R. Tinsley, S. Nkomo, and K. Showalter. Chimera and phase-cluster states in populations of coupled chemical oscillators. *Nat. Phys.*, **8**(9):662–665, 2012.

[257] P. Ashwin and O. Burylko. Weak chimeras in minimal networks of coupled phase oscillators. *Chaos*, **25**(1):013106, 2015.

[258] A. Röhm, F. Böhm, and K. Lüdge. Small chimera states without multistability in a globally delay-coupled network of four lasers. *Phys. Rev. E*, **94**(4):042204, 2016.

[259] K. Blaha, R. J. Burrus, J. L. Orozco-Mora, E. Ruiz-Beltrán, A. B. Siddique, V. D. Hatamipour, and F. Sorrentino. Symmetry effects on naturally arising chimera states in mechanical oscillator networks. *Chaos*, **26**(11):116307, 2016.

[260] R. Ma, J. Wang, and Z. Liu. Robust features of chimera states and the implementation of alternating chimera states. *EPL*, **91**(4):40006, 2010.

[261] D. Barkley and L. S. Tuckerman. Computational study of turbulent laminar patterns in couette flow. *Phys. Rev. Lett.*, **94**:014502, 2005.

[262] N. Rattenborg, C. Amlaner, and S. Lima. Behavioral, neurophysiological and evolutionary perspectives on unihemispheric sleep. *Neurosci. Biobehav. Rev.*, **24**(8):817–842, 2000.

[263] A. V. Panfilov. Spiral breakup as a model of ventricular fibrillation. *Chaos*, **8**(57), 1998.

[264] X. Tang, T. Yang, I. R. Epstein, Y. Liu, Y. Zhao, and Q. Gao. Novel type of chimera spiral waves arising from decoupling of a diffusible component. *J. Chem. Phys.*, **141**(2):024110, 2014.

[265] D. R. Brumley, N. Bruot, J. Kotar, R. E. Goldstein, P. Cicuta, and M. Polin. Long-range interactions, wobbles and phase defects in chains of fluid-coupled oscillators. *Phys. Rev. Fluids*, **1**:081201, 2016.

[266] G. M. Cicuta, J. Kotar, A. T. Brown, J.-H. Noh, and P. Cicuta. Hydrodynamic coupling in polygonal arrays of colloids: Experimental and analytical results. *Phys. Rev. E*, **81**:051403, 2010.

[267] G. L. Giorgi, F. Galve, G. Manzano, P. Colet, and R. Zambrini. Quantum correlations and mutual synchronization. *Phys. Rev. A*, **85**:052101, 2012.

[268] G. Manzano, F. Galve, G. L. Giorgi, E. Hernández-García, and R. Zambrini. Synchronization, quantum correlations and entanglement in oscillator networks. *Sci. Rep.*, **3**:1439, 2013.

[269] J. Dauparas and E. Lauga. Leading-order Stokes flows near a corner. *IMA J. Appl. Math.*, **83**(4):590–633, 2018.

[270] E. Ott and T. M. Antonsen. Low dimensional behavior of large systems of globally coupled oscillators. *Chaos*, **18**(3):037113, 2008.

[271] B. Pietras and A. Daffertshofer. Ott-antonsen attractiveness for parameter-dependent oscillatory systems. *Chaos*, **26**(10):103101, 2016.